Max-Planck-Institut
für Plasmaphysik

Scientific Report 2017 - 2020

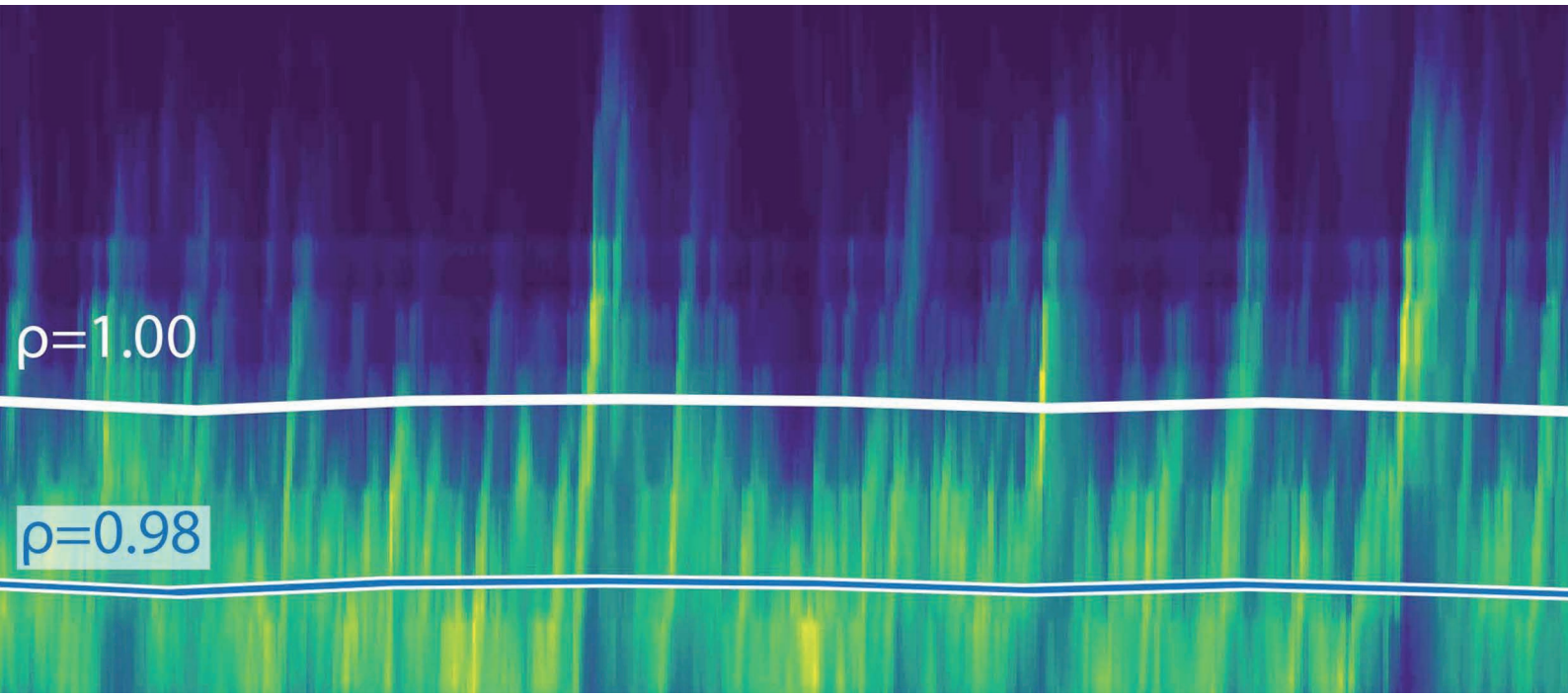

MAX PLANCK GESELLSCHAFT

HELMHOLTZ
SPITZENFORSCHUNG FÜR
GROSSE HERAUSFORDERUNGEN

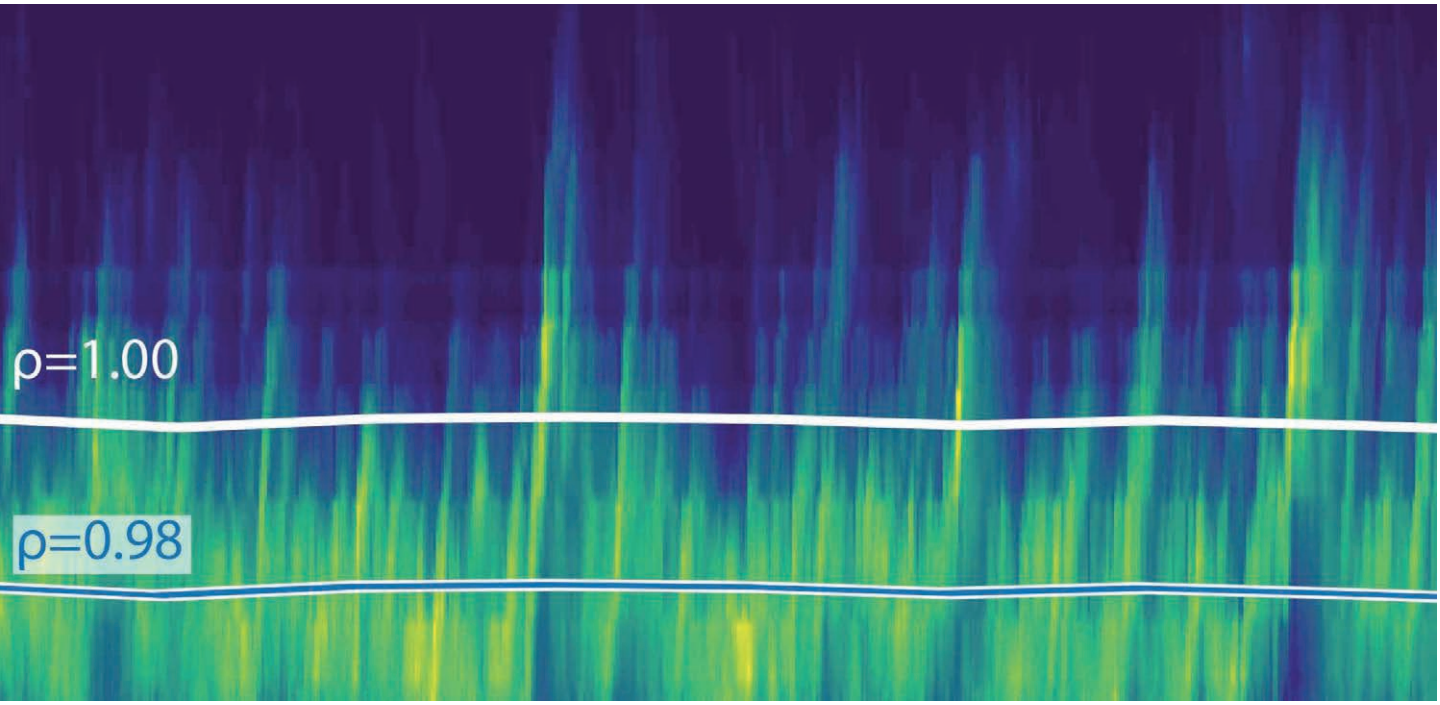

Quasi-continuous power exhaust in ASDEX Upgrade, observed by the Thermal Helium Beam Diagnostic.

Max-Planck-Institut
für Plasmaphysik

Scientific Report

January 2017 - September 2020

The Max-Planck-Institut für Plasmaphysik is an institute of the Max Planck Gesellschaft, part of the European Fusion Programme and an associate member of the Helmholtz-Gemeinschaft Deutscher Forschungszentren.

Photo: IPP, Silke Winkler

This report gives an overview of the scientific work of IPP from January 2017 to September 2020.

The goal of the superconducting Wendelstein 7-X optimized stellarator is to demonstrate high-power long-pulse plasma operation under reactor relevant conditions. After its first experimental phase with a limiter only, Wendelstein 7-X in 2017 and 2018 conducted experiments with an inertially cooled carbon test divertor. After an assembly break and commissioning of new diagnostics, heating systems and specially designed, inertially cooled divertor elements, experiments commenced again in July 2018. One of the highlights was a robust detachment scenario. In this state the divertor plasma is well isolated from the target plates, an important requirement for avoiding thermal overload. The highest plasma performance was reached with coupled electron-cyclotron resonance heating and pellet injection. With turbulent transport reduced, these discharges allowed for testing of the neoclassical transport optimization of Wendelstein 7-X – and gave a first demonstration of its effectiveness. In summary, the first experimentation phases at Wendelstein 7-X delivered impressive results, such as operation at high plasma densities, electron and ion temperatures exceeding 30 million degrees Celsius, long discharge times of up to 100 seconds, an integrated heating power of 200 megajoules and a low heat load on the first wall with divertor detachment.
Since November 2018, an extensive upgrade of Wendelstein 7-X is running to prepare the device for demonstration of high-power long-pulse operation. For this purpose, active water cooling of all plasma-facing components is required. Divertor plates, heat shields, and wall panels have to be connected to the water-cooling system; each of the ten divertor elements will be equipped with a cryopump. In total, about 600 water cooling circuits and a complex cryo-feed system have to be installed. 85 ports have to be equipped with actively cooled port liners. After being severely affected by the Covid-19 pandemic in 2020, the construction work is expected to be completed by the end of 2021.

The ASDEX Upgrade tokamak is devoted to establishing the physics basis for the preparation of ITER operation and the design of a DEMO prototype fusion reactor. Here too, the Covid-19 pandemic hampered work, in addition to a steam leak which caused operation to be suspended between November 2017 and November 2018. In the reporting period, ASDEX Upgrade operated about 20 months, with two-fifths of the operational time being devoted to the EUROfusion Consortium Medium-Sized Tokamak programme.
The experimental breaks were used to install new diagnostics and to complete the new electron cyclotron resonance heating system. It now allows a total of 6 megawatts deposited microwave power in the plasma for the full discharge duration of up to 10 seconds. The ion cyclotron heating system power which can be coupled into the plasma was increased to 5.5 megawatts by using a refurbished generator. From spring 2021, a new thyristor group will extend the capability of ASDEX Upgrade to even higher heating powers and energy.
The experiments brought substantial progress in scenario development, physics understanding and model development and validation. For example, magnetic flux pumping, a self-regulating magneto-hydrodynamic process important for shaping the central current profile was shown to be consistent with a recently developed theory. This mechanism leads to profiles avoiding sawtooth instabilities as well as neoclassical tearing modes in the plasma centre and improved overall stability of the discharge. A key topic of the last years was the development of scenarios without large edge-localized modes (ELMs). Meanwhile a large portfolio of scenarios with no or small plasma-edge instabilities exists at ASDEX Upgrade. Integration of these regimes with core and divertor radiative cooling and divertor detachment was successfully started. Preventing ELMs goes along with improved understanding of the plasma pedestal in terms of stability, transport and magneto-hydrodynamic modes. Last but not least, the L-H power threshold was studied using scans of hydrogen, deuterium and helium mixtures to explore possibilities for the non-nuclear operation phase of ITER. The physics picture for the L-H transition developed at ASDEX Upgrade could be corroborated.

The Plasma-Wall Interaction project supports exploration of the fusion devices at IPP and generates basic expertise in questions related to plasma-facing components in ITER, DEMO and future fusion reactors. An example from a variety of topics is the development of Tungsten-Copper metal matrix composites fabricated by means of copper melt infiltration. High-heat-flux tests demonstrated that these materials may be regarded as potential heat-sink materials for plasma-facing components in future fusion devices, although effects of neutron irradiation still need to be studied in detail.

At JET, the higher heating power of the neutral beam injection system now available has enabled a range of new results: in preparation of the Deuterium-Tritium campaign foreseen in 2021 IPP has contributed to record neutron yields in hybrid plasmas. Also, an increased operation space for isotope studies could be achieved and higher confinement of plasmas with strong impurity seeding. Studies of turbulence in L-modes, impurity production by ion cyclotron resonance heating and material transport in the JET divertor have been performed.

To the international ITER project IPP contributes with major efforts in the development of heating systems, diagnostics, plasma control and theoretical investigation. For the first time ever, it was demonstrated at the ELISE test facility – developing a large negative ion source for neutral beam injection – that hydrogen heating pulses with the required ITER parameters for current density, electron-ion ratio and beam homogeneity for 1000 seconds can be achieved with pulsed extraction. A new collaboration on optimization of the antenna for ion cyclotron resonance heating of ITER started in 2020. Design of the bolometer cameras progressed; port mounted cameras await their preliminary design review early in 2021. The neutral pressure gauges developed at IPP already had their preliminary design review in May 2020. The development of the plasma control system for ITER led to a successful final design review in July 2020; real-time framework and compact controller are working towards their final design review in late 2020. Furthermore, as part of contracts with ITER, theoretical investigations for runaway electrons, halo currents and alpha particle physics have been performed. In addition, IPP experts participated in several ITER design reviews and they play a leading role in contributing to ITER through the International Tokamak Physics Activity and by participating in the EUROfusion work programme.

Important results have been achieved in the theory and numeric divisions of IPP. For instance, the mechanisms underlying the stabilizing effects of energetic particles could be unveiled which in gyrokinetic turbulence simulations with the GENE code produce a strong reduction of turbulent transport. This led to the discovery of a new improved confinement regime in the ASDEX Upgrade tokamak and promising predictions for the Wendelstein 7-X stellarator. Also, a deeper understanding of the origin and course of edge localized modes could be reached. For the first time, a sequence of ELMs could be simulated in realistic tokamak geometry with characteristics being in good agreement with experiments. Experimental evidence for the successful reduction of neoclassical energy transport in Wendelstein 7-X could be found by analysis of discharges with record values of the fusion triple product. The plasma profiles which produced this record prove to be unattainable for stellarators lacking a comparable level of neoclassical optimization.

Scientific Director Sibylle Günter

Content

Tokamak Research

ASDEX Upgrade

Head: Prof. Dr. Arne Kallenbach

1 Overview

The ASDEX Upgrade experimental program is devoted to establishing, in collaboration with theory and modeling, the physics basis for ITER operation and the design of DEMO. In 2017-20, ASDEX Upgrade operated about 20 months, with a 60:40 distribution between IPP-internal and the EUROfusion MST1 programs. Major research topics were power exhaust, disruption avoidance, the physics of turbulence and MHD modes and the development of steady state, high beta scenarios and no-ELM regimes.

ASDEX Upgrade (AUG) operated in total 20 months from March 2017 till July 2020, with 1892 pulses for the internal program and 1162 pulses for MST1. All major scientific goals of the internal program and the grant deliverables of MST1 could be achieved. Experiments covering important topics of the European Research Roadmap were mostly executed jointly between IPP internal and EUROfusion MST1 programs. Operation was suspended between November 2017 and November 2018 due to a hot water steam leak which occurred at a seal in an NBI port during baking. The steam leak appeared to be much more severe compared to a water leak since the steam could reach very remote locations in ports, where electro-chemical reactions lead to corrosion of seals and feed-throughs. Substantial recovery work led to a significant extension of the regular vent, while installation of new diagnostic systems was done in parallel.

During this and other scheduled vents, a number of new diagnostics was installed, like the divertor Thomson scattering system, fast ion loss detectors (FILD), a diagnostic helium beam, microwave diagnostics for turbulence and the heavy ion beam probe. Operation in 2020 was affected by the Covid-19 pandemy, causing a reduction of the experimental days per week from 2.5 to 2 and a complete stop of operation from end of March till early May. A part of the lost experiments could be recovered between mid-May and end of July, when operation was resumed under conditions adapted to Covid requirements, i.e. a reduced number of personnel in the control room, distance rules and other protection measures.

1.1 Major Physics Results

Substantial progress could be obtained in scenario development, physics understanding and model development / validation.

The development of advanced, steady state scenarios led to improved performance in terms of confinement and beta as well as better understanding. Magnetic flux pumping, a self-regulating MHD process, that is an important player for the central current profile, was shown to be consistent with a recently developed theory. It leads to flat central safety factor profiles close to unity, avoiding sawteeth and neoclassical tearing modes in the center and improving the overall stability of the discharge.

A key topic of the last 3-4 years was the development of scenarios without (large) ELMs. Meanwhile a large portfolio of no or small ELM scenarios exists at ASDEX Upgrade, including small ELMs, I-mode, RMP ELM-suppressed H-mode or a stationary ELM-free regime similar to the EDA H-mode at Alcator C-mod. Integration of these regimes with core and divertor radiative cooling and divertor detachment was successfully started. The avoidance of ELMs goes along with improved understanding of the pedestal in terms of stability, transport and occurrence of magneto-hydrodynamic modes, both in 2D and 3D with magnetic perturbations.

A new modelling workflow was developed to overcome the deficiencies of empirical confinement scalings. This workflow requires only engineering parameters as input and combines an equilibrium code, MHD stability calculations, TGLF transport model for the core confinement and a very successful algorithm for calculation of pedestal parameters and width.

The L-H power threshold was studied using scans of hydrogen, deuterium and helium mixtures to explore possibilities for the non-nuclear operation phase of ITER with low L-H threshold. The physics picture for the L-H transition developed at ASDEX Upgrade, namely that the critical shearing rate in the pedestal is mainly related to the diamagnetic term $\nabla p_i/n$, could be corroborated. A small admixture of helium to hydrogen does not lead to a significant reduction of the power threshold in AUG, opposite to results reported from JET. The H-mode density limit, understood as the H-L back-transition, was interpreted as the effect of strong rise of ballooning mode activity close to the separatrix caused by the high local density.

Enhancements of the AUG discharge control system, which shares synergies with ITER CODAC developments, regard the development of a number of new controllers, e.g. for the electron temperature profile and the position of the 'X-point radiator', and include the use of plasma state observers and a the development towards a realistic 'flight simulator' for ASDEX Upgrade discharges.

1.2 Machine Enhancements

The reporting period saw the completion of the ECRH III upgrade, which replaced the discontinued ECRH I system by 4 powerful, 10 s dual frequency gyrotrons and now allows in total 6 MW deposited ECRH power in the plasma. Due to new dedicated power supplies (refurbished systems acquired from DESY), ECRH III is powered directly from the grid, not loading the flywheels and thus extending the maximum additional heating power and energy of ASDEX Upgrade. ICRF power was increased by the new generator 5 (an old 2 MW system modified to use a modern tretrode) allowing to increase the power to the central strap of the three-strap antenna and thus the total ICRF power to plasma by 1.5 MW.

A new thyristor group 7 has been added to the AUG power supply system and will become operational in spring 2021 after delivery of its transformer units. Group 7 will extend the AUG capability to even higher heating powers and energy, and also serve as back-up for failures of other power supply units.
The full tungsten divertor III, which in the beginning slightly suffered from the formation of cracks, was solidified by improving current paths during disruptions and adding a castellation. In 2019, active cooling of the divertor manipulator, which can be used to exchange divertor target samples without breaking the torus vacuum, was successfully taken into operation.

1.3 Preparation of the 2021 Experimental Campaign and Beyond

Preparation of the 2021 program was started with the call for participation in the IPP internal and MST1 programmes in July. During the 2020 summer vent, preparation work for the installation of a shattered pellet injector (SPI) to be delivered by ITER and dedicated diagnostic installations are scheduled. AUG restart is foreseen from end of November 2020, experiments with different pellet shard distributions are planned from summer 2021.
A major vent is foreseen for the installation of the alternative upper divertor Div-IIo and dedicated diagnostics as part of the EUROfusion PEX enhancement project for plasma exhaust planned from summer 2022 till autumn 2023. Div-IIo will feature a cryopump and two in-vessel coils for a variety of divertor configurations including snowflake and X-divertor, to be challenged by the high heating power available in ASDEX Upgrade. In parallel to the PEX enhancement, the arc sources of NBI box I will be exchanged by RF sources, giving advantages for operation.

2 AUG Machine

2.1 ASDEX Upgrade Operation 2017-2020

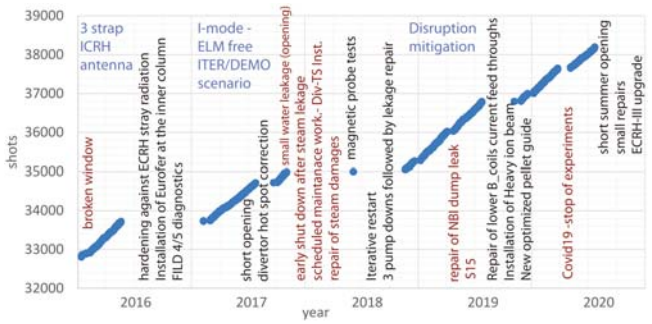

Figure 1: Shot history of the report period 2016-2020. Unscheduled interruptions are marked in red.

During the report period, three experimental campaigns of ASDEX Upgrade with 3409 successful plasma shots were performed. The maximum heating power and energy applied in single discharges was $P_{heat}=27$ MW and $E_{heat}=113$ MJ, respectively. The integral heating energy deposited into the plasma and received by the in-vessel components is $E_{heat\_17\_20}=65$ GJ.
Three scheduled openings were used for the hardening of in-vessel components to be prepared for high power/energy discharges and for installation of new key diagnostics as indicated in figure 1.

2.2 AUG Enhancements

2.2.1 Basis Machine

In addition to the scheduled openings two unscheduled openings with human access were required to fix water leaks (see figure 1). A main incident was a steam leak arising during the vessel baking following a short opening to fix a water leak in November 2017. The fixing of the steam leak damages required extensive work because the steam was redistributed all around the torus and condensed preferentially in remote areas [1]. Fortunately, the steam leak occurred shortly before a scheduled opening so that the damages were repaired in parallel to the scheduled in vessel work. During the pump down further leaks due to corrosion of seals were detected and pump down cycles were necessary to identify and repair the leaking components (see figure 1). The experiments in the 2019 and 2020 campaigns were not impaired by consequences of the steam event.
The scheduled openings were used for maintenance and adjustment work. In particular, the wide (80 mm toroidally) bulk tungsten tiles were split into two tiles. This avoids the formation of deep cracks. After testing tungsten heavy alloy tiles as target for high heat load components they are stepwise replaced by solid tungsten. In addition, in vessel components were hardened and protected against ECRH stray radiation. In particular, the vacuum bellow at the high field side was protected with reflecting sandwich (copper, stainless steel, Peek) plates [2].

2.2.2 Diagnostics

The scheduled shut downs were used to calibrate and refurbish existing diagnostics as well as to install new ones. The array of fast ion loss diagnostics was completed with FILD 4/5 in 2016. In 2018 a divertor Thomson Scattering diagnostic was installed. This required a modification of the lower outer divertor structure in one sector. An imaging heavy ion beam was installed in co-operation with the Hungarian and Spanish Research Units for measurement of the edge density, magnetic field and electrostatic potential.

2.2.3 Hydrogen Compatible Pumping System

The AUG LHe cooled in-vessel cryopump (CP) specifically designed for high gas flux in the divertor region provides a much higher pumping speed compared to the installed gas transfer pumping system (TPS). Most of the gases puffed are condensed on the cryogenic surfaces and contribute to building up an inventory inside the vacuum-vessel (VV).

Regular regeneration of the CP releases the trapped gases and transport it via the TPS out of the VV. Due to the operational restriction of the TPS based on the acceptable in-let pressure as well as the limitation for flammable gases, the amount of these gases has to be restricted. This led to the need of very frequent regenerations and already limitations in feasible plasma scenarios. A hydrogen certified pump was installed in parallel to the TPS. With the change of the system a survey by the German safety institution DEKRA was needed to comply with present safety regulations. The allowed inventory was enhanced from 4 to 190 barl, which is sufficient for one experimental day with high power detached divertor conditions. To ensure the maximal hydrogen input a volume was installed at the gas inlet system, which contains only the allowed inventory. A fully automated procedure was implemented to guarantee the compliance with the safety regulations. This includes daily tests of the components and communications with other relevant systems.

2.2.4 Boronization System

The system for boronization at ASDEX Upgrade which used B2D6 in a He glow discharge, was completely renewed. The setup with opposing gas inlets and pumping ports on the vacuum vessel and equally distributed glow anodes, which has proved to produce very homogeneous layers, was adopted from the old system. The system is built to meet the current safety standards, using an industrial gas cabinet for the process gases, fully welded coaxial piping, a dry screw pump, chemical absorbers and digital diborane detectors. The vessel pressure is held constant during the entire process at predefined 0,5 Pa by a feedback loop between a vessel pressure gauge and the MFCs. This leads to an average boron deposition of about $7 \cdot 10^{17}$ B atoms/cm^2 during a 3-hour diborane glow discharge. A fully automated procedure was implemented to guarantee the compliance with the safety regulations. This includes tests of the components and communications with other relevant systems. The hardware setup and the control concept were examined by DEKRA. The new systems allows boronization without evacuation of the building and reduces the burden on the personnel for boronizations. Also, as the plasma facing components at AUG consist of W, which stores He, discharges just after a boronization are hindered by the enhanced He content. The new system allows to use D2 as discharge gas.

2.2.5 Future Enhancements – DivIIo-ADC Project

The investigation of alternative divertor configurations to handle the energy deposition onto the divertor is a key topic for the physics program. In the framework of the EUROfusion PEX (Plasma Exhaust) strategy, a common IPP/Eurofusion/Helmholtz project was started in 2016 for the installation of a new upper divertor with in-vessel shaping coils and a cryopump. This project is ongoing and the start of physics experiments is envisaged for 2023, see [3] and references herein.

2.3 ECRH III – Project Status

In the period covered by this report the replacement of the initial ECRH system from the 1990ies (EC1) by a 4 MW, 10s dual-frequency system (EC3) was completed and taken into operation [4]. The new system follows largely design lines of an earlier extension of the ECRH (EC2), in particular for pulse-lengths, powers and frequencies. So, the nominally installed power at 140 GHz reached 8 MW end of 2018. Further improvements relate to measures to harden the air-filled transmission lines, to further improve machine protection and to extend the O2-heating possibilities.

During the period the last two technical uncertainties of the EC3 project were resolved: in 2016 the first semi-conductor based body voltage modulator was accepted, though with reduced performance (200 µs rise time instead of 100 µs) and in 2017 the new 7-MW-HV-power supplies were toughened to cope with on-/off-modulation of two independently operating gyrotrons.The gyrotrons turned out to cope fully with specifications. The first two new systems started operation on the plasma in March 2017 and the latter two in November 2018. Already in March 2019 5.4 MW were injected into the plasma for several seconds, at that time limited by arcing in the wave guides. As an addition to the project, new in-vessel gearings for the movable beam steering mirrors were constructed together with gearing engineers of the Technical University of Munich (FZG). The first unit was installed in 2016 (S08), two more in 2019 (S14). The new mirrors have twice the thickness of the old (EC1) ones, allowing for 10 s pulses (in the 2018/19 campaign, the pulse length was limited to 5 s to avoid over-heating) and the last one has just been installed in the 2020 opening.

In the past, active electronic elements of the EC systems in the torus hall were subject to neutron damage, in particular the angular encoders of the mirror drives and the SIMATIC 400 LPC controlling the fast poloidal mirror drives of the EC2 system. In the report period those components were shielded very successfully with with layers of pure and boron doped polyethylen.

Arcing in the wave guides is a self-enforcing effect due to the chemistry driven by the high-power microwaves. Without understanding the details, this is obvious from smelling. A few long high-power pulses may run through until one triggers an arc indicating that the atmosphere in the beamline changes prior to the arc. Arcing itself then strongly deconditions the beam line, not only due to the created radicals but also due to a redistribution of dust.Such dust is created on longer time scales by the oxidation of the wave guides in the reactive atmosphere and tends to accumulate on the lower mitre bend of a vertical section.

From this understanding it was decided (a) to continuously rinse the wave guide with dry air in between pulses, (b) to detect arcs to minimize the related chemistry and (c) to harden the Al surface of the wave guide against chemical erosion by chromatisation. For (b) a pair of orthogonal directional couplers was engraved in the last mitre bend to obtain a polarization independent power signal. A drop of this signal compared to the power measured

directly after the gyrotron (M2) indicates an arc and detects it typically well before any optical sensor. After testing these modifications on beam line 8, (a) and (b) were also implemented on all other beam lines which were thoroughly cleaned from the inside to remove old dust but not chromatised, yet. With these measures arcing has largely disappeared, a maximum power of 5.9 MW in the plasma has been reached. Power limiting factors are now on the gyrotron side, which are typically not run in the regime for highest power but for highest flexibility and which in the case of EC2 show aging (3.2 MW were delivered by EC3, which is less than 10 % below the expected maximum of 3.5 MW). A further power increase would require sequences of dedicated discharges for one specific scenario.
Finally the steam leak from November 2017 had a severe effect on the EC systems, since the steam condensed on the diamond windows, in the separation gate valves (which were open since the window sections are not pumped separately and were not closed since no logic was implemented (now modified)). Between the gate valves and the windows, short Aluminum wave guide sections are installed as inserts into the stainless steel ports. The intermediate volumes were filled with aggressive water. Six systems had to be completely disassembled up to the gate valves. The copper brazings of the diamond windows did not show signs of erosion nor did the absorption at 140 GHz of the diamond change significantly (measurement at KIT). Corrosion was observed in the gate valves, the inserted Al wave guides and some in-vessel gearings. These were only cleaned, not replaced, which in principle comes with the risk of continuing erosion especially at high humidity. At this occasion the diamond windows of beams 5 and 6, which still were brazed with the old Al technique requiring aggressive cooling water additions, were replaced by those foreseen for 3 and 4 (last beam lines of EC3). The old windows were dismantled, the disks were cleaned at KIT and new windows with Cu-brazings were built and finally used for beamlines 3 and 4. This allowed to remove completely the potentially hazardous cooling water additions from the torus hall.

2.4 ICRF

For the low-sputtering 3-strap ICRF antennas (further analyzed in [9]), generator 5 (old ASDEX/W7-AS generator, previously modified to fit the CPI 4CM2500KG tetrode) was added to the AUG ICRF system, with a control system upgrade for the optimized antenna feeding including the controllable phase between antennas. Operating generator 5 increased the power by about 1.5 MW at 36.5 MHz. The power coupled by all ICRF antennas exceeded 5 MW in a series of discharges during the 2019–2020 campaign [10], for the first time after introduction of the 3-strap antennas which previously required operating one generator at reduced power. A new method for the modelling of the ICRF coupling by the RAPLICASOL code was successfully benchmarked against experiments and the established tools like TOPICA [11] and was essential when accounting for 3D effects of local gas injection [12] and magnetic perturbations [13] on the ICRF coupling. Further insights into the physics of operationally critical antenna-plasma interactions in the SOL were gained via modelling: features of slow wave propagation [14], the so-called bounded states with fast-slow mode conversion layers inside filaments at unfavorable parameters [15] and scattering of the fast waves by filaments [16].

2.5 NBI

After several incidents of melt damage of the torus gate valves the design of the box exit beam scraper was modified based on simulations of the trajectories of reionised beam particles. The redesigned scrapers were installed on both boxes in 2016 and 2018. No melt damage has occurred since. Fatigue led to air leaks on two calorimeter bellows between Nov. 2018 and Jan. 2019. As a consequence, all six bellows were replaced with spares and new spares ordered. In 2019 NBI source 8 was replaced by the source previously mounted on position 5 after it had repeatedly required extensive high voltage reconditioning. The spare source was mounted in position 5.
In order to meet the demands of NBI-based diagnostics such as the fast ion measurements by FIDA, the geometry of the beams from injector 2 was determined with improved accuracy by firing beam blips into the empty torus and comparing IR images of the heated wall spots with simulated beam heat load profiles. The procedure was repeated after the source replacements mentioned above.
For the planned replacement of the arc sources of NBI 1 by RF sources practically all components have been procured and assembly of the sources has begun. The conversion will take place as soon as AUG has a sufficiently long maintenance break, which is currently foreseen in 2022.

2.6 AUG IT Infrastructure

The main operating system Solaris, which has been used for several decades for data acquisition, evaluation and desktop tasks, is now superseded by Linux. Although still being an active and powerful operating system, Solaris offers neither up-to-date office tools nor modern tools and compilers for developing drivers for data acquisition any more.
In parallel, the outdated SunRay zero clients are being replaced by IGEL thin clients, which offer much more possibilities. Whereas the old SunRay clients only allowed connections to Solaris terminal servers, the new IGEL clients allow users to choose between sessions on Linux or Windows terminal servers, or to connect to the data evaluation clusters. For special purposes they can also offer dedicated services, and they are now also equipped with videoconferencing capabilities.
Connections to the terminal servers are done using the RDP (Windows) or ThinLinc (Linux) protocol. Both of them allow smooth session roaming between different terminal devices and are not restricted to the IGEL thin clients, but can be used from almost every PC, laptop, or mobile device. This feature

enables easy remote working for guests, and it was very helpful during the Corona lockdown, since it allowed a smooth transition between working on site or in home office.
In parallel, the workflow for software development and collaborative teamwork is being modernized. Several services have been implemented with the focus on simplifying collaborative work. Software development and deployment is now being done using the standard tools Gerrit (Git repository server and code review tool), Jenkins (continuous integration/delivery) and Ansible (automation tool). This allows a professional, streamlined software development workflow, which is unified for all developers, automated as much as possible, and open to everyone. The complete discharge control system is now successfully maintained within this workflow, and the goal is to collect all relevant software for control, data acquisition and data evaluation on ASDEX Upgrade in one central repository.
Servers are now installed in a Proxmox virtual environment which avoids the necessity to use dedicated hardware for different services and offers a flexible and scalable solution to react on rapid changing demands easily.

2.7 AUG Data Acquisition

2.7.1 New and Enhanced SIO2 Diagnostics

SIO2/PIPE2-system, which is the standard data acquisition (DAQ) system at AUG, was further extended and new DAQ cards were developed [8]. Novel operation modes have been introduced in SIO2-firmware. All source code is under full AUG-CODAC responsibility and will be further serviced. An important development is a new giga-sample ADC type designed for Thomson Scattering offering an advanced time and amplitude resolution of 1 ns and 14 bit. New analogue integrators for Mirnov-Probes give a huge progress in functionality, maintenance and packing density. Integration time constant can be set by software and verified in situ. Further progress was achieved replacing legacy diagnostic hardware by SIO2/PIPE2-systems, such as interfaces for SXR cameras, AXUV diagnostics and CAMAC systems.
New systems offer important performance improvements and a wide range of self-testing and system verification features. Overall power consumption is reduced, while packaging density is increased.
The refurbished SIO2-systems run under real-time enabled Linux OS for seamless integration with plasma control.

2.7.2 Front-end Electronics Development

Decentral control of small sub-systems is now mainly done with COTS (Components Of The Shelf) solutions. AUG-Electronics uses National Instruments (NI) cRIO-system. It offers great flexibility and a wide variety of IO-modules connected to an FPGA. This gives hardware-managed real-time functionality while the connected processor provides high-level functionality and IP-communication protocols. This concept is used to control the Multi-Pass-Thomson-Scattering diagnostic and to deliver accurate timing for three actor systems: mid-plane manipulator, boron powder dropper, and pellet-system.
The foil-bolometry front-end electronics was redesigned with a first prototype operational. The new design allows more flexibility in measurement set-up, which is of high relevance for the planned ITER-bolometry electronics. An important feature is the arbitrary waveform generator for flexible excitation of the sensor bridge, which allows to compensate cable effects.
The design of a printed-circuit-board for industry standard ‘Camera Link’ interface for the IR-high-speed camera was a further undertaking. ‘Camera Link’ offers high speed data transfer from camera to frame grabber. These interfaces are used at AUG, JET and W7-X.

2.8 Experimental Power Supply

Due to huge efforts of operating staff to maintain safety and reliability of the many and various installations, ASDEX Upgrade operation was not much affected by plant failures. The few faults at generators, high current and high voltage converters were effectively overcome by rearranging the remaining plants until the failure could be found and repaired.
In 2020 IPP received a new 10 kV switchgear at the Garching 110 kV substation, including a new 32.5 MVA transformer for the 10 kV surge load network. In parallel base load feeder cables were reinforced in order to restore redundancy because of a steadily increasing power demand. At IPP, building EZ1 was equipped with automatic fire protection installation in order to enhance safety and integrity of the main 10 kV feeding substations.
Flywheel generators EZ2, EZ3 and EZ4, supplying ASDEX Upgrade with high pulsed power of up to 400 MW are presently in the age of 35 to 48 years. Coping with an increasing demand of power, the machines are in good technical condition due to regular overhauling, minor repairs and sophisticated diagnostics. In 2016, reactive power compensation – so far only connected to generator EZ3 – was extended in capacity up to 180 MVAr and assigned also to generator EZ4.
This reduces machines’ current and heating of the windings and thus increases possible AUG pulse length [5]. Diagnostics and monitoring systems of the machines were upgraded continuously in order to improve safety and to reduce downtime.
Due to the successful program of ASDEX Upgrade, the 17 high current converters supplying the magnetic field coils are coming to their limits. All converters are in use and there is no more operational flexibility. At the same time risk of failures increases because of ageing. In order to improve availability and to expand possible operating scenarios a new thyristor converter called “Group 7” is under construction and will be in operation from 2021 on. The power section is almost the same as for the already existing converter “Group 6”, but with a completely new designed, fully digital control platform [6]. In line with the new converter, signal exchange with the AUG control system will be stepwise changed from a

hardwired plug to a mostly digital interface. This is aimed at significantly reducing the error rate of the connection. The crowbar protection system was extended providing now an individual crowbar for each converter module instead of a common crowbar for a complete converter group composed of up to 4 modules. This improves the flexible use of the converters and also its protection characteristics. Change of configuration is now possible in between two plasma pulses and without manual modification of the crowbars.
In order to power the four new ECRH gyrotrons, two new 5 MW direct current power supplies were needed, each feeding two gyrotrons. The DC voltage is switched on and off by a tetrode with a pulse duty factor between 0 and 100 % and a frequency from 0 Hz (continuous wave) to 500 Hz. During commissioning of the installation, a sophisticated fast forward control has been established to operate the DC power supplies within these demanding conditions. In order to increase safety and reliability of the supply, the 10 kV 50 Hz node supplying the high voltage plants with 50 Hz surge load will be split up. New medium voltage cables were already installed. Next step is a renewal and extension of the 50 Hz switchgear Group F.
Quite a lot of systems still date back to the 1970's. Failures of components rise and availability of spare parts is becoming more and more difficult. Requirements for power, pulse duty and accuracy increase. Therefore, some technical devices like e.g. controllers and inverters will need replacement over the next years and hence major investments. This is necessary in order to keep up the high availability of the complex systems with state-of-the-art technique, improving supply of spare parts and reducing time for trouble shooting. An important first step is done within the HGF investment "Extension of heating and pulse power capabilities at ASDEX Upgrade" [7].

3 AUG Operation

3.1 Organization

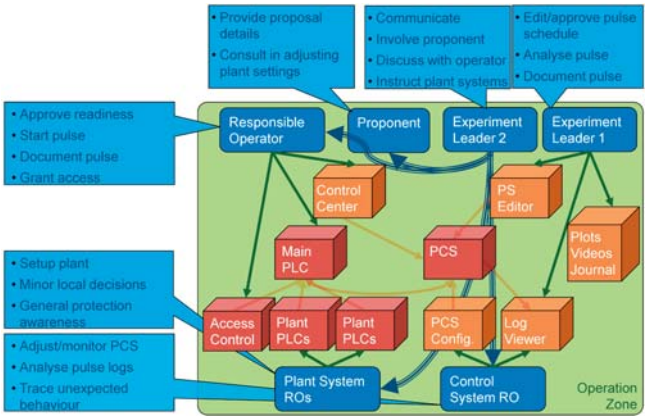

Figure 2: Simplified organigram for AUG. The boxes show the main devices (red) and the main user interfaces (orange). The main organizing staff is shown and their roles are described in blue colours.

Within the framework contract for the ITER plasma control system (PCS), the organization of AUG operation and safety was analyzed by help of multiple organigrams (see figure 2 as an example). Taken into account were automatic protection systems as well as the organization of the involved staff. The AUG team is proud of the high operational flexibility even though AUG is a complex machine, well equipped with high heating power and a strong, water-cooled copper-based magnet system. AUG operation is protected by automatic control systems: Multiple autonomous programmable logic controllers (PLC) for monitoring and supervision and a powerful central plasma control system (PCS) for exception handling during pulse operation.

3.2 Power Plant Configuration

Progress was also made in better understanding the manifold possible electric configurations of the AUG power plant. Almost each AUG coil can be operated by different current converters which can be connected to different flywheel generators. The auxiliary heating systems can also be connected to different rectifiers and flywheels. Especially for high power shots, there is often observed a strong tendency for oscillations on the local 10 kV grids which can end in early interruption of the plasma shot initiated by different protection systems (over-/under-voltage, overcurrent or force limits). Also critical are instabilities of the local thyristor converter controllers for poloidal field coil currents in case of highly shaped plasmas. Simplified electrical models are the aim for integration into our flight simulator 'Fenix' (see also below, chapter 3.5.3), sufficient to estimate the stability as well as the reactive power needs, not easy to calculate for highly dynamic situations. As a side effect, the required rotating speed of the flywheels can be better rated to save (energy) costs and reduce aging of the valuable generators.

3.3 Impurity Dust Dropper

The W influx in low density scenarios, which reduces the performance, is controlled by coating of the limiters with boron, usually by a boronization. To gather more flexibility a dust dropper was installed and commissioned at the 14 Eo Port, which allows dust particles to fall directly into the plasma, being eroded and then deposited at the PFCs. The dropper was developed and installed by PPPL. In the framework of cooperation with Princeton the system is operated, the data are evaluated and published [17]. By dropping boron dust into high heated H-mode discharges, the PFCs close to the plasma, the main source of W in the main chamber, are coated. Spectroscopic measurements verify an enhanced boron influx from the ICRH limiters, whereas at the same position the W influx is reduced. A LabVIEW based control system, which allows varying the flow rated during a discharge, was developed for remote access and data storage. Now the system is routinely used, providing drop rates of 100 mg/s of boron, sufficient to control the impurity influx for 2-3 discharges. A typical scenario is to reach ELM

suppression using the RMP coils, which was only possible with a fresh boronization, but can be achieved now after boron dropping.

3.4 Glow Discharge System

The use of metal PFCs strongly reduces the need of glow discharges (GD) for wall conditioning. Now at AUG, GD is only used after a vent, for boronizations and during operation after cryo-pump warm up or strong impurity gas puffing. As W stores He from GD, subsequent discharges were affected by He. To reduce the gas uptake of the PFCs, pulsed operation is used. Typically, 3 pulses of 10 s with 50 s pumping time are sufficient during plasma operation. This scheme offers 70 % of the removal compared to continuous operation, but reduces the He wall inventory by roughly a factor of 5 [18]. For reliable break down spark devices, supported by an additional power supply, were installed at each anode. Since the installation of a hydrogen compatible pumping system, the in vessel cryo-pump can stay at LHe temperature during an experimental day. The pressure needed for GD causes heat input to the LHe panel, which can be compensated only for 30 s. This requires to vary also the gas inlet during the pulses. The whole process is controlled by the gas inlet SIMATIC PLC to allow automatically operation. This system will also be used at the KSTAR tokamak in Korea.

3.5 AUG Discharge Control System (DCS)

3.5.1 Profile Control, Actuator Management and Real-time Observers

The continued improvement of model-based real-time observers for the electron density RAPDENS and the plasma profile RAPTOR (collaboration with Swiss Plasma Centre SPC) enabled the development and successful application of a first electron temperature profile controller at ASDEX Upgrade. The controller uses a combination of on-axis and off-axis ECRH heating. It is also the first controller at ASDEX Upgrade that is not rigidly tied to certain beamlines but operates a virtual actuator, that flexibly can allocate actuator resources to control channels based on aptitude, availability and priority. Virtual actuators are part of the actuator management concept that is being further developed and shall allow to dynamically combine different actuator systems with similar impact on the plasma and provide these groups as actuators to plasma controllers in a transparent way. Moreover, Iterative Learning Control has been successfully commissioned to optimise plasma scenarios with specified electron temperature profiles by adjusting feed-forward waveforms [19-23].

3.5.2 Detachment Control and SIO2 Real-time Diagnostic Integration

The real-time coupling of SIO2 data acquisition boards with high number of channels and transmission rates to the control system has been established, and a general purpose real-time preprocessor can now apply customizable offset correction, scaling, median and percentile filtering algorithms on the raw data to condition them for control purposes. A first control application based on SIO2 acquisition is the XpointRadiationLocator, which implements a real time detection algorithm for the radiation front in the X-point region based on divertor bolometry channels. A new detachment controller regulates the vertical position of the radiation front and thus maintains a detached regime [24,25] (see also chapter 7.1).

3.5.3 Flight Simulator

Substantial progress has been made on the development of an ASDEX Upgrade flight simulator (Fenix). Plasma, actuator and control system models have been refined such that an entire discharge with premagnetisation, breakdown and plasma L-, H- or I-mode can be simulated and achieve reasonable agreement with experimental results. Some further improvements on the plasma model (e.g. radiation, pellet, detachment) on the control system model (monitoring, exception handling) and on the automated reading of the DCS configuration are on the way, such that a public release can be expected soon [26-29].

3.5.4 Early Disruption Avoidance of the H-mode Density Limit

In the last report initial feed-forward disruption avoidance attempts based on a state space description of the H-mode density limit (HDL) have been mentioned. This state space has been generalized using dimension-less quantities ($H_{98y,2}$ - f_{crit}, with $f_{crit} = n_e\,(edge) / n_{e,crit}\,(edge)$). By investigating a larger data base compared to the original study [30], an empirical stability boundary for pure deuterium H-mode discharges has been established [31]. Joint MST1 experiments showed, that this state space also describes the HDL at TCV. Further variations in q_{95} and shaping, in particular the upper triangularity, have been performed in order to extend the validity of the state space. The additional injection of nitrogen has shown, that in this case the state space description fails and further work is required.

The state space, which is available in real-time, has been used to implement an easily applicable *disruption avoidance* controller [32]. The controller is capable of avoiding HDL disruptions by automatically applying central ECRH as actuator, which has been shown to be more efficient than co-ECCD at the q=2 surface. Feed forward experiments with NBI and ICRF heating have shown that they can also serve as actuators.

The significant differences in efficiencies in terms of the required power, will be part of future investigations. This disruption avoidance controller has been successfully migrated to TCV. There, NBI has been used as actuator, also in combination with modification of the gas fuelling rate.

The implementation of the avoidance scheme was based on a new configurable processing module for general-purpose real-time algorithms. This versatile module supports rapid prototyping also for future control applications [32].

Disruption avoidance in the HDL can only be achieved while the MARFE is still in the X-point region. Only well after the MARFE has propagated to the plasma top, n=1 modes occur.

Thus the conventional n=1 locked mode detector and even rotating MHD detectors are not suitable for avoiding HDL disruptions since the development is already irreversible. The detector can at best be used as a trigger for mitigation purposes.
A complementary sensor, based on the real-time localization of the MARFE in the lower X-point region by diode bolometers, has been established. This has been used with modification of the nitrogen puff rate as actuator for controlling the z-position of the MARFE (which is similar to the X-point radiator invoked by impurity seeding, see chapter 7.1). A first attempt to combine this sensor with the central ECRH actuator succeeded in keeping the MARFE in the X-point region and avoiding the HDL. This promising controller will be further improved.

4 Pedestal Physics

4.1 Quasi-continuous Exhaust with only Small ELMs

In next generation large tokamaks, we aim for high performance plasmas with efficient divertor protection, also against transient heat loads. While good confinement is crucial to reach the designed performance, machine integrity is also a challenge in ITER and DEMO, which, together with other conditions, means that ITER needs to operate in a partially detached regime and in mitigated or suppressed ELM conditions.
Already in earlier work it was shown that small ELM regimes appear at high density and high edge collisionality in highly shaped plasmas. Future large tokamaks will host plasmas with very similar collisionality at the separatrix as in AUG. At the inner end of the transport barrier (pedestal top) we expect much lower collisionalities than achievable in present-day machines at high density. We successfully disentangled the separatrix conditions from the pedestal top conditions by changing the fueling method from gas fueling to pellet fueling. It could be demonstrated that the appearance of small ELMs depends on the separatrix (and not the pedestal top) conditions [33] and that they are very localized close to the separatrix. This led to the hypothesis that small ELMs are caused by ballooning modes sitting at the pedestal bottom. This hypothesis is supported by a detailed analysis of the influence of different stabilizing mechanisms, namely local magnetic shear, connection length to the stabilizing HFS and radial electric field [34]. When these small ELMs cause enough transport, they flatten the gradient region around the separatrix and thereby consequently narrow the effective pedestal width. Because a narrower pedestal is more stable against global peeling ballooning modes, the stability boundary is shifted towards higher pressure gradients and type-I ELMs do not occur.
Under the same conditions, namely high separatrix pressure and high plasma shaping, small ELM scenarios could also be developed on TCV [35]. First measurements in this scenario of the divertor footprint with infrared cameras showed an increase of the wetted area by a factor of 4 in comparison to the multi-machine scaling [36].

4.2 High Performance Plasma Discharge without any Large ELM

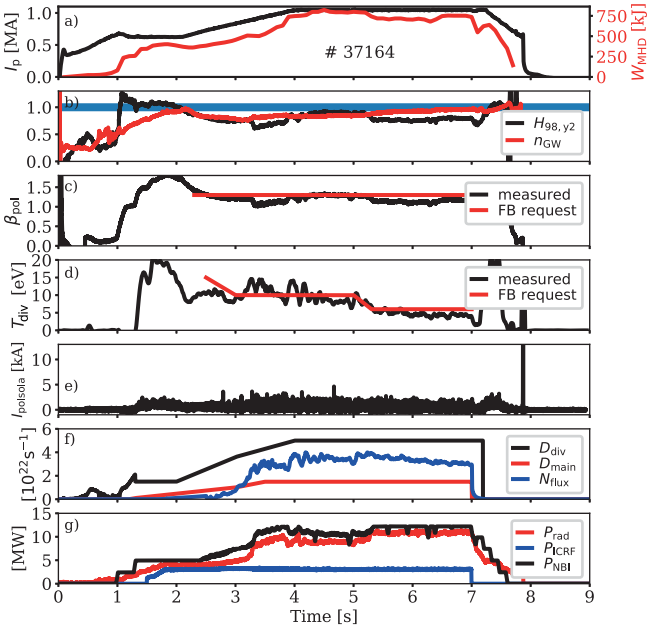

Figure 3: Time traces of a discharge without any large ELM. a) Plasma current I_p (black), stored energy W_{mhd} (red). b) Normalized confinement factor $H_{98,y2}$ (black), Greenwald density fraction n_{GW} (red). c) Measured (black) and requested (red) normalized poloidal pressure β_{pol}. d) Measured (black) and requested (red) divertor temperature. e) Divertor current as ELM indicator. f) Fueling of deuterium from the divertor valves (black) and main chamber valves (red) as well as nitrogen (blue). g) Heating power from NBI (black) and ICRH (blue) as well radiated power (red).

A plasma discharge without any type-I ELM was developed based on a scenario with quasi-continuous exhaust [33], attributed to a ballooning instability at the foot of the edge transport barrier, which occurs at high separatrix densities in highly shaped plasmas. Small pressure gradient relaxations modify the pedestal near the separatrix, leading to a peeling-ballooning stable edge. Figure 3 shows the time traces of such a discharge. In order to avoid any ELM in the whole discharge from ramp-up to end, the strategy is to start the discharge at a low plasma current I_p (figure 3a, black) of 600 kA, as ballooning modes are more easily driven unstable at high edge safety factor q_{95}. At 1.3 s the discharge is driven into H-mode at a Greenwald density fraction of 0.7, and subsequently shaping is increased towards the desired high triangularity $\delta = 0.38$ close to a double null configuration with a distance of the two separatrices of 7 mm at the midplane. Between 2 and 4 s the plasma current is ramped up at the same time as the fueling (figure 3f, black). Simultaneously, the plasma pressure is controlled to a constant value of β_{pol} (figure 3c). With around one second delay, we start the divertor temperature (T_{div}) control (figure 3d) with nitrogen

as actuator (figure 3f, blue). In this way, a double feedback control keeps the plasma in this regime without any large ELMs (figure 3e) and a partially detached divertor with average temperatures below 10 eV throughout.
The flat top time of the presented discharge shows two phases, from 4-5 s and from 5-7 s, with a lower requested T_{div} value in the second phase (figure 3d, red). As the lower T_{div} value is achieved by an increase in nitrogen impurity seeding it is compensated by more NBI heating power (figure 3g, black) to keep the requested β_{pol} value. With 14 MW total heating power from both NBI and ICRF, flattop values with an H-factor of $H_{89,y2}=0.9$ (figure 3b) and normalized pressure $\beta_N \approx 2.0$ were reached at a Greenwald density fraction of 0.8-0.9 (figure 3b).

4.3 L-H Transition Physics

To achieve its operational targets, ITER is designed to operate in H-mode. Although progress is being made in understanding the physics underlying L-H transitions, the lack of model based predictions of the L-H power threshold (P_{LH}) for ITER leads to the requirement of extrapolations from present-day devices. The limited amount of power available and the large uncertainties in the extrapolation leave doubts on the accessibility of the H-mode regime especially in the pre-fusion power operation (PFPO-1). In particular, the knowledge of the P_{LH} dependence on the plasma ion composition is both crucial in the ITER nuclear operation (mixture of D and T plasmas) and in the PFPO-1 phase (He or preferentially H plasmas with possible He-doping to lower P_{LH}). JET reported a reduction of P_{LH} of 40 % in NBI-heated hydrogen plasmas when He-doping up to 10 % is applied. Furthermore ICRH in H plasmas induced a non-linear increase of P_{LH} with increasing relative hydrogen content $n_H/(n_H+n_D)$, where $P_{LH}(H) \sim 2 \cdot P_{LH}(D)$ [37]. At ASDEX Upgrade, detailed studies of He-doping in H-plasmas with both NBI and ECR heating have been carried out showing no change of P_{LH} (figure 4a) in contrast to the JET observations [38]. Whereas at JET the increase of P_{LH} with the H-content happens already at $n_H/(n_H+n_D)<0.2$, this effect was observed for $n_H/(n_H+n_D)>0.5$ at AUG (figure 4b). Differences in P_{LH} due to the applied heating method (different colors and symbols in figure 4) could be ascribed to the requirement of a constant edge ion heat flux at the L-H transition. This condition together with the finding of a constant E×B velocity maximum at the L-H transition ($\max(v_{E\times B,LH})=6.7$ km/s) [39] can be linked to the international power threshold scaling $P_{LH,scal}=0.049 \cdot n^{0.72} \cdot B^{0.80} \cdot S^{0.94}$ [40] assuming an edge ion diffusivity of $\chi_i = 1$ m^2/s and neoclassical $v_{E\times B}$, resulting in $P_{LH}=0.5 \cdot \chi_i \cdot \max(v_{E\times B}) \cdot n \cdot B \cdot S = 0.05 \cdot n \cdot B \cdot S$. Despite its simplicity, this simple derivation captures the fundamental dependencies of P_{LH} and well reproduces $P_{LH,scal}$ giving a basic understanding of the physics behind the L-H transition: $P_{LH,scal}$ is simply the heat flux per particle required to reach a certain $v_{E\times B}$, i.e. a certain flow shear.

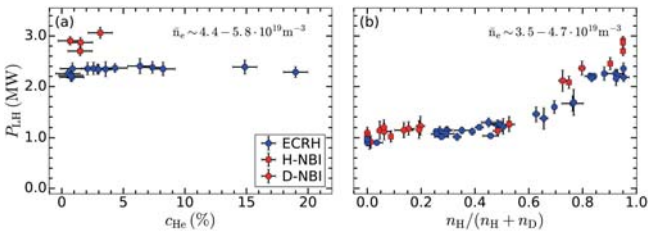

Figure 4: L-H power threshold PLH dependence on: (a) He-concentration (c_{He}) in H-plasmas, (b) relative H-content. Different colors and shapes indicate different heating schemes.

At ASDEX Upgrade, the effect or Kr-seeding on P_{LH} has been investigated to disentangle the effect of radiation inside the separatrix and within the pedestal top [41]. Detailed tomographic reconstruction combined with transport simulation show that radiation in the whole confined plasma up to the separatrix needs to be considered to reconcile the input power with $P_{LH,scal}$. Moreover, the effect of magnetic perturbations (MP), one of the possible ELM mitigation strategies, on P_{LH},scal has been characterized [42]. The L-H power threshold increases up to roughly 80 % only when the external n=2 MP field is aligned to maximize the associated plasma response at the edge. This increase is primarily attributed to a change of the fluid velocity into the co-current direction leading to a more flat and positive $v_{E\times B}$ profile, which is compensated by additional heating power.

4.4 I-phase

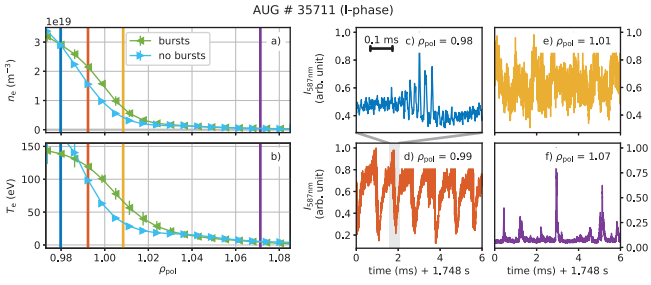

Figure 5: Measurements of the thermal Helium beam diagnostic during an I-phase. Left: Density and temperature profiles during bursts and in between bursts. Right: Temporally resolved emission intensity of the He I line @ 587 nm at different radial positions indicated by colors in the profiles (left).

The I-phase or intermediate phase is a phase that occurs after the L-H transition, in which confinement is already improved but a full H-mode with type-I ELMs is not yet developed. It is characterized by regular bursts, a signature of increased transport across the edge transport barrier. The newly installed thermal Helium beam diagnostic [43,44,45] delivers a picture of the I-phase across the whole edge region [46]. On the left hand side of figure 5 density and temperature profiles in phases with and without bursts are compared.

On the right hand side, the raw emission signal is shown with high temporal resolution (blue) and moderate temporal resolution at different radial positions. A mode is driven close to the pedestal top with increasing amplitude (blue), which induces transport and strong changes in the electron density and temperature profiles, visible as bursts in the vicinity of the separatrix (red, yellow). The filaments in the far scrape-off layer do not appear with the same frequency and are much more intermittent (purple). As heating power is increased the mode changes its magnetic structure from n=3-6 to n=9,10 and moves from q=6 to q=5 [47] continuously inducing stronger crashes. A comparison of the so-called M-mode at JET and the I-phase at ASDEX Upgrade led to the conclusion that they are identical [48].

4.5 Inter-ELM Pedestal Physics

Pedestal recovery in between ELMs has been studied in detail for a wide variety of discharges and with a large combination of diagnostics. The shape of the pedestal density profile is very important for the performance of a discharge. The density profile at the plasma edge can be affected by various different methods, such as wall conditioning, seeding or simple gas puffing. The consequence is a shift in the pressure profile relative to the separatrix, leading to improved pedestal stability of H-mode plasmas when the direction is inward [49,50], a behavior that has also been found at the three tokamaks AUG, JET-ILW and TCV for peeling-ballooning (PB) limited pedestals [51]. The leading parameter determining the separatrix density at the low field side was found to be the neutral divertor pressure, which can be considered as an engineering parameter [52]. Reflectometry measurements of the electron density in the scrape-off layer at both, the low and the high field side, revealed strong asymmetries [53]. The study confirms that the separatrix density at the LFS is better correlated with the neutral pressure at the outer target while the HFS SOL density follows the neutral pressure at the outer target, with strong variations in asymmetry due to the dynamics in the ELM cycle.

Generally, the inter-ELM pedestal evolution follows a certain sequence after an ELM crash with the density gradient recovering first together with the ion temperature gradient [54,55] followed by the electron temperature gradient, depicted in figure 6. A constant pressure gradient can be observed for several milliseconds before the ELM occurs, in which the pedestal top values seem to increase, indicating a widening of the pedestal. The same sequence of recovery phases is observed for the different ion species hydrogen, deuterium, and helium [56], as well as for different plasma shaping [57]. After an initial ~1.5 ms long quiescent phase without any modes, the inter-ELM phases appear correlated with magneto-hydrodynamic (MHD) modes with distinct frequencies and toroidal mode numbers [58]. While mode number branches n=3...6 and n=8...10 are dominant just before the ELM crash, during the ELM crash n=2...5 are observed in typical discharges with type-I ELMs [59].

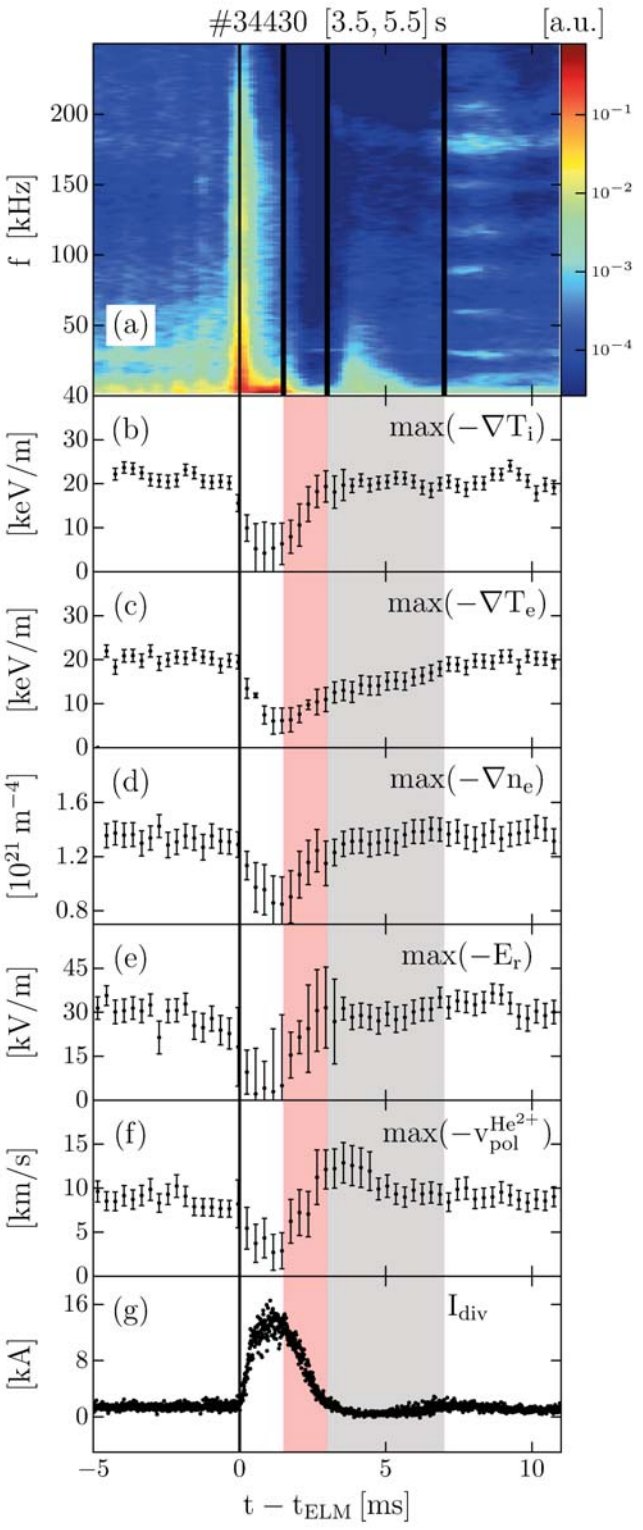

Figure 6: Temporal development of a typical ELM cycle with a) spectrogram of a magnetic pick-up coil, maximum gradients in the pedestal of b) ion temperature, c) electron temperature and d) electron density, e) minimum of the radial electric field and f) the poloidal velocity of He^{2+}, all synchronized to g) the ELM signature measured in the divertor current.

These low mode numbers that occur during the non-linear phase of the ELM crash are also found in non-linear MHD simulations using the JOREK code [60]. A database analysis shows that with higher edge safety factor q_{95} the mode numbers tend to smaller values, which can be explained by a simple geometric model for the spatial overlap of poloidal modes [61].
The propagation of cold pulses induced by type-I ELMs was studied using electron cyclotron emission measurements, finding that the edge safety factor or the plasma current are the main determining parameters for the inward penetration of the T_e perturbations with the perturbation being more shallow with increasing plasma current [62]. Also during an ELM, the acceleration of beam ions was observed for the first time through direct measurements of fast-ion losses in low collisionality plasmas. The accelerated beam-ion population exhibits well-localized velocity-space structures, showing energy gains of the order of tens of keV. This suggests that the ion acceleration results from a resonant interaction between the beam ions and parallel electric fields arising during the ELM [63].
In the steep gradient region the inter-ELM modes could also be observed with ultrafast reflectometry [64]. Additionally, a mode with n=13-14 sitting close to the pedestal top was characterized with the 2D ECE-Imaging diagnostic [65], and a bi-coherence analysis revealed that coupling to other modes is sometimes, but not always, visible.
The different inter-ELM recovery phases are correlated with distinct signatures in the divertor and differences in the behavior of high and low field side density profiles [66] and their fluctuations [67]. An analysis of the time scales of inner and outer divertor detachment phases, the high field side high density region and main chamber recycling led to the conclusion that the fast recovery of the pedestal density after the ELM crash can be best explained by a reduced particle flux across the separatrix, concomitant with the quiet phase without any modes [68].
The 1.5D code ASTRA was used for these very well diagnosed discharges to analyze the inter-ELM heat transport [69]. The ion temperature gradient was found to be dominated by neoclassical transport [70] and a combined transport analysis of all channels simultaneously revealed that the delayed recovery of the electron temperature gradient can be attributed to the depletion of energy caused by the ELM. The local sources and sinks for the electron channel in the steep gradient region are much smaller compared to the energy flux arriving from the pedestal top, indicating that the core plasma may dictate the local dynamics of the electron temperature gradient recovery during the ELM cycle [71]. This kind of analysis is very important, because it shows that dynamic processes involving the whole plasma volume dominate the early inter-ELM phases.

4.6 ELM-free Scenarios

A variety of scenarios without type-I ELMs is investigated at ASDEX Upgrade, namely I-mode, quiescent H-mode and EDA H-mode.

4.6.1 I-mode

Several key advancements can be reported on the improved energy confinement mode (I-mode). Through the inclusion of beta feedback control via the neutral beam injection (NBI) heating, stationary NBI heated I-modes can now be obtained [72]. This was not possible before due to the narrow access window in terms of heating power on ASDEX Upgrade. This development enabled the detailed study of so-called I-mode pedestal relaxation events (PREs), which constitute energy and particle losses that appear at high pedestal pressures close to the I-H transition, see figure 7. [73].While these events show some properties of type-I ELMs, like e.g. the relative size scaling with pedestal pressure, they are far from the ideal peeling-ballooning boundary and cause less relative energy losses ($\Delta W/W_{MHD} \approx 1\%$). The expelled energy reaches the divertor, where the power deposition profile is usually set by Spitzer-Härm electron conduction [72,73]. Since PREs appear close to the I-H transition, they could be used to monitor the proximity to H-mode, and hence to avoid the plasma entering an undesired ELMy H-mode. Furthermore, I-mode has been observed in both helium and hydrogen discharges [74]. This is important since any future fusion device will have to start operation in a working gas other than a 50:50 D-T mixture. It also gives central information to validate theory and simulation to check whether the I-mode existence and its characteristics scale with ion mass as expected.

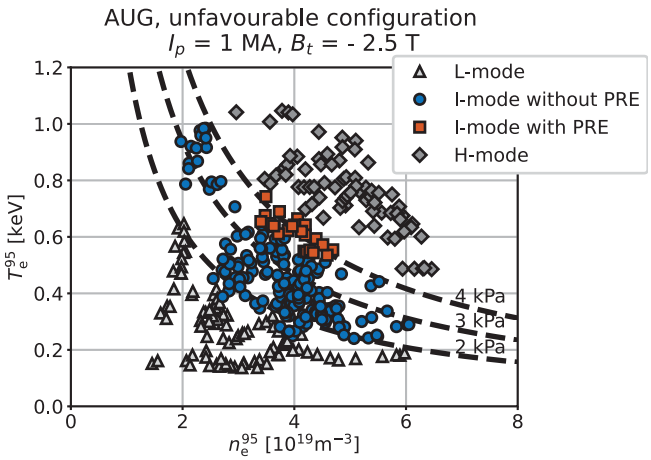

Figure 7: Existence diagram of I-mode without (blue) and with (red) pedestal relaxation events (PREs) in $T_e - n_e$ space.

Regarding reactor compatibility, for the first time, a divertor leg of an I-mode plasma has been detached by the simultaneous increase of seeding and heating power [75,153]. Through the injection of N into the divertor, the inner divertor leg cools down and eventually, the plasma detaches. The confinement is maintained at a high level, which is encouraging for future experiments that will try to detach both divertor legs.
A major breakthrough has been obtained in the theoretical understanding of the existence and the properties of the I-mode.

In particular, it has been shown that the I-mode is a result of a dominance of the drift-Alfvén turbulence in the plasma edge, which can lead to different energy and particle transport through parallel conduction. Phase randomization at large scales at sufficiently high pressures leads to the appearance of the weakly coherent mode, one of the main characteristics of the I-mode [76].

4.6.2 QH-mode

Dedicated QH-mode development experiments were carried out on ASDEX Upgrade in collaboration with U Sevilla, in forward and reversed I_p /B_t configuration. Low density plasmas with up to 8 MW NBI heating were achieved in reversed field for the first time. Transient QH-mode phases up to 300 ms showed signatures of edge harmonic oscillations (EHO) in various diagnostics. In some discharges they co-existed with ELMs when the EHO was still too weak to take over particle transport. In order to slow down impurity accumulation, ECRH was indispensable in these discharges. The resulting electron temperature was much larger than the ion temperature (T_e /T_i ~2), this being one of the main differences compared to the previous QH-mode discharges (T_e /T_i ~0.6) at AUG with carbon wall. It remains to be seen if the EHO is in general too weak to sufficiently expel heavy impurities, or if it can be established in a way that it leads to stationary conditions.

4.6.3 EDA H-mode

A stationary H-mode without type-I ELMs has been achieved in the ASDEX Upgrade tokamak in collaboration with IST Lisbon by applying central electron cyclotron resonance heating above the L-H power threshold. It is naturally obtained in favorable ∇B configuration at high shaping and has several features which are desirable for future reactors, such as dominant electron heating, low input torque, possibility of access at low input power, good energy confinement (H_{98y2}=0.9...1.3), high density with f_{GW}=0.8...0.9, and no impurity accumulation despite the absence of ELMs. The EDA H-mode always features a quasi-coherent electromagnetic mode in the pedestal region, which seems to be responsible for enhanced transport losses, as its appearance and disappearance are correlated with changes in edge and divertor parameters [77]. Recently, the EDA H-mode operational space could be extended to higher power of up to 5 MW so far by combined ECRH and NBI heating using Argon seeding for pedestal radiation [78].

5 Physics of Non-axisymmetric Perturbations

The nominally axisymmetric configuration of tokamak plasmas implies particle orbits that are closed in themselves and therefore ensure good confinement at low collision rates. Nevertheless, small non-axisymmetric magnetic perturbations (MP) can be useful to control plasma instabilities, such as Edge Localised Modes (ELMs) which are a major challenge for ITER. ASDEX Upgrade (AUG) has recently been upgraded with a versatile set of 16 active magnetic perturbation coils that mimics the MP coils of ITER and individual power supplies for each coil to provide maximum configurational flexibility. Main research topics so far have been the plasma response to the MP, ELM mitigation and suppression, and MP effects on fast particles and divertor heat load.

5.1 Plasma Response to Non-axisymmetric Perturbations

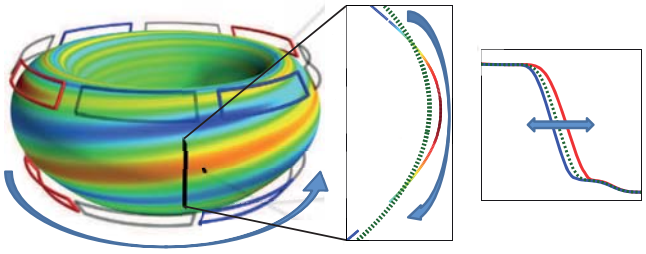

Figure 8: 3D cartoon of the plasma deformation by MPs (left). As the MP field is rotated, different toroidal phases are detected in imaging (middle) and profile (right) diagnostics.

In response to externally applied magnetic perturbations, the plasma current pattern changes. Significant effort has been made to validate plasma response models against measurements in ASDEX Upgrade [79-85]. The ability to rotate MP fields in AUG adds a toroidal dimension to the available set of excellent edge diagnostics with various poloidal sightlines and therefore allows to precisely map the plasma deformation [79,80] (see figure 8). It is found that the plasma-generated response field is of the same order as the applied ('vacuum') MP and thus cannot be neglected. The measured plasma deformation is in good quantitative agreement with predictions from the 3D ideal MHD equilbrium VMEC and the linear resistive MARS-F codes [80]. The versatile MP coil set of AUG allows to vary the alignment of the external MP pattern with the plasma field lines. Experimentally, the strongest effects of the MP on plasma density and ELM behaviour is found if the applied MP pattern is moderately misaligned with respect to the field line inclination, i.e. has a Within the project "non-resonant" (kink-like) MP component which is amplified by the edge pressure gradient in H-mode plasmas. Both the VMEC results and an extensive scan of runs of MARS-F [81-84] agree in that experimental MP effects on plasma density and ELMs are strongest if the calculated plasma response is maximal [82]. This result is confirmed in an inter-machine study [84], giving credence to predictions of optimal MP patterns for ITER [82].
A more detailed prediction of the plasma response is obtained with the non-linear, resistive model of JOREK [85]. Due to toroidicity and cross sectional plasma shaping, neighbouring poloidal modes (mode number m) couple. Therefore, kink-type modes with m>qn (q: safety factor, n: toroidal mode

number) drive resonant, resistive ("tearing") modes at m=qn, which however in H-mode are in most cases attenuated by flow-induced helical currents perpendicular to the magnetic field. Tearing and consequently magnetic islands can develop only at magnetic surfaces where shielding flow vanishes. For most plasmas, this limits the region of significant resistive plasma response to the bottom of the H-mode edge gradient region, and explains why the ideal MHD response calculated by VMEC can reproduce the experimental plasma deformation.

5.2 Mitigation and Suppression of ELMs

A main objective for the application of MP fields in tokamaks is their mitigating effect on the ELM instability. In AUG both reduction of the ELM loss [86] as well as full suppression of ELMs [87] is studied. The fraction of pedestal energy lost per ELM event is reduced by up to a factor of 10 as compared with no MP [86], but this is tightly correlated with a reduction of plasma density, the so-called "pump-out" effect. However, the divertor peak energy density, a main concern with ELMs, is reduced by only about a factor of 3. This observation agrees with a simple model for the pedestal relaxation and scrape-off layer transport [88] which assumes that the divertor load reduction is partly due to the pedestal density reduction. Extrapolation of this model for ITER Q=10 conditions suggests that ELM mitigation will not be sufficient to reduce the ELM peak energy density to below the material limits.

The non-axisymmetric deformation of the plasma by MPs has a clear effect on the mechanism of the ELM instability. The growth of ELM precursor oscillations is now localised at one of two non-equivalent zero-crossings of the plasma surface displacement [89,90] which correspond to field lines where the local magnetic shear is reduced by the MP, and which become first unstable against ballooning modes [89-91].

ELMs are fully suppressed in AUG in a scenario recently developed in collaboration with DIII-D [87]. Main emphasis was placed on identifying the necessary access criteria: MP configuration for maximum plasma response, edge safety factor in a window q_{95}=3.55...3.95, pedestal top plasma density below $3 \cdot 10^{19}$ m^{-3}. There is no clear collisionality limit, as ELM suppression can be obtained at low pedestal temperature as long as the density stays below the limit. As observed in other experiments, there is a sensitivity to the plasma shape which makes it difficult to obtain full ELM suppression at both lower and higher triangularity than that of the proven AUG scenario (see data and references in reference [87]).

The transition to ELM suppression is sharp, ELMs disappear immediately along with a further plasma density drop, making ELM suppressed plasmas the lowest density H-mode plasmas that can be obtained in AUG. This additional outward particle transport, studied in the frame of a Ph.D. thesis [92], can be attributed to medium to broad band turbulence localised in the edge pedestal region in a large but limited range of toroidal positions with respect to the orientation of the MP (figure 9). Filamentary transport is observed in the midplane scrape-off layer, which is correlated with saturation current spikes in the divertor at corresponding positions that are connected by magnetic field lines. This mode is supposed to finally clamp the pedestal pressure below that of the ELMy phase, leading to ELM suppression. The pedestal pressure, and therefore the confinement penalty, can be influenced by adjusting the MP field strength. The characteristic turbulence exists only when the MP is applied, and disappears instantaneously if the MP is switched off. The nature of this turbulent mode is under further investigation.

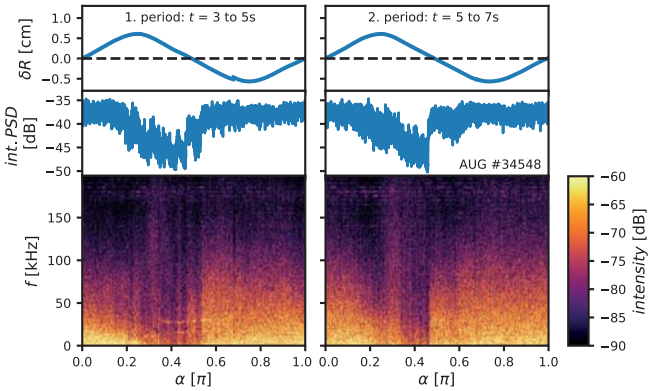

Figure 9: Plasma edge density fluctuations during ELM suppression (spectrogram and fluctuation intensity) from Ka-band microwave reflectometry as the toroidal MP orientation is scanned.

No issues arise from operation of ELM suppressed plasmas with the tungsten first wall of AUG. From pulsed injection of W a decay time of the order of the main ion particle confinement time can be inferred, indicating the outward transport is effective as well for impurities. However, high densities facilitate reactor-compatible divertor operation and therefore means to re-fuel ELM suppressed plasmas are studied. Pellet injection [93] has been found to be an efficient way to compensate for the pump-out effect. Complete ELM suppression is maintained as long as the above-mentioned critical pedestal density is not exceeded.

AUG experimental data is used to support model development. ELM suppression can be obtained in a wide range of plasma rotation, specifically as well if the field-shielding electron flow velocity perpendicular to the magnetic field does not vanish [87]. This seems to rule out early models which invoke enhanced radial transport by large static magnetic islands in the pedestal top region. The evolution of ELMs and their interaction with MP fields has been modelled with JOREK [94]. The results suggest that ELM modes couple non-linearly to the MP-induced perturbation which causes their saturation before an ELM crash can occur. In addition, the reduction of pedestal pressure gradient reduces the ELM drive.

5.3 Fast Particle Losses

The effect of plasma edge perturbations on particle orbits are especially strong for energetic ions, which undergo few collisions and -due to their wide orbits- can be diagnosed well with detectors mounted outside the plasma. One example is the acceleration of neutral beam generated ions during ELM crashes which is in contrast with the benign turbulence during MP-induced ELM suppression, during which no ion acceleration is observed [95]. The presence of MPs leads to multiple resonances of particle orbits with the toroidally and poloidally periodic perturbation field which can cause a change of the canonical toroidal momentum and thereby a radially inward or outward directed particle drift. In a collaboration with U Sevilla, this so-called edge resonant transport layer has been mapped out with ASCOT particle following simulations as a function of radius and particle pitch (see figure 10). Predicted fast ion losses at detector positions are in quantitative agreement with measurements [96].

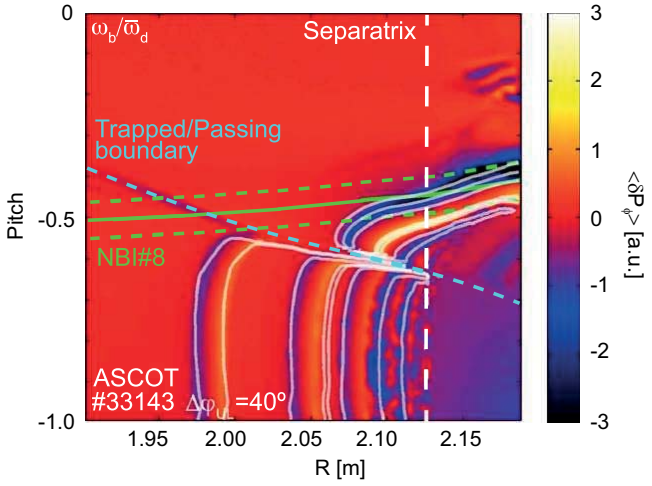

Figure 10: Map of the canonical toroidal momentum change (radial drift) as a function of pitch angle and radius, for 60 keV particle energy.

5.4 Divertor Heat Load

The impact of MPs on divertor heat loads has been studied under various plasma conditions [97-100]. The ability to rotate the MP field toroidally allows to map the heat flux pattern on the divertor target vs. radius and toroidal angle. Without MP the heat flux is toroidally symmetric, peaks near the separatrix strike zone, and decays exponentially in radial direction. The application of MPs breaks the toroidal symmetry and leads to helical diversion of field lines ("side lobes"), which in case of resonant plasma response carry a detectable heat flux (see figure 11). It is found that for attached divertor conditions both in L-mode [97] and H-mode [98] the heat flux is distributed in such a way that the toroidal average matches the non-MP radial profile within error bars, i.e. the radial decay lengths with and without MP are identical. This is studied with EMC3-EIRENE 3D transport simulations [99] which reproduce the absence of broadening of the wetted region if the resonant components of the magnetic perturbation field are shielded by sheet currents on the rational surfaces.

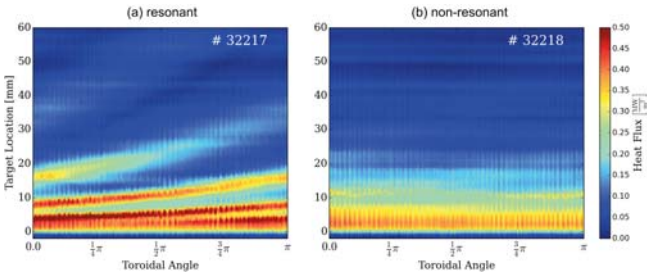

Figure 11: 2D heat flux profile on the divertor target for a resonant (a) and a non-resonant (b) rotated MP with toroidal mode number n=2.

As the plasma density is increased towards divertor detachment, the helical modulation due to the side lobes diminishes, towards an essentially axisymmetric profile in the detached case [100]. Divertor heat flux profiles for the attached and detached cases, with and without MP, are shown in figure 12. As in the case without MP, detachment sets in first near the separatrix. There is no experimental indication that under completely detached conditions the heat flux at the side lobe positions is significantly larger than in the axisymmetric case, i.e. no "burn-through" of side lobes is seen.

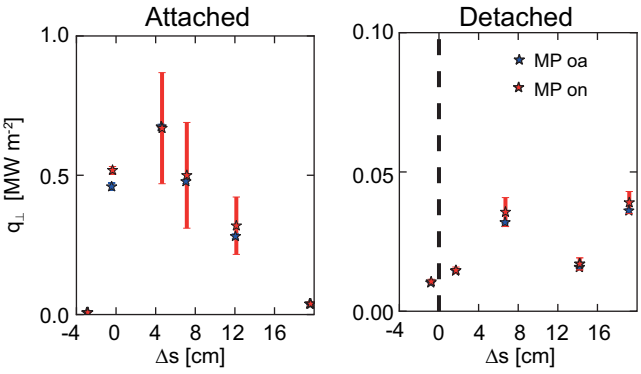

Figure 12: heat flux profile on the divertor target with and without MP for attached and detached divertor conditions.

6 Transport

The research on transport and confinement at ASDEX Upgrade (AUG) aims to increase our fundamental understanding of turbulent and collisional transport in tokamak plasmas through experimental investigations as well as the validation and improvement of our predictive capability.
The experimental research includes in particular the impact of a change of main ion species, particle and impurity transport, fast particle physics and transitions in confinement regimes.
A large hierarchy of models with increasingly high theoretical foundation are applied in interpreting and predicting the

experimental observations. A large part of the work is dedicated to the integrated modelling, based on the ASTRA transport package, with the free-boundary equilibrium code SPIDER, which has also been recently adapted to work as transport and equilibrium solver for the new flight simulator FENIX.

6.1 Isotope Effects

In the research on the impact of a change of main ion species (He, H isotopes), the confinement of helium plasmas has been experimentally documented to depend on the type of heating. With dominant electron heating it is similar to that in deuterium plasmas, while a degradation is observed with increasing fraction of ion heating. These observations can be theoretically explained by a different role of zonal flows in electron and ion dominated turbulence regimes [101]. Research in L-mode plasmas has revealed the dominant role played by the increased energy exchange in hydrogen plasmas in combination with ion dominated heat transport [102]. Interpretive simulations of these plasmas show that the experimental profiles and confinement times are reproduced with the same transport coefficients for hydrogen and deuterium plasmas. In H-mode the isotopic dependence is observed to be stronger than in L-mode, in connection with a better confinement in the deuterium edge pedestal. With increased edge triangularity, the hydrogen pedestal matches that of deuterium for the same source profiles, while deuterium core confinement is still observed to be improved compared to hydrogen in plasmas with a large fraction of NBI heating [103]. Due to different fast-ion slowing down times with different isotope mass, the fast-ion pressure is significantly larger with deuterium beams than with hydrogen beams, despite similar heating powers. The observed strong impact of the fast ion pressure in turbulence stabilization is reproduced in GENE simulations, which show an anti-gyro Bohm trend of core turbulence in these conditions. This result is consistent with a recent experimental characterization of core heat transport stiffness driven by ion temperature gradient and electron temperature gradient modes in AUG H-mode plasmas [104], revealing a strong impact of the electron to ion temperature ratio on both the threshold and the stiffness. Here GKW gyrokinetic simulations also identified a significant transport reduction by fast ion pressure with on-axis neutral beam injection heating. Isotope effects also strongly influence the properties of edge turbulence. An experimental analysis combined with an extensive linear and nonlinear gyrokinetic study with GENE revealed that the properties of edge L-mode turbulence in AUG and JET-ILW are similar, and characterized by resistive electron drift waves that are destabilized by the edge high collisionality and are strongly related to the kinetic electron dynamics [105]. The significantly larger transport in hydrogen as compared to deuterium is connected with the parallel electron dynamics and is strongly increased by electromagnetic effects. Remarkably, when considering all the effects in the non-linear simulations and the experimental uncertainties, the predicted heat fluxes can reproduce the experimental ones and their dependence on the isotope mass.

Comparative studies in AUG and JET-ILW have also been performed with the aim of exploring and understanding the negative impact of He seeding on confinement and transport of D plasmas [106]. This impact is observed to be more than a pure dilution effect and it is opposite to the confinement improvement observed with other low-Z impurities like nitrogen or carbon. In both devices He seeding is observed to lead to an increase of the electron density, a significant reduction of electron and ion temperatures, and an increase of the ELM frequency. The negative effects of He seeding can be minimized by maximizing the electron heating fraction, as well as by varying the deuterium fueling and by operating in regimes with improved pedestal stability.

6.2 Impurity Transport

AUG full W-wall has strongly motivated intensive and comprehensive research on impurity transport from both the experimental and the theoretical modelling standpoints. Turbulent transport properties are better investigated on low-Z impurities. These investigations require accurate measurements of low-Z impurity density profiles, which are typically provided via charge exchange recombination spectroscopy (CXRS), to which a significant body of work has been dedicated, resulting in three major advances. First, it was shown that CX reactions between impurity ions and thermal D neutrals with principle quantum number n=2 can contribute up to 40 % to the total measured CX intensity. Neglect of this neutral population leads to artificially high and peaked density profiles [107]. Second, to obtain accurate CXRS He density profiles it is necessary to account for the helium plume emission present in the measured spectra. This emission is comparable in magnitude to the active signal and required the development of a kinetic model to reproduce the measured spectra and obtain consistent values for the ion temperature, plasma rotation, and the He density [108]. Third, increased interest in Ar as a radiator for future devices has motivated the use of Ar in present day AUG experiments. This triggered the need for accurate information on the Ar content and the development of CXRS measurements on Ar 16^+ [109]. Analysis of AUG data has conclusively shown that all of the available Ar CX cross-sections for high-n transitions are incorrect and that corrections in both magnitude and energy dependence are needed to produce accurate density profiles from visible Ar CX lines.

These diagnostic advances have directly supported multiple investigations of core and edge transport. In particular, in the field of impurity transport they have allowed for an unprecedented comparison of He and B density profiles as a function of plasma parameters and lead to the confirmation of a disagreement between experimental measurements and theoretical predictions, particularly in conditions of strong NBI heating [110].

A parallel activity dedicated to the separate determination of the boron diffusion and convection by means of the modulation of a peripheral boron source not only lead to the development of a robust experimental approach, but also confirmed this type of deviation in the theoretical predictions of turbulent convection in plasmas with strong central NBI heating [111]. Theoretical studies have been performed to understand the nature of the observed disagreement, which was also observed to correlate with conditions of high collisionality. The impact of a neoclassical equilibrium distribution, as compared to the customary Maxwellian, on the turbulent transport of light and heavy impurities has been investigated [112] and found to have non-negligible effects on highly charged impurities at high collisionality, but to have negligible impact on light impurities. The role of beam ions on the turbulent impurity transport has also been investigated, and was shown to produce a significant increase of the convection in the outward direction from a combination of turbulent and neoclassical effects, as well as a reduction of the turbulent diffusion, connected with beam ion turbulence stabilization [113]. The combination of these effects leads to the prediction of hollow boron density profiles in the presence of strong central NBI heating, in agreement with the observations, resolving previous evidences of a disagreement. However, the theoretical predictions for helium still systematically provide a lower density peaking than the measurement by a small, but largely constant amount, a deviation which is not yet understood. On the side of heavy impurity transport, the high mass and charge of the heavy ions lead to a significant variation of their poloidal distribution, due to centrifugal and electrostatic forces, which provides an additional complication in the measurement and the modelling. A comparison of the impact of ECRH and ICRH on the W behavior has identified the dominant role of the electron heating in determining the reduction of W central peaking and the accumulation avoidance. The observations are largely consistent with the predictions of combined neoclassical and turbulent transport [114,115]. Specific experimental studies have investigated the impact of different NBI sources, producing different levels of rotation and beam ion temperature anisotropies [116]. Detailed two-dimensional SXR emissivity profile reconstructions show that the perturbation in the electrostatic potential generated by magnetic trapping of the non-thermal ions from NBI is responsible for significant changes in the W poloidal distribution. An excellent match with the results from fast particle modeling is obtained, validating the model for the poloidal fast particle distribution. Additionally, an enhancement of the neoclassical transport due to an outboard side impurity localization is measured in the experiment when analyzing the tungsten flux between sawtooth crashes, with qualitative consistency with neoclassical predictions.

In the field of particle transport, gyrokinetic studies applied to AUG pellet fueled plasmas lead to the identification of a new type of density gradient driven micro-instability and turbulence in the presence of reversed density profiles [117]. Strongly hollow density profiles lead to predicted turbulent fluctuations which are larger on the high field side, as a consequence of micro-instabilities which are more unstable at high collisionality and producing an inward particle flux. The theoretically predicted properties of particle transport in plasmas with different hydrogen isotopes have been investigated [118]. In ITG turbulence, the increase of the normalized collisionality with increasing mass leads to a reduction of the inward turbulent convection from hydrogen to tritium. A dedicated set of experiments has been performed in AUG to reproduce the conditions of a reactor plasma by matching physical operational parameters like the gyro-Bohm normalized heat fluxes and the ratios of external torque and core particle fueling by NBI to the heating power [119]. The experiments have provided independent scans of heating power and density and confirmed that in reactor conditions the role of the NBI particle source is negligible, while the density peaking can become significant at reactor low collisionality through the presence of a turbulent pinch. ASTRA modelling with the TGLF transport model shows good agreement with the experimental measurements and identifies a non-negligible impact of electromagnetic effects in reducing the predicted density peaking for typical reactor parameters.

6.3 Momentum Transport

Another topic of large interest is the understanding of the properties and sources of intrinsic toroidal rotation and the observed intrinsic rotation reversals. A large database of intrinsic rotation observations has been compared with the predictions of several local parallel symmetry breaking mechanisms, which lead to a residual stress in the momentum flux, including the impact of the neoclassical equilibrium distribution on the gyrokinetic turbulent momentum flux. None of these effects is found to be large enough to explain the observed values of intrinsic rotation gradients at AUG [120]. In contrast, unprecedented global nonlinear gyrokinetic simulations with the GKW code revealed that profile shearing can produce levels of residual stress that lead to intrinsic rotation profiles with gradients that are quantitatively comparable with those that are measured in AUG [121]. This study revealed a strong correlation of the predicted residual stress with the second derivative of the density profile, suggesting that the core intrinsic toroidal rotation profiles is mainly determined by the curvature of the density and temperature profiles.

An additional important aspect which is related to the interplay between turbulence, micro-instabilities and plasma flows is provided by the anisotropy and the tilt angle of the turbulent structures, for which a new diagnostic method based on Doppler reflectometry has been developed [122]. First measurements of this type in AUG showed a significant difference of tilt angle for different plasma conditions, as shown in figure 13, and the dominance of sheared E×B flows in determining the structure tilt was experimentally demonstrated in different turbulence regimes. The investigation of the amplitude and

properties of electron temperature fluctuations in the plasma edge can shed light on the nature of different confinement regimes, particularly those characterized by the absence of edge localized modes. These measurements are now possible at AUG by means of a Correlation Electron Cyclotron Emission (CECE) diagnostic [123], which measures long wavelength electron temperature fluctuation amplitudes, spectra, and correlation lengths. A 24-channel CECE radial comb allows the localization of edge temperature fluctuations with high level of coherence as well as the structure of broadband turbulence to be compared between the different confinement regimes.

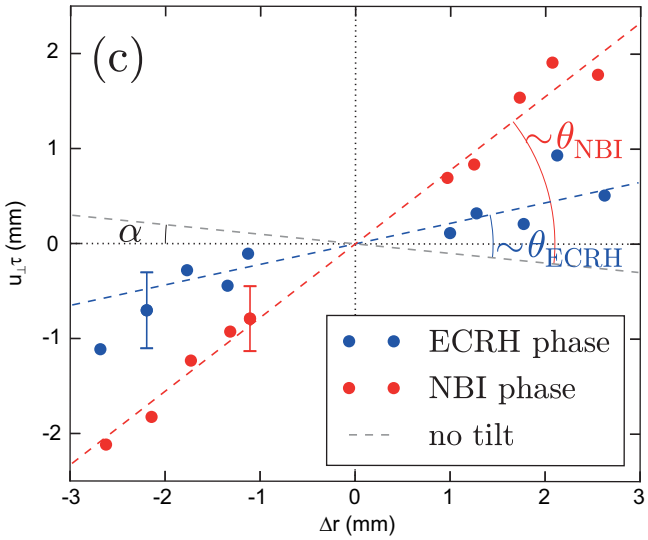

Figure 13: Product of the time delay and the perpendicular velocity measured for radially aligned structures, where the slope provides the tilt angle of the turbulent structures.

6.4 Fast Particle Transport

In the research area dedicated to fast particles, experimental evidence of core ion cyclotron emission (ICE) has been obtained [124,125]. In particular, it can be generated by the magnetoacoustic cyclotron instability (MCI), which is driven by the velocity-space inversion of sub-Alfvénic beam-injected ions [126]. The observed core ICE amplitude evolution in beam-heated plasmas results from the competition between the beam ion fraction build-up and the slowing down of the dominant beam ion velocity component, respectively destabilizing and stabilizing the MCI. The instability growth rates, calculated with the oblique MCI local theory, are broadly consistent with the observed dynamics of the core ICE. For the first time, Alfvén eigenmode activity driven by RF accelerated fast ions has been observed [127]. The mode is driven using radio frequency (RF) wave acceleration of either beam-injected deuterium ions or the thermal He^3 minority with a three-ion species ICRH scheme. In the case of beam ion acceleration, the mode only appears during deuteron acceleration at the 3rd beam IC harmonic. In discharges with a relatively low plasma current below 0.7 MA, the mode appears to be directly driven by sub-Alfvénic deuterium beam ions. Absolute measurements of the mode amplitude show that at least 1 % of the beam-injected power is transferred non-collisionally to the mode. The identity of this Alfvén mode remains to be determined.

Novel measurements of energetic He^3 ions accelerated with the three-ion species ICRH scheme have been obtained with CXRS [128]. Comparisons of the measured spectra with forward-modelled spectra evaluated using TORIC-SSFPQL distribution functions show agreement in the magnitude of the predicted CX spectral radiance and the energies of the ions that undergo CX, confirming that the wings in the CX spectra are due to ICRH-accelerated He^3. At the same time, discrepancies between the experimental measurement and the forward-modelling illuminate details of the velocity distribution function of the energetic helium ions which can be only captured by more sophisticated models.

Clear energetic tails have been observed by a scintillator-based compact neutron spectrometer (CNS) when ICRH is applied in the presence of NBI [129], proving that there is an over-proportional tail in the fast-ion distribution at the high energy end. Second harmonic absorption of ICRF waves by fast D can take place when ICRH is applied at the fundamental cyclotron frequency for H-minority, leading to a “synergy effect” in the neutron production. Evidence of this effect has been obtained examining the pulse height spectra measured by the CNS. From the unfolded emission spectra, a significant deuteron population around 500 keV has been obtained, much higher than the NBI injection energy.

Many fast ion studies have made use of the fast-ion D_α (FIDA) spectroscopy system, a charge-exchange diagnostic measuring the Doppler shifted deuterium Balmer-alpha radiation. The AUG FIDA system looks at one of the 60 keV neutral beams used for heating. This allows not only the measurement of the FIDA radial profiles, but also the reconstruction of the fast-ion distribution in the velocity space by a velocity space tomographic approach. In the core, the studies have been dedicated to the effect of neoclassical tearing modes (NTMs) on the fast ions [130]. Comparisons with TRANSP-NUBEAM simulations performed with and without additional ad-hoc fast ion transport coefficients have allowed a quantification of the effective radial transport produced by the mode. Additional comparisons have been performed with the full orbit code LOCUST, where a perturbation of the magnetic equilibrium which describes the presence of the NTM is included. A recently installed edge fast-ion D-alpha (FIDA) diagnostic provides information on the density and distribution of confined fast ions close to the plasma boundary [131]. The system makes use of two new spectrometers that allow for FIDA measurements with unprecedented temporal resolution and simultaneously measure the emission of thermal background neutrals, allowing the quantitative interpretation of passive FIDA measurements.

Measurements using the edge FIDA system show significant levels of passive FIDA radiation in discharges with large edge fast-ion populations from off-axis NBI heating. In addition, a particularly strong response of the passive emission to edge localized modes (ELM) is observed [132]. The synthetic FIDA emission calculated from the neoclassical fast-ion slowing down distribution function is in good agreement with the measured pre-ELM FIDA emission, while the post-ELM emission is overestimated. This discrepancy is concluded to result from ELM induced fast-ion losses, which are quantified to be about 60 % of the fast ions outside the last closed flux surface, with additionally a decrease in the fast-ion density of about 20 % in a range up to 4 cm inside the last closed flux surface. The observed ELM affected region is in good agreement with the radial extent of modifications to the connection length calculated by the nonlinear MHD code JOREK.

6.5 Integrated Transport Modelling

Important progress has been made in the integrated modelling capabilities and related applications. The impurity transport code STRAHL has been coupled with the ASTRA transport package. This has allowed in particular transport simulations of the pre-thermal-quench phase in AUG massive gas injection experiments [133], demonstrating that, despite the 3D nature of the physics, a 1D approach can already reproduce the main time scales of the experiment and capture important trends. The coupling with STRAHL has also been applied to model new experiments on the plasma response to peripheral cold pulses produced by laser ablation of impurities with different fractions of ion and electron heating [134]. This study, performed with ASTRA/STRAHL and the transport model TGLF, has confirmed that the fast increase of the central electron temperature in response to the peripheral cooling is produced by trapped electron mode stabilization due to the sudden flattening of the electron density profile. The electron density response is also consistently simulated by TGLF, taking into account the peripheral source produced by the impurity injection. A companion research with ASTRA and TGLF has been dedicated to the modelling of the different regimes of Ohmic confinement, from linear to saturated [135]. The interplay between the increased electron to ion coupling and the reduced impurity content with increasing density has been identified as the main cause of the confinement transition. Increased impurity content can delay the transition with increasing density, leading to improved Ohmic confinement at intermediate to high density.

The increased confidence on the modelling capabilities recently lead to the development of a full plasma integrated modelling approach, from magnetic axis to separatrix, applicable to H-mode plasmas. The integrated modelling workflow makes use of the ASTRA code, the core transport model TGLF, an improved empirical transport model for the pedestal region, the MISHKA MHD stability code and an extension of the two point model for the scrape-off layer [136,137]. It allows the prediction of the ion and electron temperatures, density and rotation profiles using as inputs only externally controlled engineering parameters and the plasma shape, but no information from kinetic profile measurements, not even as boundary conditions at the separatrix, which are consistently predicted by the model. The workflow has been recently fully automated and has been shown to reproduce dependencies of plasma stored energy on current, power, density and fueling, magnetic field and plasma shape with high accuracy, significantly closer to the experimental values than the widely used $IPB_{98(y,2)}$ scaling law, as shown in figure 14. Finally, together with JET, AUG has recently contributed to an extension of the ITPA confinement database [138], allowing the development of new multi-device statistical analyses and regressions [139] with a large number of metallic wall observations.

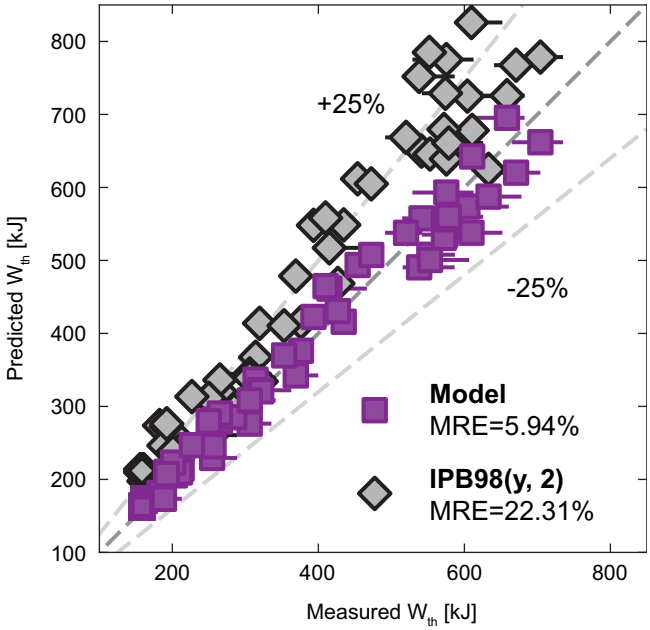

Figur 14: Predicted vs measured thermal stored energy using the $IPB_{98(y,2)}$ scaling law and the full plasma integrated modelling approach of [136,137].

7 Power Exhaust Physics

Operation of tokamaks with H-Mode characteristics at high densities and at least partially detached divertor conditions is generally foreseen for future high-power fusion systems, including ITER. Important physics elements are the radiative characteristics of impurities, the power width in the divertor region, the separatrix density and its relation to neutral recycling and the effects of drifts in the divertor.

7.1 Radiative Cooling

Major success is reported in reducing the power deposited on the divertor plates by controlling the radiation at the outermost

confinement region near the last closed flux surface. With full detachment induced by impurity seeding, radiation is dominantly emitted from a small, poloidally localized volume inside the confined region, in the vicinity of the X-point. This so-called X-point radiator (XPR) emits about 40 % of the exhaust power and leads to temperatures of only a few electron volts close to the X-point, resulting in parallel temperature gradients within the confined region. The location of the XPR is observed to vary relative to the X-point depending on seeding and power levels and is observed up to 15 cm above the X-point inside the confined region.
The XPR location can be detected in real-time using the AXUV diode bolometer diagnostic. The position of the radiator relative to the X-point can be controlled in real time by the nitrogen puff level. The active control for the position of the XPR was implemented and tested successfully (see figure 15).

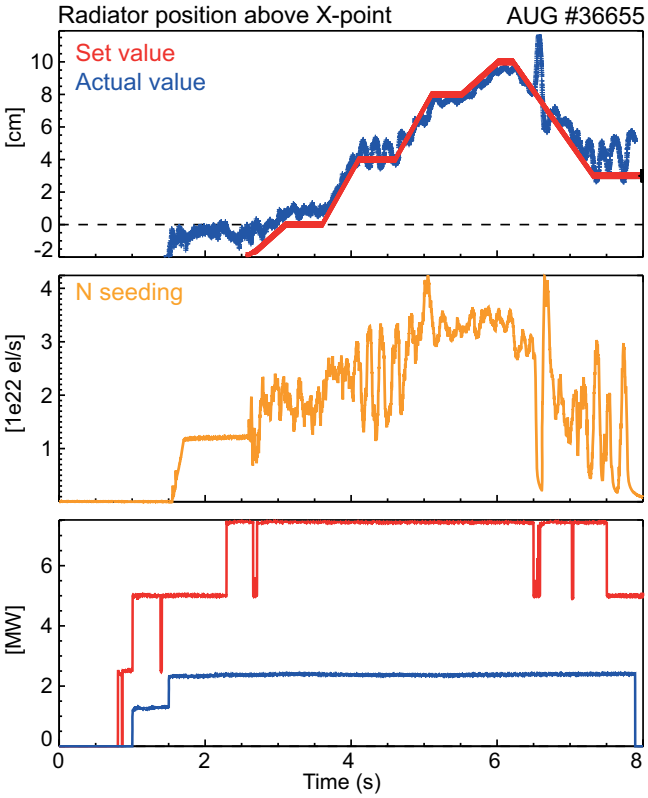

Figure 15: Time traces of AUG # 36655; Top: Programmed and measured location of the XPR; Middle: Applied nitrogen puff used as actuator; Bottom: Applied heating power. At a certain height of the XPR above the X-point, an ELM-suppressed regime is observed with minimal reduction of confinement ($H_{98} \approx 0.95$). While the control of the XPR already allows operation in full detachment at a dissipated power fraction of around 95 %, such an ELM-suppressed regime additionally eliminates the challenge of the transient, intolerably high heat fluxes by ELMs.

Supplementary, numerical simulations using the transport code package SOLPS were able to recover key elements of the transition to complete detachment. These include experimentally observed strong divertor asymmetries prior to detachment, the formation of a poloidally extended area of high plasma density on the high field side of the SOL extending from the inner divertor as well as the poloidal profile of absolute values of the measured neutral fluxes (within 20 %). Key elements for accessing numerically such conditions are the activation of drift terms combined with anomalous SOL transport in highly dissipative conditions. A key area of research has been the redistribution of radiating impurities in the SOL and pedestal in detached conditions. The observed radiation distribution exhibits a strong concentration above the X-point, which indicates low temperatures and significant plasma parameter variations on closed field lines.
To investigate mixtures of different impurity species, dedicated discharges with mixed argon and nitrogen seeding have been performed. The experiments reveal, that the radiation distribution in the plasma can be affected by the choice of the impurity mixing ratio, which could also be reproduced by numerical simulations with the SOLPS 5.0 code package. A detailed analysis of the simulations shows, that a trade-off between fuel dilution and pedestal top temperature drop can be achieved, depending on the mixing ratio of argon and nitrogen. Additionally, the simulations also reveal, that the impurities have a considerable impact on the main ion plasma flow in the scrape-off layer. At high seeding levels, a qualitative change of the flow patterns results in a redistribution of the impurities from the outer to the inner divertor.
Detailed modelling of the pedestal radiation caused by the seed impurities neon and argon with the STRAHL code revealed a strong influence of charge exchange with deuterium neutrals [140]. The charge exchange shifts the ionisation balance towards lower states, which emit more radiation for given local plasma parameters. The effect increases the radiation of neon and argon by a factor 3 for typical conditions. Predictive calculations using the available atomic data showed a decreasing effect for krypton and xenon.

7.2 Transport in the SOL

The extrapolation of power exhaust optimized scenarios require a best knowledge of the so called power width in the SOL. Divertor heat flux data from infra red (IR) from various tokamaks in attached H-Mode regime show that the power width, λ_q, scales approximately like 1.6 (a/R) $\rho_{s,pol}$. For ITER this extrapolates to very narrow power width of about 1 mm only and will require seed impurity levels that narrows the operational range of ITER.
However, the IR based scaling comes with the restriction that only discharges were considered with attached divertor conditions, unlike the conditions foreseen for ITER.
To evaluate the situation and scaling of the power width, improvements to the Thomson scattering (TS) diagnostic have enabled the study of near scrape-off layer (SOL) decay lengths

in recent years [141,142,143]. In such attached H-mode regimes, the SOL upstream dataset is shown to have the same main parametric dependencies as the scaling inferred from downstream IR measurements. An analytical accessible (collisional) relation from the two-point model is found to best relate the upstream decay lengths and downstream divertor power widths. Thus, importantly, TS and IR measurements can be used synergistically to construct a general power width data base.

A transition to flat SOL ne profiles, previously reported for L-mode plasmas in many machines, has been observed in AUG detached H-mode regimes, as foreseen for ITER. When the flattening of density profile happens in H-mode detached plasmas, the broadening of near SOL electron temperature decay length appears which is potentially a benefit for future devices which need to exhaust about 100 MW through the SOL [144]. However, such broadening needs to be weighed against a possible concomitant confinement degradation in the confined plasma.

Based on the extended data base of the power width, a study was performed in order to compare to theory based turbulence predictions. As the principal result the power width is correlated to turbulence strength, i.e. $\lambda_q \propto \rho_{s,pol} \cdot (1+2.1\alpha_t^{1.7})$ was derived where α_t describes a normalized collisionality ($\alpha_t = 3.1E\text{-}18 \cdot R \cdot q2 \cdot n \cdot Z_{eff}/T^2$). The parameter α_t quantifies the relative importance of the interchange effect on drift-wave turbulence as proposed by Scott [145]. The data base shows in the limit of low edge densities ($\alpha_t \cong 0.2$) accurate agreement to the IR based power width scaling. At elevated separatrix densities ($\alpha_t \cong 1$) the power width is broadened by a factor of up to about three accompanied by a reduction of the $H_{98,y2}$ confinement factor and this connects turbulence changes with global confinement properties.

A further element of power exhaust studies is the transfer of particles to the first wall elements. In this region, named far scrape-off layer, the transport is highly intermittent and non-diffusive as observed by the appearance of plasma filaments. Transport codes using effective diffusion coefficients are still the main workhorse investigating the scrape-off layer and divertor regions. An effective perpendicular diffusion coefficient for intermittent filamentary dominated perpendicular transport in the scrape-off layer is motivated by the telegraph equation, describing an exponentially decaying correlated random walk. On short time scales, the telegraph equation describes ballistic transport of filamentary structures with a typical velocity and typical correlation time. On long time scales or for stationary conditions the telegraph equation behaves diffusive. The diffusion coefficient can be estimated from the corresponding typical scales on the short time scale, which are the typical velocities and sizes of the filaments. This way, the transport coefficient of such intermittent transport can be applied to the afore mentioned transport codes [146].

7.3 Divertor Physics

The divertor peak energy fluence during transient events (such as Edge Localized Modes – ELMs) is a crucial quantity to predict, as it needs to be compared to divertor material limits. A considerable step forward in the prediction of divertor peak energy fluence during type-I ELMs ε_{ELM} was recently achieved by assembling a multi-machine database. Not only it was shown that ε_{ELM} scales with the pedestal top electron pressure, but also a simple model – which recovers such dependence – was introduced. This model assumes that a magnetic flux bundle in the pedestal region reconnects to the divertor targets and transfers all its energy to the divertor tiles. The model [147] prediction represents a lower boundary for type-I ELM data, while an upper boundary is found multiplying the model prediction by 3. Extrapolation of ε_{ELM} to ITER are found to be of concern, as they are above ITER divertor material limits for the Q=10 burning plasma scenario.

This model has been also compared to transient events in other confinement regimes, such as Pedestal Relaxation Events (PREs) in I-mode [148]. The divertor peak energy fluence during PREs ε_{PRE} is lower than that of type-I ELMs for the same pedestal top electron pressure. Therefore, in this case the model prediction represents an upper boundary for PRE data, while a lower boundary is found dividing the model prediction by 3. First projections to next-step devices of ε_{PRE} suggest that PREs might be of concern, but they call for a multi-machine study to investigate this further.

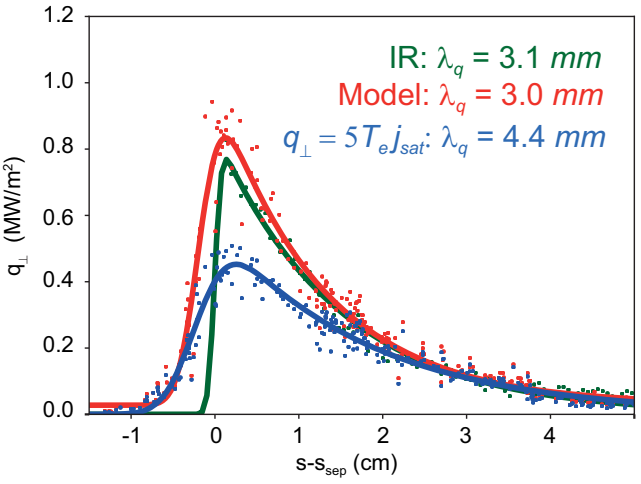

Figure 16: Heat flux profiles from IR (green, #36280) and from a heat flux model with currents (red) and without currents (blue).

Improvements for the analysis of very low density plasmas are also reported. Electric currents in the SOL are a well known phenomenon, however their effect on the heat flux transport is commonly assumed to be small. Measurements and in-depth analysis of Langmuir probe data showed that this assumption is not fulfilled at low densities. When neglecting the current in a model for the target heat flux the peak value is underestimated

and the profile width overestimated (see figure 16). Furthermore, around 50 % of the parallel heat flux might be carried by the current along the SOL for certain conditions, thus contributing to divertor asymmetries [149].
Knowledge of the hydrogen molecular behavior in diverted plasmas is crucial for the understanding of plasma fueling and detachment. For the first time in the AUG W-divertor, the Fulcher emission of the deuterium molecule has been measured at different toroidal positions starting from a divertor gas valve. A clear molecular spectrum could be detected for the sightline looking at the valve while the background, i.e. the emission from recycling deuterium, is a factor of about 4-5 lower than in the C-divertor. This difference can partially be explained by the higher ion reflection coefficient at a W-surface compared to C.
For high-recycling divertor plasmas, the volume-integrated ionisation rate and recombination rate of deuterium was estimated from spectroscopic measurements of two Balmer lines using a Bayesian methodology, which is able to add different measurements and prior knowledge about the system in a coherent fashion. Currently, an enhancement towards 2D inference of plasma parameters is being attempted by using the Gaussian process and by adding more experimental information [150].

7.4 Studies for Preparation of the Upper Divertor Upgrade

Major efforts were undertaken for Upper Single Null H-mode experiments to prepare the planned upgrade of the upper divertor e.g. to run so called snow flake configurations, potentially widening the power width locally when approaching the divertor target plates. With moderate deuterium and nitrogen puffing the inner target is attached and the outer one detached. For the first time at AUG such conditions could be described successfully by EMC3-EIRENE now including volumetric recombination (see figure 17). This improvement now allows a prediction of 3D effects in alternative divertor configurations possible after the divertor upgrade.

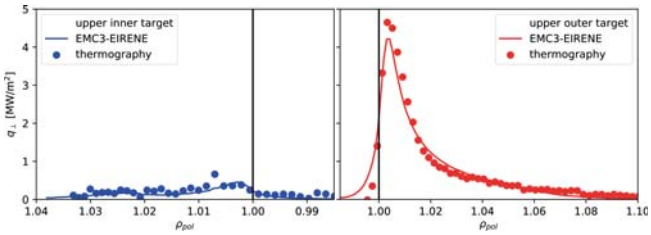

Figure 17: Heat Flux profiles of #35921 in comparison to simulations [151].

First SOLPS simulations for a low-field side snowflake minus (LFS SF-) configuration in the future upper divertor have been carried out. Compared to the conventional single null (SN) configuration with the same external input parameters and upstream profiles, the snowflake case showed a factor of 4.5 lower power fluxes at the outer target (see figure 18 (a)).

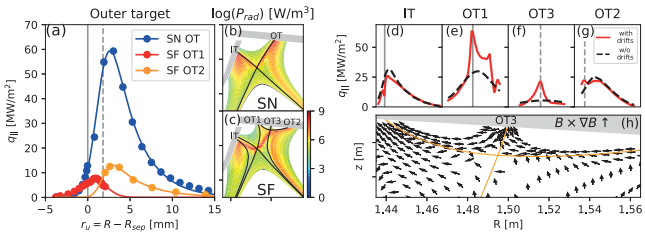

Figure 18: (a) Power fluxes at the outer target and (b,c) radiation rates comparing the single null and snowflake configurations. (d-g) Power fluxes around the strike points and (h) drift-driven particle flux in the snowflake simulation with drifts activated.

An additional radiative region was found between the primary and secondary X-points in the snowflake case (figures 18 (b,c)), leading to a 9 % higher radiative fraction compared to the SN case with a similar separatrix nitrogen concentration. In a nitrogen seeding rate scan, the snowflake divertor detached at a lower seeding rate, caused by the higher capacity of power and momentum removal via enhanced volumetric processes and cross-field transport. In addition, converged SOLPS-ITER simulations in LFS SF- with drifts fully activated were achieved. The drift-driven convective transport led to a larger inner/outer divertor asymmetry (figures 18 (d,e)), an enhanced radial cross-field transport and activation of the secondary strike point (OT3) magnetically disconnected from the upstream SOL (see figures 18 (f,h)). The activation of secondary strike points was one of the motivations for studying the snowflake configuration and observed in experiments and non-self-consistent simulations in TCV. Here the integral power at OT3 is very small (1 % of the total), but the effect might be interesting for a reactor if it would scale favorably with the machine size or the pressure.

7.5 Enhancement of SOL and Divertor Diagnostics

A second Thomson scattering diagnostic for the lower divertor was taken into operation at the end of the 2019 experimental campaign. It has access to three regions of interest: (i) the region above the outer divertor leg, (ii) the x point, and (iii) the high field side high density region. It covers the electron temperatures 1-100 eV, and densities 1E19 m^{-3} - 1E21 m^{-3}. The Thomson scattering light source is a Nd-YAG laser. A collection cell, located behind the outer divertor structure forms images of the scattering volumes on optical fibers, which transfer the scattered light to the polychromators. At the start-up of this diagnostic 26 spatial positions are available. The spatial resolution is around 1 cm. Further insight into the detachment dynamics is expected from the combined analysis of both TS systems.
To overcome the comparable poor spatial and temporal resolution of the TS diagnostic, a thermal helium beam diagnostic has been developed at ASDEX Upgrade that can simultaneously access the plasma edge and SOL region with a high spatial (3 mm) and temporal (900 kHz) resolution [152].

This diagnostic method provides electron temperature and density information by applying a line ratio technique. For the measurement, neutral helium is locally injected into the plasma edge region by an in-vessel piezo valve [153]. The emitted He I light is collected by an optical head with lines of sight, carefully aligned to the magnetic field lines. Transferred by fibers, the light is measured by a newly built four-color, 32-channel polychromator system. A collisional radiative model [154] is used for temperature and density profile reconstruction, while the change of emission intensity can be used directly to trace filaments in the scrape-off layer and high frequency modes in the confined region close to the separatrix.

7.6 PWI Aspects

To reduce the heat load of the PFCs nitrogen (as the impurity) gas seeding is well established in AUG, but in ITER the produced ammonia may influence the gas plant. Residual gas analysis at different locations of AUG and CXRS spectroscopy was used to investigate the nitrogen storage and conversion. It turned out that most of the ammonia is formed at plasma shaded surfaces in the divertor region. The produced ammonia is stored at the PFCs and released by the plasma disturbing subsequent discharges. At the inner divertor the nitrogen-to-ammonia conversion fraction can reach 50 %, independent on main plasma parameters. The nitrogen atom fluence is dominated by local effects and bypasses, whereas the ammonia production is proportional to the core nitrogen content and can be used as indication for nitrogen fluence from plasma [155,156,157].
The ASDEX Upgrade divertor manipulator allows insertion of PFC sized samples up to the size of two adjacent target tiles at the outer divertor for plasma exposure and subsequent retrieval in between experiment days without breaking vessel vacuum. Recent studies included for example the test of two actively cooled ITER target element mockups. These were exposed to a sequence of H-mode discharges up to highest available heating power and corresponding divertor power loads comparable to those expected in ITER. Post exposure metallographic analysis demonstrated that the tested manufacturing technologies fully met their thermo-mechanical performance specifications. Further experiments were carried out for validation of the code MEMOS-U, which models the motion of metallic melt layers at plasma exposed surfaces. The new strongly improved updated version of the code is now able to match the experimentally observed melt motion quantitatively including the finally emerging shape of the re-solidified surface after hundreds of transient melt events induced by large type-I ELMs [158]. The most recent experiment aimed at studying potential ion Larmor flux to geometrically shadowed side faces of toroidal castellation gaps. To this end samples with gaps similar to those between ITER vertical target monoblocks were exposed with a thin platinum marker layer whose thickness was measured before and after plasma exposure to type-I ELMy H-mode discharges. The profile of marker erosion at the gap side faces from entrance further down into the gap provided indeed for the first time direct evidence for the existence of ion Larmor flux according to the predictions of ion orbit models.
Tiles produced from tungsten heavy alloy (W-HA) were installed in the divertor of AUG as part of a strategy to prevent deep cracking of the target tiles [159]. 28 W-HA tiles out of a total of 128 divertor tiles were installed before the 2017 campaign at the segment boundaries, where the highest electromechanical loads due to halo currents were expected. During 2017 almost 1000 plasma discharges were performed and several of them were heated with up to 20 MW. During operation the W-HA tiles neither showed any specific behaviour nor was any increased Fe/Ni influx or plasma content measured. After six months of operation the W-HA tiles could be extracted and investigated microscopically. Even under the accidental exposure of leading edges as a consequence of evolving misalignments at segment boundaries, the loss of the Ni/Fe filler materials did not lead to a loss of W grains. Instead, the W skeleton remained intact and the W-HA did not reveal any macroscopic cracks. These rather positive results confirmed the preparatory investigations in the high heat flux device GLADIS (see also section on ‘Project Plasma-Wall Interaction’) and qualify W-HA as possible plasma facing material [160].

8 Scenario Integration

Investigating the development and integration of ITER and DEMO relevant plasma and heating scenarios is an ongoing experimental effort at ASDEX Upgrade which has been pursued with increasing intensity during the last couple of years.

8.1 Development of non-inductive tokamak discharges

A central challenge for plasma scenarios is the interaction of current profiles with confinement and thus kinetic profiles, which in turn feedback to the current profiles via the influence on Bootstrap current and current drive efficiencies of neutral beam current drive (NBCD) and electron cyclotron current drive (ECCD). Furthermore, the kinetic, rotation and fast ion density profiles themselves govern the transport coefficients making the parameter space strongly and non-trivially coupled. A parameter region with good confinement properties and large non-inductive fractions is obtained in ASDEX Upgrade at low densities with a relatively flat and elevated q-profile in the plasma core, while the q-profile is subject to optimization depending on which properties to put emphasis on. Such scenarios exists at 0.8 MA [161,162] and 1 MA [163]. Prior TGLF modelling [161,162] could not explain the steep ion temperature profiles in such scenarios. Investigations with an updated E×B shear saturation rule in TGLF suggested that rotational shear is the important physics missing in the prior investigations. However, a dedicated non-linear GENE modelling pointed rather to the fast ion-content as the important ingredient which for this scenario has only a small effect in TGLF.

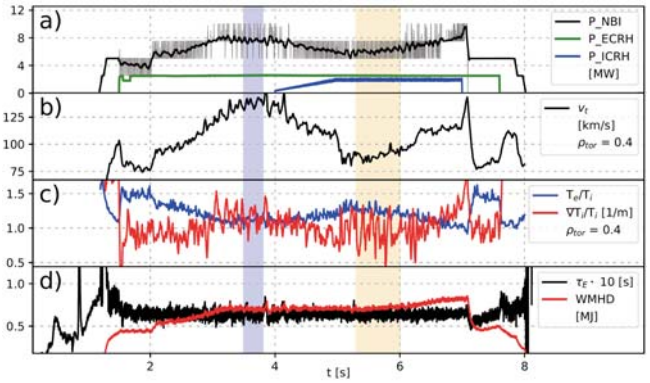

Figure 19: Evolution of the AUG discharge #35938 (I_p=0.8 MA, q_{95}~5.2).

In order to test the influence of rotational shear discharge #35938 was performed (figure 19) [164]. In figure 19 (a) one can see the heating mix; initially only ECRH and NBI is used, the latter of which is feedback controlled to keep β_{pol} constant at β_{pol}=1.8. Starting from 4.0 s, additional ICRH is applied, resulting in the feedback control reducing the NBI heating. This leads to reduced torque and toroidal rotation v_t, which can be seen in figure 19 (b). To guide the eye, two flattop phases with and without ICRF are highlighted. In figure 19 (c), it can be seen that between these two time intervals, only a very small decrease of normalized T_i-gradients is observed – if any. v_t has a discrete drop around 5 s, corresponding to the removal of one of the tangential NBI sources. Note, that the slow evolution of the normalized T_i gradient after 5.5 s should be attributed to the increase in T_e/T_i stemming from the change in the heating. Finally, in figure 19 (d) it can be seen that stored energy and confinement time are unchanged by the decrease in rotation. The density stays constant throughout the discharge.

From this, we feel confident in concluding that a reduction in rotation with concomitant constancy of R/L_{Ti} shows a very weak effect of E×B shear on ITG turbulence in the core region in scenarios similar to the one presented here.

An experimental complication for this kind of investigations is often the control of the q-profile, which requires iterative fine-tuning on a shot to shot basis. However, a much simpler approach seems feasible if self-organizing mechanisms can be exploited such as flux pumping, i.e. a theoretically described effect redistributing current and leading to a stable q-profile robust against small enough changes in Bootstrap current and driven currents. Experimental evidence for this effect had been reported from DIII-D. On ASDEX Upgrade, in particular the redistribution at the q=1 surface [165] was focus of recent experiments in order to compare to theoretical predictions. Such experiments require a high accuracy determination of the current profile in order to quantify the current redistribution. The necessary accuracy was obtained by including data from polarimetry and imaging motional Stark effect (IMSE) diagnostic [166] in the equilibrium reconstruction along with standard ingredients such as measurements of kinetic profiles and magnetic probes [167,168].

For plasmas with plasma pressures in the range of the ideal stability limit the observations suggest clear and strong flux pumping at the q=1 surface. In figure 20, such an example discharge with a well diagnosed q-profile using the IMSE diagnostic is depicted. Five phases are discussed in the following. The red shading indicates the presence of sawteeth, the blue shading their absence. Phase I starts with large sawteeth. After t = 1.55 s, the measured central q profile remains flat and clamped around unity. The last large sawtooth is observed around 1.62 s, but small sawteeth still remain. At 1.65 s (phase II), the 1/1 mode activity first appears, which is thought to cause flux pumping, i.e. moving current from the core to ouside of q=1. This mechanism prevents q_0 to drop quickly and eventually keeps q_0 at 1. Once β_N is increased above 2.4 (phase III) the small sawteeth disappear as well, even when the central co-ECCD is increased. When the co-ECCD is increased above 130 kA increasingly counteracting the flux pumping effect, sporadic small sawteeth reappear and become more frequent with more co-ECCD (phase IV). In the last phase, the driven current is reduced and the sawteeth disappear again. These findings are in line with the theoretical prediction that the strength of the flux pumping effect depends on the core beta which drives the (1,1) mode.

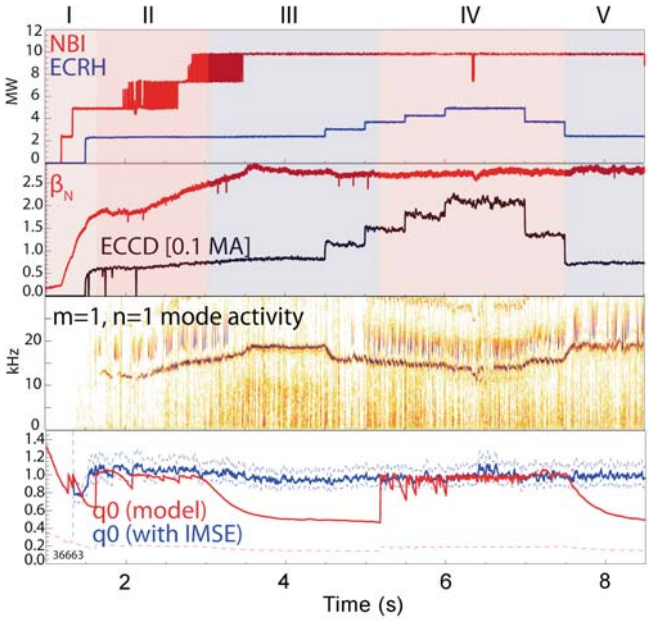

Figure 20: Time traces of the AUG discharge #36663 (I_p = 0.8MA, q_{95}~5.2, H_{98}~1.1) featuring flux pumping.

The bottom panel shows the modelled q_0 in red, resulting from an equilibrium reconstruction which takes external magnetic measurements, kinetic profiles, current diffusion and a sawtooth current redistribution model into account [168].

The blue curve shows the reconstructed q_0 when additionally taking into account the local measurements from the IMSE diagnostic, which will be referred to as 'measured q_0'. It can be seen that in phase III, without sawteeth, q_0 should drop well below unity if no other current redistribution mechanism were present besides neo-classical current diffusion. At the beginning of phase IV, the modelled q_0 is sporadically increased to unity by sawteeth, but drops well below 1 between the sawteeth. Since such a low q_0 would immediately trigger a sawooth, this suggests that the flux pumping mechanism still plays a role, but is not strong enough to completely suppress the sawteeth. This can also be seen in the measured q_0, which remains closer to 1.

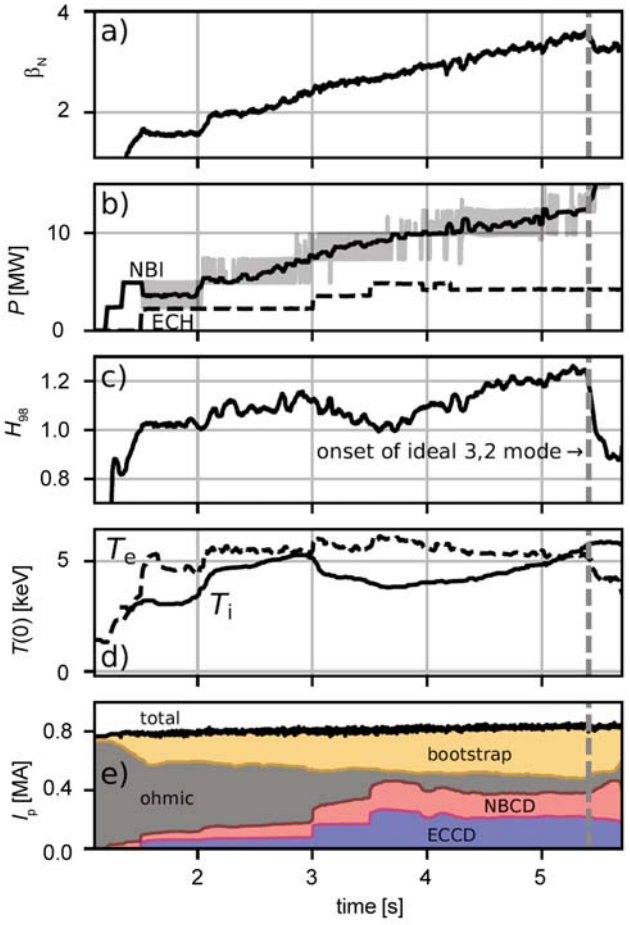

Figure 21: Time trace of the AUG discharge #36635 (q_{95}~5.1).

An example of an almost non-inductive plasma scenario exploiting the flux pumping phenomenon is shown in figure 21. Flux pumping helps to keep a relatively flat q-profile clamped to 1 in the plasma core, while a β-ramp is pursued. After the H-mode entry, on- and off-axis co-ECCD is added while simultaneously the feedback control of the plasma-β using the neutral beam heating is enabled (cf. figure 21 (a) and 21 (b)). This feedback control increases the plasma's stored energy along a pre-programmed trajectory. In this case, the goal is to identify the ideal stability limit by continuously increasing the heating.

With further addition of electron heating, the ion heat transport is increased, leading to a drop of the core ion temperature and confinement scaling factor starting at about 3.0 s (cf. figures 21(c) and 21(d)).

As β increases further, however, this drop is undone as β-effects begin to hinder turbulence more and more, thereby improving plasma confinement. This culminates in reaching the ideal stability limit at about $\beta_N \sim 3.6$ at 5.4 s where a (3,2)-mode occurs. At the same time, the composition of the toroidal plasma current changes drastically from the discharge beginning (cf. figure 21(e)): whereas at first the bulk of the plasma current is provided through induction from the central solenoid, with increasing plasma pressure and and external heating/current drive, less and less current is still provided by the central solenoid. Instead, the plasma's self-induced bootstrap current provides about half of the total, with most of the other half being provided by NBCD and ECCD.

This could allow a future fusion power plant based on a scenario similar to this one to extend its pulse length considerably, if not become fully non-inductive. This is even more true if the onset of the ideal mode may be extended towards higher beta.

This is realized in AUG by reducing the intrinsic error field mostly caused by the current feedthroughs for the poloidal field coils. In high-β experiments close to the 'no wall'-limit [169,170] these error fields are amplified via resonant field amplification (RFA). As a result, the slowdown of the plasma rotation leads to a lower beta limit. These error fields can be compensated by the magnetic perturbation coils according to the calculations of the electromagnetic code CAFÉ such that the resonant (2,1) and (3,1) components are removed. This removes the seed for RFA, preserves the plasma rotation and gives higher beta limit. It is observed that in these scenarios the ideal β-limit could be increased by about 10 % (from approx. 3.0 to 3.2-3.3) in line with stability calculations.

8.2 Negative Triangularity Plasmas

An ELM-free plasma scenario with possible relevance for a future reactor are negative triangularity (NT) plasmas in L-mode which have been found to provide H-mode like global confinement in TCV and DIII-D discharges. Despite the contour of the AUG first wall which is fitted to positive triangularity plasmas, it was attempted to realize NT plasmas. This also required a rearrangement of power supplies and thyristor sets for the poloidal field coils enabling the plasma shape as depicted in figure 22.

First scans of heating power and heating fractions have been undertaken, which demonstrated above L-mode confinement with dominant electron heating. The edge profiles and the impurity behavior are typical for L-mode discharges despite injected heating powers approximately 3 times above the

expected LH-threshold power. Further investigations will be conducted in future campaigns, as more extreme shaping seems to be possible and maybe also necessary to see the full effect of NT on plasma confinement. The comparisons to reference shapes with positive triangularity will be performed after the best NT shapes have been found.

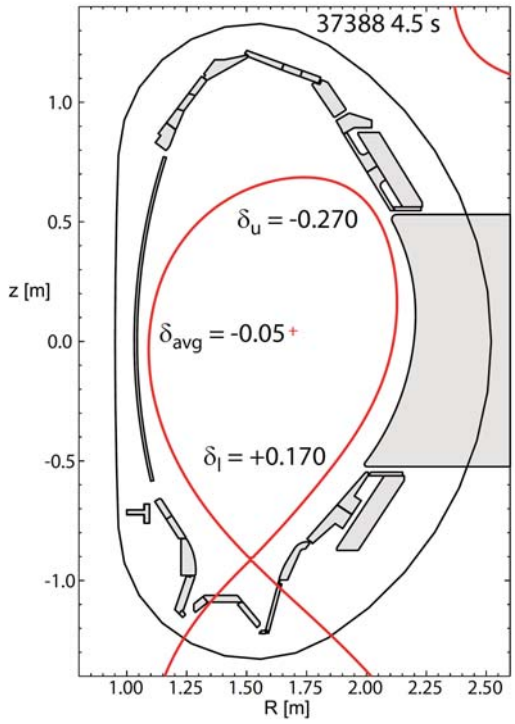

Figure 22: Separatrix of a NT plasma (I_p = 0.6 MA, q_{95}~5.9) in AUG.

8.3 Development of Heating Scenarios for Reactor-grade Devices

The 3-ion ICRF scenarios in the mixed H-D and H-^{4}He plasmas with absorbing ^{3}He ions were successfully established in AUG [171,172]. For reactor-grade devices, the 3-ion scenario promises a large ion heating fraction. In the plasmas with a hydrogen content of ~80...85 %, n(^{3}He)/n_e ≈ 0.5...1 %, at times combined with shifting the ^{3}He resonance to the high field side, were the required conditions to limit the energies of fast ^{3}He ions to approximately 1.5 MeV to ensure their good confinement in AUG and to obtain efficient plasma heating. The latter manifests itself in an increase of the core electron temperature and stored energy, as well as in the appearance of L-H transitions, if sufficient ICRF power is applied in L-mode. For the first time in the H-^{4}He plasmas (relevant for ITER PFPO-II) with the off-axis ^{3}He resonance at B_t=-2.5 T, L-H transitions were achieved with combinations of the ICRF power with ECRH and NBI as well as with the ICRF alone. In the H-D plasmas, energetic ^{3}He ions were measured by CXRS for the first time in AUG, with energies parallel to the diagnostic's lines-of-sight of up to ~35 keV [173,174]. The measured spectra agree well with forward-modelled spectra evaluated using TORIC-SSFPQL distribution functions, albeit with several discrepancies which illuminate details of the velocity distribution function of the energetic ^{3}He ions.

Experiments with controlled simultaneous variations of the confined and the non-confined parts of the ICRF-driven fast-D distribution using 3rd harmonic ICRF heating of D-NBI ions were conducted. These experiments [175] extended the earlier work with this ICRF+NBI scheme on AUG to more robust plasmas with central ECRF heating at B_T=2.5 T and f_{ICRF}=55.1 MHz which recently became possible [176]. More than a 2-fold increase of the neutron rate was observed when adding the ICRF power of 1.5 MW on top of 5 MW of NBI and 2 MW of ECRH [177]. Controlled variations of the fast D distribution were demonstrated with several physical parameters such as NBI power and acceleration voltage, ICRF power, the background electron temperature, and ICRF resonance location, in line with theoretical predictions. This efficient D acceleration scheme was also used as one of the auxiliary scenarios to study the 14 MeV neutrons due to the triton burn-up by the novel SciFi neutron detector which was tested on AUG in preparation of use on W7-X.

Scientific Staff

Tokamak Scenario Development (E1): C. Angioni, N. Arden, A. Asbach, K. Bald, K. Behler, N. Berger, V. Bobkov, A. Bock, A. Bonanomi, A. Buhler, A. Burckhart, D. Carlton, M. Cuevas, M. Dibon, R. Drube, M. Dunne, H. Eixenberger, K. Engelhardt, I. Eroveev, E. Fable, H. Faugel, J. C. Fuchs, H. Fünfgelder, L. Gianonne, F. Gis, I. Gomez, A. Gräter, A. Gude, S. Kjer Hansen, K. Hegele, J. Hobirk, I. Hofer-Maksymiw, W. Hornsby, V. Igochine, F. Janky, A. Jansen van Vuuren, A. Kallenbach, A. Kappatou, C.-P. Käsemann, B. Klesper, M. Koleva, A. Kostic, O. Kudlacek, P. T. Lang, P. Leitenstern, N. Leuthold, C. Li, L. Liu, A. Lohs, T. Luda di Cortemiglia, A. Magnanimo, M. Maraschek, P. de Marne, R. Merkel, V. Mertens, D. Meshcheriakov, A. Mlynek, F. Monaco, M. Muraca, J.-M. Noterdaeme, R. Ochoukov, F. Palermo, F. Paulus, B. Petzold, B. Plöckl, T. Pütterich, G. Raupp, M. Reich, M. Reisner, D. Rittich, V. Rohde, M. Rott, F. Ryter, O. Samoylov, G. Schall, M. Schandrul, A. B. Schmidt P. A. Schneider, G. Schrepfer, K.-H. Schuhbeck, M. Schubert, A. Seiler, G. Sellmair, B. Sieglin, A. Sigalov, E. Smigelskis, M. Sochor, F. Stelzer, J. Stober, G. Suarez Lopez, W. Suttrop, G. Tardini, M. Teschke, W. Tierens, W. Treutterer, M. Uhlmann, M. Usolceva, B. Vanovac, T. Vierle, S. Vorbrugg, D. Wagner, M. Willensdorfer, B. Wiringer, I. Zammuto, T. Zehetbauer, M. Zilker, H. Zohm.

Plasma Edge and Wall (E2M): M. Balden, M. Bernert, G. Birkenmeier, L. Bock, B. Böswirth, D. Brida, C. Bruhn, D. Carralero, M. Cavedon, G. Conway, P. David, S. Denk, A. Drenik, M. Dunne, R. Dux, T. Eich, S. Elgeti, M. Faitsch,

I. Faust, R. Fischer, S. Freethy, J. Galdón Quiroga, S. Glöggler, H. Greuner, M. Griener, G. Guedes Grenfell, T. Happel, F. Hitzler, T. Höschen, K. Hunger, K. Krieger, B. Kurzan, A. Lebschy, M. Li, T. Lunt, H. Maier, P. Manz, M. Mayer, R. McDermott, A. Medvedeva, F. Mink, C. Moon, R. Neu, D. Nille, T. Nishizawa, M. Oberkofler, T. Odstrcil, O. Pan, I. Paradela Perez, J. Pinzon, U. Plank, S. Potzel, D. Prisiazhniuk, T. Reichbauer, J. Riesch, A. Scarabosio, K. Schmid, C. Schuster, D. Silvagni, P. Simon, U. Stroth, Hong J. Sun, E. Sytova, B. Tál, E. Trier, G. Vogel, D. Wendler, M. Wischmeier, E. Wolfrum, A. Zito.

Tokamak Physics Division (TOK): V. Artigues, A. Banon Navarro, A. Bergmann, M. Bergmann, A. Biancalani, R. Bilato, T. Body, A. Bottino, R. Brzozowski, A. Chankin, D. Coster, A. Di Siena, T. Görler, F. Jenko, O. Kardaun, O. Linder, J. Martin Collar, F. Matos, I. Novikau, G. Pautasso, E. Poli, A. Stegmeir, K. Stimmel, D. Told, F. Vannini, M. Weiland, W. Zholobenko.

Magneto-hydrodynamics and Energetic Particle Physics Group (MHD-Group): V. Bandaru, A. Cathey Cevallos, S. Günter, T. Hayward-Schneider, M. Hölzl, K. Lackner, P. Lauber, A. Lessig, A. Lier, Z. Lu, G. Meng, F. Orain, G. Papp, E. Strumberger, X. Wang, F. Wieschollek, Q. Yu.

Numerische Methoden in der Plasmaphysik (NMPP): O. Maj.

Max Planck Computing and Data Facility, Garching (MPCDF): D. Beckert, V. Bludov, K. Desinger, C. Guggenberger, C. Hanke, F. Hinterland, D. Karas, J. Kennedy, E. Laure, K. Lehnberger, M. Panea-Doblado, J. Reetz, M. Rampp, K. Reuter, R. Ritz, A. Schmidt, A. Schott, J. Schuster, E. Summer, K. Zilker.

ITER Technology & Diagnostics (ITED): U. Fantz, M. Fröschle, N. de Harder, B. Heinemann, C. Hopf, W. Kraus, C. Martens, H. Meister, R. Nocentini, S. Obermayer, G. Orozco, F. Penzel, R. Riedl, J. Schäffler, T. Sehmer, J. Thalhammer.

Integrated Technical Center (ITZ): R. Blokker, R. Gliga, N. Jaksic, R. Jung, M. Kircher, H. Köhnlein, G. Lexa, R. Stadler, H. Pirsch, J. Tretter, M. Weißgerber, F. Zeus.

IPP Greifswald, Germany: O. Ford, G. Fuchert, D. Gradic, F. Reimold, R. Wolf.

TUM, München, Germany: T. Eibert, K. Höfler, C. Koenen, U. Siart.

FZ Jülich, Germany: S. Brezinsek, A. Krämer-Flecken.

IPF University of Stuttgart, Germany: S. Garland, E. Holzhauer, W. Kasparek, C. Lechte, B. Plaum, M. Ramisch, B. Schmid, S. Wolf.

ERM/KMS, Brussels, Belgium: M. Tripský.

Ghent Univ., Ghent, Belgium: M. Klevarova, G. Verdoolaege.

CCFE Fusion Association, Culham Science Centre, UK: M. Carr, S. Henderson, A. Kirk, Y. Liu, M.-L. Mayoral, H. Meyer, D. A. Ryan, S. Sharapov, M. Valovic, I. Voitsekhovitch.

University of York, York Plasma Institute, UK: B. Lipschultz.

CEA, IRFM, Cadarache, France: F. Clairet, L. Colas, N. Wang.

IPP CAS, Prague, Czech Republic: M. Komm.

DCU, University College Cork, Ireland: P. McCarthy.

LPP, CNRS, Ecole Polytechnique, Palaiseau, France: F. Brochard, P. Hennequin.

ENEA, University of Cagliari, Italy: G. Sias.

ENEA, C.R. Frascati, Italy: B. Esposito.

ENEA, Consorzio RFX, Padua, Italy: M. Gobbin, P. Piovesan, C. Piron, G. Spizzo, N. Vianello.

ENEA, Univ. of Milano-Bicocca, Milan, Italy: M. Nocente.

Dipartimento di Elettronica e Telecomunicazioni (DET), Politecnico di Torino, Italy: D. Milanesio.

FOM-Institute DIFFER, TEC, Nieuwegein, The Netherlands: T. Blanken, M. Kantor, I. Krebs, G. Ronchi.

Ecole Polytechnique Fédérale de Lausanne (EPFL), Swiss Plasma Center (SPS), Lausanne, Switzerland: B. P. Duval, F. Felici, B. Labit, P. Martica, A. Pau, O. Sauter, U. Sheikh.

Wigner Research Centre for Physics, Budapest, Hungary: G. Kocsis, D. Réfy, T. Szepesi, S. Zoletnik.

Instituto de Plasmas e Fusão Nuclear, IST, Lisbon, Portugal: D.Aguiam, L. Gil, L. Guimarais, V. Plyusnin, J. Santos, E. Seliunin, A. Silva, C. Silva, P. Varela, P. Vicente.

ÖAW, IAP, University of Innsbruck, Innsbruck, Austria: C. Ionita-Schrittwieser, R. Schrittwieser.

ÖAW, IAP, Vienna University of Technology, Vienna, Austria: G. Harrer.

ÖAW, Graz University of Technology, Graz, Austria: E. Heyn.

DTU, Lyngby, Denmark: R. D. Nem, A. H. Nielsen, S. K. Nielsen, J. Olsen, M. Salewsksi, M. Stejner.

TEKES, Aalto University, Espoo, Finland: M. Groth, J. Jarhunen, T. Kurki-Suonio, I. Paradela Perez, A. Snicker.

VTT Technical Research Centre, Espoo, Finland: A. H. Hakola, J. Likonen, T. Tala.

ICREA-BSC, Barcelona, Spain: M. Mantsinen.

Supercomputing Center, Barcelona, Spain: S. Futatani.

CIEMAT, Madrid, Spain: G. Ratta, E. Solano.

University of Seville, Spain: P. Cano Megias, D. J. Cruz Zabala, M. Garcia Muñoz, J. Gonzalez Martin, M. Rodriguez-Ramos, L. Sanchis Sanchez, E. Viezzer.

Department of Physics, Chalmers University of Technology, Gothenburg, Sweden: K. Insulander Björk.

KTH Royal Institute of Technology, Stockholm, Sweden: M. Brenzke, L. Frassinetti, S. Ratynskaia, E. Thorén.

General Atomics, San Diego, California, USA: C. Paz-Soldan, M. van Zeeland.

Plasma Science and Fusion Center, MIT, Cambridge, MA, USA: R. Bielajew, A. J. Creely, A. Hubbard, P. Molina Cabrera, A. White.

PPPL, Princeton, N.J., USA: A. Bortolon, F. Laggner, R. Maingi, R. Nazikian.

University of Wisconsin, Madison, USA: T. Cote, B. Geiger, O.Schmitz.

Chinese Academy of Sciences, Hefei, China: W.Zhang.

College of Science, Donghua University, Shanghai, People's Republic of China: L. Li.

JET Cooperation

Head: Dr. Jörg Hobirk

The JET operation with higher NBI heating power with respect to previous campaigns has enabled a range of new results. In particular, the IPP participation has contributed to record neutron yields in hybrid plasmas, an increased operation space for isotope studies and higher confinement of plasmas with strong impurity seeding. Also studies of turbulence in L-modes, impurity production by ICRH and material transport in the JET divertor have been performed.

Hybrid Scenario Development for DT

The plasma scenario development in recent years is strongly centred on the preparation of the DT campaign foreseen to start in 2021. The expected fusion power in DT is largely proportional to the DD neutron rate and a DD neutron rate of about $5\text{-}6\times10^{16}$ corresponds to about 15 MW fusion power in DT. Contrary to the last DT campaign in 1997 the emphasis in the next DT campaign will be on achieving more stationary high performance, for about 5 s. The hybrid scenario development had first to show that increasing the heating power from 32 MW (2016, 3.4×10^{16} neutrons/s) to ~40 MW can be utilised to raise the neutron rate sufficiently and, second, that the high performance phase can be extended from 2 s to 5 s. Controlling the medium and high Z impurities at the edge and in the core has been identified as the main challenge. Despite testing Pellet ELM pacing and ELM triggering by vertical kicks the most successful control was achieved by designing the gas inlet in a complicated manner. Also n=3 neoclassical tearing modes were found to cause an acceleration of the impurity accumulation and a strong reduction in performance in many cases. The toroidal magnetic field together with the corresponding ICRH heating schemes, the plasma current and the freezing time of the q-profile by strong heating have been optimised.

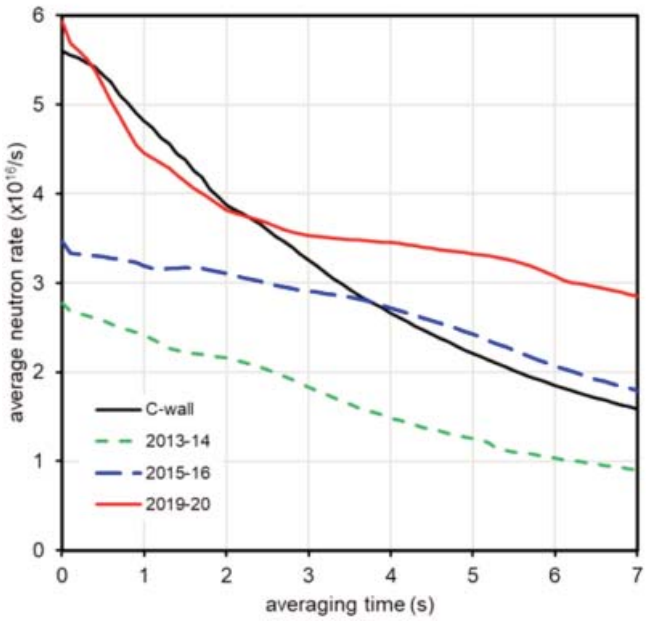

Figure: Average neutron rate in JET as function of the averaging time. The 2019-20 curve consists only of hybrid plasmas.

Furthermore, the plasma termination was optimised [1] before going to higher plasma current, avoiding disruptions. The figure shows the major progress made especially on the duration of the high performance. The red curve consists only of hybrid scenario pulses and shows that the short period neutron rate could be improved above the C-wall results and is similar or higher compared to the highest DD neutron rates worldwide. The 5 s neutron rate average has increased strongly compared to the C-wall JET results.

Understanding Impurity Generation of ICRH

Production of impurities by the ITER-like (ILA) operation was compared with that by the A2 antennas, with 20 % lower W release associated with ILA. Density perturbations in the far SOL, induced by ICRF plasma biasing, were analyzed with mapping to the areas of potential W sources. ILA antenna was extensively modeled with near-field and RF sheath calculations, and advantages and disadvantages of the curved model were highlighted. The RF image current cancellation techniques was adopted to the A2 antenna, first using near-field and RF sheath calculations, then in a dedicated experiment which agreed with the theoretical predictions.

Understanding of Isotope Effects

Quite successful experiments were in the Deuterium campaign performed which conclude most of the deuterium and hydrogen program envisaged for isotopic dependence of core transport and edge confinement. First control room analysis reveals that the findings from AUG could be largely reproduced at JET comparing high triangularity H plasmas with low triangularity D plasmas achieving the same edge density. Also with the higher NBI power available, for the first time high β_N plasmas were achieved in dominantly hydrogen plasmas. This allows to study the isotopic dependence in an important and previously inaccessible regime. This could also be found by modelling of JET L-mode plasmas [2]. At higher heating powers a larger fast ion population is created which is larger in D compared to H. The impact of the fast ions on the transport is significant and can explain the different profile shape.

Optimising Heat Exhaust

Experiments studying the radiative efficiency of N_2, Ne, Ar and mixtures of those were undertaken in JET at high heating power [3,4]. The high radiation was found mainly around

the X-point and the edge plasma density is reduced. With mixed gases at high radiation fraction a relative good normalised confinement of $H_{98y2}=0.78$ could be reached. When a total heating power of 30-36 MW was obtained with high Ne seeding rate, an ELM free L/M-mode with H_{98y} of ~0.95 was found.

Material Transport in JET during the JET ITER-like Wall Campaigns

Erosion and deposition were studied in the JET divertor and at the JET main chamber inner wall during the first three JET ITER-like wall campaigns JET-ILW1-3 using marker tiles and long-term samples. A similar general deposition pattern was observed in the divertor after all three campaigns: More than 60 % of the total deposition occurred in the upper region of the inner divertor on tiles 0 and 1, where Be was transported and deposited from the scrape-off layer (SOL). High erosion was observed only on tile 5 and tile 7. Deposits during JET-ILW campaigns consist mainly of Be with 5-20 at.% of C and O, respectively, and small amounts of Ni, Cr, Fe and W. D retention up to levels of ~1 at.% was observed up to large depths in the W protective coatings after all campaigns. The total mass of material deposited in the divertor decreased by a factor of 4-9 compared to the deposition of carbon during all-carbon JET operation before 2010.

Correlation between Near SOL Power Fall-off Length and Confinement

Two infrared thermography based power fall-off length data sets from JET operated with carbon and ITER-like wall are revisited and compared to recently published scaling laws as well as to confinement and pedestal top parameters [5]. It is shown that the power fall-off length is correlated to confinement, with the highest correlation among the tested parameters being the pedestal top density. The power fall-off length decreases with increasing pedestal top density in variance to the multi-machine scaling law. A similar trend is observed for the pedestal top pressure. This is in agreement with findings at C-Mod showing a scaling of the power fall-off length in various confinement regimes with the volume averaged pressure. Further, it is shown that a variation of the safety factor at constant pedestal top density is not changing the power fall-off length significantly in the two JET data sets.

The near SOL E_r Field and it's Impact on the L-H Transition

EDGE2D-EIRENE cases simulating JET L-mode plasma with ITER-like wall (ILW) with the input power close to the H-mode power threshold, were also run in C and W wall environments [6]. For the fixed gas puff rate and all other input parameters the highest plasma density and lowest E×B shear across the separatrix was achieved in the C case, in a qualitative agreement with experimental observations of lower E×B shear and higher input power required in the C wall (compared to metal walls) to trigger the L-H transition.

Other

Not discussed here are studies of the H-mode density limit in view of Ballooning stability at the separatrix [7], diagnostic improvement for W detection [8], dependence of turbulent particle flux on hydrogen isotopes induced by collisionality [9], effect of the isotope mass on the turbulent transport at the edge of L-mode plasmas [10] and the assessment of the strength of kinetic effects of parallel electron transport in the SOL and divertor of JET high radiative H-mode plasmas [11].

Scientific Staff

C. Angioni, V. Bandaru, R. Bilato, G. Birkenmeier, V. Bobkov, N. Bonanomi, J. Boom (NJOC), A. Cathey, M. Cavedon, A. Chankin, A. Drenik, D. Coster, M. Dunne, E. Fable, M. Faitsch, S. Glöggler, T. Görler, J. Hobirk, M. Hölzl, A. Kappatou, C. Kiefer, S. Kwak, P. Manas, G. Papp, A. Pavone, G. Pautasso, P. Schneider, M. Sertoli (NJOC), H.-J. Sun (NJOC), J. Svensson, B. Tál, W. Tierens, M. Weiland, M. Wischmeier, W. Zhang.

Stellarator Research

Wendelstein 7-X

Head: Prof. Thomas Klinger

The ultimate goal of Wendelstein 7-X is to demonstrate high-power long-pulse plasma operation under reactor relevant conditions (1800 s at 10 MW). The new key element is the actively water cooled island divertor equipped with cryo-pumps. About 600 water cooling circuits and a complex cryo feed system are constructed and integrated. New diagnostics are added, existing ones partially re-designed and extended. The heating system is extended and the control and data acquisition system is revamped. Completion of construction is December 2021.

1 Introduction

To cope with the challenges of the complex completion of Wendelstein 7-X, a dedicated project ("Wendelstein 7-X/C") was set up as a separate organisational structure besides the five scientific/technical divisions of IPP Greifswald. In 2017, the project's organisational structure was revised to meet the management requirements of such a big technical project. The project Wendelstein 7-X/C now consists of in total 13 project divisions: "Project Coordination", "Design Engineering", "Assembly", and "In-vessel Components" are in charge of core tasks of the project, "MC" deals with the extension of the cryo-system, "TS" is responsible for the extension of the water-cooling system, "ECRH", "ICRH/NBI" are responsible for the extension and completion of the heating systems, "DIA DIV", "DIA COR" and "DIA DYN" are responsible for the diagnostics extention, "CoDaC" is in charge of control and data acquisition, and "DO" stands for all matters of device operation and safety. Two staff offices at IPP Greifswald, "Safety" and "Quality Management", support the project directly. The core task of the project Wendelstein 7-X/C is the overall coordination of all activities related to the completion of the machine, including schedule and budget monitoring, quality management, change management, and design coordination. The organizational chart of the project Wendelstein 7-X/C is shown in figure 1. The current status of the completion works on Wendelstein 7-X is subsequently described in some detail.

2 Wendelstein 7-X Completion

2.1 Quality Management

The Quality Management (QM) staff unit reports to the directorate of IPP via the project director of Wendelstein 7-X, who has the direct responsibility for the maintenance and continually improvement of the QM system within the project Wendelstein 7-X/Completion. The QM unit is responsible for the planning and processing of quality assurance during all assembly, commissioning and operation phases of Wendelstein 7-X. The QM department also supports the supervision of external suppliers. The QM system is ISO9001 certified since 2010 and is audited by the authorities (the German "TÜV") every year.

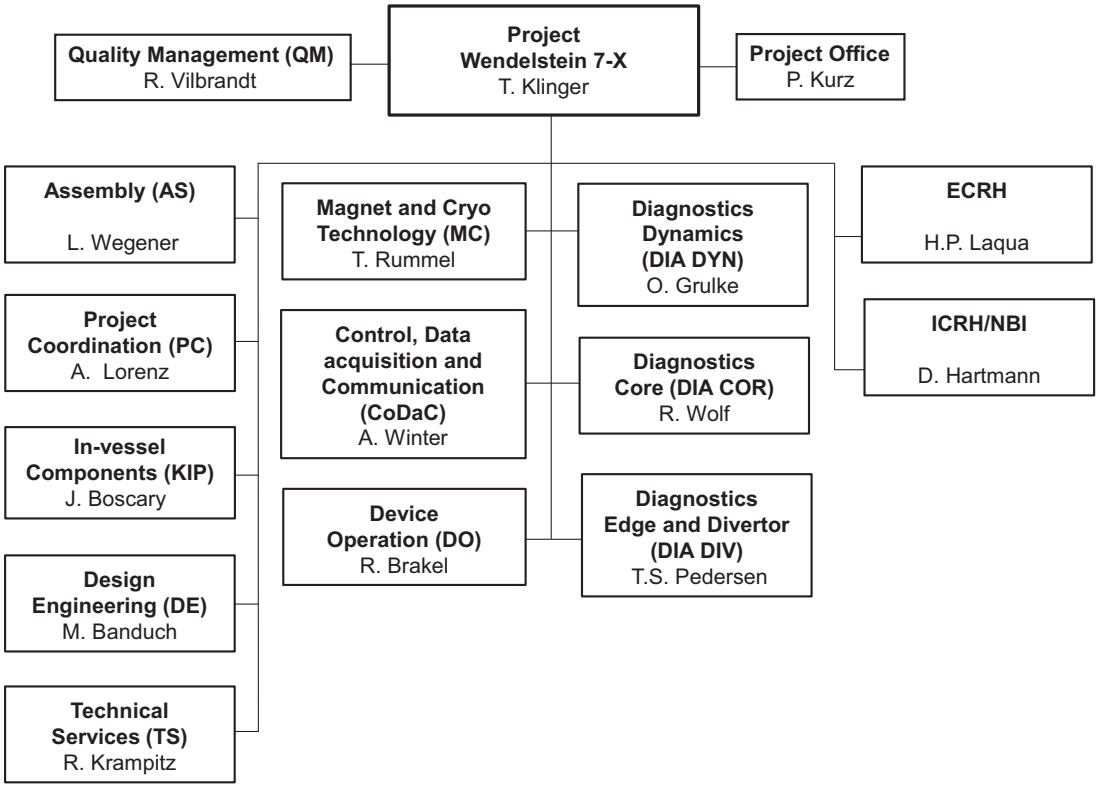

Figure 1: Organigramme of Wendelstein 7-X as of 30.09.2020.

2.2 Project Coordination

Project Coordination (PC) is a small project division (six team members and one head) serving the Wendelstein 7-X/C project. Based on many years of experience during the Wendelstein 7-X construction, PC has now taken a central role of the planning and controlling interface for all project divisions. PC is in charge of schedule and budget control in the project Wendelstein 7-X/C. The concrete tasks of PC are the following: (i) To monitor and co-ordinate component delivery and to support the component responsible officers and administration in the handling of procurement contracts, (ii) to monitor the assembly and commissioning schedules for the various devices and components, (iii) to report to internal and external supervising bodies, in particular the internal Wendelstein 7-X board and the supervising bodies of the funding institutions (in particular the Wendelstein 7-X/C Project Council), and (iv) to organize and co-ordinate the Wendelstein 7-X/C design review process. Over the past five years, PC has upgraded and refined its planning and configuration tools for more efficient and transparent information transfer. The MS Project based, integrated financial and time planning tool has been equipped with a TPG Project Link add-in to create large-scale hierarchical link networks to follow-up more than 60 simultaneously running completion projects. Since 2016, the web based "Project and Device Data Base" was extended and prepared to serve as a technical configuration (devices, components, supply media etc.).

2.2.1 Schedule

The project Wendelstein 7-X/C is currently making good progress. The project has encountered and successfully mastered quite a number of technical challenges. The currently foreseen project end (assembly works completed) is in December 2021. Directly after that milestone, the next Wendelstein 7-X commissioning and operation phase starts, called "OP2". Two critical paths for achieving this target dominate the project management: (i) The main critical path over the past 24 months has been the preparation and installation of the new high heat flux divertor (HHF) and its subcomponents. A large number of assembly and installation procedures were qualified and trained within an extensive preparation program using – among others – a 1:1 mock-up of a plasma vessel sector. Nevertheless, the extremely tight installation space for the divertor cooling supply network required a cumbersome adaption of hundreds of small pipes, supports, interfaces, leading to a larger work scope than originally anticipated and resulting in several technologically-driven schedule corrections. In addition, the 2020 pandemic situation has induced an almost complete standstill of assembly activities for several months. (ii) A second critical path has emerged after freezing the requirements for the implementation of the central experiment control systems and more than 40 diagnostic data acquisition and control systems towards long pulse operation phases. As successfully demonstrated before (before the previous operation phase OP1.2), the project division CoDaC has again turned to a „bottom up" scheduling procedure to balance the extended safety and operational requirements against time and budget constraints of the project. Strict prioritization and close monitoring measures have been initiated by the Wendelstein 7-X/C board to keep this part of the schedule on track. In the shadow of these critical paths, OP2 component design reviews and procurements have largely developed successfully and the fabrication and testing of all operation relevant components is well on track to meet the completion schedule.

2.3 Design Engineering

The project division „Design Engineering" develops design-engineering solutions for the project Wendelstein 7-X/C and provides CAD-technical standards, tools and infrastructure.

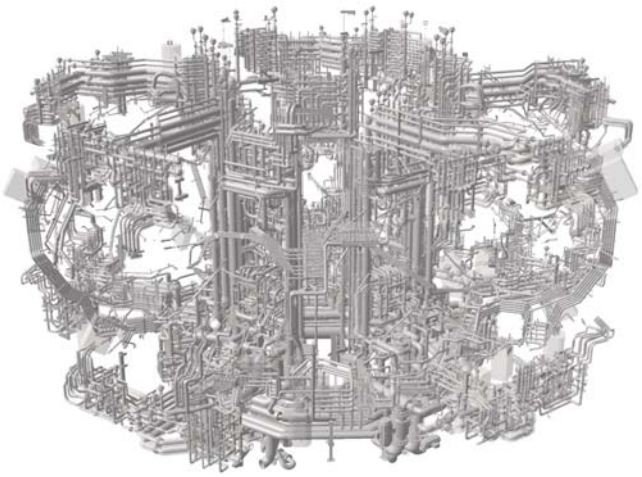

Figure 2: Wendelstein 7-X cooling water system.

One main objective for the project division was the timely design of the cooling water system. The cooling water system consists of about 2.5 kilometers of extremely complex cooling water lines. The design is dominated by tight geometrical boundary conditions, as typical for Wendelstein 7-X. The goal was successfully accomplished in close cooperation with the other project divisions involved, in particular TS, AS, PC and the procurement office of IPP administration.

2.4 Assembly

The preparation of the last planned completion phase (CP2) of Wendelstein 7-X started in the beginning of 2018 in parallel to the operation of Wendelstein 7-X. The replacement of the TDU with an actively cooled High Heat Flux Divertor (HHF) and the expansion of the associated cooling circuits are the main purpose of CP2. In addition, new diagnostics are installed and the extension of plasma-heating systems will be realized. The majority of cooling circuits (cf. figure 2)

was pre-manufactured in-house using a computer-controlled bending machine. This allows for late design changes in the pipe-layout to be executed in the shortest possible time frame. In addition, these work packages helped to keep at least some of the skilled and trained technicians busy in times, when the construction works on Wendelstein 7-X were interrupted, i.e. between construction phases CP1.2b and CP2.

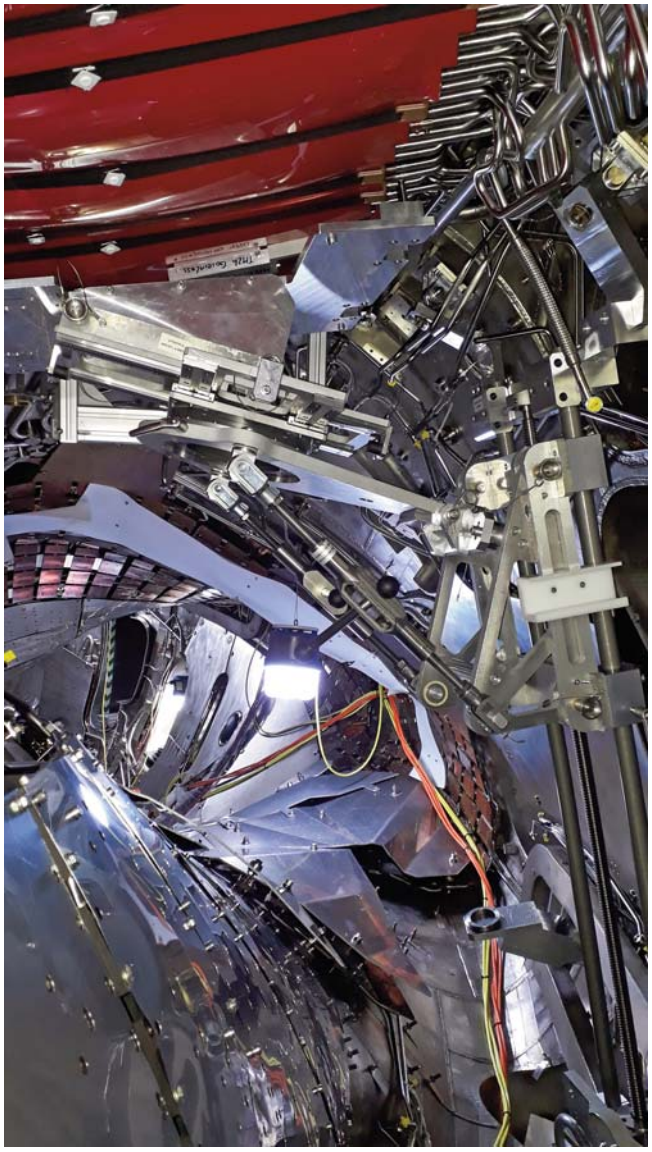

Figure 3: Positioning tool for divertor modules installed in the plasma vessel.

Hundreds of complex pipe sets were bent, welded, tested, thermally insulated, equipped with sensors and actuators, labelled and finally stored for their later installation. Accuracies below 5 mm had to be achieved to avoid clashes in the crowded installation spaces. The assembly works of CP2 started at the end of the year 2018. Six months later, nearly all in-vessel components (in particular the non-cooled test divertor unit, TDU) were removed and the installation of the HHF-divertor started with the completion of the in-vessel pipe work. Due to the limited construction space, all flange connections between the 120 HHF-modules and the associated plug-ins are to be customized to as-built positions. For that, several hundred 3D-measured positions of flanges, pipe ends and adapter pieces are mimicked outside the machine. It took more than a year in advance to develop and qualify adjustable fixtures for that purpose. The actual assembly of the HHF-divertor modules was prepared for time-period of two years. The original technology, developed previously for the TDU assembly, was massively expanded and adapted to the requirements of the HHF-divertor. Due to their increased deadweight, HHF-modules can only be transported and positioned using highly specialized tools. This frequently causes collisions with other installation equipment and the personnel during the assembly works. The transportation and positioning of each individual module requires complex motion sequences, which are often interrupted by the change of the respective tool. This has a direct impact on assembly time, work safety and position accuracy. Nonetheless, the experience during the installation of the first modules indicates that the deviation (creating steps) between neighbouring modules does not exceed the specified assembly limit of 0.2 mm. A particular challenge is the flange connection of HHF modules to cooling pipes. Due to the tight construction space between the divertor and the vessel wall, many flanges can only be tightened using specific procedures. To minimize the risk of water leaks, all known challenges in this specific process were in advance mimicked and carefully trained. Complex work instructions were developed to control the installation works on-site. All connections are leak-tested at 10^{-9} mbar·l/s, in some particular critical cases even at Helium over-pressure of 29 bar. Since Wendelstein 7-X will be operated at increased plasma energy, several hardening measures are realized during CP2. This concerns about 85 port liners (PLs) to protect heat-sensitive ports and port bellows. These PLs were successfully developed by industry. A novel coaxial-pipe design has been chosen to cope with various port dimensions and port shapes as well as to govern local hot-spots on the PL-surface. Furthermore, additional gap protections are needed to close gaps between neighbouring in-vessel components in order to minimize the shine-through on the plasma vessel wall. Gap protections consist of copper-cladded steel double-grids in various shapes and sizes. The grids are clamped on cooling pipes. Based on operation-experience, also the neutral gas flow in the divertor chambers had to be improved. The new divertor closure has a complex design due to both limited space and many crossing pipes and cables. The divertor closure plates as well as the grids for the gap protection were designed and manufactured by industry. Further work packages in CP2 comprise the repair of leaky control coils and the modification of baffle modules to enable their actual connection to cooling circuits.

The COVID-19 pandemic interrupted the assembly works, which were fully on track at the time. After the new recruitment of personnel after the implementation of the required infection precaution measures, a new planning was set-up for the remaining assembly work. CP2 will be complete at the end of 2021, which means a five months delay compared to the original plan. In total, CP2 will require about 220.000 person hours on-site, executed in a two-shift system.

Figure 4: Example of a realized port liner: AEK50.

2.5 In-vessel Components

2.5.1 In-vessel Components

The in-vessel component (IVC) system of Wendelstein 7-X consist of the high heat flux (HHF) divertor assembly (target, baffles, and toroidal closure plates), plasma vessel protection (steel panels and graphite heat shields), control coils, cryo-pumps, and port protections. The complex system of cooling water supply lines inside the plasma vessel are also part of the IVC. The HHF divertor-modules and the cryo-pumps are completed. The adaptation of the baffles to the new OP2 environment and loads, and the manufacturing of pumping gap panels are being completed in summer 2020.

2.5.2 Target Modules

The W7-X actively cooled divertor consists of three main HHF areas: the vertical, horizontal, and “high iota tail” targets, which are built from altogether 120 modules (figure 5). The latter are sets of 6 to 12 mechanically and hydraulically connected target elements each. Manufacturing and quality assurance of the target modules was mainly done at the ITZ (Integriertes Technik Zentrum) workshops of the IPP Garching. The high iota tail was completed in 2014. The vertical and horizontal targets were completed in 2019.

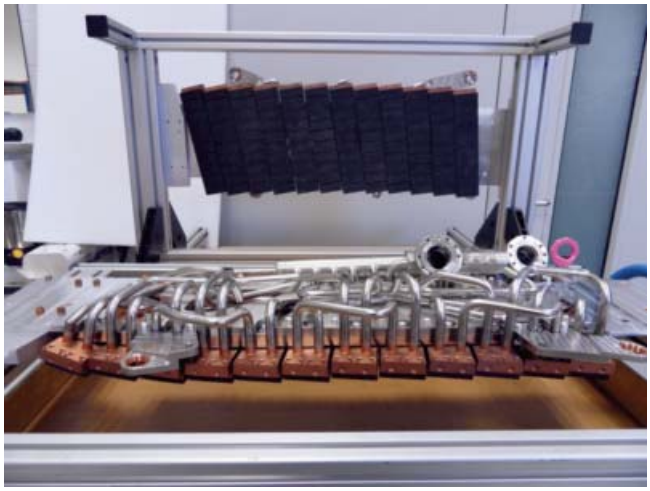

Figure 5: Top: Plasma facing surface made of CFC tiles. Bottom: Cooling system made of stainless steel manifolds to distribute water to target elements.

2.5.3 Baffle Modules

Recent multiple optimization analyses led to the decision to release thermomechanical stresses due to the high loads expected at OP2 by loosening of about half of the connections between the heat sinks and steel structures of the baffle modules. In addition, assembly trials showed the need for changes of the end parts of some baffle modules to allow the connection to the water feeding pipes within the plasma vessel. Manufacturing of these new parts was contracted to an external company. Final assembly of the modified modules as well as loosening of all baffle structures are done by ITZ.

2.5.4 Cryopumps

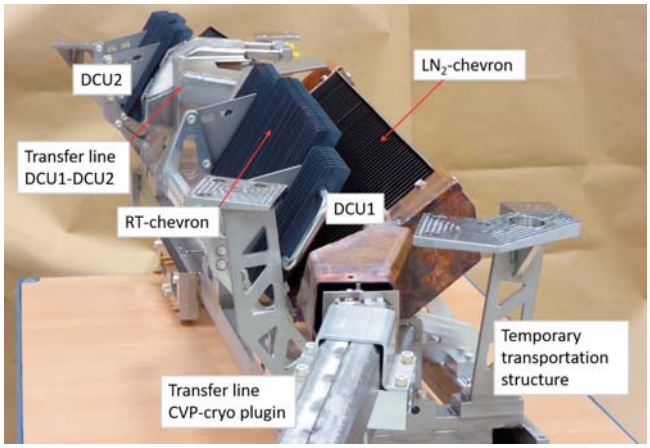

Figure 6: Picture of a cryopump made of two units placed on its temporary transport structure.

Manufacturing of the ten in-vessel cryopumps (figure 6), located behind the main horizontal HHF divertor target modules, has been completed. Based on the re-assessment of the ECRH

loads expected in OP2, additional protection shields made of copper plates have been installed around the cryopumps. The production of the vacuum feed-throughs („cryo plug-ins“) to supply the cryopumps with LN_2 and ScHe through special ports was completed in the workshops of the Technical Services (TD) of IPP Greifswald. Manufacturing of the belonging cryo-shields for the cryo feed lines was completed by an external company.

2.5.5 Plug-ins

The „plug-ins“ are used to supply water as well as diagnostic cabling through the supply ports from the outside of the machine into the plasma vessel. These plug-ins basically consist of sets of tubes which are welded onto flanges attached to the outer vessel. All 80 plug-ins required for IVC in OP2 are installed.

2.5.6 Water Supply Lines inside the Plasma Vessel

The cooling supply lines for the IVC run from the plug-ins, via a complicated system of manifolds and pipes, to the various components via flanges and are being installed.

3 Operations

3.1 Physics Operation

3.1.1 Device Operation

The superconducting stellarator Wendelstein 7-X has completed the first three experimental phases (OP1.1, OP1.2a and OP1.2b), the first one with a limiter only and two phases with an inertially cooled carbon divertor. The main goal of the divertor phases was to pave the way for the planned steady-state operation with high-power plasmas and a steady-state divertor. After installation of the inertially cooled Test Divertor Unit (TDU) the first divertor phase commenced and was completed in February 2017. The TDU was equipped with roughly 200 thermal sensors for monitoring its graphite tiles and steel support structure. The first half of 2017 was dedicated to commissioning of Wendelstein 7-X including validation of the central safety system (cSS). Between OP1.2a and OP1.2b, an assembly break was scheduled to install the two scraper elements to protect the divertor during possible build-up of a toroidal bootstrap current.

3.1.2 Organisation of Operation

The working group for Device Operation is responsible for planning and executing the commissioning and operation of the Wendelstein 7-X device. The operations plan is based on the physics planning which is a selection of physics proposals keeping in mind the technical limitations of Wendelstein 7-X. The operations plan is iterated between the lead physicists and device operation team. The “technischer Leiter vom Dienst” (TLvD or Engineer in Charge) plays a central role in coordinating and supervising the technical operation of Wendelstein 7-X. To ensure safe and reliable operation of Wendelstein 7-X several procedures have been implemented and improved. This involves commissioning templates, checklists, procedures for e.g. plasma heating energy release, operation malfunction cards, logbooks, coordination meetings, duty-on-call and shift-planning. Experiments in all phases have been run two or three days per week, alternatingly. The superconducting magnetic field has been run stationary during an experiment day (including transitions from one configuration to another), but shut down in the evening. After the commissioning of the device Wendelstein 7-X, about 2–3 weeks have been used to commission Wendelstein 7-X to calibrate diagnostics, introduce and check new field configurations, measure magnetic flux surfaces and condition the plasma vessel. The table summarizes the performance data for the three operation phases.

experiment type	**OP 1.1**	**OP 1.2a**	**OP 1.2b**
plasma discharges	776	1156	1120
test pulses	148	257	277
fault pulses	24	98	211
Total	**948**	**1511**	**1608**
start of the campaign	09.12.2015	01.08.2017	17.06.2018
end of the campaign	10.03.2016	08.12.2017	18.10.2018
weeks of operation	13	18	18
experiment days	33	40	44
thereof commissioning	4	5	8
discharges per day	28,7	37,8	36,5

Table: Summary of the first three operation phases of W7-X.

The large number of fault pulses in OP1.2b is attributed to electrical discharges in the ECRH towers due to increased humidity in the summer of 2018. Meanwhile, the ECRH towers have been upgraded by an air conditioning system to reduce arc ignition by electron radiation.

3.1.3 Boronization of the Plasma Vessel

An optimized, wall-conditioning strategy has been developed and consistently applied throughout the first three campaigns. This includes baking at 150 °C-flat top and Glow Discharge Cleaning (GDC) in hydrogen. Major outgassing impurities H_2O, CO_2, CO/N_2, and CH_4 were removed. At the end of the daily operation, the H_2-loaded walls were depleted by He-GDC. At this stage of conditioning, the plasma density achievable only with gas fuelling and ECRH heating was limited to 5×10^{19} m^{-3}due to impurity radiation losses. During OP1.2b, the first boronization at Wendelstein 7-X took place. This opened access to a new density regime of up to 1×10^{20} m^{-3} (figure 8). Due to successful boronization, the daily He-GDC was not required anymore as this condition remained stable basically for the entire OP1.2b campaign. Two further boronizations were subsequently done in four-week intervals but did not result in additional improvement.

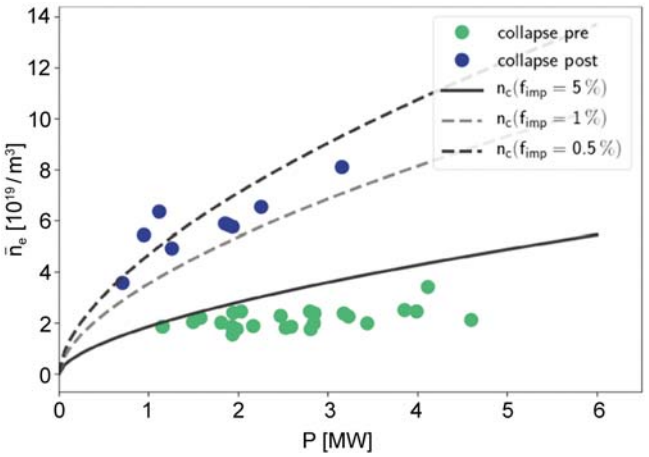

Figure 7: Line-averaged densities as a function of input power, before (green points) and after boronization (blue points). The difference in the point distribution can be explained by the impurity content, as shown by the lines for different carbon fractions.

3.1.4 Magnetic Field Scenarios

A base set of magnetic configurations (differing in shear, magnetic well/hill, inward-/outward-shift, and toroidal mirror fields) has been developed for the specification of Wendelstein 7-X. Most of these magnetic configurations have already been commissioned and used in plasma discharges. Figure 8 shows the distribution of magnetic field configurations used in OP1.2b. Newly commissioned was the low iota configuration and the configurations required for a scan from low- to high-iota configurations.

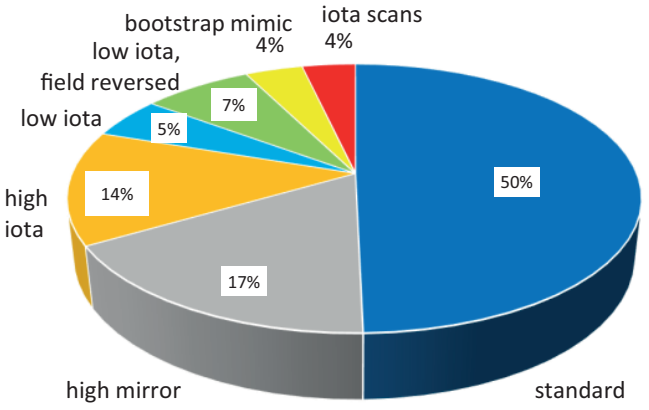

Figure 8: Distribution of the magnetic field configuration in OP1.2b.

Meanwhile, new developments in plasma physics and a better understanding of fast-ion behavior in Wendelstein 7-X, resulted in requirements for new configurations, beyond the original specification. These configurations have to be approved by the technical groups and released by the head of operation individually: Since the electric network with the coil protection system is a coupled network, not all current distributions are possible. In addition, the mechanical loads of the super conducting coils also restrict the coil current distribution.

3.1.5 Increasing the Heating Energy in the Plasma

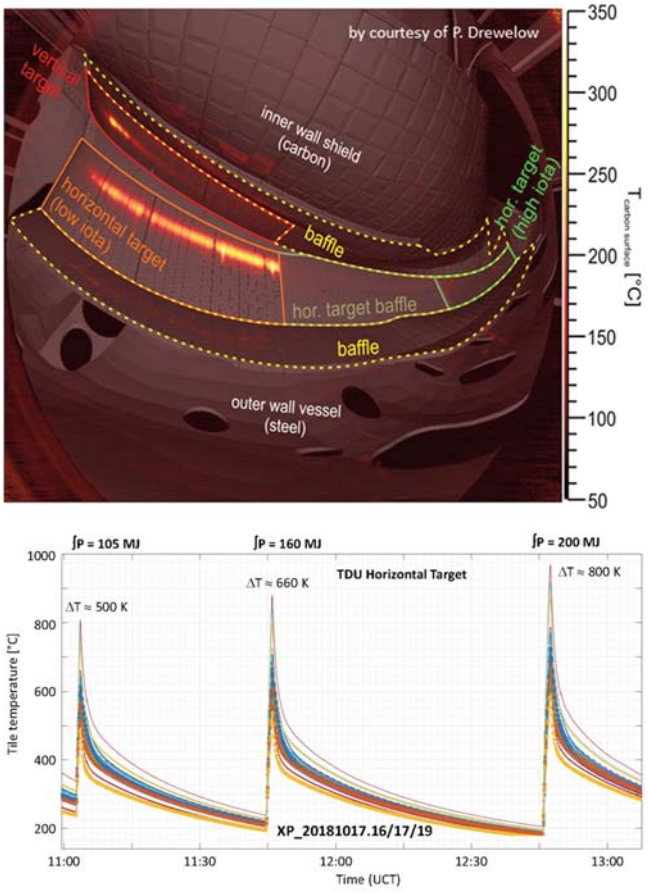

Figure 9: Typical IR thermography (one module) on top, and temperatures of divertor modules (standard magnetic configuration), below.

The specification for OP1.2a/b foresaw an integrated input energy into the plasma ($\int P_{heat}\, dt = W_{input}$) of Wendelstein 7-X of 80 MJ. In OP1.2a, this limit was increased to 200 MJ, as the load on the in-vessel components turned out to be well distributed, without significant asymmetries. For increasing W_{input} in predefined steps, again a formal organizational process was introduced. This had to be performed for each magnetic configuration separately, as the wall loads and their distribution depend very strongly on the shape and the position of the plasma. The limiting criteria to get to a higher level of W_{input} were temperature levels of the divertor components (observed by IR thermography), temperatures of the TDU tiles and support, NBI beam-dumps and on diagnostics, as well as the observation of hot spots in the plasma vessel. A layout of one TDU module, overlaid with an IR picture is shown in figure 9 top, while in figure 9 below the time

traces for the attached discharges 20181017.16 ff. are shown. Steady-state divertor discharges have to use the detached divertor regime, in which the heat load is radiated in the edge and the divertor, with relatively low thermal load on the divertor targets. Such experiments have been performed in different magnetic configurations, the longest a detached divertor plasma was a "standard magnetic configuration" discharge with 154 MJ. The development of the temperature load on the divertor is shown in figure 10. In contrast to figure 9, the temperature increase on the target plates is much smaller for the same energy input.

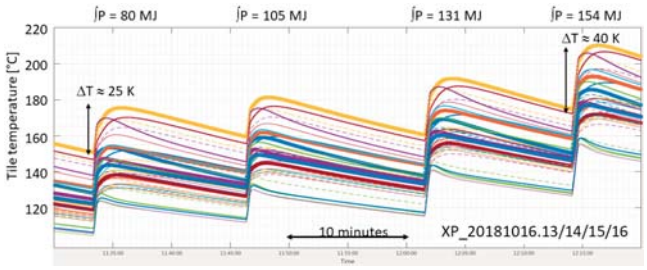

Figure 10: Divertor temperatures for detached plasma up to W_{input} 154 MJ.

3.1.6 Device Safety

The central safety system (cSS) of the Wendelstein 7-X is designed following the safety life cycle according IEC 61511. Based on the individual safety analyses of each component and the safety analysis for the Wendelstein 7-X for OP1.2b 45 Safety Integrated Functions (SIF) were defined. The validation of a large number of SIFs with individual plans in OP1.1 and 1.2a was very time consuming. For OP1.2b the creation of the validation plans was changed. All SIFs were analyzed and all sensor – actor relations were sorted. Now it was possible to generate validation plans that contain all sensors, which trigger the functions in one component and doing so to split the validation into several parts. In this way, the vacuum and cryoplant systems could be validated up front to start evacuation and cooldown. After this, all other systems (diagnostics, heating) have been validated. To protect diagnostics and components inside the plasma vessel, a Fast Interlock System (cFIS) was developed. If parameters like stray radiation, plasma density and diamagnetic energy exceed defined limits, the cFIS turns off the ECRH and NBI.

3.1.7 Preparation for OP2.1

Presently, Wendelstein 7-X is being completed, to allow the steady-state operation starting in OP2.1. The main task is the In-vessel installation of a steady-state divertor, ten cryo pumps and the completion of the peripheral cooling circuits to supply Wendelstein 7-X with sufficient cooling water and the cryo-pumps with LN2 and LHe. After the completion, the mission of Wendelstein 7-X can finally start: 30-min discharges with an input power of more than 10 MW should prove the capability of steady-state operation on all time scales. The operations department has to adapt all workflows and procedures to ensure safe operation of Wendelstein 7-X also in OP2.1 and beyond.

3.2 Machine Operation

3.2.1 Magnet Systems

Wendelstein 7-X has a superconducting magnet system consisting of 50 non-planar and 20 planar coils. Seven electrical circuits with 10 coils each (connected in series) allow providing individual currents in the seven coil types. Each of the seven coil circuits has its own power supply to provide individual currents. The Quench Detection System (QDS) monitors the superconducting components continuously, to indicate the loss of superconductivity to protect the coil system. In addition to the superconducting coils, normal conducting coils, the so-called trim coils are mounted on the outer cryostat wall, one coil per each of the five Wendelstein 7-X modules. The third set of coils is the control coil system, consisting of ten water cooled copper coils, which are placed inside the plasma vessel of Wendelstein 7-X. The behaviour of the superconducting magnet system in the first experimental phase met all the expectations, but only two of the nine predefined magnetic configurations have been used. In terms of electrical currents, the non planar coils have been operated up to 13.47 kA, and the planar coils up to 5 kA, respectively. In OP1.1 the maximum voltage during a fast discharge was 2.1 kV. For OP1.2 a maximum voltage of up to 2.7 kV was expected, due to the higher expected coil currents. Therefore, the magnet protection system was reviewed to reduce the electrical stress during fast discharges and a modification of the dump resistor was proposed. It is customized for the next operation phases only, but reduces the voltage during a fast discharge significantly from 2.7 kV to 1.8 kV. During the two experimental phases of Wendelstein 7-X in 2017 and 2018 the superconducting magnet system was energized 84 times for about 800 hours up to 80 % of the maximum current. The requested currents were achieved with the required accuracy. The long-term stability, unless not specified, is better than +/- two amps over an operation day. Only two minor events, caused by electronic components, led to an earlier than planned stop of the operation day. The magnet protection main functions worked properly during planned as well as during unplanned fast discharges. The trim coils as well as the control coils were operated on nearly each operation day according to the scientific program.

3.2.2 Cryogenics

3.2.2.1 Operation and Maintenance of the Helium Refrigerator during the Plasma Operation Phases

The availability of the cryo-system is of particular importance for the experiment. The refrigeration system ran continuously for a period of 8 months for OP1.2a and for a period of 7 months OP1.2b. Higher currents in the planar coils compared to the mode of operation in OP1.1 required a new adjustment of the mass flows for cooling the 14 current leads.

After completion of OP1.2b, maintenance work on the refrigeration system was resumed. Also the cold turbines of the helium cooling process were inspected and reassembled. At 2 out of 7 turbines, grinding marks and damaged blades were detected on the idler or impeller. The damaged parts were replaced accordingly. A significant upgrade of the helium refrigerator system is a fifth helium gas storage tank, which enlarges the total helium storage capacity by 25 %. The new tank is equipped with an internal diffusor and will be used as a storage tank for the quench gas during magnet operation. The diffusor helps to distribute the cold gas within the tank, ensures a good mixing with the gas inside the tank and avoids cold spots on the carbon steel surface. After the successful acceptance test, the tank arrived at its final place next to the existing tanks in December 2018 (figure 11).

Figure 11: Transportation of the new helium gas storage tank to the final place close to the other four tanks.

3.2.2.2 Upgrade of the Cryogenic System for the Cryo Vacuum Pump Operation

In future operating phases, 10 cryogenic vacuum pumps will be operated in the plasma vessel of the Wendelstein 7-X. These cryogenic pumps have to be supplied with cryogenic helium and LN2. This requires an upgrade of the cryogenic system of Wendelstein 7-X: A common transfer line from the refrigerator hall to the torus hall, a valve box for distributing and controlling the mass flows for the 10 cryo vacuum pumps, and 10 transfer lines from the valve box to the individual cryo pump interfaces on the Wendelstein 7-X cryostat.
The common transfer line runs from the cryo plant hall to the valve box in the torus hall. It is a multi channel, vacuum insulated line containing two process pipes for helium and two process pipes for nitrogen (figure 12). The outer diameters of the vacuum jacket and the process pipes are 273 mm and 48 mm respectively, the length is 55 m. Ten short transfer lines run form the valve box in the torus hall to five upper and five lower ports at the cryostat. These ports serve as the interface to the in-vessel-pipes, supplying the individual cryo pumps.

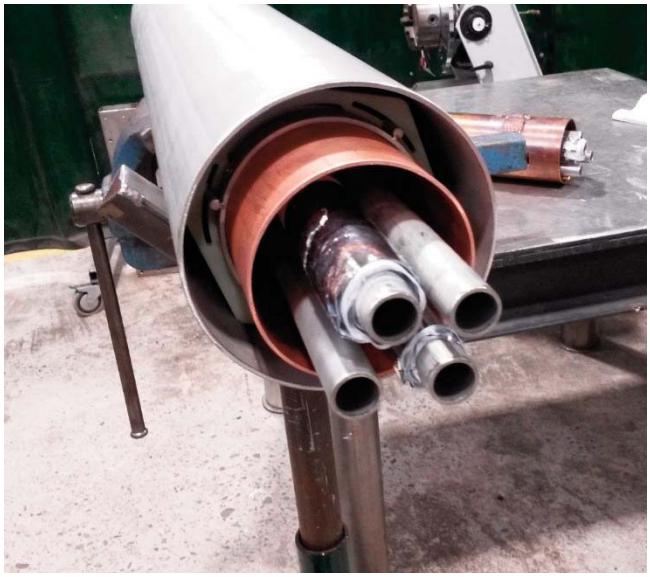

Figure 12: Production sample of a short transfer line running from the valve box to the cryo pump. Helium lines (top left and lower right tubes) are wrapped with superinsulation.

The transfer line vacuum jacket (diameter 159 mm) contains four process pipes (diameter 21.3 mm) with inner supports made of G10. The nitrogen return cooling pipe is welded to the copper thermal shield. Company Cryotherm/Germany designed, manufactured and installed all transfer lines, the common transfer line as well as the ten short transfer lines on site. The cryo vacuum pump valve box (CVB) is located in the second basement underneath the Wendelstein 7-X.

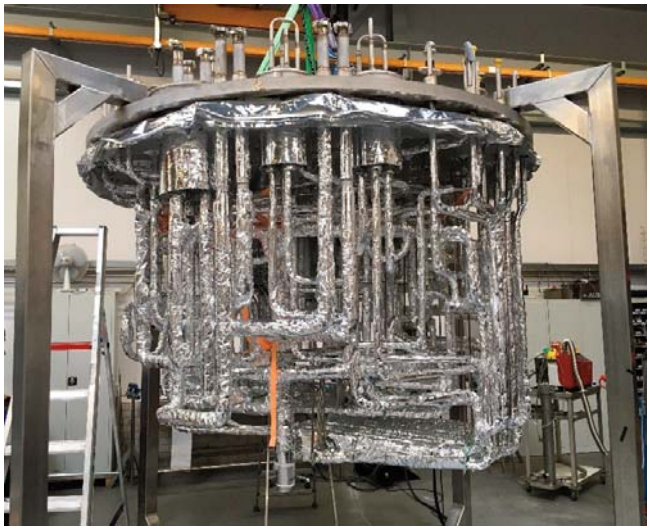

Figure 13: View on the dense pipe routing inside the valve box.

The main purpose of the CVB is to distribute the helium as well as the nitrogen flow coming via the main transfer line to the ten short transfer lines and finally to the 10 cryo vacuum pumps. 26 control valves, 24 temperature sensors, 22 mass flow measurements and 22 pressure sensors are installed to measure and control the flow condition of helium and nitrogen (figure 13).
The box is made of stainless steel and has an outer diameter of 2.5 meters and a height of about 2 meters, resulting in a mass of about 5 tons. Company Cryoworld/Netherlands designed, built and installed the box. Transport and placing the box on its final position was performed in March 2020 (figure 14).

Figure 14: Transport of the valve box inside the torus hall.

To prepare the operation phases with longer plasma pulses and running cryo-vacuum pumps, an upgrade of the LN2 supply is planned as well. This upgrade consists of a cold LN2-pump, a LN2- valve box and a phase separator. The tenders have been started.

3.2.3 Vacuum Technology

Since 2017, Wendelstein 7-X underwent two completion and two operation phases. For the transition from CP to OP, the vacuum systems of the cryostat and plasma vessel had to be set into operation again as well as leak tests on all corresponding components, like outer vessel, plasma vessel, diagnostics, and heating system components, had to be performed. The interspace vacuum system remained in operation all the time to indicate immediately degradation or accidental damages of sensitive vacuum components. The completion phases were used to improve the existing vacuum systems. The most important improvement was the adaptation for diborane glow discharges enabling wall conditioning of the inner plasma vessel surface. Two out of 10 plasma vessel-pumping systems have been equipped with a thermal diborane decomposer and all necessary safety requirements. In the completion phases, the vacuum group carried out assembly companying leak tests. For instant, in CP2 approx. 1500 flanges inside the plasma vessel and approx. 4500 weld seams at pipes have to be leak tested. During the commissioning and operations phases, the vacuum system has been operated routinely with a standby service at night and the weekends. After baking of the plasma vessel and ports, the plasma vessel has been evacuated typically to 1.9×10^{-9} mbar. First boronization took place on August 4th, 2018. Assuming a homogeneously coating of the complete plasma vessel surface (200 m^2) the resulting thickness of the borane sheet was expected to be in the order of 10 nm. In total, three conditioning campaigns have been performed in OP1.2b. The experience showed, that the vacuum systems involved are working at their technical limits. Therefore, procurement and the assembly of the 3rd diborane decomposer is in progress.

3.2.4 Engineering

In 2017–2018 the group “Engineering” has focused on the monitoring of mechanical integrity of the magnet and the cryostat systems using measurements of more than 700 mechanical sensors. In addition, the existing procedure for the evaluation of new proposed magnetic configurations on the basis of finite element model (FEM) results were refined and optimized to accelerate the process. Each operational phase was followed by the detail data evaluation. A fast plasma current decay events observed in 2018 showed significantly reduced decay time constants. Consequently, the thorough reevaluation of the eddy currents forces for all main components and diagnostics have been initiated. A sophisticated electro-magnetic model with plasma currents, superconducting coils, plasma vessel (PV) and multiple ports was developed in ANSYS® to provide required inputs for the detail component analyses (figure 15).

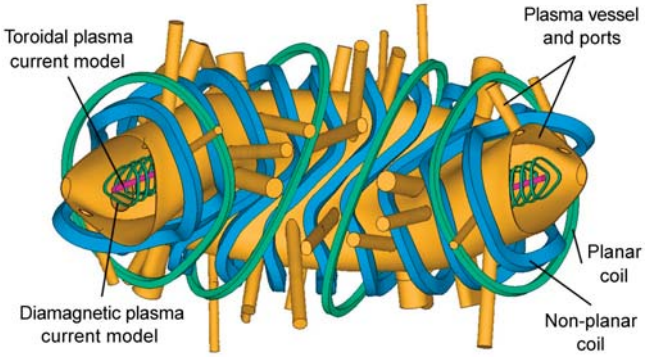

Figure 15: 72 degree sector model for EM analysis of the Wendelstein 7-X during fast plasma current decay event.

It was found, that the most critical component could be the thermal shield attached to the plasma vessel and ports. Further refined analyses are launched in 2020 to define the criticality and possible operation restrictions more precisely.

3.3 CoDaC

3.3.1 General

The group „Control, Data Acquisition and Communication“ (CoDaC) successfully supports the commissioning and operation of Wendelstein 7-X. This comprises the central safety system (cSS), the central operational management (cOPM), the fast interlock system (cFIS), plasma control and continuous data acquisition as well as the control room with virtualized desktop computers and monitoring on the video wall. Many systems have been setup and engaged for operation, e.g. the central valve control, gas inlet, interferometry, flux surface measurements, ECE, HEXOS, Magnetics, Video and support for partly integrated diagnostics. During the ongoing completion phase 2, CoDaC has engaged in the complete re-design of the central safety system and significant extensions of the central interlock system and the integration of roundabout 25 additional diagnostics and technical systems.

3.3.2 Control and Data Acquisition

With the experience gained during OP1.1, the central safety system has undergone a complete redesign for OP2. Emphasis is now on the modularity and operability of the system, while guaranteeing machine and personnel safety of Wendelstein 7-X. The design process has significantly evolved and is now fully systems engineering driven, with appropriate tools in place for requirements capture (Polarion) and the automated generation of test plans which ensures complete traceability of requirements to functions and tests as well as the completeness of the validation. The complete CSS system is now also implemented in the simulation platform SIMIT, which allows to debug and test the software before validation begins. While the safety system ensures SIL certified termination of discharges, it is speed-limited. In certain cases, it is necessary to terminate a discharge within a few ms to avoid potential damage to the machine. This is done using the cFIS system, which couples certain diagnostic inputs with appropriate logic to rapidly terminate a discharge if necessary. This system was implemented and worked extremely well during OP1.2. It is currently expanded to cope with the additional requirements of the actively cooled divertor in OP2. The cOPM system was also significantly expanded to provide support to the operator by performing automated service functions and status displays. A new component for OP1.2a/b was the fast interlock system. However, the actively cooled machine in OP2 drives the need for a massive increase of systems connected to the real-time infrastructure including some with highly demanding data acquisition devices such as high-performance infrared cameras used for divertor protection. These new requirements drove a significant change in strategy for the DAQ software. Originally, a separation between high-performance data acquisition and real-time control was foreseen. This now proved unworkable due to the high data rates of the new DAQ devices involved. The solution to the issue was the migration of the RT control system from VXWorks to real-time linux, such that data sources can be shared with the existing archiving processes using appropriate priority to ensure and real-time process is not impacted by less important tasks. With increase of supported diagnostics, also a significant increase in DAQ hardware has to be supported. Wendelstein 7-X CoDaC initiated a collaboration with international partners (DMCS at Lodz University), to provide a high-performance generic camera DAQ system. This will lead to the integration of all camera systems used at Wendelstein 7-X using one generic framegrabber and software. This system is currently past prototype stage and will be used for the complete divertor protection system, new spectroscopy and bolometer systems. During the initial operation phases, a significant number of diagnostics could only be partially supported by CoDaC and ended up using MDSplus as an independent data archiving system. In order to ensure a higher degree of coherence, a generic resource interface was developed to allow diagnostics to interact with central CoDaC services (archive, central state machine, etc.) using a standardized interface while leaving control over the detailed data acquisition to the diagnostic itself. This interface will be deployed throughout Wendelstein 7-X and MDSplus will cease operation as an independent archiving system at Wendelstein 7-X for OP2. This is a major step towards coherence of control and DAQ at Wendelstein 7-X.

3.3.3 Software Development

Software development focused on hardening the tools for operation and implementing the lessons learned from recent phases. As the physics operation of the machine starts to mature, tool support for programme planning is required, so a proposal database was developed to support the physics session leaders in their work. The long shutdown between OP1.2b and OP2 was used to completely refactor the configuration database and business processes. This allowed state of the art technologies to be used significantly enhancing the performance of the whole infrastructure. One motivation here is the integration of more systems into centrally managed experiment programs with the aim of having a complete picture of all participating technical systems and diagnostics in centrally supported configuration and editors. An international collaboration with WEST at CEA is running very successfully and the Wendelstein 7-X editor tools have successfully been transferred and are currently being used to operate WEST as well. The Wendelstein 7-X data archive has

grown to > 600 TB after OP1.2b where a continuous data streaming rate of 16 GB/s was achieved. This was possible due to a large investment in data storage and network backbone in 2017/2018. However, the projected data rate for OP 2 will again nearly double, requiring a second phase upgrade. In order to mitigate further growth in data rate, the software group has integrated the concept of live, lossless data compression into the archive API (at least a 50 % reduction).

3.3.4 Electronics Development

The electronics development focussed on the support for existing diagnostics and the development of bespoke DAQ other electronic components where dedicated expertise is required. This includes the development of high-performance ADCs for the divertor bolometer in the mTCA standard, ATCA DAQ cards for the magnetics. Support for technical systems included the design of new piezo drivers for the divertor gas inlet.

3.3.5 IT

The IT department is supporting the almost fully virtualized IT infrastructure for the whole lab. This includes all networking for the experiment, the archive and control room and the support for the central archive, virtualization and storage. A new data center was commissioned, featuring a TIER III redundant architecture with 4 data cells where all central IT components are housed. During the challenges of 2020, the virtualized system proved to have exceptional saleability when demand nearly doubled within 2 weeks due to forced home office for the majority of the personnel. For OP2, the IT department is orchestrating the work of expanding the network infrastructure to cope with increased demand as well as the expansion of the archive to 40 GB/s streaming capacity.

4 Stellarator Heating and Optimizing (E3)

4.1 Electron Cyclotron Resonance Heated (ECRH) Plasmas

All ten 140 GHz gyrotrons achieved high reliability during the operational phase (OP) 1.2, routinely. They were used for startup and long-pulse plasma operation with X2 polarization allowing densities of up to 1.2×10^{20} m^{-3}. O2 polarization was demonstrated for 10 s, achieving densities of 1.5×10^{20} m^{-3} (figure 16). O2 operation is made possible via a multi-pass absorption scheme involving the use of holographic reflector tiles, enabling ECRH absorption in the 80 to 90 % range. The highest performance plasmas in OP1.2 were achieved with ECRH heating in pellet discharges with steep density gradients [1,2]. As the latter suppress turbulent transport, the ion power flux approaches the neoclassical value enabling to test the neoclassical transport optimization of W7-X [3].

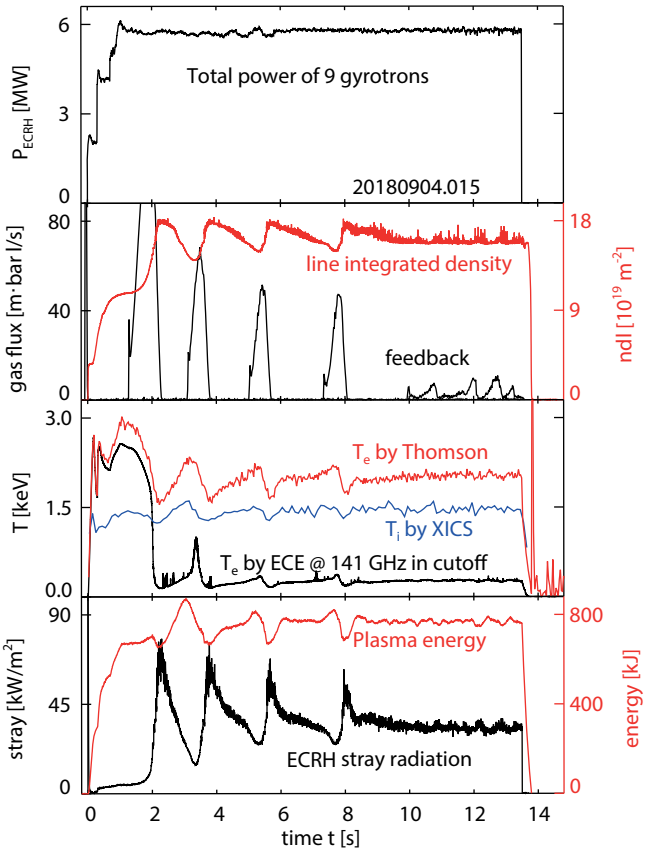

Figure 16: High-density discharge achieved with 9 gyrotrons operating for 10 s with O2 polarization. Dropout in the core electron cyclotron emission (ECE) channel and increase of the stray-radiation level is indicative of core densities exceeding the X2 cutoff.

The steady-state capabilities of the ECRH system were also demonstrated in OP1.2. A 100 s discharge was conducted using 2 MW of injected ECRH power in X2-polarization. The duration of this operation mode was solely limited by the uncooled nature of the divertor. High density ECRH operation in combination with the O2-scenario was demonstrated to be compatible with divertor detachment through a 26 s ECRH discharge [4]. Demonstration of ECRH compatibility with detachment is critical, as detachment is considered to be a crucial tool for divertor heat-load management in future reactor devices. Stationary ECRH-plasmas also showed a very low impurity confinement without accumulation [5], which is in contradiction to neo-classical predictions, indicating transport dominated by plasma turbulence. Two remote steering launchers (RSL) have been installed and tested to demonstrate ECRH compatibility with reactor relevant launch systems. The measured emission characteristic of the about 5 m long corrugated waveguide is in very good agreement with the theoretical design. Stable operation was demonstrated at medium power levels. At maximum gyrotron power, problems with arcing appeared

on the airside of the RSL due to the small input beam compared to the typical beam radii of the quasi-optical transmission line of Wendelstein 7-X. For this reason, the completion of all tests is envisaged for OP2. In preparation for OP2, the ECRH transmission line is upgraded with an air conditioning and drying system to guarantee reliable transmission at even higher power levels without the risk of arcing.

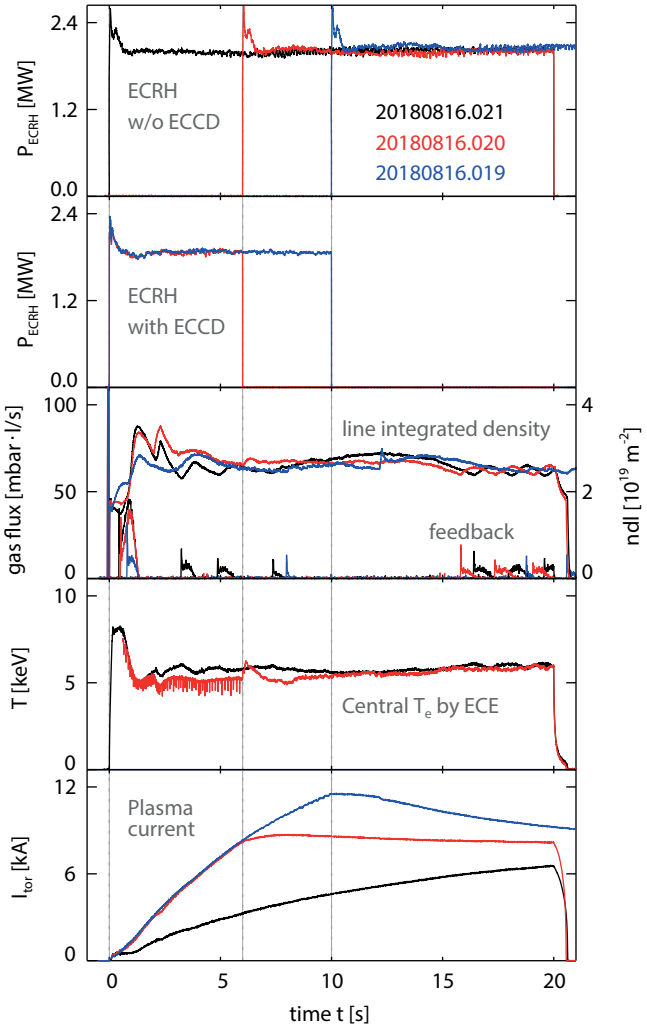

Figure 17: Comparison of ECRH plasmas with three different admixtures of ECCD. Black shows the plasma without ECCD. In this case, the plasma current evolution is determined by the L/R time of the plasma. Blue shows a case with too much ECCD producing an overshooting current. In the red case, the current is adjusted to reach a stationary level at times much shorter than the L/R time.

Further R&D work is underway to expand the capabilities of the gyrotrons from 1 MW to 1.5 MW through a collaboration between KIT, Thales, and IPP. An optional feature of the ECRH system at Wendelstein 7-X is the possibility to drive localized currents. This allows to change the iota-profile and to actively control the island divertor strike lines [6]. A possible scheme was tested using electron cyclotron current drive (ECCD) to anticipate the evolving bootstrap current at the beginning of the discharge, achieving a final strike line position more quickly than with the bootstrap current alone (figure 17). However, ECCD experiments at Wendelstein 7-X also showed the plasma stability to be drastically affected by local rotational transform modification caused by the ECCD itself [7]. These observations have led to fruitful collaborations with theory groups at IPP Garching providing interesting approaches to explain them (for details see chapter "Joint Research Projects on ASDEX Upgrade and Wendelstein 7-X").

4.2 Neutral Beam Injection Heated Plasmas

The first operational experience was gained with the neutral beam injection system in OP1.2b after extensive commissioning. The system consists of the two injector-boxes NI20 and NI21, supplemented with further peripheral components and media interfaces. Both injector boxes are installed in the torus hall symmetrically to the triangular shaped plasma in one of the five magnetic field modules. They are equipped with two positive ion neutral injectors (PINI) each. The high voltage grid spacing of the acceleration system has been optimized to produce hydrogen beams at 55 keV or deuterium beams at 60 keV. In OP1.2b, both PINIs of NI21 were operated at nominal hydrogen beam parameters. About 2.4 MW of absorbed heating power was achieved, when applying an injected power of approximately 3.1 MW [8]. Thus, the experimental flexibility and diagnostic capability of Wendelstein 7-X was extended: Wendelstein 7-X plasmas could be sustained and heated solely with NBI for about 5 seconds and active charge exchange recombination spectroscopy (CXRS) became possible with continuous NBI or short beam blips. NBI heated plasmas achieved central densities as high as 2×10^{20} m^{-3}, which cannot be obtained with the ECRH operation modes demonstrated to date. The first operation of the NBI system with plasma was carefully prepared to curb the operational risk associated with lost fast beam ions. Extensive computer calculations were done using ASCOT to identify the risks and determine optimal magnetic configurations for NBI operation [9,10]. Since in OP1.2b the Wendelstein 7-X plasma vessel liner was not completely water-cooled and contained non-graphite elements, operational boundaries were determined based on the magnetic configurations and plasma density and some heat load fortifications were installed. The observed distribution and magnitude of the heat loads during plasma experiments were compared with the predictions and validated this procedure with sufficient accuracy. Efforts to provide validation of fast ion codes and a predictive capability for fast ion wall loads continues. A multi-code validation exercise for neutral beam depositions has shown that our codes are accurately reproducing measurements of neutral beam attenuation in Wendelstein 7-X [11].

Such simulations serve as the basis for slowing down and finally wall load simulations. Slowing down simulations are being validated against profile measurements and estimates of neoclassical heat flux. The neoclassical heat flux appears to account for some of the ion channel transport in the pure-NBI discharge, while anomalous transport plays a larger role (figure 18).

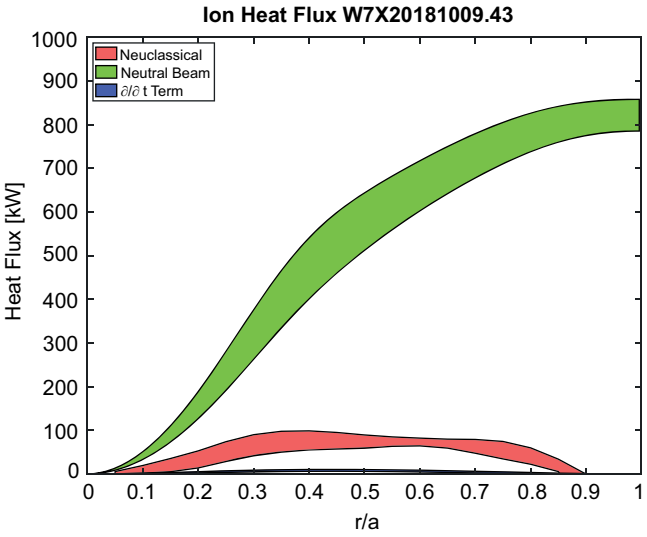

Figure 18: BEAMS3D simulated neutral beam ion heat deposition (green) plotted against neoclassical heat flux as calculated from experimental profiles showing a transport shortfall for the 5 s pure-NBI discharge in W7-X. Shaded regions indicatevariation over the discharge length.

Additional work is underway to better understand the predictions of high wall loads in the high iota configuration. Simulations of beam neutral populations are being conducted with the FIDASIM code, which has recently been updated to handle stellarator geometry. This is an essential tool in interpretation and analysis of the NBI Balmer-alpha spectrum.

4.3 Ion Cyclotron Resonance Heating

The ion cyclotron resonance frequency heating (ICRH) system is now planned to go into operation in operational phase 2, after installation of a prototype antenna in OP1.2b was not possible due to challenging fabrication issues that could not be solved in time. The ICRH system that is to be commissioned before and during OP2 will meet all system requirements of Wendelstein 7-X. It is developed, designed, installed and operated within a collaboration of the Belgium fusion institute LPP-ERM/KMS, Research Centre Jülich (FZJ) and IPP. The ICRH antenna (figure 19) has two poloidal current straps with internal adaptive capacitive pre-matching within a frequency range of 25 to 38 MHz and is fully water cooled for steady state plasma operation. It is equipped with an internal reflectometer system for plasma edge density measurements and allows radial movement and local gas puffing for optimal RF power coupling to plasmas of various magnetic configurations. For the expected plasma densities, it is expected that about ~1 MW of RF power can be coupled to the plasma [12]. The RF generators, formerly used for the ICRH system at TEXTOR, FZJ, are being refurbished and will be installed at Wendelstein 7-X to allow arbitrary current phases of the antenna via a coaxial transmission line network.

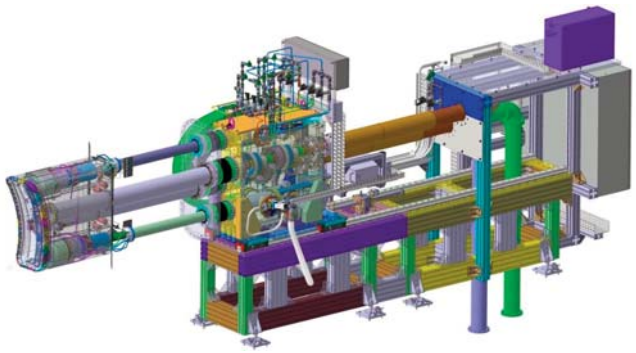

Figure 19: CAD model of the ICRH antenna system including transmission lines and antenna (left).

4.4 Diagnostic Developments

4.4.1 Profile Diagnostics

The profile diagnostics on Wendelstein 7-X, composed of Thomson scattering, interferometry, Electron Cyclotron Emission (ECE), X-ray spectroscopy (in a collaboration with the Princeton Plasma Physics Laboratory), and neutral beam emission spectroscopy, operated consistently and routinely during the OP1.2 campaign. Data from these diagnostics helps to determine electron temperature, electron density, ion temperature, and plasma rotation (radial electric fields). Additionally, such diagnostics can also provide information on impurity species densities, and ultimately main ion density information. While diagnostic hardware progress is straightforward in most cases, the routine provision of reliably calibrated and qualified profile data remains challenging and improvement of reliable in situ calibration is a focus for all of the systems. The development towards steady state discharges requires a high reliability of quasi real-time data handling. From the hardware point of view, issues relate to drifts in calibration – a particular issue for long discharges – and the identification of component failure during operation. On the DAQ and software side, the storage and assessment of large and highly reliable data streams are required. Post-processing is required at different levels of complexity which effects delivery time: Soon after or even during the experiment key quantities must be provided with a minimum of interdependencies. Versioning of the critical quantities captures refinements due to new calibrations as well as better assumptions based on more interdependencies, such as the current best knowledge of plasma equilibrium.

Bayesian analysis is being developed to provide the deepest analysis of selected experiments as well as neutral networks for very high speed evaluation (figure 20) [13,14].

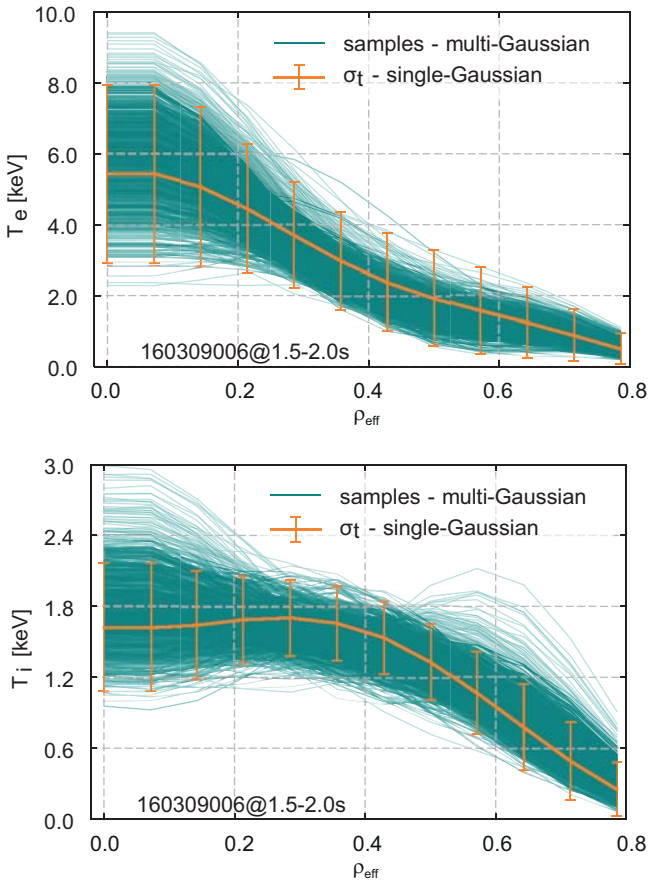

Figure 20: The neural network prediction and uncertainties calculated in the case of the multi-Gaussian sampling procedure (turquoise lines) and the single-Gaussian approximation (orange line), for both T_e (top) and T_i (bottom) profiles.

Neutral beam spectroscopy of the heating beamline has been accomplished using a multi-sightline system. The spectroscopic measurements can be used to determine neutral beam attenuation, beam fueling, ion temperatures, ion densities, magnetic field strength, fast ion distributions, and plasma rotation [15]. While neutral beam operation is a necessary requirement, excellent signal to noise ratios allow NBI blips as short as 10 ms, minimising the perturbative effect during ECRH discharges. Comparison with X-ray diagnostics show reasonable agreement with respect to ion temperatures inferred from argon emission and work is ongoing to provide impurity density profiles. The CXRS T_i measurements were considered critical to evaluation of power balance in Wendelstein 7-X high performance discharges.

During OP1.2 a dispersion interferometer (DI) was used on a regular basis for the measurement of the line integrated electron density and for feedback control of the plasma density. The instrument uses the 2nd harmonic of a laser beam derived by frequency doubling crystals for reference instead of a second interferometer arm such that spurious mechanical vibrations inherently cancel already at the interference pattern. Intermittent signal loss can be overcome by a modulation scheme and the final phase detection with an FPGA directly provides the required density signal for the device control in real-time. A multi-channel system is being prepared to allow for density profile control. Experience and progress with the DI [16,17] are incorporated in preparations for an ITER interferometer and in DEMO design studies [18].

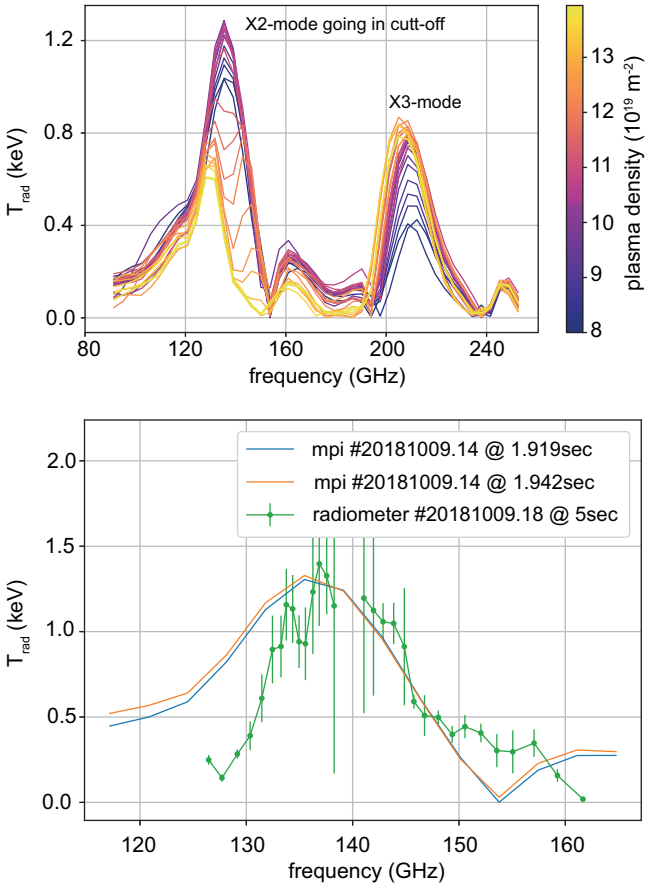

Figure 21: ECE spectrum, measured with a Martin-Pupplet-interferometer, showing an increase of the X3-signal as the X2-signal goes into cutoff due to density rise (top). On the bottom, the X2-ECE, measured by a high-resolution radiometer, is compared to the corresponding emission, measured with Martin-Pupplet-interferometer, showing adequate agreement.

An X3-ECE system is being prepared to allow for fast measurement of electron temperatures at densities beyond the X2 cut-off. Initial measurements using a Martin-Pupplet-interferometer during OP1.2 indicated the feasibility of this technique (figure 21) [19].

4.4.2 Fast Ion Measurements

The measurement of fast-ion related quantities is of critical importance to the assessment of the HELIAS line of stellarators as reactors. In Wendelstein 7-X, NBI provides a source of fast ions, which scale to fusion-alphas in a larger reactor. Coincident with the first operation of the neutral beam system on Wendelstein 7-X, fast ion measurements began. Diagnostics in OP1.2 included a faraday cup style fast ion loss detector (provided by the Japanese National Institute for Fusion Science, NIFS), collective Thomson scattering (CTS, in collaboration with the Danish Technical University and University of Stuttgart), ion cyclotron emission probes, and Balmer-alpha spectra. Given the complexity of measuring distribution function quantities in stellarators, a synthesis of these diagnostics is needed for a coherent understanding of fast ion confinement in Wendelstein 7-X.

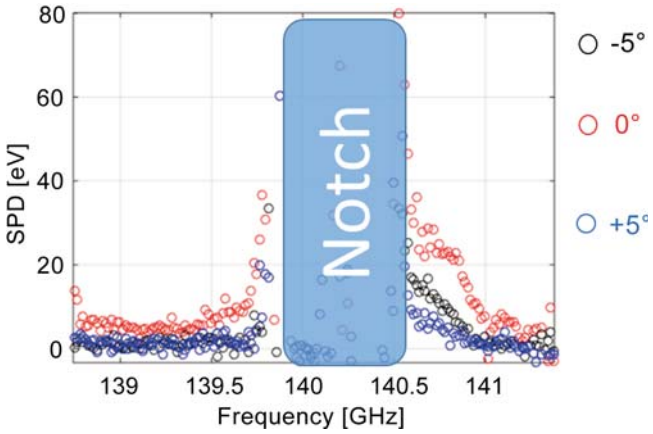

Figure 22: Three CTS spectra at different RSL angles: black circles at -5°, blue circles at +5°, and red circles at 0°. The measurements performed during different position of the receiver beam with respect to the probing beam in order to prove spatial localization of the scattering signal. Zero degrees (red dots) shows the scattering spectrum where the maximum signal is expected, the spectra at ±5° (blue and black) corresponds to the position before and after the expected overlap.

A faraday-cup style fast ion loss detector was installed on the Wendelstein 7-X multipurpose manipulator in OP1.2a [20]. This energy and pitch-angle resolving diagnostic detected particles with 1 cm gyro-radius and pitch angles between 90 and 120 degrees. Multiple positions in the far scrape-off layer were assessed. Such measurements provide validation of simulation results [21]. A 5-channel layered Faraday cup fast ion loss detector (FC-FILD) is being prepared for OP2 in cooperation with the Fraunhofer Institute for Surface Technology, IST. This detector is an evolution of thin-foil based detectors on JET and a prototype has been demonstrated showing energy discrimination in the sub-100 keV energy range [22]. A CTS diagnostic was commissioned using a 140 GHz gyrotron in OP1.2 [23]. The diagnostic is intended for ion temperature measurements, but can also provide information on the fast ion distribution through future upgrades [24]. Figure 22 shows the spectrum measured for three different steering angles utilizing the remote steering launcher from OP1.2. Measurement at the heating frequency allowed estimation of ion temperature but precluded fast ion distribution function information. A modification of an existing gyrotron to 175 GHz was identified through a collaboration with KIT [25] which would allow measurement of both ion temperature and fast ion distribution function information in the future.

Initial tests of Ion Cyclotron Detectors (ICE) in OP1.2 indicated the need for more dedicated diagnostic positioning. The water-cooled antenna for the CTS diagnostic is being instrumented with 4 ICE-probes which should greatly increase their signal to noise ratio in OP2.

In preparation of triton burn-up studies during future deuterium plasmas, the feasibility of an existing 14 MeV scintillation fiber neutron detector, SciFi, is investigated in cooperation with Aalto University, LANL, NIFS and PTB. The detector and a new data acquisition system were put into operation and characterization studies were carried out in mono-energetic neutron fields of the PTB ion accelerator facility, PIAF. Test measurements in deuterium plasmas were also carried out at LHD and AUG. Preliminary results of these measurements and a neutron rate estimation for thermal (not NBI heated) deuterium plasmas in Wendelstein 7-X [26] indicate the feasibility of time-resolved triton burn-up studies in high-performance plasmas. Further 5D-simulations on the neutron generation in W7-X (with the ASCOT and AFSI code) and on the neutron propagation from the plasma towards the SciFi detector (with the Serpent code) – both done at Aalto university – will contribute to a forward model for SciFi in Wendelstein 7-X to study the capabilities of SciFi such as the determination of triton confinement (burn-up ratio), slowing-down and diffusion.

4.5 Operational Limits of Stellarator Plasmas

For the operational space explored so far, a database of the line-averaged density as a function of the central electron temperature and ECRH power has been compiled. This database has been compared to expected operational limits, especially the radiative density limit [27] and limitations arising from ERCH physics. In the left part of figure 23 these limits are shown. Of great importance for future scenario development is the ability to operate at high densities above the X2-cutoff at 1.2×10^{20} m^3, which corresponds to a line-averaged density of 1.0×10^{20} m^3 for the flat density profiles observed for ECRH plasmas in OP1.2. For higher densities, O2-heating is required, which needs a central electron temperature above 2 keV (ideally above 3 keV) in order to be absorbed. A fit has been derived to obtain a simple empirical scaling law of the form $n_e(T_{e0}) = c \cdot P^x$.

The corresponding densities are shown as dashed lines in figure 23 (the lower one corresponds to 3 keV). It can be seen that these O2 absorption curves essentially follow the radiative density limit (gray band), but at a lower density. Both the radiative density limit and the O2 limit show that higher heating powers of at least 10 to 15 MW are required to operate above the X2-cutoff. In the case of NBI heating (right subplot of figure 23), the situation is slightly different. While the radiative density limit, which limits the edge density, is essentially the same, the fraction of the source power and the power absorbed by the plasma is lower (difference between the dashed and dash-dotted line). Due to core fueling, the line-averaged density increases during NBI operation and can surpass the density limit, since this is determined by the edge density (see [27]). This effect is indicated by the gray gradient region. Hence, the density limit as a function of source power (dash-dotted line in figure 23) indicates the maximum density of the initial target plasma before NBI is employed. On the other hand, NBI operation requires a relatively high minimum density, since the beam shine-through could otherwise damage the beam dump. This is indicated by the red gradient region. It should be noted, though, that so far the experimental database for pure NBI operation (shown as dots) is very small.

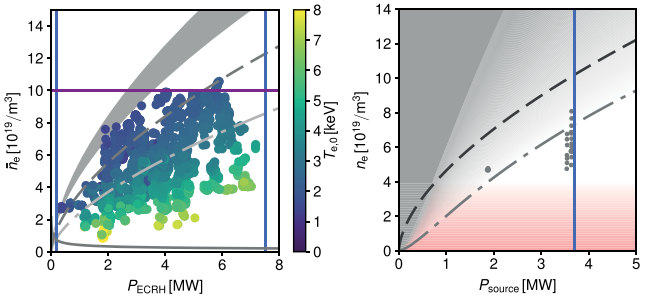

Figure 23: Left: Operational space of ECRH plasmas with TDU, before and after boronization. The blue lines indicate the maximum and minimum heating power, the gray band indicates the radiative density limit and the gray dashed lines indicate the central electron temperatures of 2 and 3 keV, respectively. The purple line indicates the line-averaged density at the X2-cutoff. Right: Operational space for NBI heated plasmas. The dashed line indicates the radiative density limit as a function of the absorbed power, while the dash-dotted line uses the source power. The blue line is the maximum source power in OP1.2b and the red gradient region indicates a shine-through power that could damage the beam dump.

An important question is how – based on the present results – the heating power extrapolates to plasmas with volume averaged β-values exceeding the ~1 % obtained during OP1.2, which will be needed for fast particle and MHD stability studies (not to be confused with the central β-values, which were as high as 3 %). The energy confinement time of typical ECRH plasma obtained during OP1.2 was below the ISS04 scaling in OP1.2. In contrast, pellet fueled plasmas achieved energy confinement times significantly above the scaling. Thus, taking the ISS04 scaling as a reference, achieving plasmas with $<\beta> = 2$ % at 2.5 T and obeying the 2nd harmonic O-mode cut-off density would require 38 MW of ECRH. Alternatively, at a reduced field with X3 ECRH (140 GHz at 1.7 T), obeying the X3 cut-off would reduce the required heating power to 20 MW to achieve the same <β>. Even though these extrapolations bear large uncertainties, more heating power is necessary and 1.7 T operation could be a viable option to investigate plasmas with higher <β>.

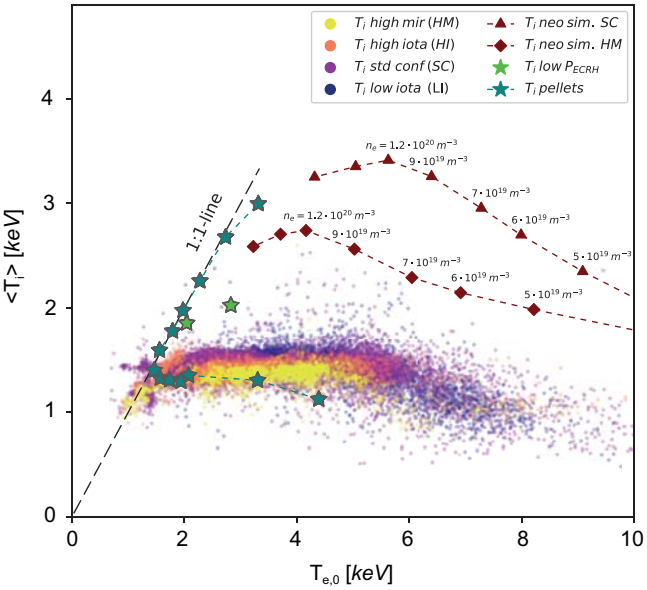

Figure 24: Wendelstein 7-X ion temperature clamping at $T_i \sim 1.5$ keV versus electron temperature in ECRH ($P_{ECRH} \sim 0.5$ MW - 7 MW) heated plasmas and $n_e \sim 1\times10^{19}$ m^{-3} to 1.4×10^{20} m^{-3} in four magnetic configurations (colored dots). Neoclassical transport simulations (dark red) are conducted for a median $P_{ECRH} = 4.5$ MW for the standard (triangles) and high mirror (diamonds) configurations, assuming flat density profiles. The clamping of $T_{i,0}$ can be overcome in plasmas with density profile peaking. The low power E_{CRH} plasmas ($P_{ECRH} = 0.2$ MW resp. 0.5 MW) shortly after a boronization are shown as light green stars, and the pellet shot is shown as dark green stars.

In plasmas with predominant electron heating by ECRH, the ions are collisionally heated by electrons as $P_{ei} \sim n_e^2 (T_e - T_i)/T_e^{3/2}$. Therefore, high temperature differences at high plasmas density provide the highest ion heating. However, figure 24 shows that during the last divertor operated campaign (OP1.2b with boronization) a variation of $P_{ECRH} = 0.5$ - 7 MW lead to a variation of electron temperatures from 1 to 10 keV at electron densities from 1×10^{19} m^{-3} to 1.4×10^{20} m^{-3}, but produced ion temperatures not exceeding $T_i \sim 1.5$ keV. As a comparison, neoclassical simulations show that for a median $P_{ECRH} \sim 4.5$ MW and densities varying between 5 and 12×10^{19} m^{-3}, much higher T_i values would be expected for

low magnetic ripple (ε_{eff}~0.8 % standard configuration, SC) and high magnetic ripple (ε_{eff}~2.5 % high mirror, HM, configurations) plasmas. However, the experiments showed a much reduced and clamped ion temperature, independent of heating power, plasma density and magnetic configuration. Non-linear gyrokinetic simulations indicate that the clamping is most likely caused by turbulent transport in which the degree of ion temperature profile stiffness increases as the ratio of T_e/T_i is raised. The clamping can be overcome by inducing a density gradient. This has been evidenced in plasmas after pellet injection, as well as occuring naturally in low power P_{ECRH}~0.5 MW plasmas shortly after boronization with low edge density (both shown by stars in figure 24). Extrapolation of ECRH heating power will therefore be most effective in plasmas where high density operation increases the exchange power P_{ei}, and where density profile control provides the density gradients required to suppress the anomalous heat transport. In the next campaign, a new pellet injector, as well as improved neutral beam injection and enhanced edge pumping can help achieve such a scenario.

For prospective reactor operation, resilience of plasmas against terminating events has strong impact both for safe operation as well as for potential maintenance costs. In tokamaks, current disruptions result in substantial technical requirements for their avoidance and mitigation. But also stellarators need proactive consideration of plasma termination. In joint experiments within an international collaboration of Wendelstein 7-X, TJ-II (Madrid, Spain) and the Large Helical Device (Toki, Japan), the reaction of substantial but well defined amount of injected impurities, leading to plasma termination, were scrutinized for the first time. First findings, in contrast to tokamaks, indicate that the termination process is governed by radiation losses. Thus, time scales appear to be in the order of energy confinement times, i.e. much longer than MHD time-scales in disruptive events. Moreover, the energy release was not found to exhibit localized heat loads otherwise leading to increasing requirements for plasma facing materials. MHD events in investigations where the low-shear rotational transform approaches rational values, ultimately lead to the end of plasma operation by induced radiation processes and not directly to abrupt termination. The investigations also revealed an additional aspect from one of the salient features of stellarators: Confinement from the vacuum magnetic field appears to be the prerequisite for frequently observed plasma recovery after large perturbations, which is – in other words – a remarkable reflection of the stability of stellarator magnetic fields [28].

Power plant studies following the HELIAS concept are conducted using the systems code PROCESS which was adapted to stellarator properties. Recent research focuses on the extension to more general stellarator geometries including smaller aspect ratios (for details see chapter “DEMO Design Activities“).

5 Stellarator Edge and Divertor (E4)

For first studies of the functionality of the island divertor concept, Wendelstein 7-X was equipped for Operation Phase OP1.2 with ten uncooled fine-grain graphite Test Divertor Units (TDUs). In the E4 division a number of diagnostics and machine components have been installed to allow exploitation of Wendelstein 7-X with the island divertor. Further developments in E4 include preparation of high heat flux campaign and transition to carbon-free device in future.

5.1 Diagnostic Hardware Development for OP1.2

Several systems were provided by the E4 division to help operate and explore Wendelstein 7 X during OP1.2. The focus of these systems is investigation of the plasma edge physics, plasma fuelling, heat and particle exhaust, and plasma wall interactions. The following sections briefly summarise the OP1.2 systems, provided, developed and operated by E4 and their collaborating partners: In each sub-divertor volume, two bolometers were mounted to measure the power flux density of the ECRH stray radiation at the locations where later the cryo-pumps will be installed. Observation of all TDU surfaces was performed by IR and filtered cameras installed either in immersion tubes or at a prototype of an IR/VIS endoscope. Additionally, sixteen metal-shielded thermocouples (type N) were installed in each TDU. A set of 20 Langmuir probes were prepared in the low iota part of the upper as well as the lower divertor of module 5. The probes were nearly flush with the target element surfaces but were faceted to have well-defined, carefully determined angles with respect to the magnetic field. In collaboration with the Wigner Institute (Budapest, Hungary), an alkali metal beam diagnostic was developed to measure the electron density profiles in the plasma edge, by measuring the electronic excitation and attenuation of the 60 keV neutral alkali metal beam, penetrating the plasma at the outer midplane in the bean-shaped symmetry plane. This diagnostic can also be used for turbulence investigations. Single-line-of-sight as well as profiles of Z_{eff} were determined by collecting the visible and near IR part of the bremsstrahlung of the plasma. Several single-lines-of-sight were connected to a multi-channel filterscope (Oakridge National Lab, USA) via optical fibres to monitor H_α, H_γ, CII, CIII and other impurity lines. Alternatively they could also be connected to a high-resolution spectrometer. In OP1.2b also the first of four spectroscopic VUV & IR endoscopes for high spatial resolution 2D divertor observation, developed by FZ Jülich, was in operation. Further important systems are described below.

5.1.1 Instrumentation of the TDU Scraper Element

Two uncooled scraper elements were installed in TDU module 39 (bottom) and 58 (top) and tested during OP1.2 as described later in this report. Both scraper elements were

instrumented with three thermocouples. In addition, the scraper element in module 58 was instrumented with a neutral gas manometer behind the graphite tiles, eight Langmuir probes and monitored by a high resolution IR and VIS monitoring system developed and build in collaboration with LANL.

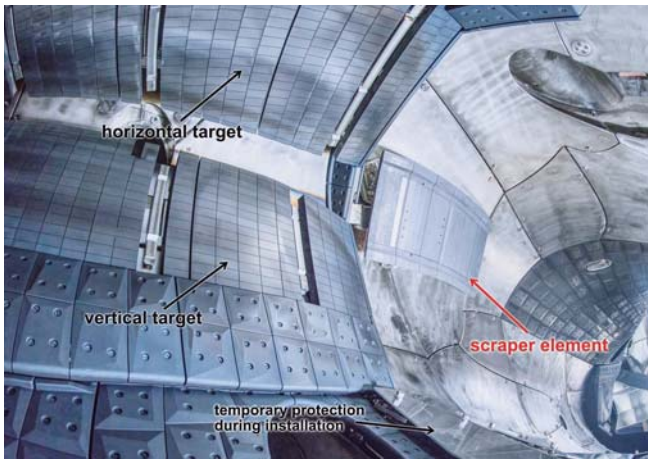

Figure 25: View inside the plasma vessel onto the low-iota end of the divertor and the scraper element.

5.1.2 Video Diagnostic

The video diagnostic (QSV) uses 10 horizontally aligned ports that allow for a toroidal view into all Wendelstein 7-X modules. The system developed in collaboration with the Wigner Institute was upgraded after OP1.1. QSV is capable of observing almost the complete inner vessel and its first wall components. Fast video cameras (Event Detection Intelligent Camera – EDICAM) are devoted to observe events that are accompanied by intense release of light such as hot spots, plasma edge radiation or pellet ablation. The cameras are located only few centimetres off the plasma, so that an active water-cooling of the surrounding in-vessel components and an active air-cooling of the camera head is necessary for longer plasma discharges, i.e. from OP2 onwards.

5.1.3 The Blower Gun Pellet Injector

During the last two experimental campaigns, pellet fueling experiments were performed. Series of hydrogen pellets were injected into Wendelstein 7-X. A blower-gun pellet injector that was originally used in the IPP in Garching, was loaned to Wendelstein 7-X, in order to investigate the fueling needs of a large stellarator. This blower-gun injects hydrogen ice pellets with a maximum velocity of ≈300 m/s. Each pellet was of cylindrical shape with a length and diameter of 2 mm, hence each hydrogen pellet contained nominally 3.3×10^{20} atoms. Helium was used as propellant gas. Up to ≈40 pellets were frozen for one plasma discharge, which could then be injected with a variable repetition frequency between 2.5 and 30 Hz. Previously being used on ADEX-Upgrade with a single-barrel, this design was changed for Wendelstein 7-X to a two-barrel injector. Consequently, pellets could be injected simultaneously into the magnetic high-field side (inboard), and the low-field side (outboard).

5.1.4 Neutral Pressure Gauges

Wendelstein 7-X was equipped with 18 neutral pressure gauges of the ASDEX type; 5 were positioned in the mid-plane, one in each stellarator module, and 13 in the divertor, either near the pumping gap or in the pumping ports. Pressure gauges with conventional thoriated tungsten cathodes suffered from a high failure rate when operated for long times (several hundred seconds). In order to increase their reliability, in 9 of the pressure gauges, the tungsten cathodes were replaced by LaB_6 crystals for the first time. With the LaB_6 crystals an order of magnitude reduction in heating current was achieved, relative to the tungsten filament based gauges, from 15-20 A to 1-2 A, and the failure rate was reduced from appr. 50 % to zero. A full setup with 18 LaB_6 pressure gauges for OP2 will allow a more comprehensive testing of this new concept during long-pulse plasma operation.

5.1.5 Coherence Imaging Spectroscopy

A Coherence Imaging System (CIS) was successfully set up and operated in OP1.2. CIS is a camera-based, passive spectroscopy diagnostic that measures 2D line-integrated particle flows (figure 26) of filtered atomic emission lines. A commercially available, fine-tuneable OPO laser was implemented as a new wavelength calibration technique in Wendelstein 7-X, significantly improving the analysis and enhancing the number of species that can be investigated with CIS.

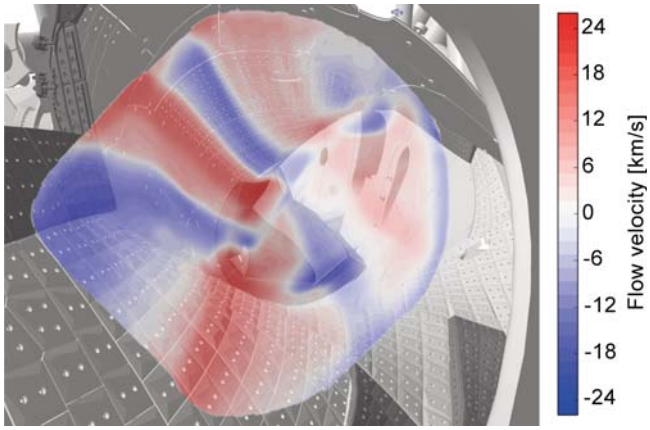

Figure 26: Carbon 2+ flow measurement (coloured) in the Scrape-off-Layer of Wendelstein 7-X. Image is overlaid with CAD model of the inner vessel.

5.2 Diagnostic Hardware Development for OP2

In preparation of the coming operation phases some systems were modified to be compatible with the HHF divertor or hardened to withstand long pulses planned for the next campaigns.

Several new systems planned for the next campaigns are developed, e.g. Manipulator for Target Exposure and Observation (MATEO). The development has been started at FZ Jülich with the installation at Wendelstein 7-X planned for OP2.2. It provides a chance to test a wide range of materials, material compositions and diagnostic concepts under high heat load conditions and as well as allowing a detailed investigation of the near-divertor plasma region. Below several other systems are described.

5.2.1 Popup Langmuir Probes for the High Heat Flux Divertor

For the operation phase OP2 a new Langmuir probe system was designed and manufactured because the flush-mounted probes of the TDU divertor could not be reused. In total 36 Langmuir probes will be integrated behind the upper and lower divertor of module M5: Two parallel rows in the low-iota part with 14 probes in total across the horizontal target and one row of four probes in the high-iota part. Each pair of probes is coupled via a drive unit inserting the foreseen tungsten probes by about 1mm above the divertor surface into the plasma edge. The heart of the actuator is an electromagnetic coil made of ceramic embedded gold conductors that transforms the tilting of the coil in the magnetic background field into an axial motion. Finally, the drive unit was successfully tested in the D-MAG test magnet with about 440,000 motion cycles – vastly exceeding the expected number of cycles in Wendelstein 7-X operation – and is now ready for installation.

5.2.2 Hardening of Immersion Tubes

The immersion tubes designed and used for short-pulse operation will still be used at the beginning of OP2. Therefore, a water-cooled protection with additional windows is added to protect the vacuum barrier of the immersion tube from overheating. This will allow for plasma exposure up to 200 s long discharges heated with 10 MW of heating power. The protection is cladded with graphite to allow convective loads from lost fast NBI particles.

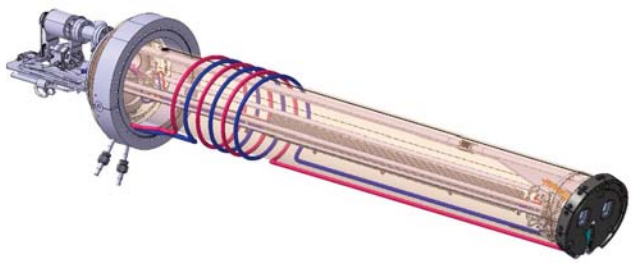

Figure 27: Water-cooled protection plate of the immersion tube.

5.2.3 Steady-state IRVIS Endoscopes

For steady-state operation, the existing immersion tubes in the AEF ports, used for divertor monitoring, will be replaced with IR/VIS endoscopes. Each endoscope consists of a vacuum-compatible plug-in inside the port and an optical box attached to the outside of the vacuum flange. The light from the divertor passes through a pinhole in a protective water cooled head at the plasma side of the plug-in and is reflected by two front mirrors towards the rear end of the plug-in, where it is collected by a telescope system that guides the light through a vacuum window. Outside the vacuum, the light is split into an IR-channel (3-5 µm) for divertor temperature monitoring, and a VIS-channel (350-900 nm) for plasma edge radiation studies. In each channel, the light passes a corrector lens, fold mirrors, a filter wheel and an objective lens, before it is captured by a camera. In OP2.1, the first two endoscopes will be installed in the AEA ports in module 3, since sightlines from the AEF ports will be obstructed by the IRCH antenna.

5.2.4 The Continuous Pellet Fuelling System

For future campaigns, a steady-state pellet injector is presently under construction in the Oak Ridge National Laboratory (ORNL), USA. That new injector will be the result of a multilateral collaboration between ORNL, Princeton Plasma Physics Laboratory (PPPL), and National Institute for Fusion Science (NIFS), Japan. The planning foresees that the new injector will inject cylindrical pellets with a diameter and length of max. 3 mm with a repetition frequency of 10 Hz. Alternatively the pellet size can be reduced to 2 mm and the repetition frequency can be increased to 20 Hz. Steady-state means that discharges with up to 30 minutes can be fed continuously with pellets. A pellet speed of up to 1250 m/s is envisaged. The resulting particle fueling rate of $\approx 10^{22}$ particles/sec will be high enough to balance the significant particle transport during pure ECR heating.

5.2.5 Preparation of Carbon-free Machine

The transition to reactor-relevant materials such as tungsten for the plasma-facing components in Wendelstein 7-X is a major and necessary step in providing the proof of principle that the stellarator concept can meet the requirements of a future fusion reactor. A workshop on this topic was held in Berlin between members from IPP-Greifswald and IPP-Garching. The transition to all-metal plasma-facing components should be done stepwise, starting with an increase of the area with baffle and heat-shield tiles coated with tungsten. As a first step, about 2 m^2 of baffle and heat shield tiles will be covered by a tungsten coating with a thickness of about 20 µm in preparation of OP2.1. The replacement of single graphite tiles at the vertical baffle modules BM1v by tungsten tiles with modified geometry (reduced thickness) is being prepared. At these positions, excess heat loads have been observed during OP1.2b, in particular in the high-mirror configurations, resulting in operation restrictions. Further steps are the full or partial coating of divertor modules (in-situ or ex-situ) and/or the design of a new tungsten divertor for OP3, able to withstand up to 10 MW/m^2 in steady-state operation.

Different technical concepts have to be evaluated with respect to their possible usage in Wendelstein 7-X, requiring the development, fabrication and tests of mock-ups.

5.3 Edge and Divertor Physics

The uncoooled divertor used in OP1.2 was identical in shape to the fully actively water-cooled High-Heat-Flux (HHF) divertor presently being installed to allow studies of quasi-stationary ($\leq$30 min) plasma operation at heating powers up to P_{ECRH}=10 MW. OP1.2 concentrated on a basic characterization of the island divertor, which included magnetic flux-surface mapping of edge magnetic islands, error field correction, and assessment of heat and particle exhaust channels. A highlight of the recent campaign was a robust detachment scenario, where the otherwise strong convective heat loads are strongly reduced, while maintaining high neutral pressures inside the divertor. This yielded a particle removal rate close to the values required for stable density control in steady state operation. This included also experiments for radiative power exhaust with impurity seeding. Overall Wendelstein 7-X shows good impurity control in low and high density discharges with $T_e/T_i>1$. We have found that despite high influx of carbon into the SOL during discharges with dedicated overloading of the leading edges, the plasmas remained stable and the carbon did not penetrate significantly to the plasma core.

5.3.1 Main Magnetic Configurations and the Resulting Divertor Heat Loads

Wendelstein 7-X has a five-fold toroidal periodicity of magnetic fields and modular machine symmetry. According to the up-down flip-symmetry in one period, the aforementioned ten divertor units are distributed toroidally with five in the upper and five in the lower part of the machine. The main magnetic configurations are characterized by the edge rotational transform iota(a)=5/6, (low iota configuration), iota(a)=5/5 (standard and high mirror configuration), iota(a)=5/4 (high iota configuration). The resonant magnetic field at the edge generates the boundary island chain intersecting the divertor target plates for control of the plasma exhaust. This is called the island divertor concept. The island chains form the *separatrix*. Unconfined plasma crossing the separatrix through perpendicular diffusion will follow the open field lines of the island until its deposition on the divertor plate. The transport of the particle and power loads depends primarily on the island topology. The intrinsic long wall-to-wall magnetic field line connection length of several hundred meters is beneficial for an enhanced perpendicular transport. Additionally, significant changes to the island geometry are possible through the use of dedicated island-control-coils, including the tuning of the island size and the rotation of the island position.
Efficient power exhaust is one of the most critical issues for future reactors and therefore it is an important experimental objective for Wendelstein 7-X. The measured strike-line patterns agree to a large degree with expectations. Most of the power, which is not radiated by plasma, is guided along the separatrix towards the divertor target plates. The effectiveness of power spreading on the divertor surface can be quantified by the so-called effective wetted area, defined as the equivalent area over which the maximum measured heat flux would extend for it to match the total heat received by the divertor target plates. Contrary to tokamaks, the definition of the wetted area needs to take into account the three-dimensional complexity of the island divertor. The wetted area increases with increasing SOL power, which is important and very beneficial for operation at high input power. Wendelstein 7-X, although a factor of three smaller (in volume) than the JET tokamak, reaches a wetted area of the same order as JET (A_{wet}=1.5 m^2).

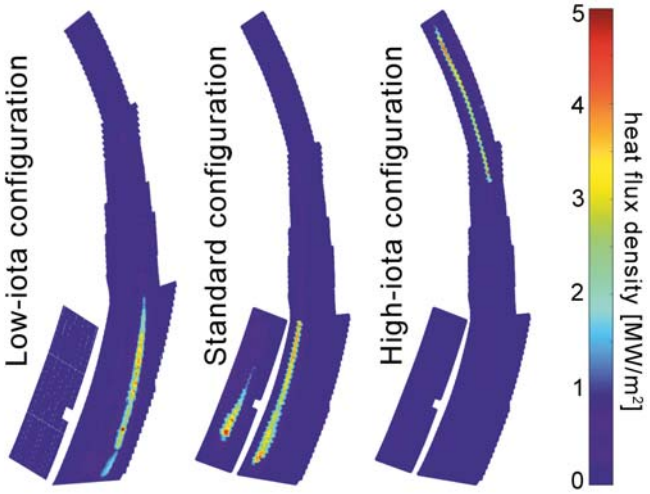

Figure 28: Measured heat fluxes to the divertor for the three main configurations.

5.3.2 Magnetic Flux Surface Measurements

In OP1.2, the experimentally explored magnetic configuration space was significantly enlarged as compared to OP1.1. This provided the opportunity to perform flux surface measurements for various magnetic configurations including the "standard" and "high mirror" configurations with an edge rotational transform of ι_a=5/5 and the "high-iota" configuration with ι_a=5/4 at magnetic field of up to 2.5 T and nominal field direction, where the existence of good and nested flux surfaces was confirmed. Furthermore, the measurements confirmed that the dominating b_{11} error field component – that should be below $<10^{-4}$ B_0 in order to avoid thermal overloads of divertor modules – were for all cases studied below that value. Utilizing the five trim coils, the b_{11} error field was compensated, resulting in a significantly better symmetrization of the divertor heat loads during plasma operation as shown in figure 29. For the "high-mirror"

configuration, the b_{22} error field component was quantified to $b_{22} \sim \iota_a = 0.6 \times 10^{-4}\ B_0$ which is, however, of the same order as the b_{11} component and needs to be compensated as well.

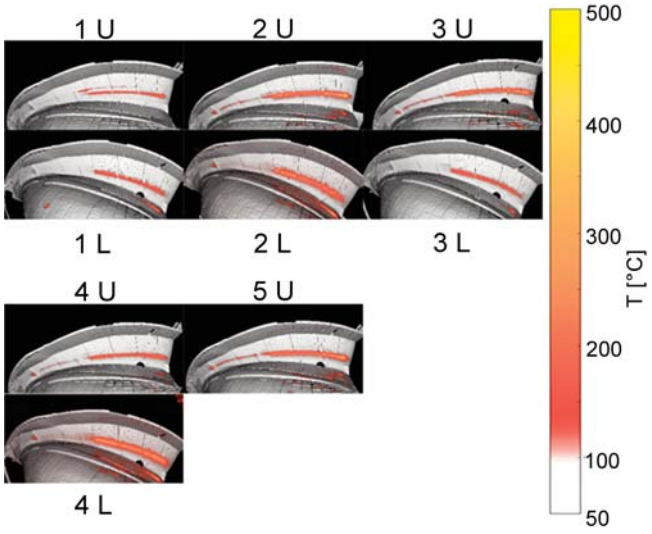

Figure 29: Divertor surface temperature with b_{11} error field correction.

Though not used during flux-surface measurements, the ten island control coils were applied during one plasma operation day for b_{22} error field compensation, resulting in best symmetrization of the target heat loads. In addition, higher order magnetic islands were detected during a scan from the "high-iota" to the "standard" configuration, indicating the presence of higher-harmonic error fields. The analysis of these data is ongoing.

5.3.3 Influence of Particle Drifts on Power Exhaust

Effects of particle drifts on the heat and particle fluxes were studied by comparing similar plasma discharges conducted with a forward- and reverse-directed magnetic field in low-iota magnetic configuration. Radial electric fields can arise from the electron temperature gradient pointing away from the separatrix inside the boundary island. The resulting E×B drift modifies the plasma flows in the island and causes the observed up-down asymmetries in flux profiles on the divertor targets depending on the main field direction.

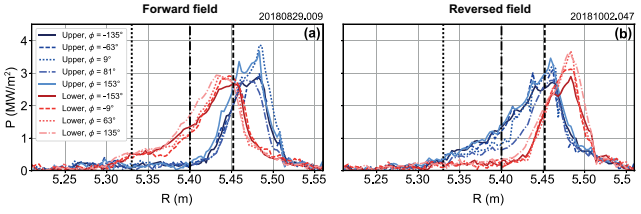

Figure 30: Comparison of the radial heat flux profiles (upper targets in blue, and lower targets in red) between (a) forward and (b) reversed field discharges with similar plasma conditions.

Coupled with perpendicular transport, drifts can either enhance or decrease plasma flows to specific shadowed areas, which are protected by other targets from parallel transport of the main heat channel.
In low-density discharges, around ±15% of the total power loads can be affected by drift effects, resulting in this power being deposited exclusively on either the upper or lower targets. The effect of drifts is smaller in high-density discharges, where the divertor particle and heat loads are rather balanced between the upper and lower targets.

5.3.4 Effects of Boronization on Plasma Performance

Oxygen and carbon were identified as the main plasma impurities in the OP1.2 campaigns with passively cooled graphite divertor. Applying low atomic number (low-Z) wall coatings onto the plasma-facing components is very effective for suppressing impurity influx and oxygen gettering. In OP1.2b, for the first time a boron wall coating was applied to tackle this issue. This led to one of the main achievements of the campaign: plasma operation at high core densities of more than 10^{20} m^{-3} in hydrogen fuelled plasmas due to the reduced radiation-induced density limit.

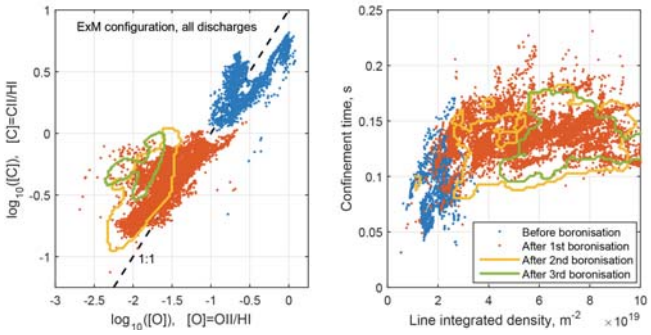

Figure 31: W7-X data samples from all discharges in standard configuration of the second divertor campaign OP1.2b, separated by 3 boronizations. Left: Oxygen and carbon radiation from passive spectroscopy viewing the Wendelstein 7-X divertor. Wendelstein 7-X data samples from all discharges in standard configuration of the second divertor campaign OP1.2b, separated by 3 boronizations. Right: line integrated plasma density and confinement time.

The boronization effect in the second divertor campaign OP1.2b of Wendelstein 7-X is illustrated in figure 31. In total three boronizations were applied. After the first boronization the oxygen to hydrogen flux ratio (normalized to influx of oxygen) at the divertor decreased by a factor of 10 (left graph). Carbon erosion, as a result, dropped significantly, resulting in a 4× lower normalised influx and supressed CO outgassing pressures in the mass spectrometer after the discharge. Between the boronizations, oxygen and carbon normalized influxes increased, but remained well below the pre-boronization values. Each subsequent boronization decreased the O level even further.

With less impurities, the operational window of Wendelstein 7-X increased in terms of higher line-integrated electron density and confinement times. Z_{eff} decreased from 4.5 down to values close to 1.2, as obtained from bremsstrahlung measurements in two reference discharges before and after boronization. Erosion of the wall coatings during steady-state operation may affect future experimental research programs. Boronization through GDC requires de-energised coils and strict safety measures regarding the toxic and explosive diborane gas. An alternative coating technique that omits these limitations is introducing boron containing powder into standard or dedicated diverted plasmas. A proof-of-principle experiment was performed in cooperation with PPPL in OP1.2b using a horizontally installed powder dropper. Further studies are however needed to determine impurity transport characteristics, examine the stability of the plasma to injected material and finally to determine whether powder injection can support the Wendelstein 7-X program by assisting in maintaining premium wall conditions.

5.3.5 Plasma Fuelling by Pellet Injection

Fast and efficient particle fueling was demonstrated successfully with the injection of a series of pellets. In all cases the pellets caused an increase in the central electron density faster than expected from a diffusive time scale. Within less than 30 ms, about 80 % of all pellet particles were deposited inside an effective minor plasma radius of 0.3 m. High-Field Side (HFS) pellets showed a modestly higher fueling efficiency than Low-Field Side (LFS) pellets, but when taking into account the measurement uncertainties, it was not statistically significant. The measured pellet fueling efficiencies were 70 % ± 31 % for LFS pellets and 88 % ± 34 % for the HFS pellets. It is assumed that the rather small difference between HFS and LFS pellets is a result of the small *grad-B* term of ≈0.8 T/m in the pellet injection plane. The technique of injection of a series of pellets worked well, even with small and slow pellets. The experiments demonstrated that the plasma cooling by the first pellets in a series supports the deeper penetration of the last pellets in the same series.

A striking effect in Wendelstein 7-X was the strong transient enhancement of the energy confinement time, that appeared a few 100 ms after the last pellet of a series. The experimental energy confinement time exceeded the expectation from the International Stellarator Scaling law ISS04 by approximately 40 %. It was, however, not possible to stabilize the phase of enhanced confinement to stationarity. Common for these discharges was a peaked electron density profile, reduced plasma radiation losses, strongly increased central ion temperatures and a strong negative radial electric field. The highest fusion triple product observed in a stellarator up to now of 6×10^{19} keV m^{-3} s was achieved. Such values could not be reproduced with gas-puff as particle source.

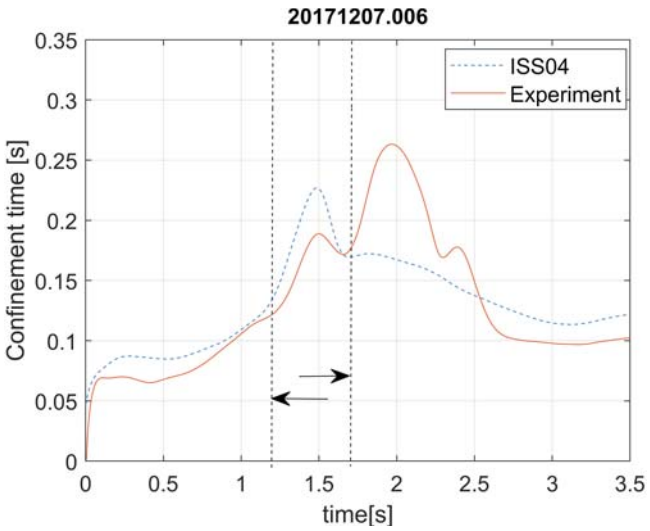

Figure 32: Time traces of the energy confinement time, for the experimental data (solid line) and the ISS04 expectation (dashed line). The two dashed vertical lines indicate the time interval of pellet injection.

Figure 32 shows time traces of the energy confinement time τ_E, both for the experiment and the ISS04 expectation. After the series of pellets, the experimental τ_E exceeds transiently the ISS04 value. It is believed that the enhanced density gradients after pellet injection stabilizes the ion-temperature gradient (ITG) turbulence.

5.3.6 Detachment and Impurity Seeding

Already in OP1.2a, with boronization not yet available and plasmas still suffering from high oxygen content, the first fully power-detached plasmas were demonstrated at P_{ECRH}=3 MW and line integrated densities of $n_{e,l}\sim2.5\times10^{19}$ m^{-2} These detached plasmas were typically initiated either by a burst of injected hydrogen pellets, in which case the density relaxed to a stable level over several seconds, or by a strong gas puff, followed by a regular sequence of small puffs to maintain a constant density. In both cases stable detachment was maintained over 2 s to 3 s, with radiated power fractions of 80-90 %, peak target heat load reduction by about a factor of 10 and only 10 % reduced plasma stored energy. The radiating mantle resulted in an efficient and stable power detachment, however, sub-divertor neutral pressures remained unaffected by the detachment transition at about 5×10^{-3} Pa, only about 7 times larger than the pressure in the outer midplane and thus insufficient for efficient particle removal via the 30 turbo-molecular pumps (TMPs). In OP1.2b, with boronisation, gas fueling feedback control on density and radiation, and heating powers up to P_{ECRH}=6.2 MW available, stable, thermally fully detached island divertor plasma operation with good pumping capability was demonstrated. During the detached phase, peak target heat loads were reduced by nearly an order of magnitude, to values below 0.5 MW/m^2,

while sub-divertor neutral pressures reached values sufficient to pump as many particles as were fuelled, a pre-requisite for stationary plasma operation. In a 5 MW high density ($n_{e,l} \sim 1 \times 10^{20}$ m^{-2}) discharge, a record 28 s stably detached phase was accomplished (figure 33), its duration only limited by the energy limits needed during this phase without an actively cooled divertor. In qualitative agreement with EMC3/EIRENE predictions, high divertor neutral pressures ($p_0 \approx 7 \times 10^{-2}$ Pa) were achieved, with radiated power fractions from carbon of up to f_{rad}=70-80 %. For higher densities, resulting in higher frad, the achievable neutral pressures started to drop. Good impurity retention in the Wendelstein 7-X island divertor helped to maintain a constant, low $<Z_{eff}> \approx 1.5$ throughout the detached phase. Feedback controlled gas fueling via the divertor target integrated helium beam gas boxes, with response times ≤5 ms, was essential for the Wendelstein 7-X detachment performance optimisation. In various discharges, feedback control was done on density, total radiation, divertor impurity radiation and the location of the radiation front in the edge region. The combination of feedback control on radiation and density (in separate experiments) allowed a fine-tuning of the density feedback programming needed to sustain stable detached conditions over 28 s.

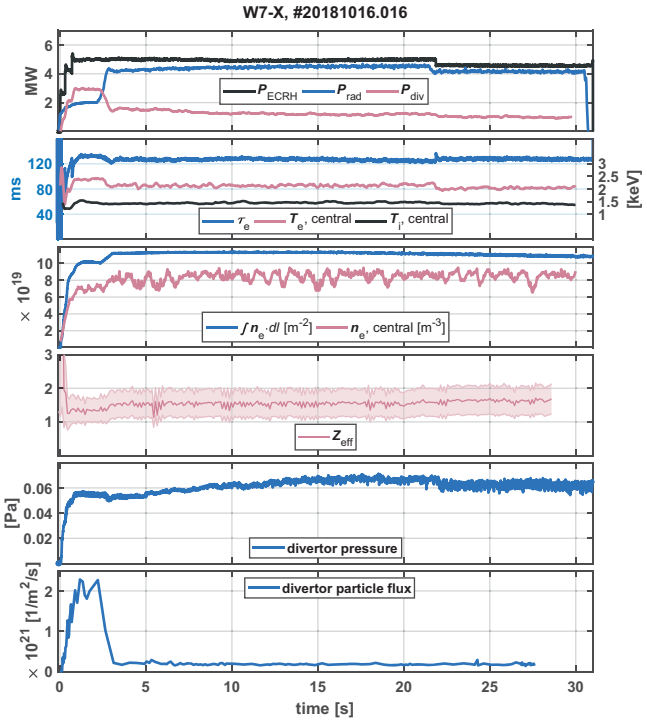

Figure 33: Main parameters of the Wendelstein 7-X experiment #20181016.016.

Controlled impurity seeding (N, Ne) also allowed driving plasmas into detachment and finding optimal radiation distributions between confined plasma edge and SOL/divertor radiation. The island divertor configuration allows for stable and sustained high radiation scenarios with impurity seeding and strongly reduced divertor heat loads in detachment, with energy confinement time reduced by about 15 %. Neon is a very efficient radiator, and short injections allow for significant and sustained enhancement of P_{rad} with a decay time on the order of tens of seconds. Nitrogen seeding requires seeding in a continuous mode in order to establish significant enhancement of radiated power and detachment of divertor heat fluxes. P_{rad} decays within less than a second for short pulses, but for several seconds in case of long and continuous injection. N_2 is, therefore, a promising candidate for radiated power control with a feedback system. Both seeding gases allowed for global control of heat fluxes across all 10 divertor units, despite the use of only a single gas injection nozzle embedded in one of the divertor modules.

5.3.7 Scraper Element Experiments in OP1.2

Simulations of certain high-power long-pulse scenarios for future operation predict overload of the divertor edges due to the changes in the magnetic topology caused by parallel currents and plasma beta. A passive mitigation strategy was explored by installing two (out of a full set of ten) new plasma facing components called scraper elements between OP1.2a and OP1.2b. These components intercept the heat and particle flux that would otherwise wet the overloaded areas. Because overload scenarios could not be directly operated due to energy input restrictions, a series of new magnetic configurations were developed to mimic the topology and heat flux patterns of these scenarios. Experiments were performed in OP1.2a, before the installation of scraper elements, as reference scenario and to test the mimic configurations. The key features of these configurations were confirmed, with a high heat flux measured at the edge of the horizontal target and the evolution of the bootstrap current (to ~5 kA) causing a poloidal shift of the heat flux profile. The heat flux patterns were found to be in qualitative agreement with predictive flux diffusion calculations.

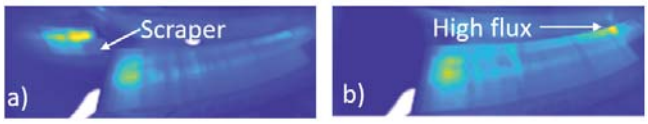

Figure 34: Infrared camera images in divertor modules a) with and b) without scraper elements showing the interception of the flux to the high flux region by the scraper.

During OP1.2b, experiments were performed using the mimic magnetic configurations. Figure 34 shows infrared camera images from divertor modules a) with and b) without an installed scraper element in the overload mimic configuration, indicating the interception of the flux to the horizontal target by the scraper. The heat flux patterns to the scraper element were again consistent with the predictive simulations.

OP1.2b experiments were also used to test a possible deleterious effect of the scraper element. The region of the horizontal target with low power handling capability is the area nearest to pumping entrance, where recycled neutral particles have the greatest probability of reaching the pump. As the scraper elements would also remove flux from this region in steady-state OP2 configurations, this implies a reduction in pumping efficiency. A ~30-40 % reduction in neutral pressure was measured by comparing modules with and without scraper elements, which is larger than the 10-15 % reduction predicted by EMC3/EIRENE simulations. In steady-state OP2 scenarios this pressure would have to be recovered by an increase in the upstream density and therefore the particle flux to the divertor. The magnitude of the upstream density increase depends on the transport regime, and would be considerably less than 30-40 % if the high recycling regime is obtained.

5.3.8 Plasma-wall Interactions

Major plasma-wall interaction (PWI) processes i.e. material erosion, deposition, mixing, material transport and fuel retention in a 3D environment of Wendelstein 7-X with graphite and stainless steel plasma-facing components (PFCs) were investigated. This was accomplished by installing a variety of samples on the PFCs exposed at three different nominal heat load levels between 0.1 and 10 MW/m^2 and employing in-situ spectroscopic observations and ex-situ surface analytical methods. To assess the first footprints of the plasma-wall interactions on the PFCs, a detailed inspection of the whole plasma vessel was performed after OP1.2b. On the whole inboard side of the plasma vessel wall, behind the graphite tiles, sharp deposition stripes (of impurities C: ~430×10^{15}, O: ~115×10^{15} and B: ~76×10^{15} atoms/cm^2) were observed, located at the gaps between the tiles. Flakes with thicknesses of several microns were found on several tiles. Nevertheless, the overall amount of loose dust was very small. The dust consisted mainly of C, partly O and Si and traces of Fe, Cu and Al. The test divertor unit (TDU) provided the attractive possibility of installing targets coated with marker layers (300 nm Mo interlayer and 5-10 µm C on top) at symmetrical positions in all ten divertor units. On 18 TDU targets, after OP1.2a, a strong erosion of up to 20 µm C erosion was observed at the strike line positions with a total erosion of 48±14 g C for all the TDUs. The erosion in OP1.2b was less severe and some net deposition areas were observed as well at the divertor targets (figure 35), this being a consequence of fewer O impurities after boronisation, resulting in lower sputtering rates. Tungsten was introduced on few PFCs during OP1.2b to investigate the compatibility in Wendelstein 7-X and prepare for the next phase of full metal PFC operations. W-deposited layers on the TDU targets were eroded at the strike line location, but tungsten spectral lines were neither detected in the core nor in the edge plasmas and plasma performance was not affected. Wafer probes mounted on stainless steel panels showed small erosion (up to about 4×10^{17} C-atoms/cm^2) and small deposition for OP1.2a, and mainly deposition for OP1.2b. An average deposited layer thickness of 10±6 nm and 25±8 nm were observed on the SS panels during OP1.2a & OP1.2b respectively. Dedicated experiments with almost identical plasma discharges were conducted at the last experimental day of the OP1.2b campaign to quantify the global C transport and migration paths by injecting ^{13}C isotope atoms over 330 s. The measurement of ^{13}C isotope distribution on the TDU targets and the analysis using the 3D impurity transport simulation code ERO-2 and WallDYN are ongoing.

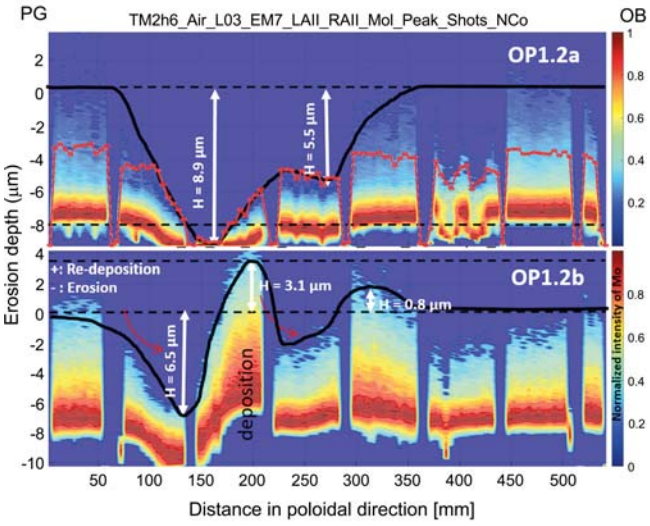

Figure 35: Comparison of erosion and deposition distributions for OP1.2a and OP1.2b at horizontal TDU-target element in half-module 50 (measured with ps-LIBS).

5.3.9 Artificial Intelligence for Machine Protection

In long-pulse operation of Wendelstein 7-X, advanced computer vision algorithms can be applied to protect the plasma facing components (PFCs) from overheating. A fully automatic system to detect thermal events is being developed based on the thermographic diagnostic. This will be used as a plasma-operation interlock system. The first divertor operation phase (OP1.2) was used to test this system with the robust uncooled TDU divertor. During OP1.2 significant thermal events were detected, some of which would exceed future operation limits, while others could potentially become critical during long plasma operation. In order to avoid overloads of leading edge an advanced algorithm is currently under development at University of Cagliari to change the strike-line position in real-time using the control coils. As a first step, the control coil currents used in the experiments were reconstructed with a neural network (NN) from the heat load patterns on the divertor (figure 36).

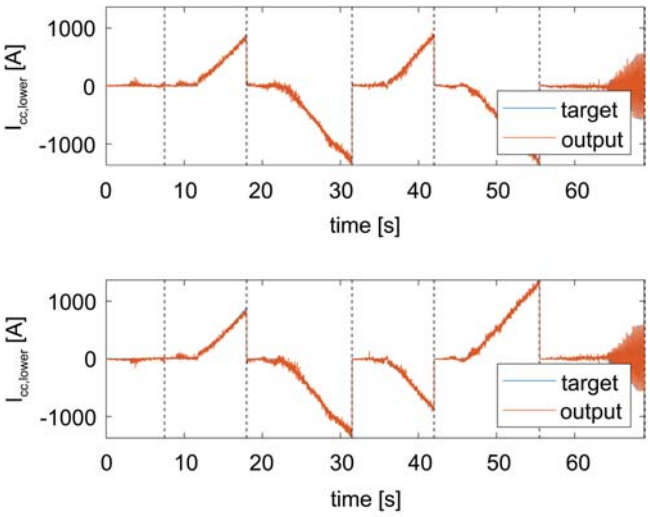

Figure 36: Neural network reconstruction based of the control coil currents superimposed on the actual current.

With the long-term objective of controlling the heat load onto the PFCs, artificial NNs were developed which are capable of reconstructing the rotational transform at the plasma edge and the radial shift of the magnetic axis from heat load images of the PFCs. These two parameters are foreseen to constitute an important input for a future heat load control system. Additionally, they can serve as a real-time virtual diagnostic. It was found that adding simulation data to the training data strongly increases the neural network performance. Detailed modelling studies of PFC heat load distributions, potential overloads and overload mitigation possibilities demonstrated that the impact of the main plasma dynamic effects can be described by such first order approximations.

6 Stellarator Dynamics and Transport (E5)

The division E5 "Stellarator Dynamics and Transport" is concerned with the wealth of collective dynamical phenomena in Wendelstein 7-X, namely plasma instabilities and turbulence and the associated particle and heat transport physics. This broad subject has natural overlaps with the experimental divisions E3 and E4 and close collaborations across the divisions is established. Also close links to the tokamak divisions E1 and E2M as well as to the theory divisions ST and TOK are maintained. The physics objectives of the division E5 are addressed within three working groups, dealing with magneto-hydrodynamic equilibria and dynamics (MHD group), plasma turbulence in the confinement and scrape-off layer region (turbulence group), and the transport of impurities and radiation from the plasma (transport group). The scientific groups are supported by a central engineering group to cover all technical aspects of diagnostics systems.

6.1 Turbulence Group

6.1.1 Microwave Diagnostics

During the latest experimental campaign dedicated microwave reflectometry diagnostics at Wendelstein 7-X allowed one to determine the structure and propagation of turbulence and coherent fluctuations in the plasma edge and scrape-off layer region. The focus of the Doppler and correlation reflectometry measurements is the perpendicular propagation, from which the radial electric field can be deduced. For various different plasma scenarios and magnetic configurations, the comparison with neoclassical transport predictions reveals good agreement. With full-wave modelling the nonlinear instrument response is addressed to assess the fluctuation level. Comparisons with nonlinear gyrokinetic simulation results have started with focus on the role of the radial electric field in the turbulence evolution. The correlation ECE diagnostics on Wendelstein 7-X have been operated in a test configuration throughout OP1.2a/b. A dedicated CECE diagnostic is under development for OP2. It will measure electron temperature fluctuations in Wendelstein 7-X. Two new antennas will be installed for OP2: One antenna is designed to measure the radial correlation length of electron temperature fluctuations, and the second antenna is designed to have overlapping measurement volumes with reflectometry diagnostics to measure the correlation with plasma density fluctuations during.

6.1.2 Probe Manipulator

The probe manipulator has been operated in co-operation with FZJ throughout OP1.2a/b. A total of 11 different probe heads, originating from various different international collaborations, have been used to asses a wide variety of physics objectives, ranging from material injection for wall conditioning and tracer studies, scrape-off layer measurements and characterization of turbulent fluctuations. Capabilities and functionalities of the probe manipulator have been constantly improved during OP1.2 and are currently further expanded towards OP2.

6.1.3 Phase Contrast Imaging

Phase contrast imaging has been operated throughout OP1.2a/b in close collaboration with the Massachusetts Institute of Technology, continuously delivering poloidally resolved, absolute line-integrated density fluctuation spectra for most discharges throughout these campaigns. This is accomplished by small angle scattering of an infrared laser beam which passes through the magnetic axis and subsequent imaging onto a detector array by purpose-built optical elements. The absolute calibration of, both the wavenumber resolution and fluctuation amplitude, enable a comparison across experimental situations, and to gyrokinetic simulations. Phase contrast imaging represents the only dedicated core turbulence diagnostics and revealed mechanisms, which lead to a stabilization of predominantly ITG turbulence in response to scenarios with central density peaking scenarios.

The experimental results are in good agreement with linear and nonlinear gyrokinetic simulations, which demonstrate that the turbulence reduction is due to ITG suppression by a core density gradient without significant destabilization of TEM. In preparation for OP2, the beam path is currently under redesign, due to space constraints, and new diagnostic features are added, including a heterodyne detection scheme for high-frequency fluctuations close to the ICRH frequency as well as improvements to enable radial resolution by spatial filtering of beam components.

6.1.4 Gas Puff Imaging

A as puff imaging diagnostics is currently under construction in close collaboration with the Massachusetts Institute of Technology and is targeted for installation before OP2. Its two-dimensional field of view includes the separatrix and near to mid scrape-off layer and will allow for imaging and subsequent statistical analysis of the spatiotemporal dynamics of turbulent filamentary density structures. The system consists of an optimized supersonic nozzle which enables collimated propagation of the gas puff through the wide magnetic island zone, and a lens and shutter mirror system within an immersion tube, designed to handle the large cumulative heat loads during steady-state operation. Image acquisition is done by a high-speed avalanche photo diode array camera, which has a rectangular field of view aligned with the last closed flux surface for filament tracking, predominantly along the poloidal direction.

6.1.5 Heavy Ion Beam Probe

The heavy ion beam probe diagnostic allows for the measurement of equilibrium electrostatic potential at all radii as well as density and electrostatic potential in the outer plasma region. The feasibility study was successfully done in collaboration with Xantho Technologies, LLC and is followed by estimation of signal levels and characterization of sample volumes. The design of beamline optics as well as the study of ion optics while passing through the plasma has been made to confirm that the desired focal lengths can be achieved, in order to optimize the sample volumes in the plasma and measure the expected parameters.

6.1.6 Numerical Turbulence Simulations in Support of Experiments

Dedicated linear and non-linear gyrokinetic simulations for experimental discharges (core plasma conditions) were performed with the local version of the GENE code. These simulations include ITG-turbulence, TEM-turbulence, and ITG-TEM mixed turbulence for different magnetic configurations. Linear simulations were carried out in Draco and Cobra (IPP local clusters). A specific project of 5 million CPU hours (HIPERF7X) in the Marconi Supercomputer (CINECA, Italy) was used for linear simulations including collisions and for nonlinear simulations. Qualitative comparisons with measurements of the PCI diagnostic, reflectometers, or impurity flux estimations showed a good agreement with the simulation results. A new project of 8 million CPU hours (turbZ7X) has been established for the activities of this year.

6.1.7 Key Scientific Achievements

Core Turbulence

Line-integrated density fluctuations are measured by phase contrast imaging. They are believed to originate from the outer plasma core region where kinetic profile gradients are large. The fluctuations have been observed to decrease considerably after a steepening of the density gradient, induced by pellet injection, and exhibits an unusual mode structure with multiple simultaneously occurring pronounced phase velocities.

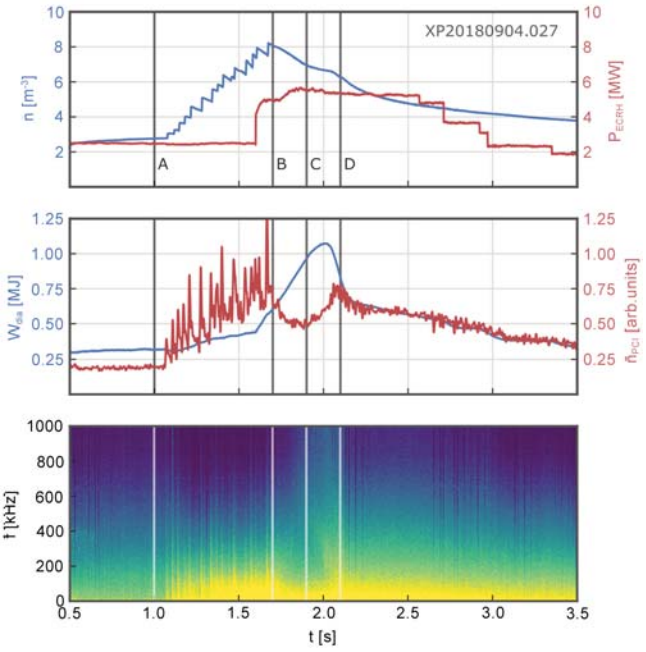

Figure 37: Time traces during a pellet injection program of the line-averaged plasma density and ECRH heating power (top), evolution of the diamagnetic energy together with the measured plasma density fluctuation amplitude (middle), and a spectrogram of density fluctuations as measured with the PCI system (bottom).

Figure 37 shows the line-averaged density (pellet injection between time instants A and B) and heating power, stored energy, PCI fluctuation amplitude and a spectrogram of the fluctuations. The density fluctuation amplitude is reduced between time instants B and D. This is accompanied by a transient improvement of confinement, as seen in the stored energy and ion temperature. Neoclassical transport accounts for only a small fraction of the total heat flux both before and after pellet injection, implying that PCI is witnessing a strong modification of anomalous transport. Other experimental scenarios with modified density gradients (specifically

after heating power steps and strong fuelling) show similar fluctuation characteristics, implying a generic profile effect independent of the particularities of pellet fuelling. Accompanying gyrokinetic simulations show that in the maximum-J magnetic configuration of Wendelstein 7-X, turbulent heat flux is significantly reduced for a given ion temperature gradient when the density gradient is increased due to the resilience of these configurations against density gradient-driven trapped electron modes. The density gradient can therefore stabilize ion temperature gradient modes by reducing the drive term $\eta_i = LT_i / L_n$.

Edge Turbulence

The fluctuations in the plasma edge are dominated by coherent low-frequency fluctuations originating from stable magnetohydrodynamic (MHD) modes. While these modes do not contribute to radial transport in the confined region, they are linked with the formation of isolated structures in the scrape-off layer (SOL). The transition region around the last closed flux surface (LCFS) is characterized by a strong gradient of the radial electric field E_r, being negative in the ion-root regime and positive in the open flux surface region outside the LCFS. The influence of the edge E_r-profile on the growth rate of MHD modes and broadband turbulence can be studied in plasma scenarios with dominant electron cyclotron heating and only transient minor neutral beam injection, such that the plasma profiles remain essentially constant.

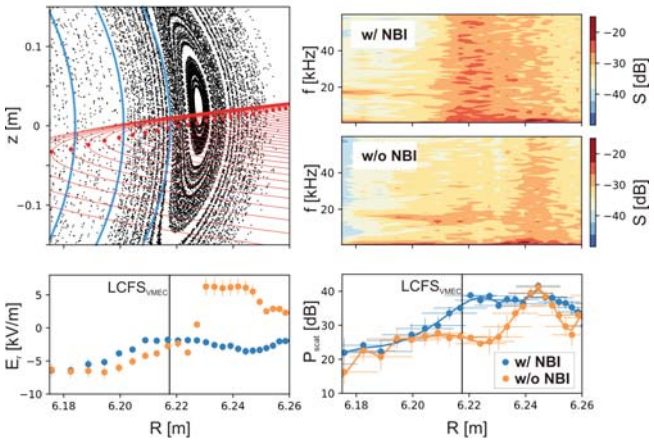

Figure 38: Reflectometry observation volumes (top left), derived radial electric field E_r (bottom left), spectrograms of density fluctuations (top right), and scattered microwave power (bottom right).

An exemplary result using Doppler reflectometry measurements is compiled in figure 38: The observation volumes cover the 5/5 magnetic island in the SOL as well as the plasma edge domain. The radial electric field exhibits a strong gradient around the LCFS without NBI but flattens when NBI is operated and fast ions are generated. The spectrograms of density fluctuations show a strong reduction of the fluctuations in the island domain, while the edge MHD mode remains unaffected. The scattered power P_{scat} is a proxy for the fluctuation level and suggests a strong reduction.

SOL Turbulence

Turbulent filaments (often called "blobs") are known to significantly contribute to cross-field transport in the SOL of tokamaks. They are created in regions of bad curvature (interchange-unstable) and ballistically propagate from the separatrix into the far SOL region due to their self-consistent poloidal dipolar electric field. The role of such filaments for the Wendelstein 7-X SOL, which has a strongly non-uniform curvature drive along a field line, has been investigated by reciprocating probe measurements, accompanied by numerical simulations. The probe measurements have been carried out with multi-pin electric probes in the SOL outside of magnetic islands.

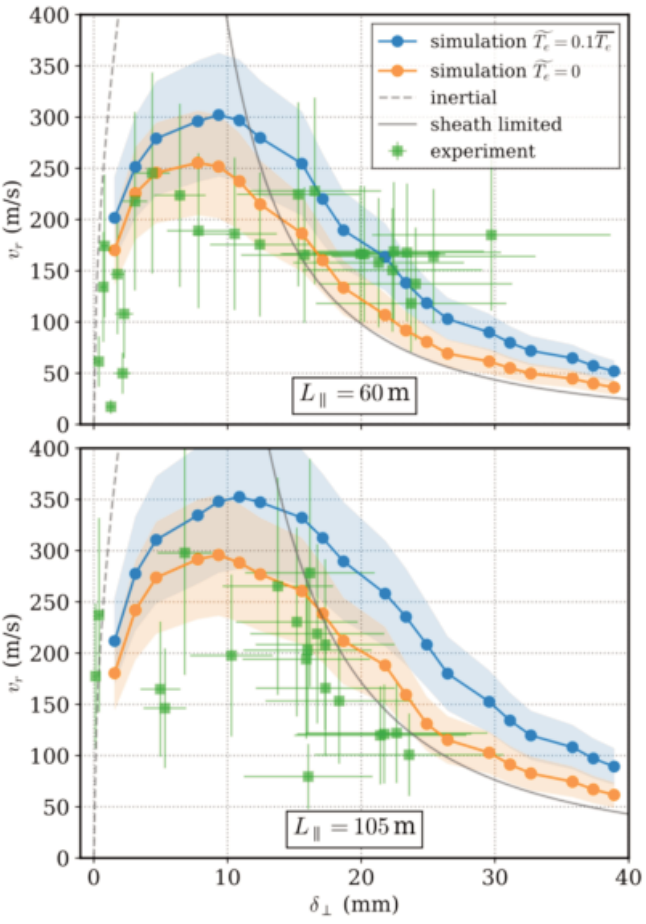

Figure 39: Measured values for radial filament propagation velocities I the Wendelstein 7-X SOL (green) in comparison to seeded filament simulation results with and without electron temperature fluctuations (blue and orange) and the expected analytical velocity scaling in the sheath and inertial regime in regions of short (top) and long (bottom) parallel connection lengths.

Filaments have been identified as monopole density perturbations with an associated dipolar potential structure. They have the expected interchange-type character and are qualitatively similar to filaments in tokamaks. A quantitative analysis, however, shows that the radial propagation of filaments is much slower in Wendelstein 7-X than has generally been observed in tokamaks. This is shown in figure 39 for two different connection lengths parallel to the magnetic field. Accompanying numerical 2D fluid simulations of seeded filaments, using not the local but the field-line-averaged curvature of Wendelstein 7-X as the filament drive, yield good agreement with the experimental results. This indicates that not the local curvature conditions but rather the average magnetic curvature defines the filament behavior. Consequently, the much smaller radial velocities are not a specific feature of the three-dimensional configuration of a stellarator, but rather the result of the large major radius of Wendelstein 7-X, which leads to a small normal magnetic curvature. The quasi-ballistic filament transport (non-local turbulence) as seen in tokamaks is only a minor transport contribution in Wendelstein 7-X.

6.2 Impurity Transport Group

6.2.1 Laser Blow-off

For OP1.2, a laser blow-off (LBO) system was designed and installed. It allows for impurity transport studies by the repetitive and controlled injection of different tracer ions into the plasma edge. A thin metal film coated on a glass target is blown-off by the interaction with laser radiation and is accelerated towards the plasma. The injections of non-intrinsic impurities (in smaller tracer amounts) barely change the plasma parameters but provide intense line emission of different ionization stages. From the temporal evolution of the emission, information about the transport properties can be inferred. The one-dimensional transport code STRAHL, which is embedded in an iterative fitting routine, allows one to determine the radial profiles of the diffusion and convection velocity coefficients. Compared with neoclassical predictions, the transport coefficients are lower by more than two orders of magnitude. This is owing to the turbulent character of the impurity transport in the OP1.2 experimental programs at relevant heating powers.

6.2.2 TESPEL

A supplementary impurity injection system using tracer-encapsulated solid pellets (TESPELs) as projectiles has been installed and successfully operated in OP1.2b. TESPELs are small polystyrene pellets filled with well-defined amounts of impurity material. The pellets are able to penetrate deeply into the core plasma and deposit there a well-localized impurity tracer. The light emission behaviour of the ionic impurity species is measured with the same spectroscopic equipment (bolometer, HEXOS, XICS, HR-XIS) as for LBO. One expects a significant improvement of the information about impurity transport in the plasma core. The comparison of the experimental data with pellet ablation codes confirm the expected ablation processes and the predicted deposition of the tracer impurities. Simulations of the impurity behaviour after injection using STRAHL are in progress.

6.2.3 HEXOS

The two defective spectral channels (during OP1.1) for the high energy range of the high-efficiency XUV overview spectrometer (HEXOS) have been repaired and successfully taken into operation for OP1.2. The availability of the full spectral range (from 2.4-161 nm) now provides the opportunity to access the spectral emission of high ionization states of the intrinsic as well as the injected impurity ions. Combined with the X-ray spectrometers (XICS and HR-XIS), the time traces of low, medium and high ionization states could be recorded as input data for impurity transport and confinement investigations using LBO and TESPEL injections (cf. section 6.2.1 and 6.2.2). Moreover, the development of semi-automatic line detection and data processing routines, complemented by additional spectral line information from intrinsic and injected impurity species, have lead to a significant improvement of the spectral calibration of the instrument.

6.2.4 Bolometer

A two-camera bolometer system, installed at a triangular cross section of Wendelstein 7-X, has been equipped with 70-channel blackened resistive-type detectors, sensitive to radiation in the spectral range from 0.5-600 nm. During OP1.2, the derived total radiative power loss P_{rad} served as indicator for plasma detachment when its value approaches the heating power. The bolometer measurements play a key role for global power balance studies. A fast radiative power loss signal for active feedback-control was developed and applied successfully to tailor the operational parameters for exhaust studies. Using tomographic reconstruction techniques, based on a novel regularization functional (smoothing the relative gradient of the local emissivity), two-dimensional radiation emissivity profiles were obtained. It has been shown that the radiation from the magnetic island regions embedded in the scrape-off layer can be resolved, which, together with the poloidally averaged radial radiation intensity profiles, allows for advanced power balance studies. For OP2.1, a second bolometer system for observations in the active divertor area (located in bean-shaped cross-sections) is prepared together with an in-situ test of an infrared imaging bolometer. A new data acquisition hardware is being developed for long-pulse operation and for the real-time radiation control.

6.2.5 C/O Monitor

A high throughput C/O Monitor system for the fast monitoring of Ly-α line emission is under construction. It uses lines for C (3.4 nm, an indicator for plasma wall interaction), O (1.9 nm,

reflecting the wall condition with respect to remaining water layers), N (2.5 nm, to detect together with the O-channel possible vacuum leakages) and B (4.9 nm, to check the quality of boron coverage of the plasma facing components). The setup uses two Johann-type double spectrometers with multilayer mirrors and a crystal with low spectral resolution. The spectrometers with the C and O channels are planned to be ready for operation in OP2.1, whereas the second spectrometer (B, N) will be added after OP2.1. The design is finished and the purchase process for the first two channels is in progress.

6.2.6 Key Scientific Achievements

Theoretical calculations, based on neoclassical theory for non-axisymmetric configurations like stellarators, predict unfavourable impurity transport in the confined plasma including impurity accumulation in the so-called ion-root regime with negative radial electric field. This regime occurs predominantly for reactor-relevant conditions when the ion and electron temperatures are comparable. The associated impurity concentrations in the confinement region of the plasma cause radiation losses that degrade the plasma energy confinement or can even terminate the plasma by radiative instabilities. Hence, it was mandatory to explore and characterize the transport behaviour of impurity ions. During the operation phase OP1.2a, boronization of the first wall of the Wendelstein 7-X device reduced the previously observed high concentrations of intrinsic impurities (C, O) by approximately a factor of 3-10 and thereby provided access to high density operation. The line-averaged effective charge $<Z_{eff}>$ dropped down to values of 1-2. The bolometer system and the HEXOS spectrometer both did not observe accumulative behaviour of impurity radiation during almost all stationary plasma phases. Short injections of small tracer amounts of impurities (e.g. Si, Ti, Fe, Ni, Cu, Mo, W) by means of a laser blow-off (LBO) system were systematically performed.

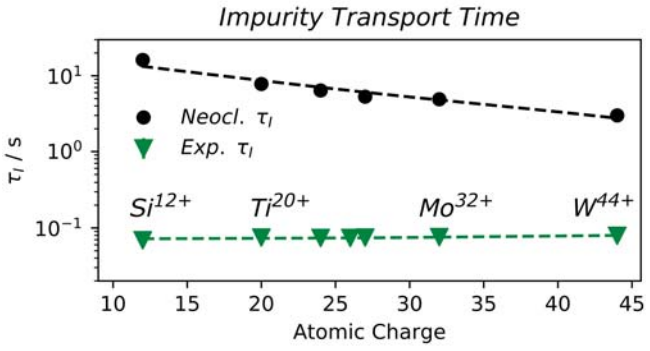

Figure 40: Transport time as a function of the atomic charge.

The time evolution of the spectral emission of these tracer ions showed that the injected impurities penetrated into the confined plasma. However, the relatively short decay times (compared e.g. to the Wendelstein 7-AS scaling) of the emission intensity indicate a comparably short residence time of impurity ions in the plasma core even at high densities. A more detailed analysis of the temporal evolution of the emission after the LBO injection of the different ionization states involved spatially resolved spectral emission in the VUV (by HEXOS) and in the X-ray range (by the imaging Johann-spectrometers XICS and HR-XIS).

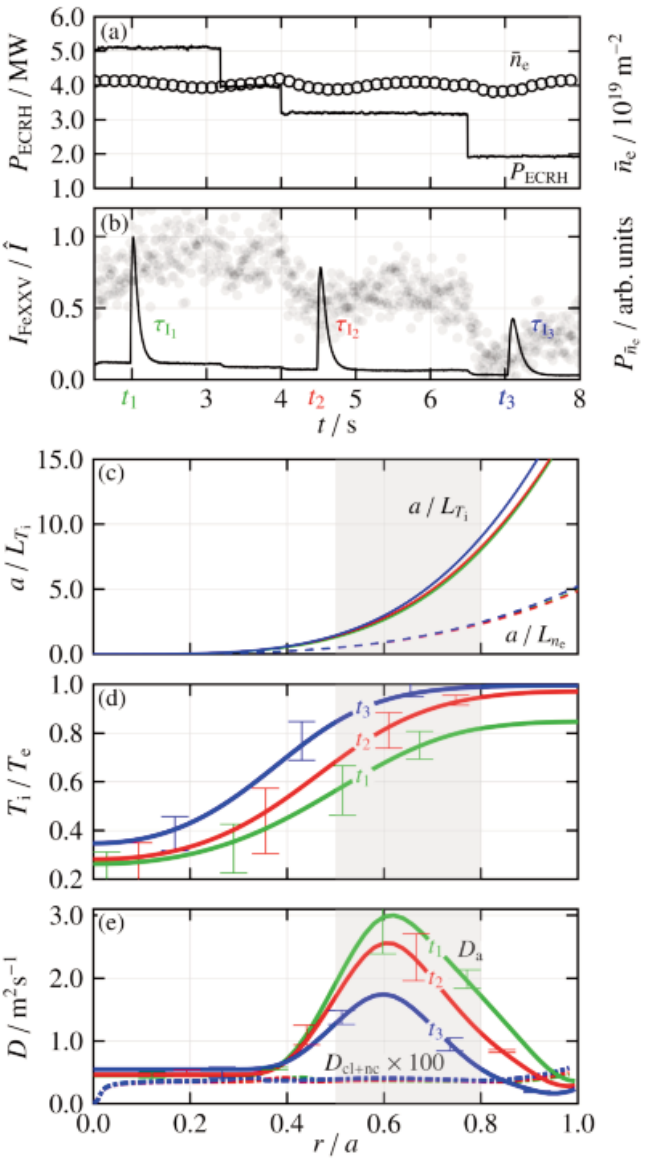

Figure 41: Heating power and the line-integrated electron density (a), normalized Fe XXV line emission and density fluctuation amplitude (b) as well as the profiles of the normalized gradient length of the ion temperature and electron density (c), the temperature ratio profile (d) and the profile of the neoclassical and anomalous diffusion profiles for the above presented injections.

The analysis has revealed diffusion coefficients that were up to two orders of magnitude larger than expected from neoclassical

calculations. Additionally, we observed a significant inverse dependence of the decay times on ECRH heating power, but only a weak dependency on the atomic charge of the injected tracer impurities, as shown in figure 40. The latter is in contradiction to an expected drop of the decay times by a factor of 5, changing from Si to W as predicted by neoclassical theory. These observations suggest a strong role of anomalous impurity transport in Wendelstein 7-X plasmas. The region of measured enhanced diffusivity is located in radial regions with steep ion temperature gradient, which is the main region of ITG turbulence. As shown in figure 41, the diffusivity is strongly correlated to the measured turbulent density fluctuation level and anti-correlated to the temperature ratio of ions and electrons T_i/T_e, which is a key parameter regulating the intensity of ITG turbulence. This behaviour strongly suggests the strong turbulent transport contribution to the radial flux of impurities. This experimental finding is supported by nonlinear gyrokinetic turbulence simulations, which predict diffusivities on the same order of magnitude than the experimentally observed values.

6.3 MHD Group

6.3.1 Magnetic Diagnostics

The complete set of magnetic sensors, namely diamagnetic loops, continuous and segmented Rogowski coils, saddle loops and Mirnov coils have been assembled inside the vacuum vessel and the cryostat before operation phase OP1.1. A precise calibration of the continuous Rogowski coils was done, using a current conductor temporarily installed in the vacuum vessel. The measurements are benchmarked with data from other diagnostics and agree well with theoretical predictions for the profile evolution and resulting bootstrap current. Equilibrium reconstructions, based on magnetic flux, electron temperature and density measurements, were done for all relevant magnetic configurations and discharge parameters. A fast interlock signal for the plasma heating systems, based on the diamagnetic plasma energy, represents the key signal for real-time detection of rapid plasma decays. Its time derivative as additional trigger signal is implemented into the OP2 control system, in order to prepare for the investigation of the occurrence of fast plasma collapses. The ultimate goal is to develop counter-measures to mitigate fast plasma collapses in future high performance long pulse operation with strong central current drive. The investigation of magnetic fluctuations and associated mode activity in Wendelstein 7-X is crucial to understand the MHD stability and energy losses due to electromagnetic phenomena. A total number of 125 Mirnov coils, mounted at the inner plasma vessel wall, are designed to measure broadband magnetic fluctuations and allow for the reconstruction of the dominant poloidal and toroidal mode numbers. The setup is suited for a wide range of expected signal amplitudes, frequencies and mode numbers, taking into account the three-dimensional geometry of Wendelstein 7-X. The individual coils including all relevant data acquisition components are amplitude and phase calibrated, which is a prerequisite for a quantitative spectral and spatial mode analysis.

6.3.2 X-ray Pulse Height Analysis System

After the commissioning during operation phase OP1.1, the Pulse Height Analysis (PHA) system at Wendelstein 7-X has been operated in close collaboration with IPPLM Warsaw. The system is a broad energy range spectrometer (energy range 0.5-19.6 keV) that delivers information about plasma impurity radiation and its temporal behaviour. During the operational phase OP1.2a, all three PHA channels were delivering spectra with sufficiently high photon numbers to identify various plasma impurities over a broad X-ray energy range. Identification of plasma impurities from low- to high-Z elements was possible by choosing different energy ranges for each of the three PHA channels. In operation phase OP1.2b the temporal resolution could be improved and spectra were acquired with 50 ms temporal resolution. The first PHA channel, dedicated to the observation of line emissions from medium- and high-Z elements, was equipped with an additional 1 mm thick Be foil to cover the energy range from 3.6 to 19.6 keV. With appropriate settings, the observation of all impurities injected by LBO and TESPEL during a single experimental program was possible. For discharges with TESPEL injection, medium- and high-Z elements were clearly observed and impurity transport times were obtained. The PHA data provides also the effective charge state Z_{eff}, averaged along the line-of-sight. An analysis of selected discharges revealed a clear impact of the boronization on the effective charge state, ranging from $Z_{eff} \approx 2.6$ before to $Z_{eff} \approx 1.4$ after the boronization.

6.3.3 Soft X-ray Tomography System (XMCTS)

The soft x-ray multi-camera tomography system XMCTS consists of twenty pinhole cameras, up–down symmetrically arranged in a triangular poloidal cross-section of the plasma vessel. The XMCTS diagnostic was commissioned during operation phase OP1.2a. The X-ray emissivity is measured with 16 bit amplitude resolution at 2 MHz sampling rate along 360 lines-of-sight by silicon photodiode arrays. The bandwidth of the preamplifiers (located inside the cameras near the detectors) is ≈200 kHz and the sensitive energy range is 1-12 keV. First of its kind, the X-ray cameras are equipped with shutters in front of the apertures in order to protect the camera filters during conditioning procedures and for calibration purposes during long pulse operation. It turned out that slight misalignments of the delicate shutter mechanics resulted in partially blocking of some of the 360 lines-of-sight. To achieve nevertheless an accurate tomographic reconstruction of the measured data, these shadowing effects needed to be included in a Bayesian forward model.

6.3.4 Key Scientific Achievements

In the operational phase OP1.2, a first set of magnetic configurations was investigated. Data from the soft X-ray tomography diagnostic indicate an up–down symmetric emissivity distribution in the triangular poloidal cross-section. Tomographic reconstructions of different magnetic field configurations are consistent with the calculated flux surface topology, as reconstructed using the VMEC code (figure 42).

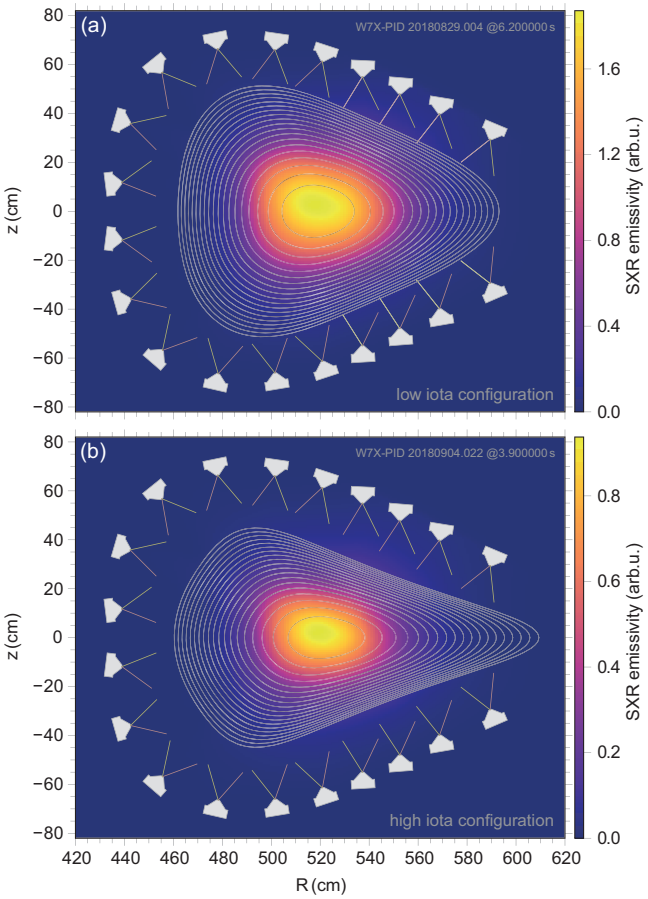

Figure 42: SXR tomograms for a low iota (a) and a high iota configuration (b). VMEC flux surfaces are plotted from the magnetic axis to the last closed flux surface. The tomograms are calculated on a 60×60 rectangular grid with a resolution of Δ_R= 3.0 cm and Δ_z= 2.25 cm.

A dependency of the confinement (increase of the diamagnetic energy for constant heating power) on the rotational transform was observed in a dedicated series of experiments. This is consistent with previous observations on Wendelstein 7-AS. Bootstrap currents between -7 and 17 kA were measured for several magnetic configurations at line-integrated plasma densities ranging between $1 \cdot 10^{19}$ and $1.6 \cdot 10^{20}$ m^{-2} and heating powers between 0.5 and 6 MW. The values of the measured currents agree well with predictions from neoclassical calculations and confirm this particular property of magnetic field optimization. The bootstrap current changes its sign with reversal of the magnetic field and the measured magnitude decreases with the magnetic mirror term and the rotational transform of the magnetic configuration. It also decreases when the line-integrated plasma density is increased. Due to the limited heating power in operation phase OP1.2, MHD equilibrium and stability properties could be investigated for relatively moderate volume-averaged beta values of up to $\langle\beta\rangle \approx 1$ %. The associated Shafranov shift could directly be observed in XMCTS measurements. The evaluation of the Shafranov shift indicates agreement with expectations and the flux surfaces calculated with VMEC using experimentally measured pressure profiles confirm the optimized magnetic field of Wendelstein 7-X. MHD modes and their dependence on plasma parameters could be monitored and analyzed with the Mirnov diagnostic. Independent of magnetic configuration and heating scenarios, broadband fluctuations with frequencies ~180 kHz have been observed. These fluctuations are likely to be associated with ellipticity-induced Alfvén eigenmodes in the outer regions of the plasma. This was inferred by studying corresponding theoretically predicted Alfvén continua, calculated with the 3D-MHD continuum code CONTI. An important topic is the study of fast plasma collapses, observed in plasma scenarios with strong central electron cyclotron current-drive. Fast collapses of the plasma current and diamagnetic energy show a clear magnetic signature: The analysis of the tomography time series from soft X-ray measurements shows a m=1 mode (with m being the poloidal mode number), moving radially outward during the collapse.The correlation of collapse events observed with XMCTS and changes in the electron temperature profile data from the ECE diagnostic indicate an uneven toroidal mode number n. This is consistent with an (n/m)=(1/1) mode. Mirnov data shows short-time scale Alfvénic bursts, which occur during these sawtooth-like collapses.

Scientific Staff

W7-X

I. Abramovic, S. Äkäslompolo, J. Alcuson, P. Aleynikov, K. Aleynikov, A. Ali, T. Andreeva, J. P. Bähner, J. Baldzuhn, M. Banduch, C. Beidler, A. Benndorf, C. Biedermann, M. Blatzheim, T. Bluhm, D. Böckenhoff, L.-G. Böttger, M. Borchardt, H.-S. Bosch, S. Bozhenkov, M. Beurskens, R. Brakel, C. Brandt, T. Bräuer, H. Braune, K.-J. Brunner, R. Burhenn, R. Bussiahn, B. Buttenschön, V. Bykov, A. Carls, N. Chaudhary, M. Cole, M. Czerwinski, H. Damm, S. Degenkolbe, C. P. Dhard, A. Dinklage, M. Drevlak, P. Drewelow, P. van Eeten, G. Ehrke, M. Endler, J. Fellinger, Y. Feng, O. Ford, G. Fuchert, B. Geiger, J. Geiger, D. Gradic, M. Grahl, H. Grote, O. Grulke, P. Hacker, D. Hartmann, D. Hathiramani, B. Hein, P. Helander, S. Henneberg, M. Hirsch, U. Höfel, A. Hölting, Z. Huang, M. Jakubowski, H. Jenzsch, J.-P. Kallmeyer,

U. Kamionka, C. Killer, R. Kleiber, T. Klinger, J. Knauer, A. Könies, R. König, P. Kornejew, J.-P. Koschinsky, R. Krampitz, J. Krom, M. Krychowiak, G. Kühner, P. A. Kurz, S. Kwak, A. Langenberg, H. Laqua, H. P. Laqua, R. Laube, S. Lazerson C. Li, J.-F. Lobsien, J. Loizu, Cisquella, A. Lorenz, H. Maaßberg, S. Marsen, M. Marushchenko, P. McNeely, A. Mishchenko, B. Missal, A. Mollen, T. Mönnich, D. Moseev, M. Nagel, D. Naujoks, U. Neuner, H. Niemann, T. Nishizawa, C. Nührenberg, J. Nührenberg, J. W. Oosterbeek, M. Otte, N. Panadero, E. Pasch, A. Pavone, T. S. Pedersen, V. Perseo, D. Pilopp, S. Pingel, G. Plunk, P. Pölöskei, A. Puig Sitjes, F. Purps, K. Rahbarnia, F. Reimold, J. Riemann, K. Risse, D. Rondeshagen, P. Rong, L. Rudischhauser, K. Rummel, T. Rummel, A. Runov, N. Rust, J. Schacht, F. Schauer, J. Schilling, G. Schlisio, M. Schneider, W. Schneider, P. Scholz, M. Schröder, T. Schröder, R. Schroeder, E. Scott, B. Shanahan, P. Sinha, S. Sipliä, C. Slaby, H. Smith, A. Spring, T. Stange, U. Stridde, J. Svensson, H. Thomsen, H. Trimino Mora, Y. Turkin, I. Vakulchyk, S. Valet, L. Vano, H. Viebke, R. Vilbrandt, A. von Stechow, A. Vorköper, F. Wagner, Z. Wang, F. Warmer, L. Wegener, T. Wegner, G. Weir, J. Wendorf, U. Wenzel, A. Werner, F. Wilde, T. Windisch, M. Winkler, A. Winter, V. Winters, R.C. Wolf, P. Xanthopoulos, M. Zanini, D. Zhang, J. Zhu, A. Zocco.

Other IPP Divisions, Garching

M. Balden, B. Böswirth, J. Boscary, M. Dibon, S. Elgeti, H. Frerichs, H. Greuner, B. Heinemann, P. Junghanns, P. Lang, M. Mayer, B. Mendelevitch, R. Neu, R. Nocentini, S. Obermayer, G. Orozco, R. Riedl, V. Rohde, O. Schmitz, R. Stadler, J. Tretter, A. J. van Vuuren, M. Zilker.

Cooperating Research Institutions

Greifswald University, Germany: P. Helander, T. Klinger, T. S. Pedersen.
Technical University of Berlin, Germany: F. Köster, R. C. Wolf.
Physikalisch Technische Bundesanstalt (PTB), Braunschweig, Germany: A. Lücke, H. Schumacher.
Research Center Jülich GmbH, Institute for Energy and Climate Research Plasma Physics, Jülich, Germany: W. Behr, W. Biel, V. Borsuk, S. Brezinsek, J. Cai, A. Charl, J. Coenen, G. Czymek, T. Dittmar, P. Drews, A. Freund, Y. Gao, X. Han, M. Henkel, K. P. Hollfeld, D. Höschen, M. Hubeny, M. Jia, A. Kirschner, M. Knaup, A. Knieps, A. Krämer-Flecken, M. Lennartz, C. Li, Y. Li, Y. Liang, C. Linsmeier, S. Liu, O. Marchuk, P. Mertens, O. Neubauer, D. Nicolai, G. Offermanns, J. Ölmanns, M. Rack, D. Reiter, G. Satheeswaran, F. Schluck, H. Schmitz, S. Sereda, J. Thomas, B. Unterberg, E. Wang, N. Wang, Y. Wie.
Karlsruhe Institute of Technology (KIT), Eggenstein-Leopoldshafen, Germany: W. H. Fietz, G. Gantenbein, M. Huber, H. Hunger, S. Illy, J. Jelonnek, T. Kobarg, R. Lang, W. Leonhardt, M. Losert, A. Meier, D. Mellein, D. Papenfuß, A. Samartsev, T. Scherer, A. Schlaich, W. Spiess, M. Thumm, S. Wadle, J. Weggen.
Institute for Surface Process Engineering and Plasma Technology, University of Stuttgart, Germany: T. Jesche, W. Kasparek, M. Krämer, C. Lechte, B. Plaum, F. Remppel, H. Röhlinger, B. Roth, K.-H. Schlüter, S. Wolf, A. Zeitler.
Technical University of Denmark, Lyngby, Denmark: L.-G. Böttger, O. Grulke, S. K. Nielsen, M. Salewski, M. Stejner, A. Tancetti.
Aalto University, Espoo, Finnland: T. Kurki-Suonio, S. Sipliä.
Eindhoven University of Technology, Eindhoven, Netherlands: H. Brand, J. Howard, S. Paqay, J. Proll, M. Zuin.
Royal Military Academy, Brussels, Belgium: F. Durodie, A. Goriaev, Y. O. Kazakov, J. Ongena, B. Schweer, M. Vergote, M. Vervier, T. Wauters.
Culham Centre for Fusion Energy (CCFE), Abingdon, United Kingdom: S. Schmuck.
Commissariat á L'Energie Atomique (CEA), Cadarache, Saint-Paul-lez-Durance, France: D. Chauvin, A. da Silva, H. Fernandes, B. Goncalves, A. Grosman, M. Houry, V. Moncada, T. Ngo, S. Renard, J.M. Travere.
Instituto de Plasmas e Fusao Nuclear, Lisboa, Portugal: B. Carvalho.
CIEMAT, Madrid, Spain: A. Alonso, E. Ascasibar, E. Blanco, I. Calvo, A. Cappa, D. Carralero, F. Castejon, A. de la Pena, H. Esteban, T. Estrada, J. Fontdecaba, J. García Regaña, C. Guerard, J. Hernandez, C. Hidalgo, D. Loesser, K. McCarthy, L. Pacios Rodriguez, N. Panadero Alvarez, E. Sanchez, B. van Milligen, J.-L. Velasco, H. Zhang.
Universidad Carlos III de Madrid, Spain: A. Gogoleva, L. Vela.
University of Cagliary, Italy: B. Cannas, F. Pisano.
Consorzio RF X, Padova, Italy: L. Carraro, N. Vianello.
University of Salerno, Fisciano SA, Italy: R. Citarella, V. Giannella.
ENEA Centro Ricerche Frascati, Italy: G. Claps, F. Cordella.
University of Milano-Bicocca, Italy: A. da Molin.
Istituto di Fisica del Plasma Piero Caldirola, Milano, Italy: M.-E. Puiatti, M. Romé.
Austrian Academy of Science, Vienna, Austria: F. Köchl, R. Schrittwieser.
Wigner Research Centre for Physics, Budapest, Hungary: G. Anda, G. Cseh, T. Ilkei, G. Kocsis, G. Náfrádi, S. Récsei, V. Szabó, T. Szabolics, T. Szepesi, Z. Szökefalvi-Nagy, S. Tulipán, S. Zoletnik.
Institute of Plasma Physics and Laser Microfusion, Warsaw, Poland: A. Czarnecka, W. Figacz ,T. Fornal, A. Galkowski, M. Gruca, S. Jablonski, J. Kacmarczyk, N. Krawczyk, M. Kubkowska, G. Pelka, L. Ryc.
University of Szczecin, Poland: K. Czerski, M. Sleczka.
University of Opole, Poland: I. Ksiazek, E. Pawelec.
Institute for Nuclear Research, Kiev, Ukraine: Y. Kolesnichenko, V. Lutsenko.

Ioffe Physical-Technical Institute of the Russian Academy of Sciences, St Petersburg, Russian Federation: F. Chernyshev.
Princeton Plasma Physics Laboratory (PPPL), Princeton, NJ, USA: D. Gates, B. Israeli, S. Langish, D. Mikkelsen, J. Mittelstaedt, H. Neilson, N. Pablant, A. Reiman, M. Sibilia, M. Zarnstorff.
Massachusetts Institute of Technology (MIT), Cambridge, MA, USA: S. G. Baek, S. Ballinger, E. Edlund, M. Porkolab, J. Terry, A. White, B. Wiegel.
University of Wisconsin Madison, USA: T. Barbui, F. Effenberg, E. Flom, J. Green, T. Kremeyer, L. Stephey.
Oak Ridge National Laboratory (ORNL), Oak Ridge, TN, USA: M. Cianciosa, M. J. Cole, J. H. Harris, J. Lore, A. Lumsdaine, D. A. Spong.
Auburn University, USA: D. Ennis, D. Maurer, J. Schmitt, P. Traverso.
University of Maryland, College Park, MA, USA: M. Landreman.
Los Alamos National Laboratory (LANL), Los Alamos, NM, USA: G. Wurden.
National Institute for Fusion Science, Toki, Gifu, Japan: T. Funaba, X. Huang, K. Ida, H. Kasahara, N. Kenmochi, S. Masuzaki, T. Morisaki, K. Ogawa, B. Peterson, S. Ryosuke, R. Sakamoto, S. Satake, C. Suzuki, N. Tamura, H. Tsuchiya, T. Tsujimura, H. Yamada, I. Yamada, R. Yasuhara, M. Yokoyama.
Kyoto University, Japan: T. Mizuuchi, S. Murakami, F. Sano.
The Australian National University (ANU), Canberra, Australia: B. Blackwell, J. H. Matthew, A. Wright.

Joint Projects

Joint Research Projects on ASDEX Upgrade and Wendelstein 7-X

Head: Prof. Dr. Ulrich Stroth, Prof. Dr. Robert Wolf

Operating two leading fusion devices, the tokamak AUG and the stellarator W7-X, puts IPP in a unique position for developing the best solutions for a fusion power plant. To make best use of the individual strengths and to generate synergies, IPP actively promotes cooperation between the two sites through an number of joint workshops and postdoc projects. This section reports on highlights from experiments carried out jointly on the two devices.

Summary of Collaboration Effort

Among the many existing cooperations, plasma-wall interaction, divertor physics, 3D MHD effects and transport can be identified as focal areas. Some examples are highlighted below. Further examples are the development of the ITER manometer, with prototypes used on both devices, hardware exchanges like a Doppler reflectometer for turbulence studies, detectors for collective Thomson scattering (coll. DTU and Uni Stuttgart), detectors for measuring the ion-cyclotron-emission from the plasmas, or scintillation detectors (coll. LANL, and PTB) to measure 14 MeV neutrons for tritium burn-up studies.

Sawtooth-like Instabilities

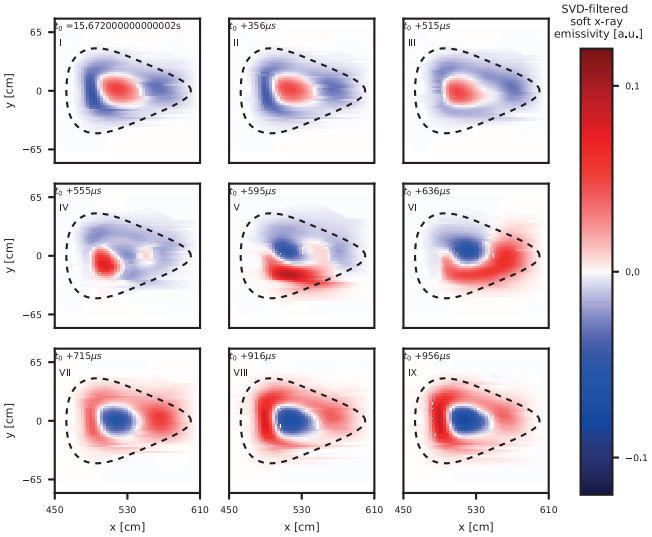

Figure 1: SVD-filtered soft X-ray emissivity tomogram.

In ECCD experiments at W7-X the plasma stability was strongly affected [1] and collapses similar to sawtooth crashes in tokamaks appeared in two forms, with different amplitudes and crash volumes. For bigger crashes up to 50 % of the minor radius is affected. They are generally anticipated by a fast (100 µs) displacement of the plasma core (figure 1, III and IV). The hot core is expelled in about 20 µs (V and VI). Between two big crashes, several smaller crashes were detected. In collaboration with the MHD-group in Garching linear stability calculations were conducted [2] with the resistive code CASTOR3D, showing that the plasma is unstable to double-tearing modes. Solving nonlinear two-fluid equations in a cylindrical geometry indicated nonlinear mode coupling between a resistive kink mode dominated by (m,n)=(1,1) components. The typical times for development and core expulsion agrees with the experimental times. A second type of crash is found as well, consistent with experimental observations.

Divertor Physics

Although the AUG single-null and the W7-X island divertor are different in many aspects, the requirement to detach the plasma and the fundamental processes to achieve this are comparable. Code and diagnostics development and experiments are collaborative efforts. The divertor simulation code EMC3 is used on both sites. Volume recombination was included to allow modelling of detachment and impurity seeding on both devices [4]. The impurity migration and wall dynamics code WallDYN was coupled to EMC3 making it applicable to 3D plasma and wall geometries. Impurity migration experiments in AUG (^{15}N) and W7-X (^{13}C) are analysed with this new code WallDYN3D [5,6]. It will also be used to interpret W layer erosion measurements of targets exposed on the TDU of W7-X where a low maximum erosion of 0.5 µm tungsten was measured at the TANDEM accelerator.

For the analysis of particle sources and sinks in dense divertors, Bayesian analysis is developed and tested based on SOLPS runs [7]. It is envisaged that 2D profiles of electron density, temperature, and neutral density can be obtained from multiple diagnostics like Balmer-line, Stark broadening, and helium beam spectroscopy. Spectroscopic analysis of molecular nitrogen spectra is developed to have access to impurity concentrations in the high-recycling or detached divertor regimes triggered by nitrogen seeding.

Coherent imaging spectroscopy (CIS) is a powerful technique to obtain 2D images of particle flows in SOL and divertor. CIS was implemented on W7-X [9] (Coll. Auburn Univ.) and then transferred to AUG. Figure 2 shows flow structures of C^{2+} impurity ions in AUG and W7-X, reproducing the different magnetic field topologies in the SOLs.

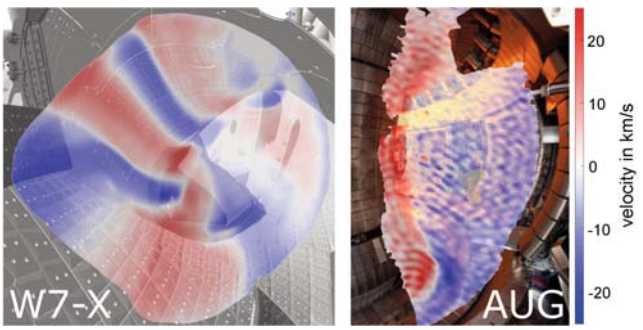

Figure 2: Line-integrated flow velocities of C^{2+} measured with CIS in the SOL of W7-X and AUG.

The counter-flows helped to validate modeling with EMC3-Eirene [8]. To improve our understanding of the SOL particle dynamics, measured CIS flows during detachment and neutral particle flows are investigated on both devices. The success of CIS lead to a favorable design review of the diagnostic for ITER.

Impurity Transport

High Z impurity transport was studied in low-density L-mode plasmas on AUG and W7-X [10,11]. The decay of the Fe^{+22} line radiation intensity after laser blow off of iron was measured in the two devices with the same electron density and steps in the ECRH power. Figure 3 shows characteristic decay times between 20 and 300 ms that drops, as expected from confinement degradation, with heating power. Similar values for the decay times are observed when plotted as function of the power normalized to the plasma volume; the values are comparable with the energy confinement times. This points to turbulence as the dominant impurity transport mechanism.

For low-Z impurity transport studies, the data analysis suite for the exploitation of active charge-exchange recombination spectroscopy from AUG is being implemented on W7-X. It includes codes to evaluate impurity density (CHICA) [12] and transport (STRAHL). It will be used to evaluate boron transport from laser-blow off experiments and to compare the results with data from AUG.

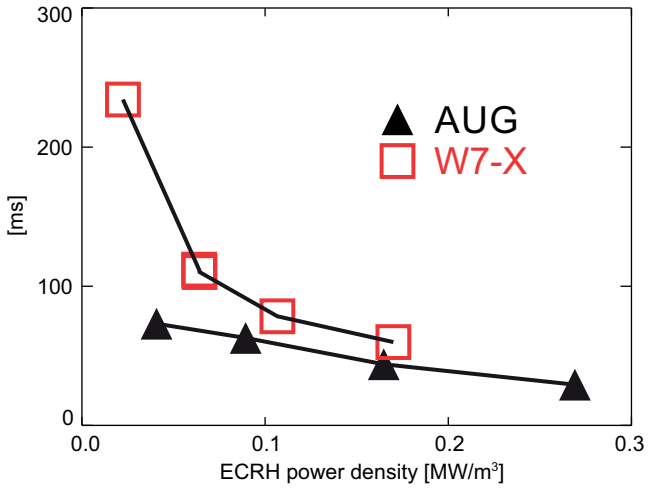

Figure 3: Impurity decay time as a function of ECRH power density.

Turbulent Transport and Confinement

Similar poloidal correlation microwave reflectometers are installed on AUG and W7-X (collab. Jülich), equipped with clusters of one launching and 4 receiving antenna. A first comparison of the turbulent structure size was carried out. The distribution of perpendicular correlation lengths from a database of 110 W7-X and 44 AUG discharges showed by a factor from 2-5 smaller values in AUG. In W7X the correlation lengths is found to be shorter in low-iota than in standard magnetic configuration.

A large operational space in W7-X hydrogen plasmas was covered with densities of up to $1.4 \cdot 10^{20}$ m^{-3} and central electron temperatures of 10 keV while the ion temperature appeared to be "clamped" at about 1.5 keV (see figure 4). In a comparison experiment with AUG L-mode plasmas with densities up to $7.5 \cdot 10^{19}$ m^{-3} and similar ECRH power, the ion temperature appeared also "clamped" (figure 4) although the electron-ion collisional energy transfer varies by a factor of three in both devices. The lack of ion temperature response appears regardless of the electron heating level, electron density and magnetic configuration. For both devices turbulent heat transport dominates over the neoclassical transport. Non-linear gyro-kinetic simulations indicate that the a degree of ion-temperature profile stiffness increases with the ratio T_e/T_i and therefore when enhancing electron heating.

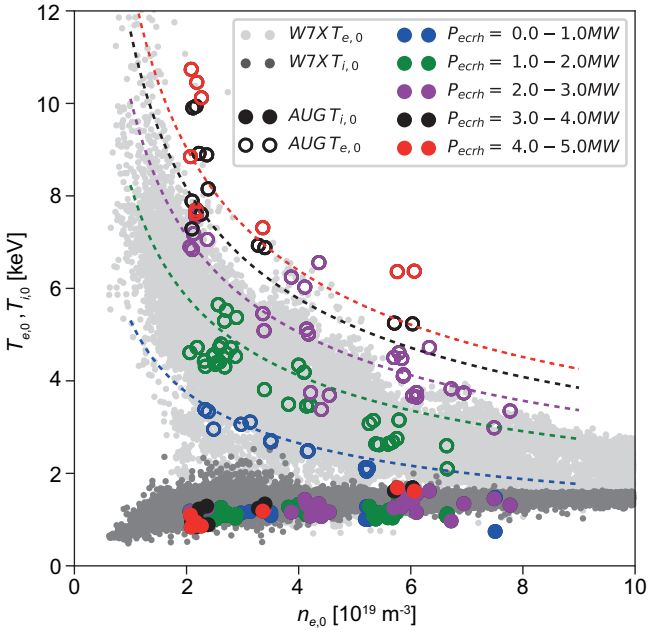

Figure 4: Ion temperature clamping in ECRH AUG L-mode plasmas (closed colored symbols) and W7-X (dark grey points). Open symbols and light grey points represent the central electron temperature in AUG and W7-X, respectively. The color coding represents ECRH power levels for AUG.

A confinement database from AUG L-mode and W7-X standard discharges was assembled. Stellarator confinement scaling expressions describe the database well and indicate a similar quality of energy confinement in both devices. While the energy confinement time in AUG benefits from the smaller aspect ratio, the transport coefficients in W7-X appears to be smaller possibly due to reduced average magnetic field curvature. A physics based confinement scaling is derived from a tokamak transport model. The dimensionally correct scaling has very similar parameter dependencies as the stellarator scalings and reproduces also the trends in the data from ITER L- and H-mode databases reasonably well [13].

ITER

ITER Cooperation Project

Head: Dr. Hans Meister

Introduction

IPP contributes to the ITER Project with a wide range of activities. There are large R&D efforts for heating systems, diagnostics and the development of integrated control scenarios as well as specific tasks in theoretical modelling. In addition, IPP is playing a leading role in contributing to the ITER physics through the International Tokamak Physics Activity (ITPA) and by participating in the EUROfusion Work-programme.

The ITER cooperation project at IPP continued its efforts along the major contributions for the development of heating systems, diagnostics and plasma control as well as theoretical investigations. For the development of RF driven negative hydrogen ion sources for ITER IPP operates two test facilities, ELISE and BATMAN Upgrade. Demonstrated at ELISE were for the first time ever at a large negative ion source for NBI hydrogen pulses with ITER relevant length and a performance that is comparable to what can be achieved during short pulses. In order to better understand the temporal behaviour of the caesium redistribution and to bring the operational scenario closer to the one of the ITER NBI system, ELISE will be upgraded with a CW extraction system. BATMAN Upgrade uses a new ITER-like extraction system for an improved beam optics and space charge compensation in combination with an extensive set of diagnostics. This helped to better understand the beam divergence which is of great relevance for the ITER NBI system as it indicates that the corresponding ITER requirement can be met. The grant related to the development of the ECH upper launcher for ITER ended successfully in 2018. IPP's physics analyses demonstrated the capability of the revised design to sufficiently focus the ECH beam for NTM stabilization purposes. A new collaboration between IPP and the ITER Organization on optimizations of the ITER ICRF antenna has been started in 2020.

For both diagnostics the design integration and engineering analyses proceed and are accompanied by prototype testing. For bolometer cameras the design progressed and port mounted cameras await their preliminary design review (PDR) early in 2021. Some camera components like 3D shaped ceramic substrates with printed electrical tracks or high-temperature compatible signal cables have been prototyped and two sensor types successfully passed an irradiation up to 0.3 dpa. Neutral pressure gauges already had their PDR in May 2020. While mechanical components are well accepted, issues identified for the filament lead to further prototyping and testing. Variations of filament shape and material, partially in cooperation with colleagues from W7-X, shall help to identify the optimal solution for ITER.

IPP's support of the development of the ITER Plasma Control System (PCS) led to a successful final design review (FDR) for the 1st Plasma phase in July 2020. The tests of the ITER PCS Real-Time Framework (RTF) and Compact Controller (CC) are working towards their FDR in late 2020.

Furthermore, as part of contracts with ITER, theoretical investigations for runaway electrons, halo currents and alpha particle physics have been performed.

Finally, IPP experts participated in several design reviews at ITER. Based on their input and expertise, additional contracts with ITER are expected in the near future in particular for supporting diagnostic developments.

Heating Systems

Development of RF Driven Negative Hydrogen Ion Sources for ITER

The two test facilities at IPP, ELISE (equipped with a half-size ITER source) and BATMAN Upgrade (with the IPP prototype source), both using RF driven ion sources, are part of the European roadmap towards the ITER NNBI (Negative ion based Neutral Beam Injection) systems. ELISE and BATMAN Upgrade were included in the Neutral Beam Test Facility working program up to the end of 2019 and are supported since then within the scope of a direct agreement between ITER and IPP via EUROfusion.

The experience gained at ELISE and BATMAN Upgrade provides valuable input for commissioning and operation of the Neutral Beam Test Facility (NBTF) in Padova, Italy. In particular, the start-up of the SPIDER test facility at NBTF in 2018 was accompanied and supported by IPP personnel. Several experimental campaigns at ELISE and BATMAN upgrade were dedicated to support SPIDER commissioning and operation. Examples are investigations on the mitigation of RF breakdowns and the operation of the RF sources without transformer.

The main aim of ELISE is to demonstrate the ITER requirements with respect to the extracted negative ion density (286 A/m^2 D^-, 329 A/m^2 H^-) at an electron-to-ion ratio below one, a source pressure of 0.3 Pa and a global beam homogeneity better than 90 % for 1 h in deuterium and 1000 s in hydrogen. In the past years, focus was on extending the plasma pulse length up to the required ITER values with high extracted negative ion currents. Only pulsed extraction is possible, 10 s extraction blips every ≈ 150 s. In the initial setup of ELISE such long high-performance pulses, related to an RF power of more than 60 kW/driver, were prevented by frequency flips of the oscillator-based RF generators and by breakdowns in the RF system. These limitations were mitigated by an improved design of the RF drivers and by changing to solid-state amplifier RF generators with a fixed frequency [1]. Replacing the RF generators, however, is a temporal solution since the solid-state generators are a loan from ASDEX Upgrade and will be returned by 2022.

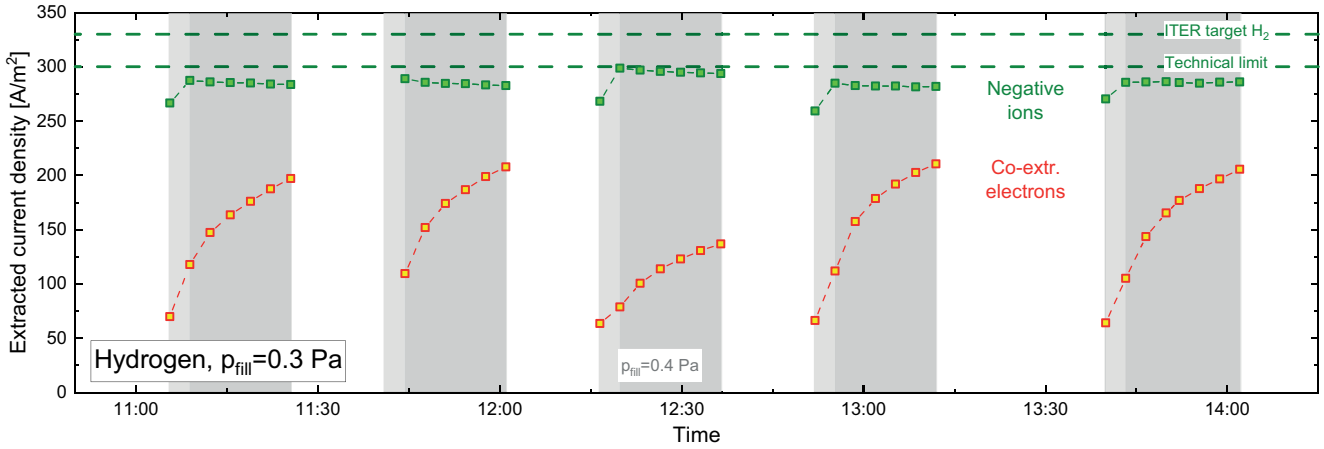

Figure 1: Extracted negative ion current density and co-extracted electron current density for a series of 1000 s hydrogen pulses done at ELISE with ITER relevant pressure (exception: the third shown pulse was done for a slightly increased pressure) and pulse length. Dashed horizontal lines indicate the ITER target value and the technical limit for the extracted current density. The grey areas indicate the plasma-on time and the symbols the average of currents measured during the 10 s extraction blips.

The applicable RF power and therefore the negative ion current density extracted and accelerated is limited mainly by the amount of co-extracted electrons, their increase in time and their vertical asymmetry, in particular in deuterium operation. A unique feature of ELISE is that the electron current can be determined individually for both extraction grid segments, enabling investigations on the top-bottom asymmetry. Additionally introduced surfaces above the plasma grid for applying electrostatic potentials in the plasma together with a new caesium conditioning procedure resulted in a distinct improvement of the vertical plasma symmetry in hydrogen. The symmetry of the co-extracted electron current is also improved and the absolute value of the co-extracted electrons as well as their temporal increase is significantly reduced. This operational mode enables achieving in hydrogen the required ITER parameters for the current density, the electron-ion ratio and the beam homogeneity for 1000 s plasma pulses with pulsed extraction [2]. The remaining difference (≈ 9 %) between the extracted ion current density and the ITER target is caused by the maximum current that can be drawn from the currently available HV power supply. Series of high-performance 1000 s pulses can be performed without the need of lengthy caesium re-conditioning phases in between (see figure 1).
The top-bottom ratio of the beam power measured at the two grid segments is better than 90 %. These results represent a significant step toward the hydrogen operational phase of ITER (up to 2035): for the first time ever a large negative ion source for NBI demonstrated hydrogen pulses with ITER relevant length and a performance that is comparable to what can be achieved during short pulses. An additional highlight is the reduction of the caesium consumption: the evaporation rates per caesium oven are below about 2.5 mg/h which is much lower than previous estimations for ITER and DEMO (up to 10 mg/h per oven).

Up to now, similar pulses are not possible in deuterium: a maximum value of ≈ 67 % of the ITER target has been achieved for long pulses, limited by a higher co-extracted electron current than in hydrogen and a much stronger temporal increase of these electrons. Dedicated experiments on the physics of this strong isotope effect demonstrated for identical operational parameters the presence of a higher atomic caesium density in deuterium, caused by a more effective caesium removal from inner surfaces of the ion source [3]. However, a negative ion density diagnostic, set-up in cooperation with the Japanese National Institute for Fusion Science (NIFS), demonstrates that for both isotopes the negative ion density close to the extraction system is comparable [4]. In order to better understand the temporal behaviour of the caesium redistribution and to be closer to the ITER operation, ELISE will be upgraded for CW extraction (up to one hour). A new HV power supply (supported by EUROfusion) is under commissioning and a new beam dump calorimeter is in fabrication.

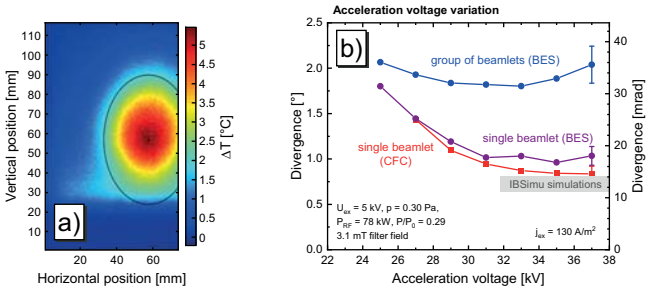

Figure 2: a) Temperature increase of a CFC calorimeter at BATMAN Upgrade caused by the impact of a single beamlet. b) Divergence versus the acceleration voltage measured for a group of beamlets using BES and for a single beamlet using BES and the CFC calorimeter. The grey bar symbolizes results of IBSimu.

The upgrade of BATMAN was finished at the end of 2017 and BATMAN Upgrade is in routine operation since 2018 [5]. The test facility is still using the prototype source but a new ITER-like extraction system similar to the one of ELISE with the aim of enabling dedicated studies of the beam optics. The diagnostic capabilities have been extended significantly, with emphasis on the optics and uniformity of the exacted beam and – for the first time – on the properties of single beamlets.

Figure 2a shows the footprint of a single beamlet (the neighboring extraction apertures were masked) at BATMAN Upgrade as seen by a 1D Carbon Fiber Composite (CFC) calorimeter. Figure 2b compares the divergence determined from this footprint with the single beamlet divergence from Beam Emission Spectroscopy (BES), the range of divergences predicted by the IBSimu beam code and the divergence of the whole beam from BES. While measured and calculated single beamlet divergences are in good agreement, the whole beam divergence is significantly larger, caused by the overlap of the beamlets composing the large beam and their zig-zag deflection due to the magnetic field needed for electron deflection [6]. This result is of great relevance for the ITER NBI system since it indicates that it should be possible to achieve the required overall beam divergence for ITER (7 mrad for the beamlet core) by additional magnets in the extraction system, compensating the zig-zag deflection.

Additionally, investigations have been started at BATMAN Upgrade – in close collaboration with NIFS and ITER – on the impact of the extraction system design on the extracted ion beamlets and the co-extracted electrons.

BATMAN Upgrade has been upgraded during the last years for CW pulses and CW beam extraction. A cryo pump was installed and a new beam dump calorimeter was developed and installed. The latter represents a prototype of the new calorimeter currently in fabrication for ELISE. These activities have been finished in 2020 and first data evaluation is in progress with still short pulses.

The research carried out at IPP is supported by a close cooperation with the AG Experimentelle Plasmaphysik (EPP), Universität Augsburg).

ITER Upper Launcher for Electron Cyclotron Waves

The grant 161/615 between Fusion for Energy and the ECHUL Consortium involving KIT (project leadership), CRPP/SPC, CNR-IFP, DIFFER and IPP ended in November 2018. Goal of the grant was the development of the design of the Upper Launcher for Electron Cyclotron (EC) waves for ITER. In this process, a constant compatibility check of engineering and physics constraints was necessary, the role of IPP being an assessment of the latter. While most of the fundamental parameters of the injected wave beams (frequency, launch angles, steering range) were fixed during earlier phases of the project, in the last phase the contributions from IPP concentrated on issues related to the beam size. The reasons for this analysis were connected both to changes in the design constraints and to the possibility to have realistic estimates of the beam broadening due scattering from turbulent density fluctuations through new theoretical and numerical tools. A good focusing of the EC beams onto the rational magnetic surfaces prone to Neoclassical Tearing Modes is essential in order to achieve efficient NTM stabilization within the allocated power. Among the various effects that can spoil the high localization of the power deposition as inferred from ray/beam-tracing calculations, the potentially most dangerous one is likely to be the scattering of the electromagnetic beam radiation from turbulent density fluctuations [7]. A detailed numerical study of the expected beam broadening was performed employing the recently developed solver for the wave kinetic equation WKBeam [8], which accounts for absorption, diffraction and can compute the statistically averaged effect of electron density fluctuations in realistic tokamak equilibria. Detailed tests of the numerical model, in order to guarantee its applicability to the ITER case, were performed, in particular through comparison with full-wave simulations. The so-called Born approximation adopted for the scattering operator was shown to be applicable for typical fluctuation levels to be expected at the ITER edge [9]. The parameters typical for ITER turbulence (particularly the radial profile of the fluctuation amplitude and the perpendicular correlation length) cannot be predicted by theory with a sufficient reliability. Based on present-day observations, edge fluctuations of the order of 20 % with a correlation length scaling as 5 to 10 times the ion gyroradius (i.e. 1-2 cm), were assumed as a reference and extensive scans were performed. The standard (ELMy H-mode) scenario was analysed. For the reference values quoted above, a beam broadening by a factor of ≈ 3 was observed for both upper and lower steering mirror and for both q=3/2 and q=2 flux surfaces [10]. NTM stabilization should still be possible within the allocated power, but depending on the marginal island size of a NTM (the size of the magnetic island below which it self-stabilizes), power modulation might become necessary. Mode-to-mode scattering (in the ITER case, ordinary-to-extraordinary mode) was found to be small for ITER parameters, i.e. at the level or below the contribution from linear mode conversion in the outer plasma or from a possible spurious polarization of the injected radiation.

Ion Cyclotron Range of Frequencies (ICRF)

A new collaboration between the ICRF group in IPP and the ITER Organization (IO) on optimizations of the ITER ICRF antenna has been started in 2020. The scope of work encompasses: a) minimization of the near-fields to minimize plasma-wall interactions; b) calculations of 3D density

distribution and assessment of gains of the effect of the local gas injection on loading of the ITER ICRF antenna represented by latest antenna geometries; c) calculations of the RF properties of the ITER ICRF antenna by the COMSOL based RAPLICASOL code; d) review of testing and operational procedures of the ITER ICRF antennas. A contract about this scope has been signed between IPP and IO in July 2020.

Diagnostics for ITER

Bolometers

The development of the ITER bolometer diagnostic continued within the areas design integration, prototyping, sensor development and performance assessment. Since 2017 the definition of many interfaces could be improved and some finalized as well as load specifications consolidated.
Following the re-assessment of radiological maps of ITER and the consequences for electronic components, the location of bolometer cubicles has been revised in agreement with ITER and F4E by moving all of them into the diagnostic building. This increases the cable length but keeps the requirement on electronics to cope with radiation to a very low level. The cabling diagrams and the estimated power consumption for cubicles have been updated accordingly.
The design of the vacuum vessel (VV) mounted cameras has been analysed in view of the need to adapt the final line-of-sigh (LOS) position to the one of the blanket modules after their alignment between the first plasma and the pre-fusion 1 operation [11]. After agreeing on the final space envelope and finalizing the interface with and cut-outs on blanket modules, the conceptual design has been amended by adding critical details for bolometer operation, e.g. electrical connections or sensor holder. The mechanical fixation of these cameras to the VV has been defined by ITER to use so-called bosses. However, the definition of acceptable loads through the cameras was provided with delay. While the thermal analysis demonstrated compatibility of the conceptual design, the estimated forces during disruptions would be too high. Accordingly, the material foreseen for the cameras has been re-assessed and now AlNi-bronze, a Cu-alloy with acceptable thermal properties but significantly lower electrical conduction compared to CuCrZr, has been chosen. Revised electro-magnetic (EM) analyses have been commissioned through F4E and shall demonstrate by a subsequent structural analysis the final feasibility of the proposed design. In support of these activities, a crucial design feature is being prototyped. Thermal interlayers are foreseen to optimize the thermal contact of the camera to the VV wall, as no active cooling will be available. Measurements on prototypes are being performed which shall identify the material best suited to cope with mechanical and thermal loads over the life-time of ITER.

The start of design activities for divertor mounted cameras revealed a clash of the foreseen space envelopes with the Cassette Toroidal Mover (CTM), a device used to install divertor cassettes. Intense discussions with all involved parties led after about 1.5 years to a revised definition of the space envelope for bolometer design, which also considers design changes of divertor structures and a revised remote-handling procedure. Based on these agreements a conceptual design for a generic divertor mounted bolometer camera could be proposed in 2020.
The interfaces of the port mounted cameras with the port plug structures have further been improved and agreed. Also, the design could be improved and details added [12]. Manufacturability of 3D-shaped ceramic printed circuit boards (3D-PCBs), in particular foreseen for mounting and electrically contacting the sensor, has been demonstrated by prototyping with three different technologies. Subsequently, tests demonstrated that all prototypes are compatible to wire bonding, capacitive discharge welding and laser welding of Cu cables. An assessment of the compatibility of large ceramic track plates to expected mechanical loads led to the decision to replace them by high-temperature cables. Based on a market survey, suitable components could be identified, procured and shielded cables successfully prototyped in the lab. The design of the sensor holder has also been revised, simplified and developed to be compatible with these internal cables.

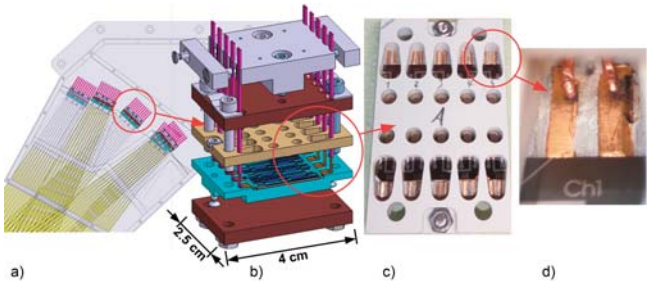

Figure 3: Design of a sensor holder for port mounted cameras (b). Several of these holders are used within one camera (a). Prototypes of front and back plate clamp the sensor, demonstrating manufacturability (c). Internal wire laser welded to the bond pad (d).

As seen in figure 3 the design features a bond pad made of Cu onto which the internal cables are laser welded and from which a wire bond connection shall be made to the sensor. Prototyping activities could demonstrate the manufacturability of the design and feasibility of laser welding within the confined space. Wire bonding could already be demonstrated on sensors outside a holder. Now it remains to demonstrate it within the holder onto the bond pad. Furthermore, a ceramic paste is foreseen to protect the thin bond wires against mechanical loads. Future testing is planned to demonstrate this. An initial thermal analysis suggested that port mounted cameras will not require active cooling.

The analysis activities continue now with a detailed assessment of EM forces during disruptions and revised thermal and nuclear analyses in cooperation with F4E. These are then the input to the structural integrity report, which is part of the input package for the preliminary design review (PDR) of port mounted cameras, planned for early 2021. The PDR of VV and divertor mounted cameras is expected to follow one year later. For all three generic locations a feasibility and manufacturability study commissioned by F4E confirmed the suitability of the proposed designs.

Sensor development successfully continues in cooperation with Fraunhofer-IMM. Since November 2017 two sensor types have been developed within a Specific Grant from F4E: Au absorbers supported by a Si_3N_4 membrane based on the previous developments done between IPP and IMM, and Au absorbers on a self-supported ZrO_2 foil based on the concept of previously used Mica bolometer foils. The latter have been developed on specific demand from F4E to broaden the available technologies and reduce risks of common mode failures for ITER. Both sensor types could be manufactured successfully. Versions of the supported membrane types are being used successfully in bolometer systems of most fusion devices. Additionally, F4E placed another contract with an external company (CSEM, Switzerland) for the manufacture of self-supported substrates to broaden the market availability. In 2019 first samples were received for testing from both suppliers and demonstrated good handling and, for supported substrates from IMM, performance during tests in the ITERBolo laboratory. The final sensor prototypes have been produced and will be delivered for testing until September 2020. For these tests, the facility IBOVAC is being upgraded to feature bonded electrical connections in the sensor holder so that reliable measurements at temperatures up to 400 °C can be acquired. Due to the pandemic discussions with industry were delayed, so that the production of critical items is expected by the end of 2020. This procurement will be financially supported by F4E.

Two ITER relevant sensors prototypes, 20 µm thick Au-absorbers supported by 3 µm Si_3N_4 membrane or placed on a Si-disc supported by flexure hinges, have been irradiated in the Budapest Neutron Centre as part of a direct collaboration. Both samples are still operational after having received a radiation dose corresponding to 0.3 dpa in Si_3N_4 [13]. This is higher than the ITER requirement of 0.1 dpa. Final irradiation tests are now planned with F4E featuring online measurements to fully demonstrate their successful operation under irradiation.

The operation of bolometer sensors under varying thermal environments requires a closer look into the temperature dependence of calibration parameters. A procedure could be defined which extrapolates their actual value for measurement evaluations in case the bridge current is measured in addition to the bridge voltage [14]. As shown in figure 4 for the heat capacity, it varies over measurement time similarly as the temperature at the sensor. However, the actual value can be reproduced based on the calibration at the start of the measurement and the measured bridge current as indicator for the actual temperature.

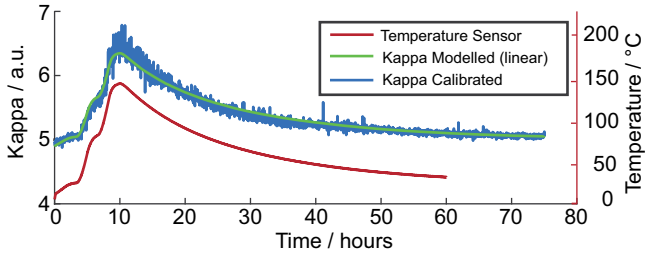

Figure 4: Heat capacity of a bolometer sensor over measurement time varying according to the temperature. Using the calibration at the start of the measurement, the temperature dependent value can be extrapolated using the bridge current measurement.

Until end of 2019 F4E and ITER agreed on a set of requirements which were the basis for the technical part of the Procurement Agreement for the ITER bolometer diagnostic, signed in March 2020. These requirements are now being assessed and flown down onto sub-systems. Implementation into the design and their verification in view of the upcoming PDRs is ongoing. The reliability analysis in close collaboration with F4E revealed that electrical connections are the most critical items to secure the high availability of the diagnostic (99.9 % required). Furthermore, IPP's proposal for the definition of observation areas in the plasma has been accepted and agreed. An assessment of estimated signal intensities for all LOS led to an optimisation of their distribution and demonstrated that most channels will receive signals well above the expected noise level [15]. However, those LOS observing mainly the plasma edge and the upper plasma region will be critical and need further improvements.

Diagnostic Neutral Pressure Gauges (DPG)

IPP's neutral gas laboratory has been upgraded in 2017 with financial support from F4E through the framework contact on the development of the ITER neutral pressure gauges. An advanced control system allowing monitoring and control parameters of the pressure gauges and test stand including vacuum system, magnet, gas-flow system etc. has been implemented and tested. The magnet was commissioned and calibrated up to 2 T using a pick-up coil and a commercial gauss meter. The extrapolated maximum field at a current of 4000 A, corresponding to the magnet's technical limit, is 7.9 T. An additional vacuum facility for performing long term tests of various filament samples has been developed and assembled.

The test campaign began with long-term emission tests of filament samples made of five different materials. After more than 1500 hours of continuous operation at pressures below 10^{-5} Pa the filament sample made of W-Re alloy and coated with yttrium oxide required the lowest heating current of about 15 A to keep the electron emission current constant at 300 µA [16]. A mechanical rupture and deformation test of this filament demonstrated that under applied magnetic fields in the range from 1 T to 7.9 T neither elastic nor plastic deformations occur [16]. Based on results of these tests it was decided to update the baseline design of the DPG head to use this filament type and to perform all subsequent tests with it.

The upper pressure limit of the DPG prototype has been tested in hydrogen gas for the pressure range from 10^{-2} Pa to 30 Pa for magnetic flux densities from 1 T to 7.9 T. Variations of electron emission current, electrode potentials and acceleration grid transparency (see figure 5) led to the conclusion that no parameter set demonstrates absolutely superior performance and thus, the reference configuration defined earlier is suited to fulfil the upper pressure limit of 20 Pa [17].

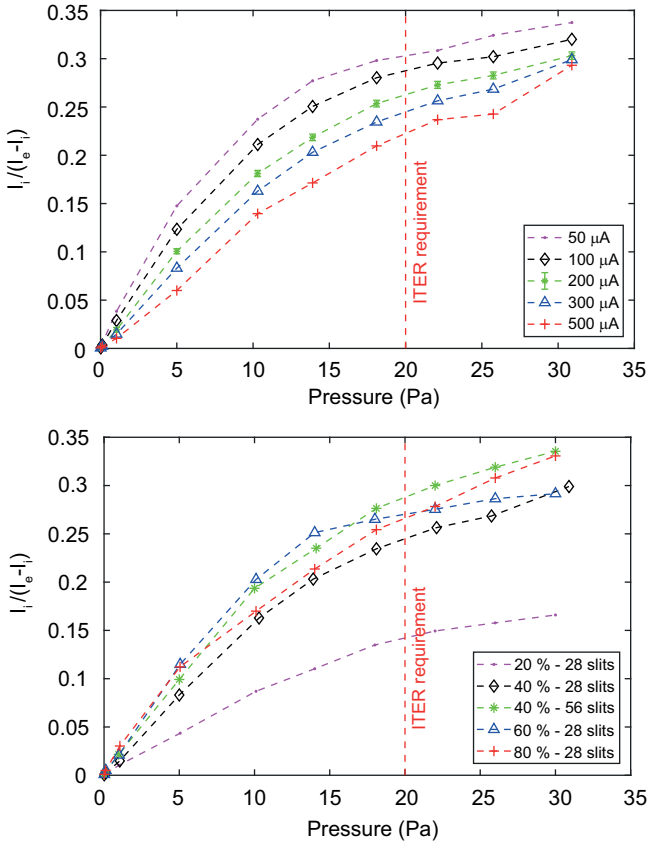

Figure 5: Calculated normalized gauge output $I_i/(I_e-I_i)$ as function of the H_2 gas pressure for B=7.9 T and the baseline bias configuration under variation of electron emission current (left) and transparency of acceleration grid (right). Legend of right graph shows the transparencies in % and number of slits, respectively.

Besides that, it was demonstrated that thermocouple measurements taken either at the acceleration grid or at the base plate are meaningful to correct for measurement errors induced through temperature variations. It should be noted that already after the first set of measurements the filament coating broke into small flakes and delaminated partially, especially at the hottest parts in the centre of the filament, while the gauge prototype was able to operate stably. Tests in lower pressure ranges revealed that the registered ion current at 10^{-4} Pa for a prescribed electron current of 300 µA is in the range of 1 nA and thus, it was recommended to increase the prescribed electron current for pressures below 10^{-3} Pa in order to improve the signal to noise ratio.

Long-term reproducibility tests of the same DPG prototype demonstrated a statistical scattering of pressure readings between 4 % and 22 % within a range of 10^{-2} Pa to 30 Pa in hydrogen gas. The assessment of the overall gauge accuracy showed that the measurement accuracy of 20 % required for operation in ITER cannot be met. It was assumed that the situation could be improved if the issue with the delamination of the filament coating will be solved. As a first step, it was proposed to test filaments with reduced thickness of yttrium oxide coating. Long-term emission tests and testing in hydrogen performed for such filament samples showed no coating degradation although thinner coatings require higher temperatures and, thus, higher heating currents for the required electron emission. Nonetheless, the recommendation is to use thinner coatings in future to avoid the peeling effect.

Creep tests have been conducted for four spiral filaments made of W-Re and W-K alloys [18]. The latter samples demonstrated in general a much better resistance against creep. However, due to the high electrical conductivity, W-K filaments have to be heated with high currents, which is an obvious drawback. Although the loads applied to the filament during creep tests are similar to the real j×B forces, the latter are not represented exactly. Thus, to be on the safe side, it was recommended to increase the safety margins for the next prototyping phase.

To validate the reliability of prototypes during repeated on/off cycles at magnetic fields up to 8 T, 12 simplified DPG prototypes with W-Re filaments were subjected to 3000 on/off cycles in the superconducting magnet JUMBO of KIT [18]. The outcome demonstrated that fatigue is not a problem, neither for filament nor for brazing. Accordingly, pressure gauges equipped with filaments identical to the tested ones will survive the required operational cycles in ITER.

To complete this DPG head test camping, 6 filaments made of different materials and one DPG prototype have successfully been exposed to several cycles of hot steam of water, proving that filaments remain operational after water leaks in case there is no heating current.

The subsequent prototype testing aimed to overcome the remaining issues with creep and coating of the filaments by

further optimizing the tungsten filament as well as by investigating several alternative concepts of the electron emitter. The LaB_6 coating of the filament demonstrated a better emission stability in comparison to the yttrium oxide coating within pressure ranges from 0.3 Pa up to 30 Pa. Creep tests of filaments with a planar shape of a filament sample made from W-K (figure 6a) demonstrated much better stability against creep; it was just marginally deformed after more than 1500 hours of continuous operation, whereas the W-Re sample failed already after 100 hours under a relevant load.

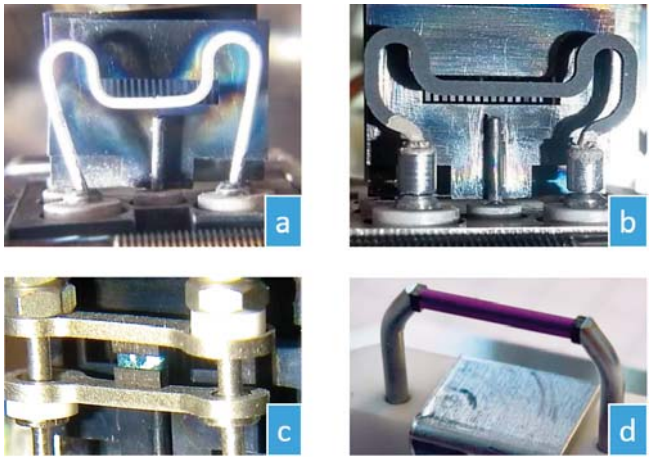

Figure 6: Variants of electron emitters for DPG under investigation: a) meander filament, b) carbon emitter, c) indirectly heated cathode with "sandwich" design, d) LaB_6 crystal emitter.

A LaB_6 crystal emitter developed at IPP-Greifswald (figure 6d) has been irradiation tested at Wigner Research Center for Physics in Hungary. After the test the emitter assembly keeps its integrity. Detailed assessments of electrical properties will be investigated in the hot-cell once the prototype is cooled down.

A DPG prototype with indirectly heated emitter of electrons, the so-called „sandwich" design (figure 6c), which is similar to the design of the crystal emitter, demonstrated stable operation in various hydrogen pressures with heating currents lower than 2.5 A. Based on already available experimental results, improvements of the design have been proposed and will be implemented in the upcoming design phase. An emitter made of graphite and coated with yttrium oxide (figure 6b) also demonstrated good measurement performance. Creep tests and repeated start-ups in hydrogen are ongoing.

Based on the results of the previous System Level Design phase, an integrated electronics system for the DPGs operation has been developed and tested together with prototypes of the DPG head at IPP's neutral gas laboratory. The length of the used signal cables was 200 m, which corresponds to the maximum cable length in ITER. To avoid oscillations on the electron current signal, the grounding scheme has been optimized.

The prototype of DPG electronics has also been tested successfully at ASDEX Upgrade. The system was powered up and kept ready for operation during 11 days while data was recorded on 5 experimental days and covered in total 9 discharges. During this test period, the DPG electronics were able to completely fulfil their function. Additionally, a stable operation of DPG electronics was demonstrated under temperature variations inside the cubicle between 17 °C and 27 °C. Finally, EMC and EMI compatibility tests were performed successfully, too. During burst pulses, the output signal was disturbed but afterwards the system returned to normal operation with no permanent defects.

In parallel with prototyping activities, IPP's DPG design team has prepared the data package for the Preliminary Design Review (PDR). Overall more than 20 documents concerning the documentation of diagnostic design, on-site assembly and testing, operations and maintenance etc., as well as CAD models and drawings of gauge heads and electronics have been prepared and submitted for the review. The diagnostic design and the data package have been presented to the panel and discussed at the PDR kick-off meeting. Overall, 54 chits have been raised initially but after closure and merging of some chits at the PDR final meeting only 37 remain open. As agreed with F4E, category 1 chits will be closed when IPP will integrate the required actions in its work plan. These planning activities are ongoing. The current strategy is to define only one suitable option for DPG cathode until the end of 2020, update the base line design of gauge head and electronics and to complete the validation of the design before the Final Design Review (FDR) of the diagnostic, which is planned for 2022.

CODAC

Development of the ITER Plasma Control System (PCS) Final Design for 1st Plasma

Responding successfully to a call for tender in 2017 IPP has lead the consortium with the partners CREATE/Univ. di Napoli (I), CCFE (UK) and CEA (F), and subcontractors General Atomics (US) and Critiware (I) to assist the ITER team in the preparation of the Final Design of the Plasma Control System (PCS) for ITER 1st plasma operation. The activity included

- to design the ITER PCS architecture and exception handling
- to develop and assess control algorithms for First Plasma Operation
- to provide models and simulation capabilities
- to define pulse schedule and editor functionality and schedule validation requirements
- to plan model validation, PCS and Integrated Commissioning steps, and First Plasma Operation activities
- to describe the architecture, controllers and the First Plasma Operations aspects in a Control Database
- to prepare and participate in the PCS Final Design Review

The goal of the first plasma operation is to carry out all required steps for integrated commissioning of initial plant systems, diagnostics and PCS and culminates in the use of these systems to create a small plasma with moderate key parameters between 100 ms and few seconds pulse duration and currents between 100 kA and <1 MA. However, designing that restricted PCS functionality was extremely challenging considering the immediate need to also develop and demonstrate a comprehensive and consistent methodology for many complex and connected aspects: to define and describe the plasma characteristics, pulse scenarios, plasma control and exception handling requirements and features, diagnostics and actuator plant system specifics, system interfaces and interactions, operation and commissioning procedures, validation and verification processes, and to document all that in a control database, and finally demonstrate the prototype solutions in the IO Plasma Control System Simulation Platform (PCSSP) environment. The task was completed within three years, with an initial nine months "Rapid Prototyping", to converge on principles and base methods, followed by a two years phase to broaden and deepen the coverage and develop complex methods for exception handling, simulation and performance assessment. The FDR in July 2020 was passed successfully, with no significant obstacles for the final approval of the design. However, a number of useful recommendations have been given how to further improve several aspects of the system to ease the implementation and upgrading.

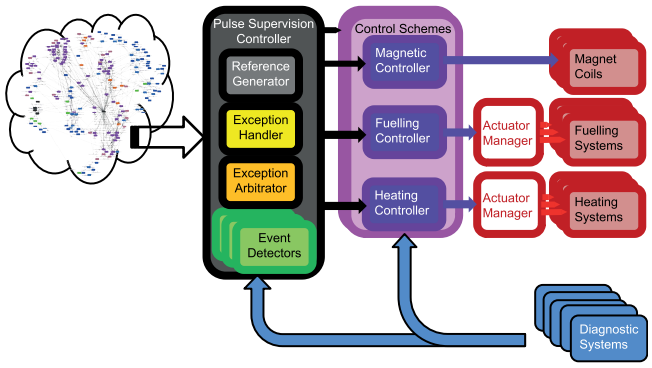

Figure 7: Control functions of the ITER PCS and their breakdown as presented for the PDR of the first plasma PCS.

Within the design team IPP had been responsible for the development of a PCS architecture ready to support the full ITER Operations lifecycle, for the definition of an exception handling strategy which enables PCS to act as first line-of-defence within the ITER machine protection hierarchy, and for the identification of the required pulse schedule elements and editing functions to configure and operate PCS with a complete set of information to steer the plasma through the envisaged plasma scenarios. The review panel found the proposed structures comprehensive and convincing and suiting the needs of ITER to operate reliably as well as to provide the required flexibility for future upgrades according to the staged experiment plan. To develop the architecture the IPP team collected initial requirements and use-cases from the experiment plan and identified about 190 high-level control functions with a complex interdependency (figure 7 left). The architecture design activity categorized these functions and their connections into a clear breakdown with the required potential of scalability and extensibility for future functions (figure 7 right).

Key features of this architecture are highly configurable and re-usable components such as the Compact Controllers (CC) for all continuous feedback operations, and a combination of distributed exception handling for quick interventions and centralized global exception handling according to the strategies laid down in the Pulse Schedule. For this reason, the global exception handling is integrated in a central Pulse Schedule interpreter, the Pulse Supervision Controller (PSC) that produces all reference waveforms to steer the continuous control. Both key modules, PSC and CC, have been developed as function blocks of the PCSSP simulation platform.

Complementing this design, PCS requirements for a Pulse Schedule structure and a Pulse Schedule editor have been derived. A straw man PCS Pulse Schedule satisfying these requirements has been developed and is, together with the PCS architectural model and its functional blocks, used in a complete simulation model of the ITER PCS and the ITER plant on base of the PCSSP.

This design will form the fundament for the implementation of ITER PCS on base of the Real-Time Framework (RTF).

Test of the ITER PCS Real-Time Framework (RTF) and CompactController (CC)

While the design of the required PCS functionality is being finalized, the ITER CODAC division is developing the technology needed to implement PCS hardware and software. To execute a pulse, PCS must connect to a great number of diagnostics and actuator plant systems, to orchestrate the plant operation and to control and monitor plasma and technical quantities. The required low-latency real-time data exchange and control process management functionality is provided by a distributed component, the Real Time Framework (RTF). Having participated in the RTF requirements definition and system design, IPP was chosen to assist IO to demonstrate the combination of the first RTF version with a complex key PCS functionality, the Compact Controller (CC). Being a highly generic functional block, each CC instance can be individually configured to provide a choice of real-time control functionality to manage control mode transitions, select process input data, execute control laws, limit the command output and to handle exceptions. IPP plans together with its subcontractor Cosylab (SLO) to demonstrate a functional prototype in PCSSP until the FDR in late 2020.

Theory

Halo Currents

The JOREK-STARWALL non-linear free boundary MHD code for realistic divertor tokamak geometries was completed using Green's functions methods for efficiently addressing disruptions and VDEs including eddy and halo currents in 3D conducting structures. For this purpose, active and passive coils were implemented self-consistently, STARWALL and the coupling between both codes was parallelized (with support from the EUROfusion HLST) and optimized for simulations with many toroidal harmonics. Several approaches for extending to Halo currents were tested (together with C.V. Atanasiu, Romania). The most efficient numerical scheme for this purpose was selected, implemented, validated against analytical solutions, and benchmarked against another code. To guarantee continuity of the halo currents from one domain into the other, a numerical solution for determining the mapping of the degrees of freedom between the two codes was developed, implemented, and validated. First studies of VDEs together with a fluid model for runaway electrons developed at IPP were made to investigate the effects onto the 2D and 3D dynamics of the plasma [19]. Based on the described developments, an international benchmark for 2D VDEs was carried out [20] confirming that the plasma dynamics as well as the eddy and halo currents in such a scenario are described correctly in JOREK-STARWALL (in the limit of a low wall conductivity for halo currents). The joint work on this topic between IPP and the ITER Organisation is presently taking place without a formal contract. Based on a 2D NSTX case, a 3D benchmark between JOREK-STARWALL, NIMROD and M3D-C1 is ongoing, to which IPP is contributing. The agreement is very good on plasma dynamics and forces in spite of the different numerical representations for plasma, vacuum and conducting structures. Further model developments, experimental validation, and predictive simulations for ITER are performed in collaboration with the ITER Organisation.

Runaway Currents in ITER Disruptions

Possible generation of a large runaway electron current during disruptions is an outstanding safety issue for the ITER project. IPP contributes to the development of runaway electron models, their benchmarking and experimental validation. Within the scope of a service contract (IO/CT/4300001355 (2017)) IPP has provided an assessment of runaway seed generation and its suppression by disruption mitigation in ITER. Relevant current quench parameters for a range of impurity densities injected prior to the quench were calculated. It was found that for the ITER Q=10 baseline scenario the use of neon as a mitigation gas offers a broad and safe operational window. In the density range 10^{19}-10^{20} m^{-3} it provides current quench times consistent with ITER disruption constraints. It was also found that the seed current associated with the decay of tritium ensures the formation of a-few-MA runaway beam with any amount of injected impurities, therefore posing a significant issue for the ITER D-T operation phase.

Runaway electrons form particularly easily when the electron distribution function has a high-energy tail. This process has been modelled using a kinetic model that self-consistently treats the energy balance during the thermal quench [21]. Important and non-trivial features being related to the radial profile of the runaway electrons were identified. It was found that the formation of a large runaway electron current is almost always associated with a peaking of the current profile. It was also found that deuterium admixture is an effective tool, which allows the current quench length to be decoupled from the parameters of the thermal quench.

This theoretical model has been validated in experiments on DIII-D [22], [23], where novel spatial, temporal, and energetically resolved measurements of bremsstrahlung hard-x-ray (HXR) emission from runaway electron populations revealed non-monotonic runaway electron distribution functions, whose properties depend on the interplay of electric field acceleration with collisional and synchrotron damping. Figure 8 shows a comparison between the RE distribution function predicted with the modeling and the one obtained experimentally.

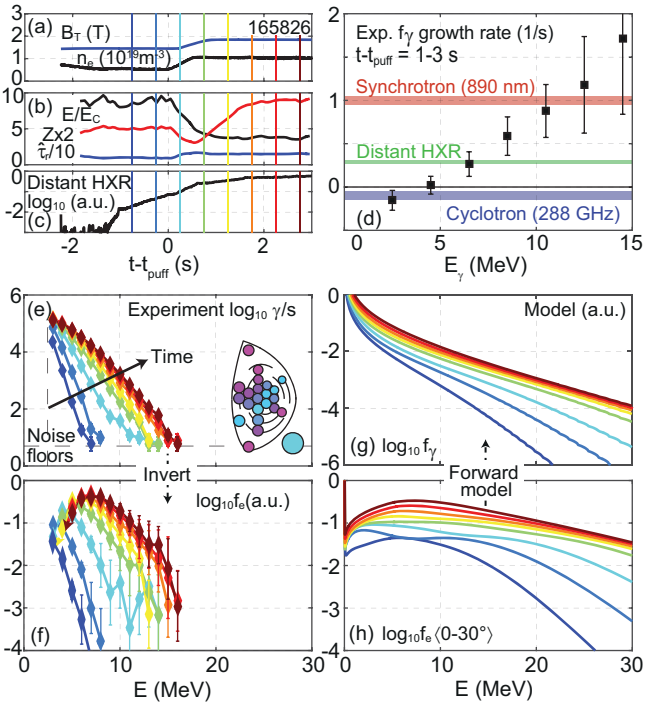

Figure 8: Comparison of the modelled runaway electron distribution function (h) and the corresponding emitted gamma-ray spectrum (g), with the experimentally measured gamma-ray spectrum (e) and the distribution function reconstructed from this measurement (f). Different time slices are represented by different colours.

Most of the progress in the area of runaway electron research over the past two decades was summarized in a review paper [24], written in collaboration with the experts from the ITER Organization, the University of Texas in Austin, and the DIII-D team (General Atomics, San Diego).

Alpha Particles Physics

The physics of fusion-born alpha particles is one of the topics that for the first time will be explored in full detail on ITER. The understanding and the prediction of various elements of this complex self-organisation problem is the topic of a direct cooperation with ITER. Weakly damped Alfvén eigenmodes (AEs) are known to deplete the fast ion confinement in the regions of steep α-particle pressure gradients and thus change the self-heating profile. Due to the large parameter space of various operational scenarios it is necessary to survey the time-dependent equilibrium and profile evolution as given by different transport codes in a systematic albeit computationally efficient way. To this end, two codes mainly developed at IPP Garching, LIGKA and HAGIS, were ported into the ITER IMAS framework. LIGKA calculates the linear stability properties with various hierarchically nested kinetic models of different accuracy and speed. HAGIS provides the non-linearly saturated amplitudes based on the linear LIGKA information. Time dependent workflows have been established that automatically trace the properties of various types of Alfvénic modes. Both input and output rely on standard data structure formats. A representative result is shown in figure 9.

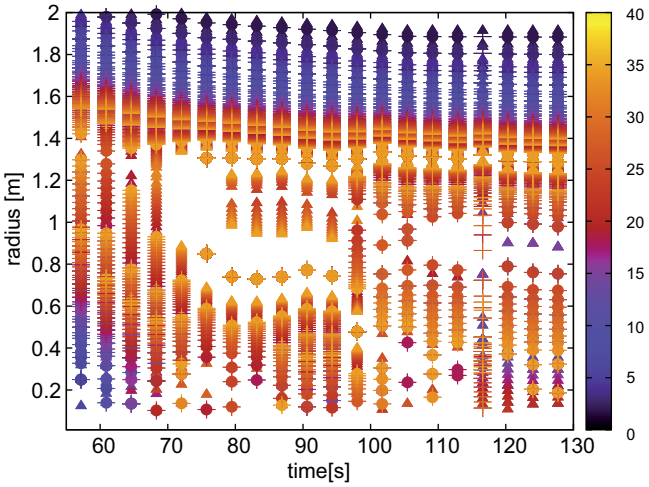

Figure 9: Time evolution of the radial location for various Alfvén eigenmodes (AEs) for an ITER pre-fusion H plasma based on a METIS transport code simulation [ITER database]. Five different bands, i.e. BAEs at ~30 kHz, (circles), even/odd TAEs at 60-80 kHz (triangles) and even/odd EAEs at 110-160 kHz were traced. The color indicates the toroidal mode numbers, ranging from 1 up to 35. One can observe the sensitivity of the AE spectrum with respect to the scenario evolution, in particular the q surface that crosses q=1 at t=75 s. Regions with scarce resonant AE surface in the steep fast ion gradient region (minor radius of 0.9 m – 1.4 m) can be observed.

One can see the strong sensitivity of the AEs during the current and pressure ramp up before t<100 s. Especially the appearance of the q=1 surface at t~75 s significantly changes the AE locations, the toroidal mode number spectrum and the expected type of resonance overlap. Also, it demonstrates the attractiveness of hybrid scenarios with q≳1 (just before t=75 s) that lack any AE resonances in the mid-core region where the strongest fast-ion gradients are expected in burning ITER plasmas.

Scientific Staff

Alpha particles: Ph. Lauber, V.-A. Popa (Master student, TUM), Th. Hayward-Schneider.
ECHUL: C. Angioni, F. Casson, O. Maj, E. Poli, A. Snicker, H. Weber.
Halo currents: M. Hölzl, K. Lackner, E. Strumberger.
ICRF: V. Bobkov, H. Faugel, R. Ochoukov, W. Tierens, M. Usoltceva, W. Zhang.
ITERBolo: H. Eixenberger, B. Glasauer, J. Hare, D. Hermann, N. Jaksic, A. Kampke, M. Majewski, H. Meister, E. Neitzert, A. Pataki, F. Penzel, A. Seiler; M. Mitulla, S. Schmitt (IMM).
ITER-CODAC: W. Treutterer, I. Gomez, O. Kudlacek, F. Janky, B. Sieglin, G. Raupp; P. De Vries, J, Snipes, L. Zabeo, D. Karkinsky (IO); G. Ambrosino, M. Cinque, G. De Tommasi (CREATE); S. Bremond, P. Moreau, R. Nouailletas (CEA); F. Rimini (CCFE); D. Humphreys, M. Walker, B. Sammuli (GA).
ITER-DPG: A. Arkhipov, H. Eixenberger, B. Glasauer, J. Hare, N. Jaksic, J. Koll, F. Mackel, H. Meister, E. Neitzert, A. Seiler.
NNBI: F. Bonomo, S. Briefi, S. Cristofaro, U. Fantz, M. Fröschle, N. den Harder, A. Heiler, B. Heinemann, R. A. Hurlbatt, W. Kraus, I. Mario, F. Merk, A. Mimo, M. Montellano Duran, R. Nocentini, G. Orozco, R. Riedl, G. Starnella, L. Schiesko, C. Wimmer, D. Wünderlich, D. Zielke.
Runaways: P. Aleynikov.

DEMO

DEMO Design Activities

Head: Prof. Dr. Hartmut Zohm

The 'DEMO Design Activities' project focuses on aspects of physics and technology relevant for tokamak and stellarator designs, in line with the unique position of IPP following both lines. Many of the activities are carried out under the EUROfusion PPP&T Programme, where substantial EU collaborations exist. On the national level, the German DEMO Working Group, chaired by IPP, joining scientists from FZJ, IPP and KIT serves to strengthen collaboration and strategic planning.

DEMO Technology Studies

IPP contributes to the EU DEMO technology studies in several areas of expertise, most prominently the divertor targets, the Heating and Current Drive (H&CD) systems, and the control system and its sensors and actuators. Also the possible impact of promising emerging technologies is studied, such as the use of supercapacitors as energy storage or high temperature super conductors (HTSC) for high field devices.

In the area of H&CD, different aspects of all three candidate systems for EU DEMO, namely ECRH, ICRH and NBI, are studied. For ECRH, analysis focused on the question if ECRH alone could be sufficient for DEMO. This question does not arise for the other systems, since there are tasks such as breakdown and NTM stabilisation that can only be fulfilled by ECRH. First studies using the time dependent DEMO 'flight simulator' (see also below) indicate that a possible obstacle is the decoupling of electrons and ions leading to low ion temperatures, as observed in experiments in ASDEX Upgrade and W7-X (see section "Joint Research Projects on ASDEX Upgrade and Wendelstein 7-X"), which could prohibit access to burn. Applying transport models verified on ASDEX Upgrade indicates that at sufficient density, the fusion power is enough to bootstrap itself into the high ion temperature regime, but it is not yet clear if this result is robust enough to rely on ECRH only.

Studies of an ICRH antenna for DEMO, which is predicted to supply substantial ion heating, with some of the scenarios in the 3-ion scheme (see section "ASDEX Upgrade"), focused on an in-port antenna. Building on the experience of ASDEX Upgrade operation and the ITER design, a 4-strap antenna, as is planned for ITER, was optimised to fit into a DEMO port. Operation is foreseen in $0\pi\pi0$ phasing, i.e. effectively in the ASDEX Upgrade 3-strap configuration to minimise impurity production.

Concerning the DEMO NBI system studies focus on an increase of the overall efficiency of the system by studying different alternatives for the neutralisation of the accelerated particles, namely photo detachment in a laser cavity and plasma neutralisation. Both concepts are in an exploratory phase at present. Moreover, a conceptual study of energy recovery from the residual ions showed that up to 95 % of the residual ion energy could in principle be recovered, with the upper limit given by particles escaping the geometry at too low residual energy.

IPP leads the EUROfusion work package WPDIV (DEMO divertor), and in the course of the development of DEMO divertor targets, several W monoblock designs were tested in the IPP high heat flux test stand GLADIS. The results were very encouraging, with all 4 candidate designs meeting the requirements of surviving at least 500 pulses at 20 MW/m^2. A variant similar to the ITER design was chosen due to its design simplicity, but a risk mitigation option is kept in the form of the fibre re-inforced design variant by IPP, since it is at present not clear how the mechanical properties of these components will change under the intense n-irradiation in DEMO. Figure1 shows infrared thermography pictures of these two variants in the 1st and the 500th cycle of the test.

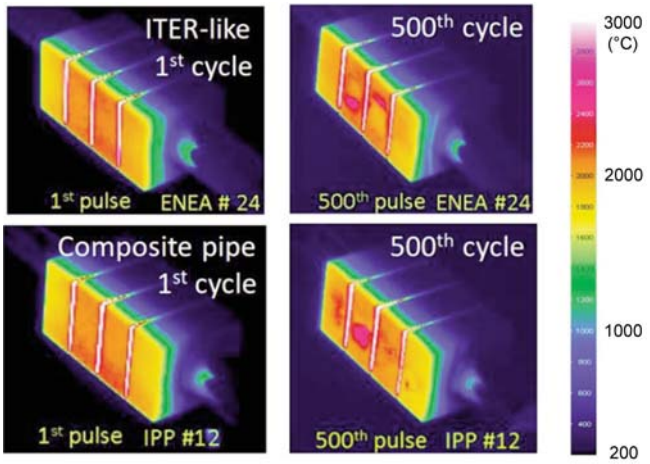

Figure 1: Test of DEMO divertor targets in GLADIS: both variants (the default ITER-like concept, upper row, as well as the risk mitigation design, lower row) survived 500 cycles at the nominal value of 20 MW/m^2.

Studies on a Stellarator Fusion Power Plant (FPP)

Studies continued on how the stellarator concept can be introduced into the development of future FPPs. In previous work (SR2015), the physics module of the tokamak systems code PROCESS had been adapted to account for a simplified stellarator plasma. More recently, further constraints on the technology side, such as stress on components or space restrictions between coils and blanket, have been reduced in dimensionality by calculating effective parameters that can be dealt with by PROCESS. PROCESS' modules were further generalised to model any kind of stellarator, directly from the output of stellarator optimisation (optimised coil filaments and plasma boundary). This makes it possible to use PROCESS to map out the configuration space of various future stellarator power plants, to include technological constraints, to compare different stellarator types, and to assess the impact of new technologies, such as e.g. HTSC.

Figure 2 shows, as an example, the configuration space for a HELIAS-5 type configuration with conventional coil technology, taking into account the different constraints from the plasma and technology side. With the generalised models, these studies can be done for any class of stellarator, taking advantage of the vast design space.

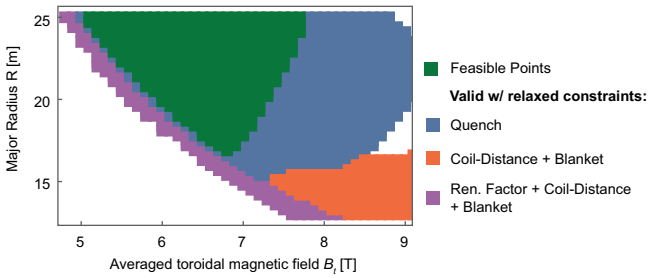

Figure 2: Results of a multi-disciplinary-stellarator design optimisation of the HELIAS-5 family employing conventional (Nb_3Sn) coil technology using PROCESS (1 GW net electricity output). The different plasma physics and technology limitations indicated in the figure lead to a restricted valid design space in the B_t-R plane (green area).

Another important question studied in this area is to what extent the stellarator power plant technology development can benefit from the R&D done for the tokamak line in the EUROfusion programme. An analysis of this question points out that in the majority of the EUROfusion work packages, the additional stellarator-specific work required for the fundamental technology R&D is of the order of 20-40 % of the effort done for the tokamak or lower, while critical areas are in the specific design, namely the plant level systems engineering, the remote maintenance and the magnet design. Currently, a strategy is developed to address these issues, but is dependent on the available resources from EUROfusion in the next Framework Programme.

Plasma Scenarios for a Tokamak DEMO

Concerning the development of a tokamak operational scenario for DEMO, work proceeds in parallel in the area of improving physics models in the time dependent transport code ASTRA, and its application to modelling specific scenarios. Moreover, ASTRA is used within the 'flight simulator' FENIX that mimicks a full feedback control system and can be used to constrain the requirements for the DEMO sensors (diagnostics) and actuators (magnets, H&CD and fueling systems).
Concerning the physics models, recent additions to ASTRA include a multi-chamber model for the SOL and the divertor that is used to study more realistically also the dynamic particle balance in DEMO. An important result of these studies was the finding that, assuming a finite divertor compression for impurities used to increase radiative losses from SOL and divertor, the concomitant core contamination can be prohibitive for solutions at large R and lower B_t. This effect had not been found previously since systems codes usually assumed infinite divertor compression. Another important study addressed the loss of performance expected from the application of ELM-free regimes such as QH- and I-mode, where the latter was found to need an increased device size, albeit using simplified assumptions about the pedestal structure in these scenarios. It will be important to obtain a better understanding of these in present day devices (see also section "ASDEX Upgrade").

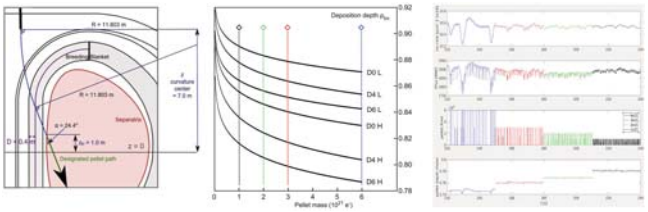

Figure 3: Example for a model based actuator design: a variation of pellet injection geometry (left) yields the deposition width (middle) which is parametrised and fed into the FENIX flight simulator (right) that determines the achievable density control as function of pellet size.

Finally, figure 3 shows an example of an integrated actuator design for the fueling using pellets. From a variation of pellet injection paths, cutting into the blanket with different width D (left part, 0.0 m, 0.4 m, 0.6 m) one can determine the pellet penetration as function of the pellet size (middle part) and apply these values to a density feedback control simulation in FENIX (right part, pellet sizes correspond to those marked by colored diamonds in the middle graph). Varying the pellet size and injection frequency to keep the density constant, it can be found that smaller, high frequency pellets lead to much reduced excursions of the density (uppermost trace on the right) and fusion power (second trace on the right) when the finite success rate of pellet injection is taken into account by randomly suppressing a fraction of pellets to be injected. These studies are also used to minimise the D-T throughput for given plasma density to be achieved.

Scientific Staff

C. Angioni, C. Beidler, M. Beurskens, V. Bobkov, K.-J. Brunner, A. Dinklage, E. Fable, U. Fantz, H. Faugel, S. Fietz, G. Fuchert, L. Giannone, H. Greuner, C. Hopf, F. Janky, F. Jenko, A. Kallenbach, O. Kudlacek, P. Lang, J. Lion, A. Magnanimo, M. Maraschek, A. von Müller, N. Nemati, R. Neu, R. Ochoukov, F. Palermo, G. Pautasso, B. Plöckl, E. Poli, R. Schramm, M. Siccinio, B. Sieglin, J. Stober, G. Suarez-Lopez, G. Tardini, W. Tierens, W. Treutterer, M. Usoltceva, F. Warmer, R. Wolf, J.-H. You, K. Zhang, H. Zohm.

Plasma-Wall Interactions and Materials

Plasma-facing Materials and Components

Head: Prof. Dr. Rudolf Neu

Within the project "Plasma-Wall Interaction" the areas of plasma-surface-interaction studies, material modification under plasma exposure, development of new plasma-facing materials and their characterisation have been merged to form a field of competence at IPP. The work supports exploration and further development of the fusion devices at IPP and also generates basic expertise with regard to PFC-related questions in ITER, DEMO and future fusion reactors.

Surface Processes on Plasma-Exposed Materials

New High Current Source "SIESTA" for Materials Research

The former IPP High Current Ion Source for investigation of Plasma-Surface-Interaction processes, which was the basic instrument for about 200 Publications during the last 40 years, was decommissioned in the end of 2015. During this time, it was dominantly used to measure erosion processes und retention of hydrogen in fusion-relevant materials. The construction of the follow-up experiment was started at another site a bit earlier. The concept of the new device follows closely the former one, but includes some improvements.

The first plasma in SIESTA (Second Ion Experiment for Sputtering and TDS Analysis) was ignited in February 2016. After about 2 years of thorough characterisation and optimisation SIESTA was ready for routine operation at the end of 2018. Thanks to the installation of a magnetic quadrupole lens (the most significant improvement compared with the predecessor) the reachable ion current at the target is higher by about a factor of 4.

SIESTA was applied to investigate the influence of surface roughness on the sputter yield as a function of the angle of incidence. Smooth and rough Fe and W samples with roughnesses on the nm length scale were exposed to a 6 keV D_3^+ ion beam (2 keV/D) under various angles of incidence ranging from 0° to 75° with respect to the surface normal. The resulting sputter yields were compared with simulations performed with SDTrimSP (static and dynamic) and SDTrimSP-3D (static), showing good qualitative agreement in all cases, as well as agreement with literature data at normal incidence. This constitutes the first experimental benchmark of the newly developed code SDTrimSP-3D.

Sputtering of EUROFER

EUROFER is a Reduced Activation Ferritic Martensitic (RAFM) steel developed as structural material for future fusion power plants and is considered as first-wall material in recessed areas of DEMO. Recent work has shown a fluence-dependent decrease of the sputter yield for bombardment with deuterium ions in the energy range of 100 to about 500 eV. This decrease was previously attributed to preferential sputtering of the lower mass constituents in EUROFER, such as Fe and Cr, compared with the higher-mass alloying elements. This leads to an increase of the surface tungsten concentration. However, modeling with tools such as SDTrimSP with simulated W enrichment fails to reproduce the reduction in the sputter yield measured in experiments. It was also observed that, after sputtering, the samples had developed a very rough surface morphology. In this work, the combined influence of surface roughness and W surface enrichment on the sputter yield of EUROFER under bombardment with 200 eV deuterium ions was studied. After bombardment to a fluence of 10^{24} D m^{-2} (at 200 eV per deuterium) a reduction of the sputter yield to 29 %±5 % of the initial value was measured. This reduction is in good agreement with published values.

Two distinct surface morphologies, consisting of smooth and nm-spiked surfaces, were observed on the EUROFER sample after sputtering. Based on the experimental results, the combined effect of the two factors, surface roughness and W surface enrichment, is estimated to be responsible for a reduction in the sputter yield to 27 %±4 % of the initial value, which is in excellent agreement with the measured value. Our assessment shows that both surface morphology and W surface enrichment contribute significantly to the reduction of the sputter yield of EUROFER under the given experimental conditions, and are sufficient to fully explain the experimentally observed reduction in the sputter yield.

Is There a Crystal Orientation where Sputtering Corresponds to Amorphous Material?

It is commonly assumed that polycrystalline materials sputter with the same rate as amorphous material. Even though sputtering is well known to be lower in some low-index crystal directions, the assumption is that there are broad regions of crystal directions in which the sputter yield is essentially the same as in amorphous material. Therefore, a systematic study is highly desirable for characterizing properties such as sputtering over many different crystal orientations. Nowadays, these studies are far easier to achieve because of the recent developments in the electron backscatter diffraction (EBSD) technique. The new EBSD system at IPP allows measuring crystal orientations by several orders of magnitude faster than with the old system. With this system extended EBSD orientation maps of polycrystalline samples can now be measured in reasonable time.

Using experiments and molecular dynamic (MD) simulations that, independently of each other, obtain the sputter rate over thousands of individual grains, we found that the sputter rate for 30 keV Ga ions on metals changes continuously, and that there is no extended region of crystal directions that would behave like amorphous material.

Migration of Materials in Fusion Devices

Experiments with the Divertor Manipulator

The ASDEX Upgrade divertor manipulator allows insertion of plasma-facing-component (PFC) samples up to the size of two

adjacent target tiles at the outer divertor for plasma exposure and subsequent retrieval in between experiment days without breaking the vessel vacuum. Recent studies within the internal program of ASDEX Upgrade are presented in section "ASDEX Upgrade, 7.6 PWI Aspects". Additional studies in the field of plasma-material interactions focused on the investigation of the influence of prompt redeposition and of surface roughness on net erosion of plasma-facing materials. To that end customized target tiles with embedded intarsia samples were exposed to series of identical plasma discharges for a number of different plasma scenarios (L-mode, H-mode with small ELMs, H-mode with large ELMs). The intarsia samples were covered with Au and Mo marker layers (10-100 nm thick). The net erosion of the marker material was characterized by measuring the difference of pre- and post-exposure areal density by Rutherford back-scattering analysis and the erosion flux by spectroscopy in the visible spectral range. The fluence of incident plasma ions during exposure and estimates of their energy were derived from Langmuir probe measurements. The L-mode measurements confirmed the difference of net to gross erosion in the range predicted by theoretical models. Furthermore, erosion measurements of Mo layers on substrates of varying roughness confirmed qualitatively predictions based on models taking into account the dependence of the sputtering yield on the local incidence angle of projectile ions. For the H-mode exposures analysis is still ongoing.

Arcs and Dust Particles in ASDEX Upgrade

Arc traces play a significant role for the erosion of high-Z PFCs. Generated by arcs, droplets may effectively contaminate the fusion plasma. So far, essential characteristics of the droplets (diameter, velocity, and emission direction) and their interrelations are poorly known. An experimental setup able to measure in-situ diameters and velocities of individual droplets emitted from vacuum arcs was developed and successfully tested. Based on a drift tube arrangement, which combines a time-of-flight technique with the registration of light scattered by droplets, the installed technique was able to register cathode droplets with diameters larger than 0.5 µm in flight. The measured velocities reached from 10 to 120 m/s. The distribution of the number of particles with the observed peak-intensities representing the particle size follows a potential law with an exponent of about -3.74 ± 0.11. The angular distribution of emitted particles declines with the angle against the cathode surface and consists of a small-angle group ($\leq 20°$) and a group for large angles ($>20°$).

WallDYN Modelling of Impurity Migration in 3D Wall and Plasma Geometry

During interaction of the scrape off layer (SOL) plasma with the first wall the evolution of both wall and plasma are tightly coupled: The erosion of the first wall leads to an impurity concentration in the plasma which affects the particle and power balance in the plasma. In turn the impurities, when leaving the plasma via transport, can form (co-)deposits and mixed materials, far away from their initial source location. These deposits can be (re-)eroded, allowing the impurities to stepwise migrate through the fusion device until they end up at a location where the plasma at the wall is cold enough and no further erosion occurs. To describe these processes an integrated model of surface evolution and plasma transport of impurities is needed. The WallDYN code achieves this required coupling of processes by parameterising the output of surface-evolution and plasma impurity-migration codes by analytical models. For a given fixed background plasma it evolves the surface composition, derives impurity fluxes into and from the plasma and calculates the resulting impuritiy densities in the plasma. Originally, WallDYN uses the 2D trace-impurity-transport code DIVIMP for impurity transport data which limits it to 2D toroidally symmetric cases. To enable WallDYN to handle 3D wall and plasma geometries it was recently coupled to the 3D plasma solver EMC3-Eirene. As part of the coupling, EMC3 was augmented by a new kinetic impurity transport module which, in contrast to the EMC3's intrinsic fluid impurity transport model, takes into account the inertia of the impurity and thus makes it suitable also for heavy impurities such as tungsten. After benchmarking it with the 2D version of WallDYN, this new code package was then applied to the interpretation of the $^{13}CH_4$ seeding experiment performed at the end of OP1 in Wendelstein 7-X (W7-X). The coupled evolution of surface composition and impurity influx from the plasma was calculated using WallDYN yielding the ^{13}C layer deposition on the complex 3D first wall of W7-X. A comparison with first available post mortem data shows good agreement with the modelling results. Further analysis of the WallDYN results suggest that the influx of ^{13}C onto the wall leading to ^{13}C layer formation is dominated not by ^{13}C originating from the $^{13}CH_4$ seeding valve, but by ^{13}C originating from re-erosion of previously deposited ^{13}C. This shows the importance of impurity recycling and the need for integrated modelling of surface dynamics and plasma transport.

Material Erosion and Deposition in W7-X

The net erosion and deposition patterns of carbon from the Test Divertor Unit (TDU) of the stellarator W7-X were determined during the operational phases OP1.2a in the year 2017 and OP1.2b in 2018. Special target elements with marker layers consisting of about 300 nm molybdenum and 5-10 µm carbon on top were used. The thicknesses of the marker layers were determined by elastic backscattering spectrometry (EBS) using 2.5 MeV protons before and after plasma exposure. In addition, laser-induced breakdown spectroscopy (LIBS) and gas analysis after laser-induced ablation (LIA-QMS) were used on selected target elements after exposure.

The surface morphology before and after exposure was investigated with scanning electron microscopy (SEM). Massive

erosion of up to 20 µm carbon was observed at the strike line of all 10 TDUs in both campaigns. In total 48 ± 14 g carbon were eroded from the 10 TDUs during OP1.2a. The erosion was laterally non-uniform on the micro-scale. Strongly eroded surfaces were considerably smoother as compared with the original material. Only very little deposition of carbon was observed on the TDU: This means that the TDU is a strong net erosion source. According to first analyses of the erosion processes, carbon erosion at the TDU was mostly due to self-sputtering by carbon ions and to physical and chemical sputtering by oxygen ions. While OP1.2a was characterised by high concentrations of oxygen and carbon impurities in the plasmas, OP1.2b had much lower impurity concentrations due to regular boronizations and showed considerably better plasma performances with higher plasma densities.

A large number of regular wall elements and divertor baffle tiles was analysed after OP1.2b. Re-deposition of carbon in remote areas of the TDU was small, but a noticeable deposition of boron on the TDU was observed after OP1.2b. Thicker re-deposited carbon/boron layers with thicknesses of a few microns having a layered structure (carbon and oxygen in OP1.2a; carbon, boron and higher oxygen contents in OP1.2b) were found on divertor baffle tiles after OP1.2b. These tiles contained also higher H-inventories of up to 10^{22} H-atoms/m^2 due to codeposition. The nearby inner wall showed net deposition of about 100 nm thick boron/carbon layers due to the boronizations.

The global carbon balance is currently unclear. However, carbon eroded from a test divertor unit was to a significant amount not redeposited back onto the divertor targets of this TDU or other units in the divertor region, but was transported out of the divertor area, especially for OP1.2a. Some carbon was redeposited at the divertor baffles, but some was also pumped out as CO, CO_2, or CH_4. During OP1.2b, larger deposition has been found, the balance between net deposition and erosion will be investigated by further surface analysis of the target elements removed after this campaign.

Three TDU tiles coated with thin tungsten layers were exposed during OP1.2b and showed a maximum tungsten erosion of about 500 nm during the whole campaign. About 20 tungsten-coated tiles were exposed at the inner wall. The observed tungsten erosion of these tiles was negligible; instead, the tiles were covered with thin (a few 10 nm) mixed boron/carbon layers after plasma exposure.

Tritium Inventory – Understanding and Control

Deuterium Retention in MeV Self-implanted Tungsten

Recrystallized as well as single-crystal tungsten samples were irradiated with protium, deuterium, helium, silicon, iron, copper, and tungsten ions at energies between 0.3 and 20.3 MeV to two different calculated damage levels of 0.04 dpa and 0.5 dpa (= displacements per atom). In this experimental series not only the energy of the primary knock-on atoms varied by more than three orders of magnitude, but also the average peak damage rates varied by up to about three orders of magnitude. Despite this large variation the observed differences in the samples were small. For the medium- to high-mass ion irradiations, the open-volume defect structure, dislocation line density, D retention and D desorption spectra were indistinguishable. Only for the light-ion irradiations clear differences in the microstructure were observed and could be interpreted as consequence of the gaseous inclusions. However, even for those samples the differences in maximum D concentration were insignificant. This study bolsters the confidence that the displacement damage neutrons will cause will result in a similar D retention and, hence, the applicability of high rate self-ion implantation being a valid method to prepare displacement-damaged tungsten as proxy material for neutron-irradiated tungsten to study hydrogen isotope (HI) retention.

To study defect annealing, tungsten single crystals were irradiated with 200 keV hydrogen ions to 0.006 dpa to introduce mainly Frenkel pairs and then annealed at 500-1800 K. The evolution of the sizes and concentrations of the defects was studied using positron annihilation lifetime spectroscopy. Substantial vacancy mobility at 700 K resulted in their agglomeration into clusters containing 10-15 vacancies. Annealing at 800 K and above resulted in the formation of large clusters containing about 20 or more vacancies. Considerable reduction of the defect concentration likely accompanied by further coarsening of the clusters started at 1300 K and ended at 1800 K with the complete defect recovery. High temperature (1600-2100 K) annealing of defects was also studied for samples irradiated by 9 MeV self-ions to 1.1 dpa. In that case, complete removal of the defects occurred only after annealing at 2000 K. The results also suggest that D_2 gas precipitation can be substantial in large vacancy clusters (voids) formed at high temperatures.

Until recently fuel retention studies in displacement-damaged tungsten were performed in a way that first the displacement damage was created by MeV energy ion irradiation in a hydrogen free material and only afterwards HI exposure was performed by ions or plasma. However, in a future fusion environment damage creation and HI transport will take place simultaneously. In order to study the mutual influence of these two processes a different experimental approach was undertaken. Tungsten was first irradiated with 20.3 MeV tungsten to create defects within the first 2 µm. Next, these defects were decorated with a deuterium plasma at 370 K to reach a D concentration of 1.7 at.%. Then, the material was irradiated again with 20.3 MeV tungsten ions. In this last step, the newly created displacement damage takes place simultaneously with mobile deuterium being present due to the kinetic de-trapping of the previously retained deuterium. After another D decoration sequence D concentration increased to 2.8 at.%, a value beyond the saturation value that was known for initially deuterium free, displacement-damaged tungsten. Repeating the W irradiation and D decoration sequence again increased the D concentration to 3.6 %.

Rate equation modelling can describe the measured deuterium desorption with the same de-trapping energies as for the initial material, assuming only increased trap densities. Both observations together indicate that deuterium is stabilizing the defects created within the collision cascade. A newly developed model that takes the presence of D in the material during W irradiation into account was used, to extrapolate the experimental results to an even larger number of sequential W irradiation and D exposure steps. This model predicts that after many sequential irradiations a stationary state is achieved and the maximum reachable D concentration is 4.2 at.% when D is present during the irradiation for the given irradiation conditions.

Solute Diffusion of Hydrogen Isotopes in Tungsten

For the design of future fusion devices the transport and retention of hydrogen is of particular importance. Diffusion and trapping of radioactive tritium through plasma-facing materials can result in intolerable in-vessel inventories and undesired losses to the coolant. For reliable code-based predictions precise knowledge of key parameters entering the simulation is crucial – notably the diffusion and solubility constants. The data of Frauenfelder measured in the late 1960s have been assumed the most reliable and thus simulations within the fusion community have almost exclusively been based on Frauenfelder's values for protium in tungsten. Comparable data for deuterium and tritium were not available.

Given the importance of these basic quantities, a new device was designed and commissioned to derive reliable values. It uses inductive heating and allows gas loading and degassing at temperatures up to 3000 K. A diffusion model was developed, based on the diffusion equation in 3-D cylindrical geometry corresponding to the shape of the specimen to derive the four basic transport parameters from the measured data. For deuterium in tungsten an activation energy of 0.28+0.02-0.01 eV is obtained. For protium the activation energy is almost identical. This value for the hydrogen activation energy differs significantly from the previously used value of 0.39 eV. On the other hand, the data for hydrogen solubility are in good agreement with the data of Frauenfelder. Harmonic theory predicts that the ratio of the absolute values for the diffusivities of H and D should scale as the square root of the mass ratio. The new results appear compatible with that prediction. Therefore, these new result provide a solid basis for the extrapolation of the diffusivities measured for H and D to tritium.

Deuterium Retention in Tungsten Heavy Alloy

Tungsten heavy alloy can be a low-cost alternative to bulk tungsten as a plasma-facing material with favourable mechanical properties. For the commercially available alloy HPM1850 (97 wt.% W, 2 wt.% Ni, 1 wt.% Fe) a number of relevant properties have already been investigated. The section "Materials and Components" below reports about high heat flux testing of this material and its application in ASDEX Upgrade. Here we report investigations of its HI retention using deuterium.

The material consists of tungsten particles embedded in a Ni/Fe binder. These constitute two separate phases with distinctly different properties concerning the solution and transport of hydrogen isotopes: the heat of solution as well as the activation energy for diffusion are both lower in the Ni/Fe binder phase than in the tungsten particles. Therefore, one can expect that the presence of the binder phase limits the deuterium uptake. Deuterium will preferentially go into the energetically more favourable binder phase from where it can quickly diffuse out of the sample. This has been confirmed by a systematic study, where deuterium was implanted into HPM1850 and into tungsten reference samples simultaneously at temperatures up to 250 °C and with implantation fluences up to 4×10^{25} m^{-2}, which corresponds to a plasma exposure time of four full days. The retained amount was determined by nuclear reaction analysis and thermal desorption. Compared with the pure tungsten reference samples the deuterium retention in the heavy alloy decreases systematically with increasing implantation fluence and temperature. At the highest implantation temperature and fluence, the retained deuterium in the HPM1850 samples was less than 20 % of the amount retained in the tungsten reference samples. Therefore, we can say that we have identified a class of materials with an intrinsic limitation mechanism for tritium retention.

Materials and Components

Tungsten-copper Metal Matrix Composites

Tungsten-copper (W-Cu) metal matrix composites (MMCs) are currently of interest as potentially advanced materials for the heat sink of highly loaded PFCs for future fusion devices. At present, Cu alloys are regarded as most appropriate PFC heat sink materials for highly heat-loaded water-cooled PFCs. In future D-T fusion devices, however, PFCs will be exposed to high neutron doses leading to significant PFC material damage which is why the use of Cu alloys in such an environment implies issues. This is mainly due to the behaviour of Cu alloys under neutron irradiation which is characterised by a pronounced loss of ductility at lower and a loss of strength at elevated operating temperatures. Against this background, the use of W-Cu composite materials is expected to be beneficial as W reinforcements in the W-Cu MMC enhance the mechanical properties of the material. In this context, the development of W-Cu MMCs fabricated by means of Cu melt infiltration techniques was pursued at IPP Garching during recent years. The viability of such materials was ultimately assessed by means of high-heat-flux (HHF) tests that were conducted in the GLADIS facility on PFC mock-ups that comprised W-Cu MMC heat sinks. Overall, these investigations demonstrated that W-Cu MMCs can be regarded as suitable potentially advanced PFC heat-sink materials. In the nearer future, the effects of neutron irradiation on the developed W-Cu MMCs will have to be investigated in detail in order that an assessment regarding the application within a real fusion environment can be made.

Fibre-reinforced Tungsten – Mechanical Characterisation and First High-heat-flux Tests

Due to its unique property combination tungsten (W) would be the ideal material for high-heat-flux-loaded areas in a future fusion power plant. However, tungsten is brittle at room temperature and prone to operational embrittlement by overheating and/or neutron irradiation. Tungsten fibre-reinforced tungsten composites (W_f/W) utilize extrinsic mechanisms to improve the fracture toughness and thus mitigate the brittleness of W. After proofing that this idea works in principle the project has been working on providing the relevant characterisation and production routes for the development of complete mock-ups of plasma-facing components for thermomechanical characterisation and testing.

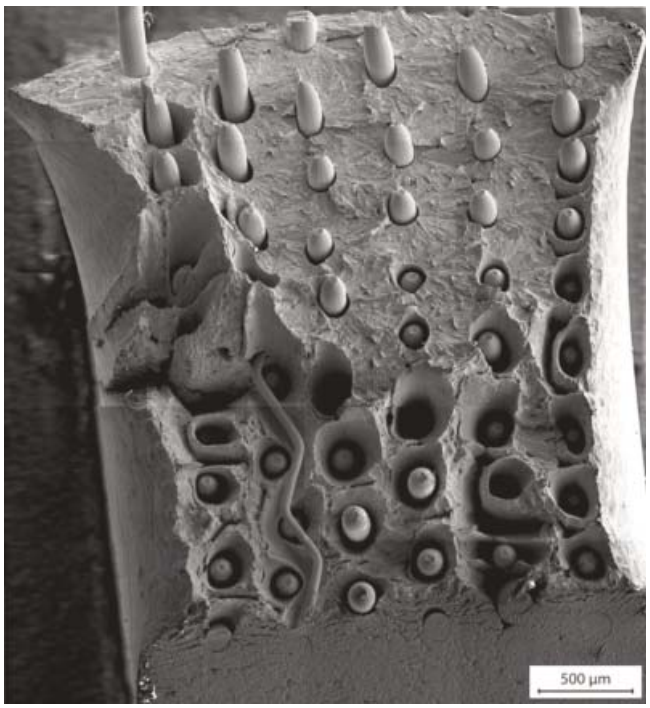

Figure: Fracture surface of a W_f/W sample after a charpy impact test at 1000 °C. Both fibres and matrix show a ductile deformation.

Three-point bending tests on as-fabricated and heat-embrittled samples were conducted to evaluate the fracture toughness of bulk samples. In both types of samples a stable crack propagation and compared with rolled W an increased fracture toughness was detected. Tensile tests and cyclic tensile test with 10000 load cycles and increasing load were performed. During the cyclic loading, no degradation with increasing number of cycles was visible even when matrix cracks are formed. Moreover, charpy impact tests in the range of -150 °C to 1000 °C were performed (see figure). During these tests the fibres showed a DBTT of around -100 °C while the CVD matrix showed ductile behaviour only at 1000 °C. Brick-based mock-ups have been used to assess the manufacturing quality and to get first results on the HHF behaviour. Several brick shaped samples with a base area of 5×10 mm^2 and different heights were soldered onto an actively cooled structure. By the different heights different surface temperatures are reached for a given heat load. The mock-ups were exposed to up to 10 MW/m^2 for 30 s for a screening test and in a second step to a cyclic loading of 100 cycles at 10 MW/m^2. During the tests, the samples reached temperatures up to 2000 °C for the largest height and did not reveal an obvious damage.

Tungsten Heavy Alloys as Plasma-Facing Material

In order to qualify the tungsten heavy alloy HPM1850 for use in the divertor of AUG dedicated laboratory investigations (see above) as well as HHF tests in GLADIS were performed. These investigations revealed that the thermal conductivity at high temperature is close to that of W, the magnetisation is small and saturates already at low magnetic field. In HHF tests at power densities up to 20 MW/m^2 no failure was observed up to the melting temperature (~ 1500 °C) of the binder phase. Even at surface temperatures of up to 2200 °C the mechanical integrity persisted. SEM investigations show a segregation of Ni and Fe at the top surface after the thermal overloading, but no signs of micro-cracking. Mechanical tests confirm the ductile behaviour of the W heavy alloy at room temperature and finite element analyses using the aforementioned data suggest a lower tendency for cracking when used as AUG divertor tiles. The impact of heat treatment on tensile properties has been studied at different temperatures (600, 1100, and 1350 °C) with various durations up to 100 h. After the heat treatment, the tensile properties were improved by more than 30 %. The increase of the interfacial strength between W grains and matrix phase is considered as the main reason for this behaviour. The long-term dose rate resulting from the activation of Ni under neutron irradiations appears to be moderate. During the 2017 campaign more than one fifth of the AUG divertor tiles consisted of W heavy alloy. Under nominal operation conditions the tiles showed no macroscopic failure and no increased Fe/Ni influx into the plasma was detected. Even though a few tiles showed strong melting at the edges due to accidental misalignment no failure due to cracking was observed (see also AUG section).

High Heat Flux Facility GLADIS

The powerful high-heat-flux (HHF) test facility GLADIS is dedicated to the investigation of plasma-facing materials and components. Two independently controlled ion sources of up to 1 MW power each and a water cooling system up to 230 °C inlet allow the operation with heat loads and cooling conditions similar to the expected operating parameters in current and future fusion experiments such as ITER and DEMO. In the reporting period we improved our IR monitoring system for a better surface temperature analysis of transient and highly heat-loaded W components which reach typical surface temperatures between 1000 to >2000 °C during 10–20 MW/m^2 loading.

After 15 years of development and HHF testing of the actively cooled divertor targets of W7-X the last HHF tests of complete target module were performed in 2019. For each type of target modules a thermal mapping was performed. More details about the manufacturing and installation of the W7-X divertor targets are given in section "Wendelstein W7-X, 2.5.2 Target Modules". Highlights of the target testing were the following achievements which illustrate the high thermal performance of the actively water-cooled divertor targets, e.g.:

- 10000 cycles at the design heat flux of 10 MW/m^2 were performed without damage of the target covered with CFC flat tiles.
- Overload tests of 1000 cycles at 16 MW/m^2 were performed. The target survived with minor defects.
- 1000 cycles at 10 MW/m^2 on a pre-damaged target do not cause the growth of defects.
- Extreme loading tests of 30 s pulses up to 32 MW/m^2 do not destroy the target, even more the target integrity is not affected after such excessive heat load.

Furthermore, an extensive HHF test program has been carried out in the framework of the EUROfusion DEMO divertor project to assess eight different advanced design concepts of hot-water-cooled divertor targets. The components to be finally developed should allow a reliable DEMO operation for 2 h long pulses with 10 MW/m^2 heat flux and maximum heat flux excursions up to 20 MW/m^2 for several seconds. The HHF qualification program has been performed to explore both, the thermal fatigue behavior under 20 MW/m^2 cyclic loading and the limits of thermal performance for a low number of pulses up to 32 MW/m^2. Up to now, two concepts survived without damage 1000 cycles at 20 MW/m^2 with hot-water cooling. However the resulting surface temperature of 2000 °C causes strong morphology changes due to grain growth and accumulation of plastic strain. The 32 MW/m^2 loadings were performed with cold-water cooling to ensure stable heat transfer conditions to the cooling water. Surface temperatures between 3200 °C and 3420 °C (melting temperature of W) were reached depending on the design concept. Subsequently performed cycling tests with loads between 20–25 MW/m^2 confirmed the integrity of the tested components after such extreme events.
In total we tested 45 monoblock components with 4200 pulses of 10 MW/m^2, and 10000 pulses of 20 MW/m^2. These GLADIS test results were considered as key selection criterion to identify the most promising concepts for further development in the next step of the DEMO divertor project.

Integration of and Collaboration in the EU Programs

Within the EUROfusion work programme some members of the project are involved in the scientific exploitation of the European tokamaks under the Taskforces WPJET1 and WPMST1, but the project's main activities under EUROfusion are centred within the following work packages:

Work Package Plasma Facing Materials (WPPFC): The work within WPPFC comprises seven subprojects dealing with subjects centred around investigations on plasma-material interaction in linear and laboratory devices as well as fusion devices. IPP is strongly involved in five of the subprojects and provides the subproject leaders for 'Erosion, deposition and mixing' and 'Fuel retention, fuel removal and damage'.
Work Package Materials (WPMAT): Within WPMAT materials for a Demonstration Fusion Power Plant are developed. The work of IPP concentrates on the development of high-heat-flux materials namely tungsten fibre-reinforced tungsten, tungsten copper composites as well as tungsten alloys as armour for plasma-facing components.
Work Package Divertor (WPDIV): The scope of the Divertor Project (WPDIV) covers all elements of conceptual design for the whole divertor system of the first DEMO reactor. IPP provides the project leader of WPDIV and is responsible for the design and construction of two divertor component mock-ups. Further, the project provides the thermo-mechanical analysis of all European mock-ups and their high-heat-flux testing in GLADIS.
Work Package JET2 (WPJET2): The work package JET2 (WPJET2) aims at the exploitation of the JET ITER-Like Wall (ILW) in view of the erosion/deposition pattern and fuel inventory of the plasma-facing components. IPP is responsible for the nuclear reaction analysis of specific tungsten components.
Work Package Liquid Metal Divertor (WPLMD): The work package LMD (WPLMD) investigates the possibility of using liquid metal as armour material for plasma-facing components. IPP performed detailed investigation on the behaviour of (solid/liquid) tin under low-energy plasma irradiation.

Scientific Staff

A. H. Abdelhameed, P. Almanstötter, R. Arredondo Parra, N. Ashikawa, M. Balden, A. Bauer, J. Bauer, L. Bock, J. Boscary, B. Böswirth, D. Brida, M. Brucker, V. Burwitz, R. Caloudis, D. Carralero, B. Curzadd, T. da Silva, R. de Luca, G. Debaille, C. P. Dhard, D. Dickes, J. Dorner, G. Dose, A. Drenik, T. Dürbeck, R. Dux, G. Ehrke, S. Elgeti, R. Endoh, M. Faitsch, A. Feichtmayer, M. Fuhr, M. Fußeder, L. Gao, H. Gietl, H. Greuner, M. Guitart Corominas, A. Herrmann, G. Holzner, T. Höschen, K. Hunger, W. Jacob, P. Junghanns, M. Kandler, S. Kapser, A. Kärcher, A. Khan, S. Krat, K. Kremer, K. Krieger, S. Lederer, M. Li, Q. Li, S. R. Lim, C. Long, T. Lunt, H. Maier, A. Manhard, G. Matern, M. Mayer, D. Naujoks, N. Nemati, R. Neu, M. Oberkofler, S. Olbrich, M. Poitner, T. Reichbauer, M. Reisner, J. Riesch, L. Ru, F. Salamon, K. Schlüter, K. Schmid, T. Schwarz-Selinger, M. Stienecker, U. Stroth, F. Valentini, A. van Roessel, A. von Müller, M. Wagner, A. Weghorn, B. Wielunska, M. Will, M. Wischmeier, J.-H. You, H. Zhang, K. Zhang, M. Zibrov, M. Zielinski.

Plasma Theory

Theoretical Plasma Physics

Heads: Prof. Dr. Sibylle Günter, Prof. Dr. Per Helander, Prof. Dr. Frank Jenko, Prof. Dr. Eric Sonnendrücker

The project "Theoretical Plasma Physics" is devoted to first-principle based model development with emphasis on magnetic confinement. It combines the efforts of the divisions Tokamak Physics, Stellarator Theory and Numerical Methods in Plasma Physics and of the HLST Core Team of the EUROfusion work package WPISA. It is also a major partner in the Max Planck Princeton Center for Plasma Physics.

Tokamak Physics Division

Heads: Prof. Dr. Sibylle Günter, Prof. Dr. Frank Jenko, Dr. Daniel Told

The Tokamak Theory Division (TOK) at Garching consists of three independent units, the main unit led by Prof. F. Jenko, the MHD Group lead by Prof. S. Günter, and a Helmholtz Young Investigator Group lead by Dr. D. Told.

Tokamak Theory

In the following, we will first provide an overview of the main unit. The research activities span a wide range of topics and approaches, from the development of analytical models and simulation codes to their application to addressing fundamental theoretical questions and interpreting specific experimental results. While most of these efforts are dedicated to tokamaks, extensions to stellarators are also pursued. Moreover, there exist significant activities in the area of plasma astrophysics, in particular in the context of the Excellence Cluster ORIGINS (F. Jenko is a member of the Research Board and the Council, and Coordinator of a "Connector" on "Cosmic Accelerators") which involves two large universities as well as several Max Planck Institutes (IPP, MPP, MPA, MPE) at Munich.

Analytical Calculations

Methodologically, our analytical and computational studies are deeply intertwined. More recently, rather extensive analytical calculations were employed, e.g.:

- to explore the limits of gyrokinetic theory [1]
- to implement advanced gyrokinetic collision operators [2]
- to develop refined descriptions of ion-orbit loss effects [3]
- to provide analytic formulas for the ion-orbit motion in tokamaks [4]
- to construct reduced models of fast-particle effects on turbulence [5]
- to investigate and refine an existing quasilinear model of turbulent transport [6]
- to improve multi-component fluid models for the edge [S. Makarov, to be published].

These analytical calculations are essential, among other things, for putting our studies on a firm mathematical basis, for providing fundamental insights into the physical properties of the systems under investigation, and for creating reduced models to interpret and guide experiments.

State-of-the-art Simulation Tools

A second methodological pillar of our work is the development and deployment of state-of-the-art simulation tools. In this context, our flagship effort is the continuous evolution of the GENE family of gyrokinetic turbulence codes. The flux-tube and global axisymmetric versions of GENE are widely used (at IPP and by a large, worldwide user base) to explore a very wide range of tokamak physics questions. Here, a recent trend has been to examine situations in which turbulence interacts with other physical features, like magnetic islands or energetic particles. Meanwhile, two new members joined the family: after several years of code development, the first publications based on GENE-3D, a global non-axisymmetric version of GENE, were published in 2020 [7,8] (see figure 1). In contrast to other stellarator turbulence codes, GENE-3D describes the full dynamics of the system, i.e., the turbulent motion of the ions and also of the electrons over the entire inner volume of the plasma, including the resulting fluctuations of the magnetic field.

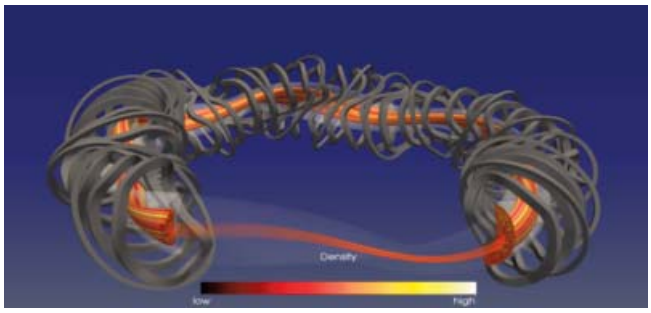

Figure 1: Snapshot of a turbulence simulation with GENE-3D for Wendelstein 7-X.

Another effort, which started about two years ago, is focused on the development of a full-f version of GENE for the edge and scape-off-layer. This code, called GENE-X, leverages the mathematical and computational infrastructure originally developed for the fluid edge turbulence code GRILLIX [9]. It is based on a Flux Coordinate Independent (FCI) approach that allows it to naturally treat closed and open field line regions on the same footing. First simulations in an AUG-like X-point geometry have been carried out recently, demonstrating the power of this method. At the same time, GRILLIX has seen very significant extensions, leading to a first wave of interesting physics results. And as a complement to GENE-X and GRILLIX, we have also started to develop a gyrokinetic PIC code for the edge, PICLS. Other codes, like RABBIT, will be described later in this text. In parallel to pushing the envelope of numerical plasma simulation in these ways, we continue to support existing codes, including ORB5, SOLPS, TORBEAM, and TORIC.

Using a mix of analytical and computational methods, we were able to address a variety of important open issues in fusion theory, as has been documented in a large number of publications. In the following, we will focus on some particular recent highlights.

Highlight 1: Turbulence Suppression by Energetic Particles

A few years ago, it was first observed in gyrokinetic turbulence simulations with GENE that including energetic particles can lead to a strong reduction of the turbulent transport levels [10]. However, the physical mechanisms underlying this effect remained elusive until recently. In a series of pioneering theoretical investigations since 2018, the nature of these stabilizing effects could finally be unveiled. This discovery became possible by means of a combination of analytic calculations and gyrokinetic simulations on large supercomputers. In this way, a coherent picture emerged, involving two newly discovered physical mechanisms: (1) wave-particle resonances between the suprathermal particles and the microinstabilities driving the turbulence and (2) nonlinear interactions between these microinstabilities and Alfvénic instabilities which are excited by the fast particles. On the basis of reduced analytic models which are able to capture the essence of these mechanisms, it became possible to help guide the design of experimental studies targeted at maximizing the turbulence suppression effects of the energetic particles. This led to the discovery of a new improved confinement regime in the ASDEX Upgrade tokamak and promising predictions for the Wendelstein 7-X stellarator.

Regarding the first point above, energetic particles are found to strongly interact with ion-temperature-gradient (ITG) instabilities when their perpendicular drift frequencies match those of the instabilities. Under certain conditions (identified in references [11-13]), this effect can significantly reduce the resulting turbulent transport. This resonant stabilization has been explained with a reduced model, derived from first principles, providing relevant insights into the identification of further key parameters controlling the beneficial fast ion role on plasma turbulence. GENE simulations for an ITER standard scenario were carried out of this basis, exhibiting a substantial turbulence suppression due to wave-fast particle resonance effects (see figure 2 left). The effectiveness of this mechanism in suppressing turbulent transport also in optimized stellarators has been addressed for the first time in reference [13]. Exploiting the flexibility of the non-axisymmetric magnetic geometry, optimized configurations can be identified, allowing for enhanced turbulence suppression via fast particles by design.

Regarding the second point above, an effort was made to provide a physical understanding of the nonlinear electromagnetic effects in the presence of fast particles observed in many experiments and simulations [14]. By applying sophisticated energy-transfer diagnostics, it was shown that marginally stable MHD-type modes can be excited by a nonlinear coupling with the ITG turbulence (see figure 2 right). The resulting energy redistribution decreases the turbulence and overall transport levels. If the energy injected into these MHD-type modes is sufficiently large, an increase in stationary axisymmetric (zonal) perturbations is typically observed.

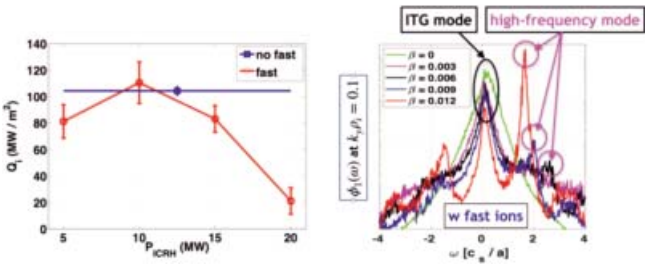

Figure 2: Left: Main-ion heat flux as a function of the injected ICRH power for an ITER standard scenario. Right: Frequency spectra of the electrostatic potential for different values of the plasma beta, illustrating the nonlinear interaction of ITG and MHD-type modes.

Highlight 2: Energetic-particle Dynamics in the Presence of Turbulence

Complementing the work just described, the global gyrokinetic particle-in-cell (PIC) code ORB5 has been used to investigate the dynamics of energetic particles and the MHD-type modes driven by them in the presence of background turbulence. For this to become possible, ORB5, originally developed as an electrostatic code, had to be extended in the last years to an electromagnetic multi-species version. In this context, a crucial step has been the implementation of control-variate and pull-back schemes [15] for the mitigation of the so-called cancellation problem. This new version was benchmarked successfully within ITPA-led efforts, demonstrating the capability of ORB5 to carry out electromagnetic simulations, which generally remains a challenge for PIC codes.

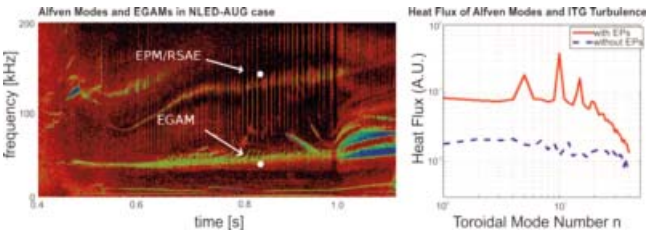

Figure 3: Spectrogram of AMs and EGAMs in AUG compared with theoretical predictions of ORB5 (left), and heat fluxes of BAEs and turbulence in simplified magnetic equilibria (right).

On this basis, the nonlinear saturation of EP-driven instabilities has been investigated in simplified configurations, focusing, in particular, on the nonlinear modification of the radial structure of Alfvén Modes (AMs) [16] and on the saturation level and EP redistribution of EP-driven Geodesic Acoustic Modes

(EGAMs) [17]. The study of the nonlinear dynamics of Beta-induced Alfvén Eigenmodes (BAEs) in the presence of turbulence in simplified configurations has shown an increase of the levels of heat flux of the turbulence spectra in correspondence with the toroidal mode numbers of the BAE and its harmonics, and a smaller increase at the tail of the spectrum at higher toroidal mode numbers, especially for the electron heat flux. The linear and nonlinear dynamics of AMs and EGAMs has been studied in experimental configurations of AUG. Despite the simplifications in the EP distribution functions, a good match of the predicted and observed frequencies has been found for EGAMs and AMs [18]. Electron Landau damping has been found to be the dominant damping mechanism of these modes [18,19]. The nonlinear relative frequency chirping has been recovered for EGAMs [19], and studies are underway for AMs. The ultimate goal is the study of the EP dynamics in the presence of turbulence, in realistic configurations.

Highlight 3: Predictive Model for the Generation of Runaway Electrons

The generation of runaway electrons (RE), following massive material injection (MMI), was studied with the 1.5D coupled transport codes ASTRA and STRAHL, applied to gas injection scenarios of ASDEX Upgrade. For this purpose, the capabilities of these codes have been extended to calculate RE densities and source rates arising from relevant generation mechanisms (hot-tail, Dreicer, avalanche), as described by state-of-the-art models. The codes have been further enhanced to allow for the treatment of MMI and therefore to consider the interaction between background plasma, material injected, and REs. In particular, the impact of non-fully ionized impurities on RE generation is taken into account. Applied in simulations of ASDEX Upgrade, the model was found capable of calculating the evolution of key plasma parameters in agreement with experimental observations (e.g., plasma current and electron density), thus demonstrating the suitability of a 1.5D treatment of MMI and RE generation. Simultaneously, it was shown that the impact of non-fully ionized impurities on RE generation cannot be neglected in MMI scenarios. Omitting these effects, simulations fail to capture experimental trends such as the onset of RE generation and post-disruption currents. Consequently, state-of-the-art models describing RE generation have to be applied in these scenarios instead of commonly used formulae. The inward propagation of ionized material was observed to be governed by both neoclassical and MHD phenomena, with neutral transport being adequately described by inward propagation with thermal velocity. The respective MHD modes are triggered as the cold gas front reaches the q=2 surface, resulting in rapid inward transport of impurities. Neoclassical transport alone was found insufficient to cause rapid ionization of material and hence the occurrence of a thermal quench on the sub-ms time scales observed experimentally, thus highlighting the importance of additional MHD effects.

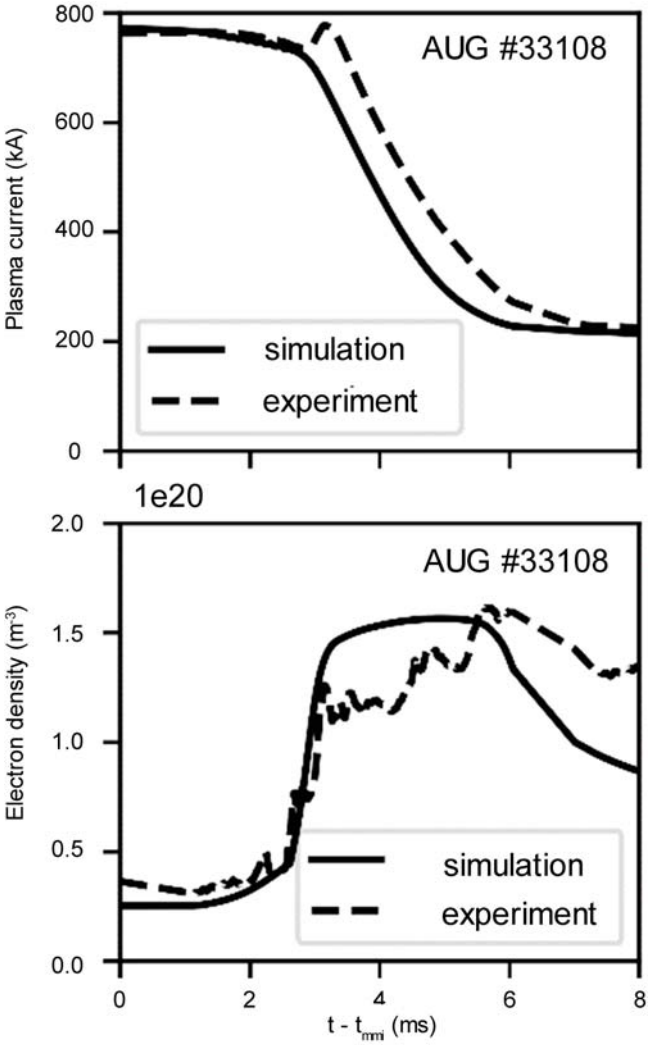

Figure 4: Time evolution of the plasma current and electron density in ASDEX Upgrade experiments, following massive material injection. The simulations, based on state-of-the-art models, agree favorably with the measurements [20].

Highlight 4: Real-time Simulation of the NBI Fast-ion Distribution

In 2018, a novel code, RABBIT, has been developed to simulate Neutral Beam Injection (NBI) fast-ion distributions in real-time, running about 1000 times faster than the reference code NUBEAM [21]. Since then, the focus was on further developments and applications. A module to calculate neutron rates has been added [22] and used by colleagues at DIII-D for fast control-room decision making (using the comparison to measured neutron rates as indicator for Alfvén-eigenmode induced fast-ion transport). RABBIT has also been coupled with the IDE code for better equilibrium reconstructions [23]. It was made available in ASTRA and is part of the newly developed ASDEX Upgrade flight simulator (FENIX).
The fast computation time of RABBIT allows to apply the code to huge databases of entire discharges. In one example,

it was used to study the isotope effect, where it could be demonstrated that the poorer confinement in hydrogen discharges is linked with lower fast-ion content (compared to deuterium discharges). As a side effect of this study, it was discovered that the fast-ion stored energy, evaluated routinely to estimate the energy confinement time (τ_E), was underestimated by roughly 30 %. As a consequence, RABBIT will replace the formerly used scaling laws, and τ_E as well as the H-factor (one of the most important quantities characterizing the plasma confinement quality) will be re-evaluated also for older discharges.

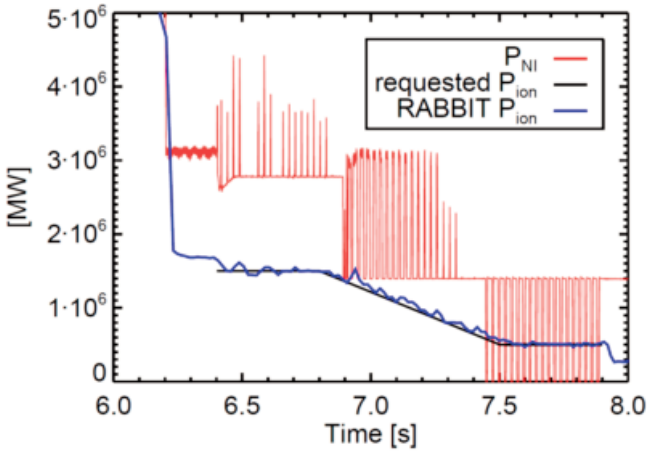

Figure 5: Real-time RABBIT calculations allow to control NBI properties directly. In this test, a ramp of ion heating (P_{ion}) was requested and achieved successfully by adapting the NBI power (P_{NI}) via pulse-width modulation.

A major project was the inclusion of RABBIT into the Discharge Control System (DCS) of ASDEX Upgrade. Software to handle this connection (a so-called Application Process) was developed within the DCS framework. Rabbit runs now as a DCS satellite on its own computer, asynchronously with the DCS main cycle. This means that RABBIT can run as fast as possible and publish its results as soon as they are finished. As a result of these efforts, all properties of NBI heating, such as deposition profiles, the ratio of ion and electron heating, and even the fast-ion distribution are now automatically available in real-time, while they were previously only available after manual and time-consuming calculations, e.g., with the TRANSP-NUBEAM code. Having this detailed knowledge about NBI heating already in real-time allows to control it much more directly and efficiently. In a first test, it could be demonstrated that it is now possible to request directly the ion heating (Pion) from the control system. As shown in figure 5, the control system was able to adapt the total NBI power (via modulation) to match the requested ion heating with the RABBIT calculation in very good agreement. In the future this will allow more complex experiments and could also be of relevance for future fusion devices such as ITER, where sophisticated plasma control is essential.

Highlight 5: Towards a Predictive Capability for Turbulence in the Edge and Scrape-off-layer

With the long-term goal to develop a predictive capability for turbulence in the edge and scrape-off-layer (SOL), a lot of effort has been put into the development the 3D fluid code GRILLIX. Thanks to the FCI approach mentioned above, simulations in complex and realistic geometries, including a separatrix and X-point(s), are possible. Since 2017, the physical model in GRILLIX has been extended significantly to a global full-f drift reduced Braginskii model, relaxing the Boussinesq approximation and implementing thermal dynamics as well as electromagnetic effects [24,25]. Various algorithmic improvements have enabled ab initio simulations of edge/SOL turbulence in ASDEX Upgrade over several milliseconds at realistic parameters and in realistic geometry. The self-consistently obtained turbulent transport is close to experimental observations. Furthermore, the development and origin of the radial electric field was studied and found to be determined by a combination of the ion pressure gradient and zonal flows. Due to a sheath-induced counter-propagating SOL flows, a strong shear layer forms at the separatrix, breaking turbulent eddies (see figure 6).

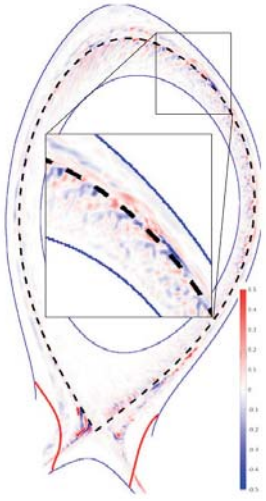

Figure 6: Snapshot of relative density fluctuations of ASDEX Upgrade simulation with GRILLIX. The decorrelation of turbulent eddies around the separatrix (black dashed line) due to a poloidal shear flow is visible.

This results in the formation of a transport barrier but also intermittent, large-amplitude SOL turbulence. A module for processing numerical equilibria has been added to GRILLIX that allows to study turbulence in the presence of advanced (X, Super-X, and snowflake) divertors [26]. It was found that secondary instabilities are triggered in long divertor legs that cause a broadening of target profiles with highly intermittent pulses. Finally, GRILLIX has been subject to an ongoing refactoring process since 2019 following modern software design standards from which a significant performance gain and parallel scalability is expected that would make direct

simulations at ITER scale feasible. In this context, the core functionality of GRILLIX has been extracted into a separate FCI library called PARALLAX that also serves as basis for the gyrokinetic code GENE-X (described below). In parallel to these fluid-based efforts, we have also been developing two gyrokinetic edge turbulence codes, GENE-X (grid-based) and PICLS (particle-based), since 2018 [9,27]. As is well known, the transition from closed to open field lines, as well as the correct representation of the plasma-wall interactions and the physics of neutrals/impurities present considerable challenges to such an approach. Nevertheless, we were able to make significant progress in this relatively short amount of time. Both of these tools employ a "full-f" approach, i.e., they do not split the distribution into a background and a perturbation, given that the fluctuation amplitudes in the edge region can be as large as several ten percent. Moreover, both of them use kinetic electrons and are currently based on an electrostatic model, a linearized field equation, a simplified collision operator, and logical sheath boundary conditions in open-field-line regions. Both codes have been tested extensively and are being applied to 3D geometries. In the case of GENE-X, first nonlinear simulations in the diverted geometry of a complete fusion device were recently performed, demonstrating the power of the FCI approach. In figure 7, we present – as an example – the almost fractal-like density fluctuations of the plasma during the onset of ion temperature gradient turbulence.

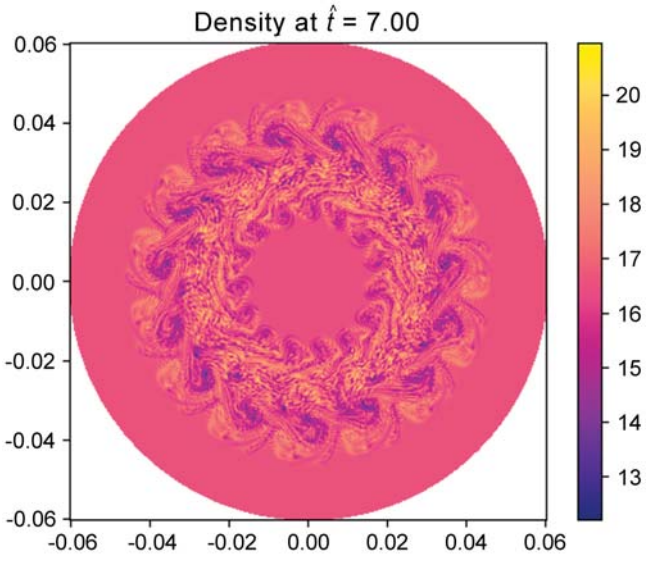

Figure 7: A snapshot from a GENE-X simulation in a circular plasma. Shown is the fluctuating total density.

Highlight 6: Unravelling the Nature of Dissipative Processes in Astrophysical Turbulence

Given that the same physical phenomena, based on the same mathematical equations, govern plasma systems both in nature and in the laboratory, it is often possible to transfer insights, methods, and tools from one area to the other. In this spirit, we have been active in exploring some key questions in theoretical plasma astrophysics. In a series of pioneering investigations, we addressed two controversial and fundamental questions related to the nature of dissipative processes in astrophysical turbulence: First, which plasma waves characterize the turbulence in the dissipation range? Second, should the latter be regarded as an ensemble of weakly interacting waves or is it dominated by inherently nonlinear structures? By means of fully kinetic simulations on some of the world's most powerful supercomputers (see figure 8) and innovative data analysis techniques applied to spacecraft observations in the solar wind, he is able to make groundbreaking contributions to this field of research.

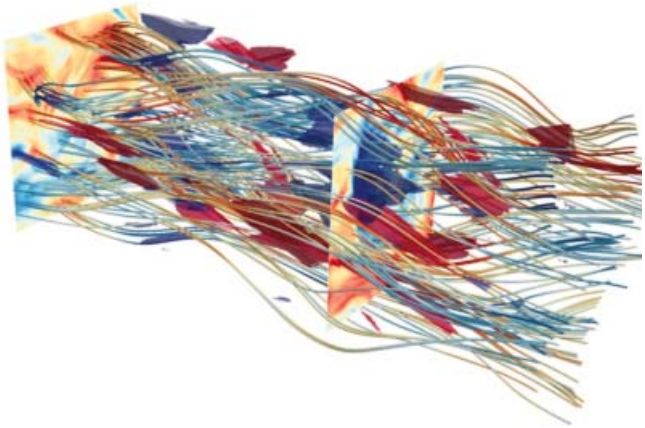

Figure 8: An area ~300 km wide in the solar wind is reproduced by this 3D fully kinetic simulation of astrophysical plasma turbulence. Featured are magnetic field lines and (color coded) electron density fluctuations.

Regarding the first question, we were able to provide compelling evidence in favor of kinetic Alfvén waves, and with respect to the second question, we put forth a novel view, unifying both traditional views in an unexpected way: The turbulent structures consist of spatially localized wave packets. These findings led to a series of high-profile publications [28,29,30] and was recognized by the larger community by several awards for the lead researcher, including an Otto Hahn Medal.

Scientific Staff

V. Artigues, P. Astfalk, A. Banon Navarro, A. Bergmann, M. Bergmann, A. Biancalani, R. Bilato, T. Body, M. Bösl, A. Bottino, R. Brzozowski, A. Chankin, D. Coster, A. Di Siena, T. Görler, J. Graw, R. Greif, D. Groselj, D. Jarema, F. Jenko, O. Kardaun, J. Lakhlili, L. Leppin, O. Linder, S. Makarov, J. Martin Collar, F. Matos, M. Maurer, D. Michels, A. Mustonen, I. Novikau, N. Oliveira Lopes, G. Pautasso, E. Poli, K. Pommois, A. Ross, B. Rettino, A. Stegmeir, C. Stephens, K. Stimmel, E. Sytova, D. Told, P. Ulbl, F. Vannini, M. Weidl, M. Weiland, F. Wilms, Y. Yudin, M. Zhao, W. Zholobenko, R. Zille.

Guests

V. Bratanov (Uni Texas, Austin, USA), J. Chen (USTC, Hebei, CHN), P. Crandall (UCLA, Los Angeles, USA), D. Hatch (UCLA, Los Angeles, USA), P. McCarthy (Univ. College, Cork, IR), W. McCorkindale (St. Johns College, Cambridge, UK), Q. Pan (UCLA, Los Angeles, USA), E. Panoutin (UNIMIB, Milano, IT), V. Rozhansky (SPBU, St. Petersburg, RU), M. Schneller (PPPL, Princeton, USA), I. Senichenkov (SPBU, St. Petersburg, RU), A. Shevelev, IOFFE (St. Petersburg, RU), A. Snicker (Aalto Univ., Espoo, FIN), S. Voskoboynikov (SPBU, St. Petersburg, RU).

MHD Transients – Studies of Large Scale Instabilities

Three Visco-resistive MHD Codes

Three visco-resistive MHD codes are being developed and used in the group to study large scale plasma instabilities in tokamaks and stellarators. Complementary features are intensely used for benchmarks and joint studies. Help with code optimization by EUROfusion HLST and MPCDF is acknowledged. The CASTOR3D linear stability code [31] is used for tokamak and stellarator geometries including 3D conducting structures. The code is the only non-ideal stability code able to deal with stellarator geometry world-wide. It was recently extended to account for parallel viscosity, and toroidal plasma flows [32]. The TM1 non-linear extended MHD code is now applicable to circular toroidal plasma configurations [33]. Both the single fluid and four-field models were upgraded to include toroidal mode coupling and benchmarked with CASTOR3D. The JOREK non-linear extended MHD code [34] addresses realistic divertor tokamaks including 3D conducting structures (JOREK-STARWALL). The solver efficiency was improved in terms of memory consumption and performance. The preconditioner is presently being generalized to increase numerical stability and convergence in highly non-linear scenarios [35]. A Runaway Electron (RE) fluid model was developed allowing to self-consistently include REs [36]. An impurity model without coronal equilibrium assumption is in development for edge/SOL and disruption mitigation studies. An extension to stellarators was started by deriving a hierarchy of stellarator capable full and reduced MHD models [37] that are presently tested in the tokamak limit. In parallel, a 3D grid extension was implemented and is presently being tested. The related solver adaptation is on the way. The JOREK-STARWALL coupling was fully parallelized and consistent 3D active/passive coils were added. An international benchmark on 2D and 3D VDEs with IPP contribution showed excellent agreement between JOREK, M3D-C1 and NIMROD including halo current distribution and wall forces in spite of different models and methods [38,39]. IPP is one of the main hubs developing and using JOREK; it coordinates the code development in the international community and is leading a EUROfusion Enabling Research project (and a proposed TSVV project within the new E-TASC framework of EUROfusion) on disruption and ELM physics.

Neoclassical Tearing Mode (NTM)

Regarding neoclassical tearing mode (NTMs), the triggering by sawteeth was studied using TM1 [33]. Based on the four-field equations, NTMs are found to be triggered by sufficiently strong sawtooth crashes at higher beta and bootstrap current (BC) density and/or a lower electron diamagnetic drift frequency. Detailed investigations were carried out to develop a deeper understanding of the interaction between NTMs and external resonant magnetic perturbations (RMPs). Using JOREK, the seeding of tearing modes (TMs) under controlled conditions by RMPs was also studied based on AUG L-mode experiments [40]. The penetration of 2/1 TMs qualitatively reproduces experimental features in all regimes from weak response over penetration to non-linear saturation. A hysteresis in plasma rotation and island width was found between ramp-up and ramp-down. The evolution of NTMs into (partial) thermal quenches (TQs) in AUG was studied. Mode coupling leading to stochastization is induced by the non-uniform background magnetic field and non-linear coupling. Virtual coil signals show a pronounced LFS/HFS asymmetry not captured by a widely used scaling law for locked-mode amplitude at TQ onset.

VDEs

Regarding VDEs, besides contributions to benchmarks and ITER simulations lead by collaborators, dedicated AUG simulations were performed with JOREK. Over many orders of magnitude from the (artificial) limit of no passive stabilizing structures to the fully realistic AUG configuration, excellent agreement on linear growth rates was obtained with CASTOR3D. Non-linear studies including a vertical position controller are on the way and will be advanced to detailed validation studies and eventually allow incorporating all relevant disruption phenomena in the same simulations. First simulations of VDEs with REs were performed [36].

Disruption Mitigation

Shattered pellet injection (SPI) was simulated with JOREK for AUG in preparation of future experiments [41]. Parameter variations confirmed that TQ triggering at experimental resistivity is not easy with deuterium only. With LFS injection, outwards oriented convection cells were observed reducing material assimilation and core penetration. Nevertheless, effective core mixing was observed during/after the core-TQ, such that density increases by almost an order of magnitude on axis was observed before flux surface re-formation. Studies of SPI into MHD active plasmas were started to assess the impact of pre-existing islands onto TQ dynamics. Impurity SPI will be studied soon based on the ongoing model developments.

Runaway Electrons

The termination of a runaway electron (RE) beam in JET was studied using the RE fluid model in JOREK [42], reproducing key experimental features including dominant 4/1 island formation, current spike amplitude, and nearly complete RE losses due to the strong MHD induced stochastization (figure 9).

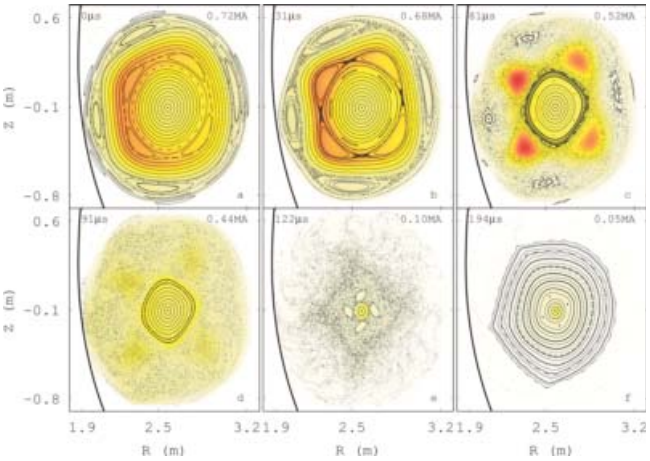

Figure 9: Poincare plots at six phases during the RE beam termination event in JET that has been simulated with JOREK. The formation of a large 4/1 double tearing mode is visible and leads to a complete stochastization of the domain. The REs (color) are lost along the magnetic field lines leading to a back conversion of the RE beam current into a thermal current. After the crash, the nested magnetic flux surfaces re-form.

The latest collisional model of runaway electron dynamics in the presence of partially ionized high-Z impurities in mitigated disruptions has been implemented in relativistic kinetic solvers. Reduced models were also implemented in fluid transport codes. Experimental comparison utilizing also synthetic diagnostics for the Bremsstrahlung and synchrotron radiation of runaways have shown that this model gives an accurate description for runaway dynamics on ASDEX Upgrade and other medium-sized tokamaks. MHD fluctuations in the Alfvenic frequency range have been experimentally observed and simulation results indicate that these may be able to contribute to runaway electron suppression in ITER burning plasmas.

ELM Crashes

Single type-I ELM crashes were simulated with JOREK and successfully compared to many experimental findings in AUG including non-linear mode spectrum [43,44]. To understand the physics of ELM cycles, i.e., the appearance of a quiet/saturated mode phase before the sudden explosive growth of an instability, significant effort was spent on establishing realistic full ELM cycle simulations (figure 10). Using ad-hoc diffusion profiles to model the pedestal build-up, type-I periodic ELMs with explosive onset are obtained for the first time [45]. A reduction of E×B flows by precursor modes as well as non-linear mode coupling leading to the formation of localized explosive ballooning fingers (as were predicted theoretically) play a crucial role. The experimental dependency of the ELM frequency on the heating power is recovered. Although not yet in an ITER relevant regime, the transition between small and large ELMs was observed. The interaction of RMPs with ballooning modes was studied with JOREK showing that non-linear mode coupling directly influences the instabilities - not only via profile modifications [46]. Pellet ELM triggering is studied based on the most recent ELM simulations (partly in collaboration with Shimpei Futatani from CIEMAT) reproducing the experimentally observed sharp transition during the ELM cycle between no-ELM response and ELM triggering [47,48]. Comparison between natural and triggered ELMs shows good agreement to experiment.

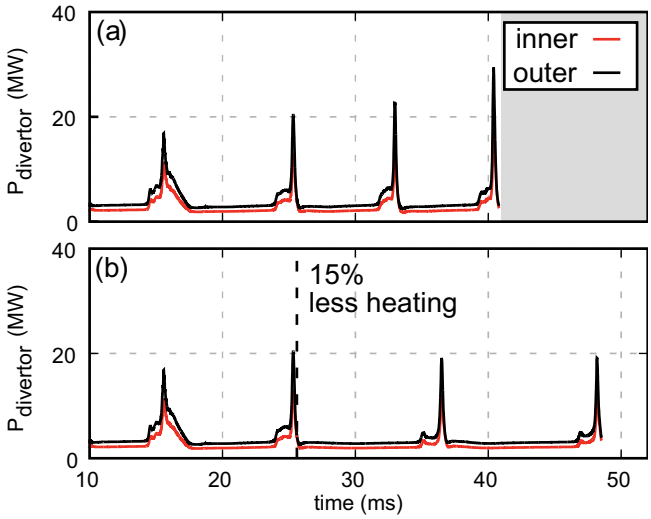

Figure 10: Power incident on the inner (red) and outer (black) divertor tiles during type-I ELM cycles simulations. The simulations feature a direct dependency between the input heating power and the ELM repetition frequency f_{ELM}. At nominal heating power (a), the simulations feature $f_{ELM} \approx 120$ Hz. When a reduced heating power is considered (b), the frequency is reduced to $f_{ELM} \approx 87$ Hz.

Quasi-axisymmetric Stellarator (QAS)

The unstable external kink modes of a quasi-axisymmetric stellarator (QAS) configuration were studied with CASTOR3D including plasma flows and resistive walls and compared to an axisymmetric approximation of this equilibrium [32]. Two major differences in the stability properties were found: (i) in contrast to the axisymmetric approximation, the QA equilibrium is vertically stable (ii) a variety of modes becomes unstable due to the mode coupling induced by the 3D geometry. To allow for an easy access to non-linear MHD simulations in QA geometry, simulations based on the axisymmetric equilibrium were also performed also with a “virtual current model”

in JOREK, allowing to incorporate the external rotational transform of stellarators in axisymmetric simulations. Simulations without virtual currents reproduce the CASTOR3D results for the axisymmetric case. With the virtual current included, the vertical stabilization as well as the growth rates for external kink modes generally are recovered well (with some increased differences at high mode numbers at high plasma pressure) in spite of the simplified simulation domain. Further linear and non-linear studies are ongoing.

Sawtooth-like Crashes

Sawtooth-like crashes of the electron temperature in W7-X experiments with electron cyclotron resonance heating were studied as well using the above-mentioned codes and are reported in section "Max Planck Princeton Research Center for Plasma Physics" dedicated to Garching-Greifswald joint work.

Energetic Particle Physics

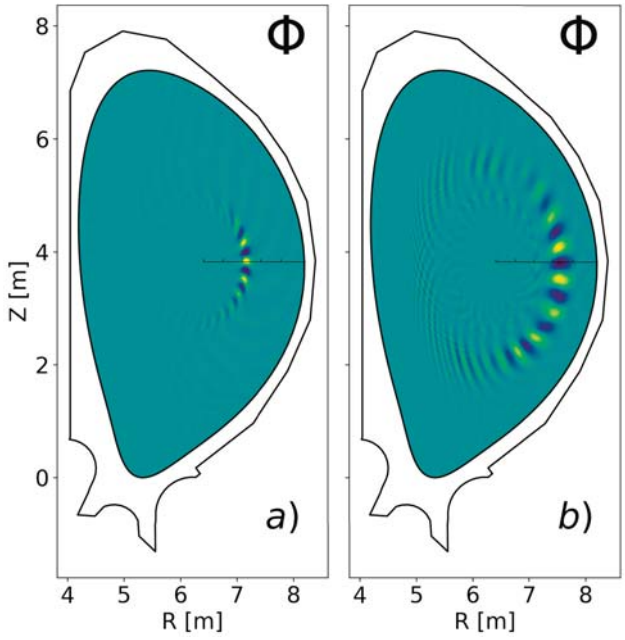

Figure 11: 2D mode structures (electrostatic potential) of unstable TAEs in ITER as calculated by ORB5, left in the linear phase, right in the non-linear phase, demonstrating the importance of linearly sub-dominant modes.

Studies of Alfvén eigenmodes in the ITER 15 MA scenario have been performed with the global fully gyrokinetic particle-in-cell code ORB5. The effect of the real finite electron mass on the linear stability was investigated, as well as the stabilising effect due to the gyro-averaging of the α-particles. It was confirmed that there exist radially extended toroidal Alfvén eigenmodes (TAEs) for which the linear properties require a full radially global simulation, as well as radially localized TAEs that can be well modeled on annuli. Through nonlinear simulations, the saturation of the TAEs by wave-particle trapping was observed, with the peak amplitude increased in the presence of multiple modes over the levels with single modes present (figure 11). This enhanced saturation is linked to the adjacent steepening as the individual modes flatten the local density gradient. Despite well-understood differences, in particular with respect to the role of the anti-ballooning TAE branch, the obtained results largely confirm the physics picture of previous non-linear kinetic hybrid simulations (LIGKA/HAGIS), giving confidence that both approaches are conceptually valid and numerically converged for the investigated regime. This agreement opens the path not only for more comprehensive and increasingly realistic ORB5 simulations, but also for the further development of reduced models.

The kinetic effects of both thermal ions and energetic particles (EPs) on the properties of global Alfvén modes, in particular on the mode structure symmetry breaking (SB) were studied. This SB, i.e. the distortion of ideal MHD modes into e.g. triangular shaped structures in the poloidal plane has been observed experimentally (via electron cyclotron emission imaging measurements) and was reproduced in various simulations, but the fundamental mechanisms and dependencies were not understood. Motivated by this, the EP effects on the mode structure SB were investigated analytically, extending the underlying local-global gyro-kinetic model appropriately. The results based on the numerical evaluation of the analytical expressions were successfully compared with simulations using the MHD-hybrid code HMGC. The non-perturbative effects of the EPs on the global mode structure SB could be consistently demonstrated. In particular, when the EP drive shifts away from the mode rational surface leading to an asymmetry of the EP population with respect to the mode localization layer, volume averaged parallel and radial wave numbers are generated in the plasma leading to the same distortions as observed experimentally.

Building on this insight, the effects of the non-perturbative mode structures on the EP transport have been analysed using the HAGIS code. Mode structures with SB properties were generated using the analytical understanding in order to mimic the experimental and simulation observations. Analyses based on ASDEX-Upgrade parameters show that non-perturbative mode structures can be important for EP transport modeling: the asymmetry of radial wave number modifies the EP transport, especially the toroidal momentum transport. For the considered case, mode SB effects change the linear growth rate only by 10 % and the saturation level by 20 %. The resulting EP density and energy transport is also modified only by about 10 %, whereas the EP parallel velocity distribution can change significantly. Even a parallel velocity reversal in the core region can be observed when varying the mode structures. This large effect (~100 %) on the mean parallel flow could have implications for EP current drive and transport in the burning plasmas.

The frequency chirping features of energetic particle modes (EPM) were investigated with XHMGC, using a kinetic description for both the EPs and the thermal ions. Under certain conditions for the equilibrium q profiles and the EP distribution functions, kinetic TAEs instead of gap TAEs can be driven unstable in the shear Alfvén continuum near the lower TAE accumulation point. Such modes can induce large range frequency chirping. The modes move along the Alfvén continuum until they reach the lower kinetic thermal ion gap. The radial mode structures are strongly modified. As a consequence, the saturation level is enhanced, and the radial redistribution of EPs is enlarged. Also, the saturation amplitude scaling is different from the cases with constant frequency modes, allowing one to estimate and predict the EP transport for strongly chirping EPMs.
A triangular mesh based gyro-kinetic code (TRIMEG) has been developed in order to explore the efficiency of structured and unstructured meshes for complicated geometries and for the accurate treatment of the magnetic axis. In the electrostatic delta-f version, valid for small perturbations, the gyro-kinetic Poisson system is solved with finite Larmor radius effects for realistic tokamak geometry, including the open field lines. Linear ITG simulations using an ASDEX Upgrade equilibrium have been performed, that demonstrate the capabilities of the TRIMEG code for simulations with realistic experimental equilibria in the whole plasma volume, including the open field line region. In the electromagnetic full-f version, an implicit scheme has been developed for the study of the Alfvén eigenmodes and EPs, using structured meshes. An analytical treatment is introduced to achieve an efficient convergence of the iterative solution of the implicit field-particle system. TAEs were simulated using an ITPA TAE benchmark case, and promising results were obtained. The full-f electromagnetic particle scheme established in this work provides a natural choice for EP transport studies where large profile variations need to be captured during a simulation.

Scientific Staff

V. Bandaru, A. Cathey Cevallos, I. Chavdarovski, S. Günter, T. Hayward-Schneider, F. Holderied, M. Hölzl, K. Lackner, P. Lauber, A. Lessig, A. Lier, Z. Lu, G. Meng, D. Meshcheriakov, N. Nikulsin, F. Orain, G. Papp, R. Ramasamy, E. Strumberger, X. Wang, F. Wieschollek, Q. Yu.

Guests

J. Artola-Such (AMU, Marseille, FRA), C. Atanasiu (Inst. of Atomic Physics, Bukarest, ROU), A. Bierwage (QST, JP), W. Guo (IPP CAS, Hefei, CHN), I. Krebs (DIFFER, Eindhoven, NL), R. Matteoli (ENS, Paris-Saclay, FRA), J. Na (IPP CAS, Hefei, CHN), H. Wang (NIFS, Toki, JP), N. Wang (Huazhong Univ., Wuhan, CHN.

Helmholtz Young Investigator Group „Hybrid Gyrokinetic Computations for Weakly Magnetized Plasmas in Nature and the Laboratory“

An independently funded research group was formed in 2017, aiming to tackle the numerical modeling of turbulence in weakly magnetized plasmas. These are defined as plasmas, where the gyrokinetic approximation applies to the electrons, but not for the ions. Such plasmas exist in space, where high frequency waves break the gyrokinetic ordering, but also in the edge of fusion plasmas, where temperature and density scale lengths can be comparable to the ion gyroradii.
The project consists of several steps that are being addressed in parallel as far as possible:

Model Equations

A consistent electromagnetic system of equations has been derived using the variational Hamiltonian approach. Given the combination of fully kinetic ions and gyrokinetic electrons, the electric field is computed from a quasineutrality equation whose dominant contribution is the electron polarization density.

Dispersion Solver

An electrostatic kinetic/driftkinetic dispersion solver has been developed to study the basic wave physics contained in the model. Comparisons with hybrid-kinetic/fluid and fully kinetic solvers have indeed found some improvements already at this simple stage, e.g. in the fidelity of ion-Bernstein wave frequencies and damping rates. This solver is presently being upgraded to include electromagnetic fluctuations, significantly expanding the zoo of waves that can be analyzed.

Nonlinear Turbulence Code

The ultimate step is the development of a fully nonlinear turbulence code involving our hybrid model. The development of the ssV code has been undertaken in collaboration with the Ruhr University Bochum, where the underlying code framework as well as part of the numerics have been developed. ssV presently employs the same electrostatic kinetic/driftkinetic version of our model. Initial studies of turbulence in a 2d spatial setting have been performed, as well as first exploratory runs of ITG turbulence in a 3d slab geometry.

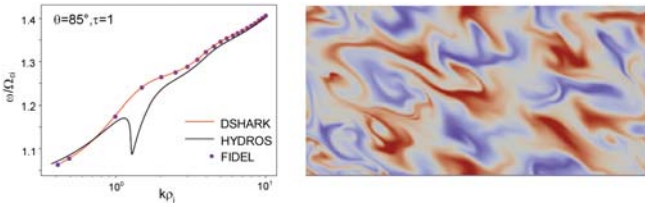

Figure 12: Left panel: Comparison of ion-Bernstein wave frequencies between hybrid-kinetic/fluid (black), our hybrid-kinetic (blue) and fully kinetic (red) wave solutions. Right panel: Snapshot of the electron guiding center density from a 2d turbulence simulation using the ssV code.

Stellarator Theory Division

Head: Prof. Dr. Per Helander

The Stellarator Theory Division is devoted to the development of the theory of three-dimensionally shaped plasmas and is deeply involved in the preparation and interpretation of experiments in Wendelstein 7-X.

Confinement and Transport

Experimental Evidence for the Successful Reduction of Neoclassical Energy Transport in Wendelstein 7-X

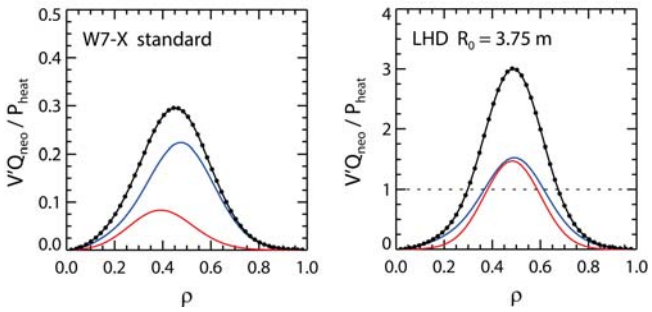

Figure 13: The neoclassical energy fluxes normalised to the heating power are plotted as a function of normalised minor radius for the experimental density and temperature profiles of a high-triple-product discharge at t= 3.35 s. Electron energy fluxes are shown in red and those of the ions in blue; their sum is given by the black curve. The high temperatures of this discharge produce an experimentally relevant level of neoclassical energy transport in the Wendelstein 7-X standard configuration for which these results were obtained. This provides experimental confirmation for the successful reduction of neoclassical transport in Wendelstein 7-X as such temperatures would otherwise imply neoclassical losses well in excess of the heating power as is demonstrated by repeating the calculations for the LHD configuration having its magnetic axis at R_0= 3.75 m.

In the majority of Wendelstein 7-X discharges, central ion temperatures are observed to have a ceiling of roughly 1.5 keV. Due to their strong temperature dependence, the neoclassical energy fluxes for such discharges are quite modest and only of secondary importance when considering the plasma energy balance. A notable exception to this rule has been achieved in plasmas fuelled with series of pellets. In the aftermath of pellet fuelling, substantial increases of both density and ion temperature are observed transiently, after which the ion temperature relaxes to its pre-pellet level. During the transient phase, the stored energy in the plasma reaches large values, confirmed both by measurements of a diamagnetic loop as well as the plasma profiles obtained from several diagnostics. This has been achieved in spite of the rather modest heating power currently available at Wendelstein 7-X, and has produced record values of the fusion triple product for high-temperature stellarator plasmas, for example the discharge 20180918.045, during which a maximum diamagnetic energy of 1.02 MJ was maintained for 230 ms, which corresponds to the energy confinement time given the 4.5 MW of ECRH used to heat the plasma. This confirms the successful reduction of neoclassical energy transport in Wendelstein 7-X, as the plasma profiles which produced this result prove to be unattainable for stellarators lacking a comparable level of neoclassical optimization (see figure 13).

Local Gyrokinetic Turbulence

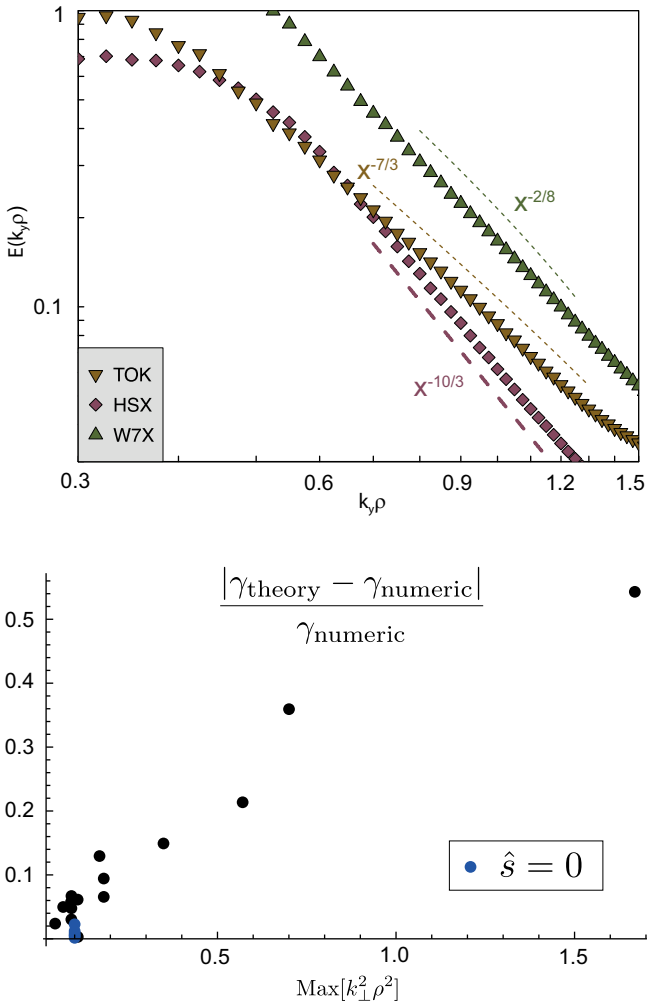

Figure 14: Spectra of electrostatic energy for distinct saturation regimes in stellarators and a tokamak (top). Zonal flow instability growth rate including magnetic geometry effects agreement with theory (bottom).

The main focus in this research is to develop fundamental understanding of turbulence and micro-instabilities in stellarators, with emphasis on Wendelstein 7-X. Several varieties of turbulence exist that are considered as candidates to cause sufficient transport to limit device performance, and each has received considerable attention during the last few years. Historically, one of the main tools for predicting turbulent transport, and related properties, has been so-called “quasi-linear” theory.

An upgrade to stellarator geometry was made [49], focusing on particle transport, showing that certain properties like the direction of the implied particle fluxes can be inferred directly from the magnetic geometry. Conclusions can also be drawn for issues of density fuelling and impurity transport. Among the different varieties of turbulence, the ion-temperature-gradient (ITG) driven type is regarded as the greatest threat to confinement, due chiefly to its large spatial scale. An important question for stellarators is to what degree the complex magnetic geometry can influence this turbulence. A theoretical investigation of ITG turbulence was carried out, examining the Wendelstein 7-X and HSX stellarators, compared with tokamak geometry [50], revealing different regimes distinguished by the saturation mechanisms at play. For Wendelstein 7-X, there is a sensitivity of the turbulence to zonal flows levels, whereas for HSX, the saturation mainly occurs without the influence of these flows. The fluctuation spectra are also distinct, reflecting a change in the cascade physics (see first panel figure 14).

It was also shown that zonal flow generation mechanisms are generally weaker in stellarators with localised turbulence, but the overall effect on the turbulence is balanced by other saturation mechanisms. Subsequent work carried out by independent groups has confirmed some of these conclusions. Two theoretical works [51] were published following [52], to support the results, and provide more detailed derivations. A theory of zonal flow growth rate, accounting for magnetic geometry, was derived and verified (see second panel of figure 13). Finally, a study of the variation of ITG modes within a magnetic surface explains a stabilizing "finite ρ*" effect observed previously in turbulence simulations [53].

Another key micro-instability attributed to thermal transport is the electron temperature gradient (ETG) mode. Despite its small scale, this instability is known, under certain conditions, to generate transport that can compete in magnitude with that of ITG turbulence in tokamak devices, due in part to the formation of radially elongated convective cells termed "streamers". In the stellarator context, the question of the potential role of ETG turbulence had largely been unexplored, and experimental results concerning core electron root plasmas in Wendelstein 7-X promised ideal conditions to observe ETG in isolation. Therefore, a study of ETG turbulence was undertaken [54]. It was found, however, that simulated electron thermal transport generated by ETG turbulence was inconsistent with a power balance analysis of the experiment, implicating trapped electron modes as the likely cause, instead of ETG turbulence. Anticipating future plasmas with equal ion and electron temperatures, conditions of equal ion and electron temperature gradients were also simulated, showing the transport generated by ETG to be much smaller than that driven by ITG. The low thermal transport was explained by the absence of large-amplitude streamer structures that appear with ETG simulations of high shear tokamak plasmas (see figure 15).

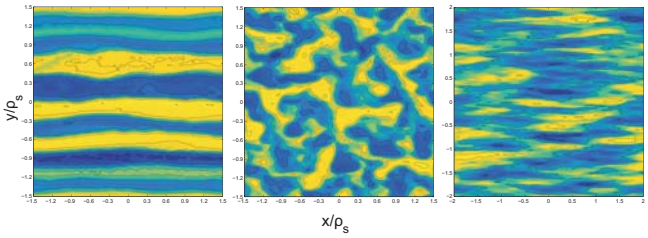

Figure 15: Density fluctuations plotted in the plane perpendicular to the magnetic field. The positive-shear tokamak shows characteristic radial streamers, while the negative-shear tokamak and the stellarator Wendelstein 7-X show more isotropic flow patterns.

The results imply that turbulent transport in stellarators might be accurately computed using affordable single-scale simulations, and that ETG turbulence can be expected to play only a minor role in a wide range of experimental conditions in stellarators. One of the theoretical results of [54], a two-dimensional cascade model, was derived and further developed in [55]. Experimental evidence is mounting in support of the theoretical prediction that a maximum-J stellarator like Wendelstein 7-X can exhibit a significant degree of "resilience" to density-gradient-driven micro-instabilities. Two theoretical works have advanced the understanding of this [56,57]. The influence of the maximum-J property can be directly applied to the trapped electron mode (TEM), which gives rise to TEM-driven turbulence, the third main source of transport in magnetic confinement devices. With classical TEMs expected to be stable in "max-J" devices, it is important to consider a broader class of instabilities associated with trapped electrons. One work on this topic [58] identified an "ion-driven" trapped electron mode, whose resonance mechanism depends on trapped electrons but whose energy source is the ion species. Building on this discovery, a second work [59] explored the question of how the maximum-J criterion affects stability in actual Wendelstein 7-X configurations, including the important interaction it has with the ITG mode. It is in this work that the term "stability valley" was introduced to describe an overall stabilization of ITG and TEM instabilities observed as the plasma density gradient scale length becomes comparable to the ion temperature gradient scale length (see figure 16).

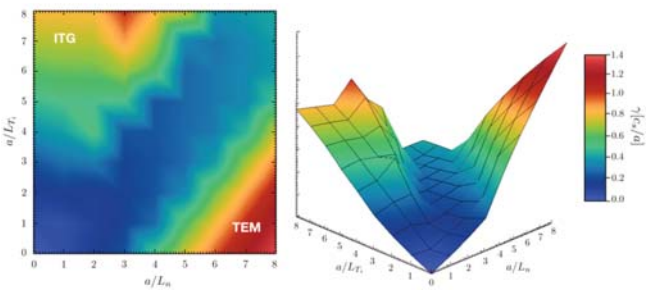

Figure 16: Stability valley of ion-scale micro-instabilities in a max-J stellarator.

This idea, and max-J stabilization in general, is being applied to explain enhanced confinement in density fuelling experiments in Wendelstein 7-X. The valley is absent in tokamak plasmas, where the increased density gradient strongly destabilises TEM modes. Moving beyond linear stability, a new and rather general measure of plasma stability was proposed, called "available energy" [60,61]. This idea has allowed, among other things, a nonlinear extension of the previous linear results for maximum-J stellarators and other devices, allowing definitive statements about the existence of turbulence-free parameter regimes.

Anticipating plasmas of increasing pressure in future experiments, and the general potential importance of magnetic fluctuations due to finite plasma β, a study of kinetic ballooning modes (KBM) has been carried out with gyrokinetic theory and simulations [62,63,64]. These works clarified basic theoretical limits relating gyrokinetics to MHD, with quantitative comparison to simulation. A full surface study revealed stellarator-specific effects on the KBM stability. In Wendelstein 7-X, increasing β was found to cause stabilization of ITG and TEM, followed by destabilization of the KBM, matching an analytic prediction. Results also hint at finite-β limits to the stability valley phenomenon. On a practical note, the work enabled the geometry code GIST to be extended to compute Mercier stability.

Global Gyrokinetics

The primary computational tool for global gyrokinetics developed at IPP is the EUTERPE code, which has been developed to enable gyrokinetic electromagnetic calculations of global modes deep into the MHD domain. The rationale is the necessity to address global stability beyond MHD in stellarators on one hand, and the desire to pave the way for simulations of electromagnetic turbulence on the other. The requirements on numerical accuracy are considerable and are tackled partly in cooperation with the NMPP division of IPP. Furthermore, the interpolation and time integration schemes have been improved on the numerical side (Hochbruck-Ostermann exponential integrator), while the numerical gyrokinetic model has been extended by including fluctuations in the magnetic field strength and E×B flow effects. The electrostatic version of EUTERPE has been used to simulate the linear instability in Wendelstein 7-X using equilibria and profiles derived from the experimental findings of the operational phase OP1.1. The focus was set on the possible impact of trapped electrons. In addition to growth rates and frequencies, secondary mode properties like power spectra and spatial mode structures were studied systematically. Using these results, a simple semi-empirical model for ITG mode structures in standard Wendelstein 7 X geometries was developed.

The mixed-variable or pullback scheme that was developed for electromagnetic simulations with EUTERPE has meanwhile been implemented and successfully tested in the ORB5 and XGC codes. As a consequence, such simulations using ORB5 have become feasible and robust for realistic plasma parameters. The method has been used to simulate fast-particle destabilisation of Alfvén modes in ASDEX Upgrade and ITER geometries as well as the interaction between Alfvén eigenmodes and microturbulence in the presence of fast particles in tokamaks. Electromagnetic simulations with the XGC have also become possible, and has enabled the transition from ITG to KBM dynamics in tokamak plasmas to be calculated [65]. EUTERPE was also used to calculate energetic-particle driven modes in LHD with dominantly low mode numbers (n=-1). Although the modes are almost marginal, numerically clean results could be found including the m=0 mode as well as two competing ones: an EAE (m=1 dominant) and an EPM (m=2 dominant) close to the TAE gap.

Global Stability and Equilibrium

A central issue in stellarator theory is the calculation of magneto-hydrodynamic (MHD) equilibria and assessing their stability. IPP Greifswald is involved in the development of several codes in this area, which are of great use for planning and evaluating experiments in Wendelstein 7-X and other stellarators.

MHD Equilibrium

The calculation of MHD equilibria for experiments in Wendelstein 7-X usually involves the VMEC code, which has been used to provide several hundred equilibrium calculations to a web service interface. The use of VMEC is, however, limited by restrictions in the computational domain and by the assumption of nested flux-surfaces, which precludes magnetic islands and regions with chaotic field lines. Divertor investigations need the field outside the VMEC boundary, and for this purpose the EXTENDER code has been constructed and is under continual development. The interplay between the two codes has recently been improved, and now allow coil systems inside the vacuum vessel such as the sweep coils in Wendelstein 7-X. The VMEC/EXTENDER approach has also been systematically validated against codes such as HINT, which allow for islands and chaotic field regions. Furthermore, several configuration studies in support of the experimental campaigns in Wendelstein 7-X have been undertaken, and particularly useful configurations for future experiments have been identified.

MHD Stability

In the field of ideal-MHD stability, work concentrated mainly on studies of experiment-related data. Examples include the investigation of plasma-pressure-induced Alfvén eigenmodes in Wendelstein 7-X [66] and the modelling of ELM-suppression in the AUG tokamak. The latter experiments rely on applied external magnetic perturbations which break the axisymmetry of the ideal tokamak equilibrium. Highly resolved, and thus computationally demanding, CAS3D stability computations reveal perturbations of the peeling-ballooning type localised

near the plasma edge. A study of ideal MHD unstable cases in the Wendelstein 7-X configuration space was undertaken in order to identify experimental scenarios in which the importance of the magnetic well can be assessed. Easing the requirement for the depth of the magnetic well potentially decreases the geometric complexity of magnetic configurations apt for fusion and would thus lead to simpler stellarators. The radial electric field present in stellarator plasmas has also been included in the calculation of sound and Alfvén spectra in Wendelstein 7-X. The code CONTI is now routinely used for diagnostic interpretation of magnetic fluctuations measured by Mirnov probes.

Wendelstein 7-X Current Quenches

Current quenches during electron cyclotron current drive in Wendelstein 7-X limit machine performance and affect machine safety, and are thus the subject of detailed theoretical modelling, both in Greifswald and in Garching. It could be shown analytically that for current profiles similar to the one in Wendelstein 7-X, the plasma can be unstable to kinetically mediated pressure-driven long-wavelength reconnecting modes of the infernal type [68]. The modes are destabilised either by the electron temperature gradient or by a small amount of current, depending on how much the rotational transform departs from unity. Related instabilities are also being investigated with a number of fluid codes such as EUTERPE and MEGA.

Fast-particle-driven Instabilities

A number of phenomena concerning the interaction between fast particles and MHD instabilities have been investigated numerically.

a) CKA-EUTERPE, the hybrid version of the gyrokinetic EUTERPE code, non-linearly evolves a pre-calculated MHD mode structure interacting with kinetic fast particles. Thanks to its speed, this code is the work horse for fast-particle studies in Wendelstein 7-X. The effect of collisions on the nonlinear saturation dynamics of TAE had been investigated in tokamaks and stellarators, and the scaling for the saturation amplitude predicted by theory is recovered in the resonance detuning regime in tokamaks (if the collision frequency is small enough). The stellarator Wendelstein 7-X is found to behave differently [69].

b) A model distribution function for the fast ions (slowing-down with steps in energy) where the relevant parameters are taken from particle-following simulations by the ASCOT code allowed for more realistic nonlinear simulations including collisions [70].

c) Nonlinear frequency chirping – and how it is affected by collisions – has been investigated in tokamaks and stellarators. It was possible to confirm several observations made in earlier works, which treated the one-dimensional bump-on-tail-model where the drive and collisions both act in velocity space. It was found that collisions act differently in the more complex simulations done here. One noteworthy consequence is that a Krook operator (restoring the distribution function) is required to achieve periodic chirping (which is often observed experimentally). Collisions in velocity space, on the other hand, are not sufficient [71].

d) Finally, experimentally observed mode activity in Wendelstein 7-X has been analysed using advanced signal-processing tools (DMUSIC and SSI). In order to understand and classify the experimentally observed frequencies, shear Alfvén continua (CONTI) and the discrete eigenmodes in the gaps (CKA) were calculated and compared with experimental measurements. Using a realistic distribution function (slowing-down) for the fast ions, it was found that the fast-ion drive is insufficient to overcome the damping due to the background plasma. This leads to the conclusion that some destabilisation mechanism (probably related to the bulk plasma gradients) is missing in the modelling [72].

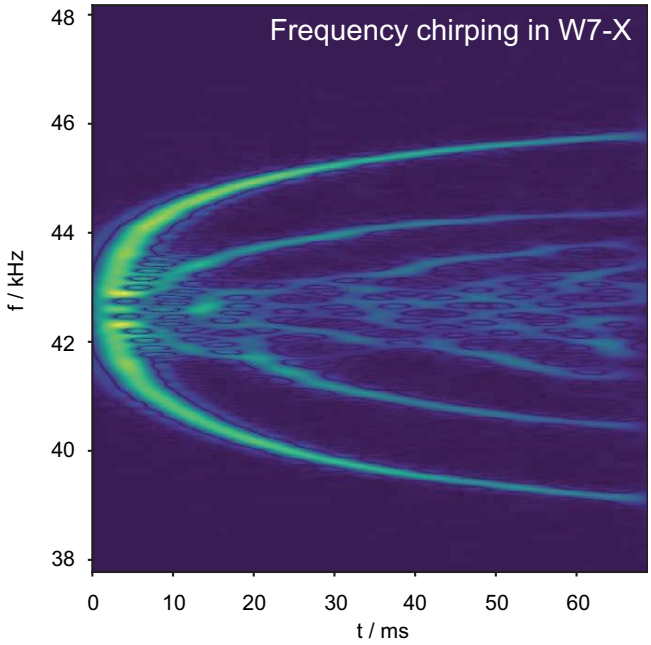

Figure 17: Frequency chirping of an almost marginal fast-particle-driven TAE mode in Wendelstein 7-X.

Other Examples of Theoretical Support for Wendelstein 7-X

Pellet Injection

Injection of cryogenic pellets into a magnetically confined plasma serves several purposes: plasma fuelling, diagnostics, and plasma termination using large killer-pellets. In Wendelstein 7-X small cryogenic pellets injected using a blower gun are used for plasma fuelling and density-profile control. The study of the pellet cloud dynamics has shown that the injection is accompanied by a considerable transfer of thermal energy from the electrons in the background plasma to the ions [73]. The reason relies on a well-known circumstance: when a plasma cloud expands into a region of lower density, the electrons, being more mobile than the ions, pull the latter with them by

setting up an ambipolar electric field, which accelerates the ions. The resulting ion heating can be significant, particularly in plasmas with disparate electron and ion temperatures, and can affect the energy balance of the plasma. In those limits where the equations describing the expansion of the pellet ablation cloud can be solved analytically, half of the energy by which the hot background plasma electrons heat the pellet cloud ends up as ion kinetic energy, which is later thermalised by collisions. In recent Wendelstein 7-X experiments, this mechanism can account for a substantial fraction of the ion heating power during pellet injection.

Baffle Load Study and Exploration of Possible Solutions

In the first Wendelstein 7-X divertor experiments with the high-mirror configuration, a permanent hot spot on a baffle plate was detected by the thermographic system, and was confirmed by post-campaign inspection of the plasma-facing components. The maximum heat load on three baffle tiles reached 4.5 MW/m^2, which is almost an order of magnitude above the design value of 0.5 MW/m^2 and thus limits plasma operation with the high-mirror configuration. A detailed analysis with the EMC3-Eirene edge transport code has been made to understand how the baffle plate, which is actually designed to screen the recycling neutrals and is therefore hidden from the hot plasma, can receive such a high heat load – a level that is normally expected only for target plates. Three main causes have been identified:

1) the three baffle tiles are radially only ~5 mm away from a main heat channel towards a target, a distance much shorter than the radial power decay length of 15-20 mm derived from the thermographic measurements in this region;
2) The three baffle tiles are intersected by field-lines that are about 30 m, which is long enough to collect a considerable amount of heat via cross-field transport;
3) The baffle tiles have locally large grazing angles.

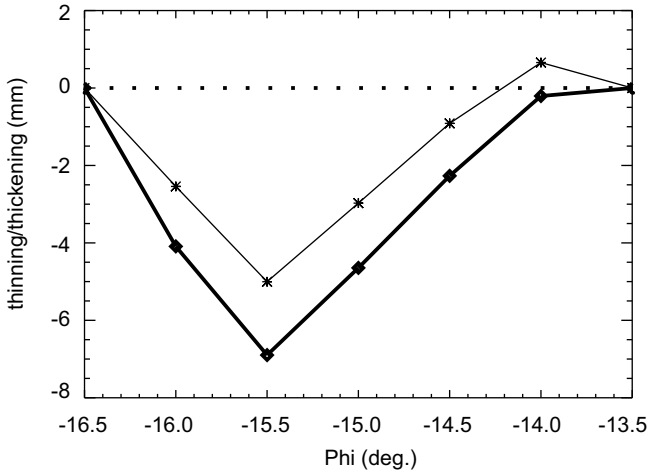

Figure 18: An option for reshaping of the heavily loaded baffle tiles calculated using EMC3-Eirene. The two optimised cases can be used as a reference for technical tolerance.

Taking the technical feasibility into account, a short-term solution has been found for OP2, in which the heavily loaded baffle tiles are reshaped (figure 18) in order to reduce the peak heat load. EMC3-Eirene simulations show that a factor-of-2 reduction of the peak load is possible by thinning 6 tiles in each divertor unit by up to 5-7 mm. Long-term solutions require either extending the vertical target to partially replace the baffle, or pulling the vertical baffle several cm outwards.

Electron Cyclotron Emission

During the OP1 experimental campaign, ECE measurements were interpreted with help of forward modelling by the TRAVIS code [74] with the Bayesian analysis framework MINERVA [75]. The accuracy of electron temperature profile reconstruction was significantly improved due to a further development of the code. In order to estimate the range of parameters required for experiments in Wendelstein 7-X with high plasma pressure, scenarios with reduced magnetic field and ECRH heating at the X3-mode for high mirror-ratio (15 % and 24 %) magnetic configurations have been performed [76].

Analysis of Plasma Current Experiments

Plasma current experiments in the Wendelstein 7-X standard configuration (EIM) have been analysed with the NTSS transport code. The measured plasma profiles were used to model the time evolution of the toroidal plasma current and the results were compared with experimental observations. Without any special measures, the toroidal plasma current in experimental program rises exponentially on the L/R time scale (usually >10 s) to its expected neoclassical bootstrap current level. The time evolution of the toroidal current can however be significantly affected by strong electron cyclotron current drive (ECCD) applied at the beginning of the discharge for a period of time shorter than L/R. The development of the plasma current current in such experiments is well explained by transport simulations with neoclassical bootstrap current and parallel conductivity calculated for the measured plasma profiles. It could thus be demonstrated through theory and experiment that it is possible to accelerate the convergence of the plasma current to its asymptotic value (that of the bootstrap current) by proper application of ECCD, whose amplitude and duration is chosen according to the theoretical modelling.

Stellarator Optimisation

Stellarators use magnetic fields that are intricately shaped in all three dimensions, and there is thus great freedom in the choice of magnetic-field geometry. The parameter space possesses as many 50 degrees of freedom, which raises the important and mathematically interesting question of how to choose the "optimal" magnetic field. To what extent can the magnetic field be tailored to maximise plasma performance? This is the subject of stellarator optimisation, which involves fundamental 3D

plasma theory and complex computations aiming at identifying the best way of designing future stellarators.

Code Development

The central computational tool for stellarator optimisation developed at IPP is the ROSE code [77]. It optimises a target function characterising an MHD equilibrium, whose properties are calculated using a number of additional codes. The shape of the plasma boundary is modified iteratively so as to seek an equilibrium with particularly favourable qualities. The code is able to address and optimise a wide range of plasma properties, including quasi-symmetry and neoclassical transport, fast-particle confinement, and MHD stability. Recent developments aim at making the code more modular and extendible. A first internal interface allows easy addition of more physics modules without the need of modifying the main code. A second interface allows users to choose their own set of free parameters and allowing them to optimise not only the plasma boundary but also other properties, such as the radial profiles of current, rotational transform or pressure. The ONSET code has also undergone recent extensions that make it capable of the first design of a configuration with permanent magnets. This capability may also be useful in the search for configurations created by magnetic-field coils of mixed topology.

Quasi-axially Symmetric Stellarators

Quasi-axsymmetric (QA) stellarators offer the prospect of achieving good fast-particle confinement in devices with smaller aspect ratio than that of other configuration types. Moreover, the inherently large bootstrap current could contribute to the rotational transform and thereby ease the requirements on the magnetic-field coils. In an attempt to identify a particularly attractive design, a scan over various possibilities within the spectrum of QA stellarators was performed, and a promising design was identified with two field periods and an unusally small aspect ratio of 3.4 [78]. It is ideal-MHD stable up to an average normalised pressure of $<\beta>=3$ % and offers better fast-particle confinement than earlier designs.

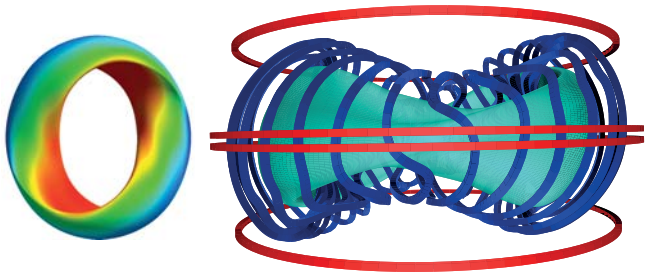

Figure 19: Outermost magnetic surface and coils set of a quasi-axisymmetric stellarator configuration identified as the results of a major design effort. The magnetic field strength is colour-coded and ranges from red (large) to blue (small).

The latter property is achieved by optimising for near-perfect quasi-axisymmetry in the middle of the confinement region rather than at the magnetic axis or the plasma boundary.

Quasi-isodynamic Stellarators

An alternative to quasi-axisymmetry is offered by quasi-isodynamic (QI) stellarators, which combine good confinement of fast particles with low bootstrap current, but have larger aspect ratios. The small bootstrap current makes these configurations suitable for island divertors, and the experimental success of Wendelstein 7-X makes QI configurations important candidates for a stellarator power plant. Nevertheless, confinement of fast particles has to be improved beyond the levels achieved in Wendelstein 7-X, where this property was optimised only in a region close to the magnetic axis. A particularly promising 6-period QI configuration with small bootstrap current and fast particle losses was identified.

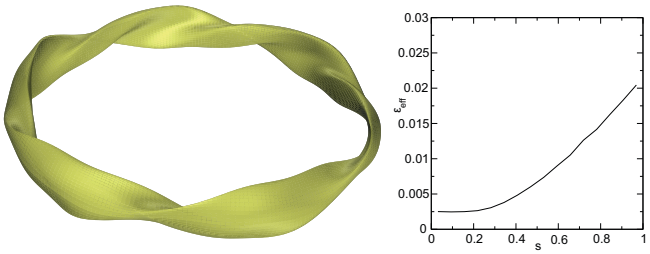

Figure 20: Left: Plasma boundary of a 6-period QI stellarator optimised for good fast-particle confinement. Right: Effective ripple of this configuration as function of normalised toroidal flux..

Stochastic Optimisation of Stellarator Coils

Not only the plasma shape needs to be tailored carefully in a stellarator. The coils creating the magnetic field also need optimisation. There are, typically, many different coil sets creating approximately the same magnetic field but no practicable coils creating exactly the desired field. A suitable compromise must thus be found, and for this purpose a novel stochastic optimisation algorithm has been developed. The initial motivation for this work was to try to improve the robustness of coil design by reducing manufacturing tolerances, but it also turned out that the coils could be simplified and higher fidelity could be achieved in the magnetic field [79,80].

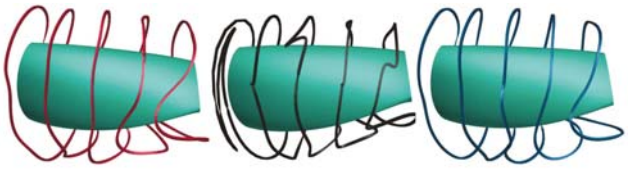

Figure 21: Coils calculated with a novel stochastic optimisation algorithm (left and right) compared with a reference case (middle) obtained by more traditional means.

Electron-positron Plasmas

Plans to create magnetically confined electron-positron plasmas in Garching are supported theoretically by an effort in the ST Division, which aim at predicting and understanding the most important properties of such plasmas. Linear gyrokinetic theory/simulations of microinstaiblities and nonlinear considerations involving the concept of "available energy" mentioned above lead to the prediction that such plasmas could essentially be free from turbulence in certain magnetic geometries. The quality of the confinement should then be excellent since the plasma is in a lowest-energy state somewhat analogous to that of the stratosphere, which is stably stratified and therefore does not support convection [81-84].

Scientific Staff

P. Aleynikov, K. Aleynikova, A. M. Arnold, C. Beidler, M. Borchardt, S. Buller, K. Camacho Mata, M. Drevlak, Y. Feng, J. Geiger, A. Hallenbert, S. Henneberg, D. Kennedy, R. Kleiber, M. Kuczynski, A. Könies, J. Lobsien, M. Marushchenko, O. Mishchenko, C. Nührenberg, J. Nührenberg, G. Pechstein, G. Plunk, L. Podavini, J. Proll, J. Riemann, G. Roberg-Clark, A. Runov, F. Sardei, B. Shanahan, C, Slaby, H. Smith, Y. Turkin, P. Xanthopoulus, A. Zocco.

Guests

S. Beguyal (Princeton University, USA), A. Brizard (St. Michaels College Colcheste, USA), J. Cao (University of South China, China), S. Dai (Dalian University, China), F. N. de Olivera Lopes (Barcelona Supercomputing Center, Spain), P. Drews (FZJ, D), J. Garcìa Regaña (CIEMAT Madrid, Spain), A. Gogoleva (University Madrid, Spain), A. Gonzáles Jerez (CIEMAT Madrid, Spain), A. Herbst (Universität Hannover, D), P. Huslage (Universität Würzburg, D), K. Kauffmann (Comisión Chilena de Energía Nuclear, Chile), S. Lazerson (PPPL, USA), C. Liotine (Princeton University, USA), M. Mikhailov (Kurchatov Institute Moskow, Russia), C. Mora Moreno (Eindhoven University of Technology, Netherlands), G. Pełka (IFPILM Warsaw, Poland), J. Proll (Eindhoven University of Technologies, Netherlands), S. Reguyal (Princeton University, USA), M. Rome (Università di Milano, Italy), J. Schmitt (Auburn University, USA), D. Schwörer (Dublin City University, Ireland), M. Stein (Universität Heidelberg, D), P. Szabo (TU Wien, Austria), A. Tanzetti (Politecnico di Milano, Italy), T. van Overveld (Eindhoven University of Technology, Netherlands), F. Vannini (Università di Milano, Italy).

Numerical Methods in Plasma Physics

Head: Prof. Dr. Eric Sonnendrücker

The division "Numerical Methods in Plasma Physics" is devoted to the development of efficient and robust computational methods and algorithms for applications in plasma physics and more specifically for the models and problems of interest to other divisions of IPP.

Structure of the Division

The emphasis of the division lies on the development of new models suited for efficient and robust simulation, the optimization and analysis of numerical methods and is tightly coupled with the group "Numerical methods in plasma physics" at the Mathematics Center of the TU Munich. Recently an important effort has also gone into model order reduction, the derivation of new machine learning tools based on Gaussian Processes and Neural Networks and Uncertainty Quantification. In addition to inventing some new methods specifically for the problem at hand, the division aims to maintain a knowledge of state of the art methods in the general area of numerical mathematics and scientific computing in order to be able to adapt them where needed to plasma physics problems. The division consists of five research groups: Kinetic Modelling, Fluid and MHD Modelling, Structure Preserving Methods, Plasma-Material Modelling and Foundations, Zonal Flows and Structure Formation in Turbulent Plasmas. Moreover, the EUROfusion High Level Support Team (HLST) is attached to the division.

3D MHD Equilibrium Code

A basic step in the modelling of a tokamak and a stellarator is to describe the confined plasma state, where the magnetic field forces balance the pressure gradient of the plasma, and where the contours of constant pressure form a set of nested tori or „flux surfaces". The problem can be derived from a steady state of the ideal magneto-hydro-dynamic equations (MHD). While in the tokamak case, the equilibrium problem reduces to solving a non-linear PDE, the two-dimensional Grad-Shafranov equation, this is not possible in the three-dimensional case, such as stellerators or tokamaks with resonant magnetic perturbations. In 3D, the existence of nested flux surfaces is not guaranteed, however, it is important for good confinement in the plasma core. Thus, the main idea of the well-established equilibrium code VMEC is to minimise the total 3D MHD energy under the assumption of closed nested flux surfaces. Given the shape of the outer surface and radial profiles for pressure and current, an equilibrium magnetic field is found via the minimisation algorithm. Adopting the same strategy as VMEC, a new 3D MHD equilibrium code GVEC (Galerkin Variational Equilibrium Code) was developed from scratch at NMPP, also revisiting thoroughly the theoretical derivations for the minimization algorithm.

A main difference to VMEC is the radial discretisation. In VMEC, the radial grid spacing is uniform in the normalised flux, which leads to a higher resolution at the outer boundary and a lower resolution at the axis, affecting the accuracy of the equilibrium solution. In comparison, in GVEC, B-Spline Finite Elements with a non-uniform grid spacing are used, allowing to accurately resolve the full radial domain including the magnetic axis and allowing local refinement of the grid. The B-Splines can be of arbitrary polynomial degree with a high continuity, which means that less radial grid points are needed for a certain accuracy, leading to a faster convergence of the minimisation algorithm. They also allow to smoothly represent radial derivatives needed to evaluate equilibrium quantities, such as metrics and magnetic field. It is possible to input VMEC solutions as initialisation in GVEC, and GVEC is benchmarked against VMEC solutions of tokamak and stellarator configurations with a fixed boundary. GVEC is already used within IPP to provide the final equilibrium solution. It can be converted back to VMEC netcdf output files. In collaboration with TOK, specific interfaces for the linear 3D MHD stability code CASTOR3D and also for the gyro-kinetic turbulence code GENE-3D were developed. In collaboration with MPCDF (M.Rampp), GVEC was fully parallelised with OpenMP, exhibiting a speed-up of 32 on 40 threads (INTEL Skylake) for a high resolution W7-X equilibrium solution.

Relaxation Dynamics and Application to Equilibrium Solvers

In several applications one needs an efficient way to compute equilibrium solutions rather than time-dependent solutions. For instance, a magnetohydrodynamical equilibrium is the needed input of many kinetic and fluid calculations. The construction of an equilibrium however can be challenging since it often requires the solution of ill-posed problems admitting multiple solutions. In many cases of interest one can characterize equilibrium points as the solutions of a constrained variational principle, which can then be solved by a constrained optimization method, but still existence of many local minima has to be addressed. A way to select a unique solution consists in constructing a fictitious time evolution which "relaxes" a given initial condition to an equilibrium point of the considered physical systems, while preserving the constraints. The term "relaxation" refers to a dynamical system in which a given function, usually referred to as entropy, is monotonically dissipated. The prototype example is the Boltzmann equation with the Landau collision operator, which was shown by Morrison to possess a specific geometric structure referred to as metriplectic. Based upon Morrison metriplectic framework, we have constructed numerical relaxation methods for two-dimensional Euler's equations, axisymmetric MHD equilibria, and three-dimensional linear Beltrami fields. An appropriate discretization via the finite element exterior calculus has been designed and tested.

Numerical Methods for Wave Propagation

Theory and numerical methods for the description of radio-frequency wave beams in fusion plasmas have been investigated due to their importance in plasma diagnostics, heating and control. Wave-beam physics is linear, yet the multi-scale nature of the problem and the complex response of the plasma to the wave field are such that several aspects of the problem still pose a challenge. We have considered in particular three issues of present interest for fusion applications: (1) wave-kinetic models for the transmission of beams through turbulent plasmas; (2) the efficient description of diagnostic beams (specifically, in reflectometry diagnostics); (3) numerical methods for cold-plasma waves. A physically complete wave-kinetic model describing wave beams with frequencies in the range of the electron cyclotron frequency in tokamaks has been implemented in the WKBeam code by the tokamak theory division; in a collaborative effort we have derived a Monte Carlo scheme for the solution of the relevant wave-kinetic equation accounting for the effect of turbulence on the polarization of the wave and we have proven mathematically that the scheme preserves the essential properties of the model. Numerical experiments show convergence to the analytical solutions in simple cases. The code WKBeam has been used in collaboration with the Swiss Plasma Center of the EPFL (École polytechnique fédérale de Lausanne) in the framework of the EUROfusion Enabling Research project RFSCAT which aimed at a comprehensive study of wave scattering in turbulent plasmas of the TCV tokamak in Lausanne. As a result of this effort, simulations and comparison with dedicated diagnostic systems on TCV have outlined a rich physics governing the average wave energy density transport: Depending on the parameters, one can have diffusive or super-diffusive broadening of the beam (cf. figure 1). From a mathematical point of view those regimes can be captured qualitatively by a reduced model which is characterized by a hypocoercive linear operator responsible for the relaxation of the beam cross-section. A detailed analytical study of this model leads to relatively simple estimates that can be used in the preparation of the experiments or in the analysis of simulation results. For the description of reflectometry beams, we have developed a prototyping code based on the idea of reconstructing the wave field around the turning point (where the beam is reflected) from the paraxial solution of a "probing packet" (a Hagedorn wave packet); since the paraxial solution is computationally very fast and the reconstruction operation can be ideally parallelized, this method is promising at least for the calculation of the beam in the plasma equilibrium, that is without turbulent fluctuations. The full problem of reflectometry beams including turbulence is usually dealt with by the direct numerical solution of Maxwell's equation coupled to the linearized, pressureless Euler's equation for the electron fluid. We have recently discovered that this model has a Hamiltonian structure and

derived the corresponding Poisson bracket. A new scheme has been designed leveraging the work on structure-preserving methods for Hamiltonian system developed within the division. This opens the way to a new class of full-wave solvers.

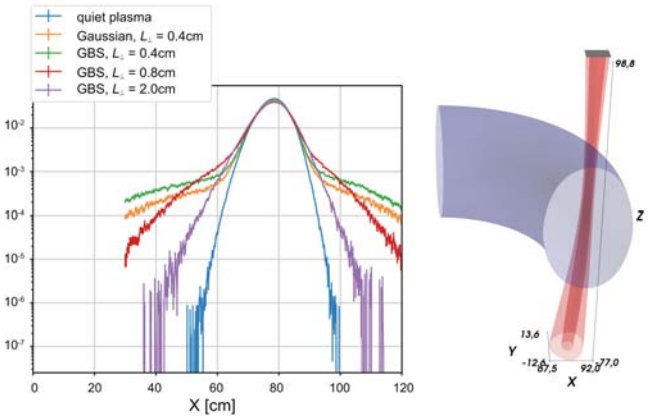

Figure 22: Left: Effects of turbulence on the beam cross-section in the TCV tokamak. Without turbulence ("quite plasma") the cross-section is Gaussian. Turbulence models, either a simple Gaussian model or more complex models based on validated simulations with the GBS code, show a transition from a Gaussian a heavy-tailed distribution basically controlled by the turbulence correlation length L. Right: Beam amplitude contours (red) and a section of the last closed surface in TCV (gray). The cross-sections are measured at the bottom.

Machine Learning and Uncertainty Quantification

Novel methods of data science and machine learning have an enormous potential to process and better understand a large variety of data from simulations and experiments at IPP. During the reporting period, members of the NMPP division participated in several interdisciplinary projects targeted at these developments: The Helmholtz Foundation grant on Reduced Complexity models, the VECMA project for verified exascale computing and the Munich School for Data Science. In addition, the division organized and hosted the 39th International Workshop on Bayesian Inference and Maximum Entropy methods in Science and Engineering (MaxEnt2019). Furthermore, there has been active involved in the Helmholtz Information and Data Science Academy and Incubator.

Quantifying Uncertainties in Simulation and Experiment

Uncertainty quantification in the results of not only experiments, but also simulations is a topic that has received an increasing amount of attention in the recent years. Complex numerical models in plasma physics and other areas depend on a number of input parameters that are often subject to uncertainties. On the one hand this includes parameters derived from measurement data which may deviate from an exact value due to limited accuracy, fit uncertainties or inherent statistical nature. On the other hand, discretization errors and statistical noise in numerical computations directly introduce additional uncertainty in simulation results.

To tackle these issues, the strategy during the recent years has been the development of tools for automatic construction of data-driven response models that leverage information from computationally expensive simulations in an efficient way. Several techniques have been implemented in the Python toolkits EasyVVUQ and proFit as well as customized high-performance Fortran codes leveraging OpenMP and MPI parallelization. The principle consists in estimation of the relation between input parameters and simulation output based on point samples in parameter space.

One way to realize uncertainty quantification uses a polynomial expansion that leads to spectral accuracy in the estimation of statistical errors and sensitivity analysis within the framework of polynomial chaos expansion (PCE). The PCE technique has been successfully applied in cooperation with FZ Jülich to EIRENE calculations for the sputtering yield at the plasma wall, and within VECMA for large-scale tokamak transport computations. Interdisciplinary cooperation was realized together with Helmholtz partners on simulation data from oceanography and river ecology within the REDMOD-project .

A second possibility leverages Gaussian process (GP) regression based on kernel functions. Besides the construction of physics-informed surrogate models discussed below, GP regression with derivative observation was applied in collaboration with the ASDEX Upgrade team to analyse experimental plasma profiles and their gradients including uncertainty information.

Machine Learning and Global Optimization

Novel machine learning methods are powerful and flexible when treating large amounts of unstructured data. In contrast to generic applications, data from physics simulations and experiments contains important structure information, usually encoded in the form of partial differential equations. Recently, special techniques of physics-informed learning via GP regression have been developed at NMPP and applied to data from wave and heat equation. The first results are promising and further investigations are planned to treat complex inverse problems in plasma diagnostics.

For dynamical systems, GP regression has been specialized to represent symplectic maps, enabling long-term stable surrogate models for Hamiltonian systems with large time-steps. To retain this structure also after reduction of degrees of freedom in particle-in-cell simulations, proper symplectic decomposition has been employed and developed further towards the collisional case.

An important topic that builds on GP regression is the construction of gradient-free global optimizers applicable to challenging inverse problems and to stellarator optimization.

Such optimizers (figure 23) construct a GP surrogate of a possibly bumpy utility function and provide an active learning strategy that balances the exploration of unknown parameter regions with local search close to a predicted optimum. Also here, physics constraints can be leveraged to provide more accurate and stable results. Based on promising recent results, global optimization methods are planned to be investigated further and applied to challenging problems in plasma physics during the coming years.

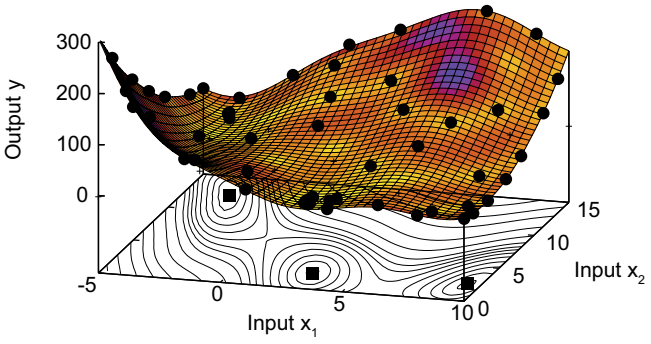

Figure 23: All minima of a 2-D Branin-surface (indicated by filled squares at the bottom) were successfully located by the GP global optimization approach. The superimposed color represents the utility for the expected utility of function evaluations at these locations.

Geometric Electromagnetic Particle-in-cell Methods

The Vlasov-Maxwell system exhibits a Hamiltonian and a variational structure. Related to the symmetries in Hamiltonian and Lagrangian, respectively, the system features a number of conserved quantities. Numerical discretizations that conserve these symmetries have favorable stability behavior. In particular for simulations over long time and where microscale features are underresolved structure-preserving methods can provide solutions, that are physically more correct than those obtained with standard methods. In the group, we have developed a framework of structure-preserving particle-in-cell discretizations of the Vlasov-Maxwell model. The Vlasov equation is discretized with a standard particle-in-cell method and the Maxwell's equation based on a discrete de Rham complex. By a rigorous analysis we have shown that this general framework is sufficient to provide a discrete Hamiltonian structure for the variational semi-discretization of the Vlasov-Maxwell equations. We commonly use compatible spline finite elements for the structure-preserving discretization of Maxwell's equation, but have also considered mimetic finite difference and the Fourier-de Rham complex. In particular, for spectral field solvers we have derived new particle coupling schemes that are both local and compatible with the de Rham structure, while allowing arbitrary smoothing and back-filtering techniques. Moreover, they lead to very good energy and momentum conservation properties for the discrete schemes.

A structure-preserving algorithm on curvilinear meshes with compatible B-spline finite element has also been obtained as a first steps towards simulating complex geometries.

For the temporal discretization, a Poisson integrator has been developed based on a Hamiltonian splitting that yields explicit integration of the particle equations of motion on Cartesian grids. In a collaboration with Aalto University, we have also derived an explicit and an implicit subcycling scheme based on a discrete variational principle that allows for multi-scale time stepping in multi-species simulations. On the other hand, energy-conserving schemes have been derived based on the discrete gradient method, a semi-implicit scheme and a fully implicit scheme where the latter also conserves the divergence constraints. Energy-conserving schemes can also be enriched by substepping techniques. A prototype code has been developed within the SeLaLib library and a current effort is on an implementation for low-order finite difference based on the exascale software tool WarpX. This offers also mesh refinement capabilities and support for embedded boundaries which can prove useful for future enhancements towards complex geometries. This project has received funding from of the Bavarian Competence Network of Technical and Scientific High Performance Computing (KONWIHR). Together with the MPCDF, we have also evaluated the use of performance portability frameworks for particle-in-cell simulations. Our experiments have shown that Kokkos can yield rather good results without spending too much effort as a programmer.

Collisions Operators

Many conservative systems in physics feature a Hamiltonian or variational structure, that is their dynamics can be described in terms of a bilinear operator, called Poisson bracket, and an energy functional, called the Hamiltonian or in terms of an action principle. In order to include certain non-ideal effects, such as collisions in kinetic models, these formulations can be extended: the Hamiltonian formulation by a metric bracket and an entropy functional that is dissipated, leading to the so-called metriplectic framework; and the variational formulation by the inclusion of forcing terms, leading to the Lagrange-d'Alembert framework. These formulations feature a rich geometric structure including conservation laws that are sought to be preserved in computer simulations in order to describe the underlying physics correctly, in particular the laws of thermodynamics.

We developed a novel framework for the discretization of the nonlinear Landau and other operators that describe the macroscopic effects of collisions. Using a Discontinuous Galerkin or Finite Element discretization for the velocity space, we transform the infinite-dimensional metriplectic system into a finite-dimensional, time-continuous metriplectic system. Temporal discretization is accomplished using discrete gradients.

The same techniques can be applied to particle methods, where they provide evolution equations for the particle weights. The resulting integrators feature exact conservation of mass, momentum and energy as well as monotonous dissipation of entropy (H-Theorem).
Collisions can also be modelled microscopically by stochastic processes. To enable the structure-preserving simulation of such processes, we developed variational integrators for stochastic forced Hamiltonian systems. The derivation is based on a stochastic discrete Hamiltonian which approximates a generating function for the stochastic flow of the Hamiltonian system. The generating function is obtained by introducing an appropriate stochastic action functional and considering a stochastic generalization of the deterministic Lagrange-d'Alembert principle. Our approach presents a general methodology to derive new structure-preserving numerical schemes. The resulting integrators satisfy a discrete version of the stochastic Lagrange-d'Alembert principle, and in the presence of symmetries, they also satisfy a discrete counterpart of Noether's theorem. Mean-square and weak Lagrange-d'Alembert Runge-Kutta methods have been constructed, showing superior long-time numerical stability and energy behavior compared to non-geometric methods.

Reduced Order Models

Reduced order models (ROMs) aim to capture the behavior of a complex system while at the same time saving computational cost. For parameter-dependent systems, such ROMs can be developed using the results of sample 'training' runs using select parameter values to then simulate the system for numerous other parameters using the cheap ROM. This is particularly attractive for many-query applications (e.g. parameter optimization) or real-time simulations (e.g. control problems). We have started investigating several recently proposed algorithms for ROM generation and applied them to kinetic charged particle models. The focus is at guaranteeing stability of the reduced simulations, aided by conserving select physically important properties (Hamiltonian structure and/or conserved quantities) of the full order model. For simple problems, speed-ups of an order of magnitude can be achieved this way. More complex problems, for example involving self-consistent electromagnetic fields, prove to be more difficult to reduce. First trials were able to approximately half the simulation time while reproducing important diagnostics of the system within error margins of less than two percent.

Zonal Flows and Structure Formation in Turbulent Plasmas

Zonal flows (ZF), plasma spanning turbulence generated large scale flows, are not just accessory parts but exercise an important effect on the overall intensity of the turbulence and the associated particle and heat transport in plasma confinement devices like tokamaks. While they exist essentially everywhere in the confined plasma, probably their most important, yet still not understood action occurs at the boundary (or edge) of the plasma in relation to the low-to-high confinement transition (L/H). Apart from the highly nonlinear nature of this plasma region with fluctuation amplitudes of order of 100 %, collisions tend to become important in this region.
Central subjects of the group have been the linear collisionless and collisional physics of the zonal flows and their oscillating variant, geodesic acoustic modes (GAM), as well as the proper and equivalent treatment of the collisional edge turbulence by fluid, gyrokinetic codes and, lastly, using a 6D fully kinetic framework without the assumption of approximate Larmor-orbits.

Linear GAM and Zonal Flow Damping by Electrons and Collisions

As a starting point the Braginskii equations for the fluid code NLET and the at present most sophisticated gyrokinetic Sugama model collision operator for the collisional gyrokinetic code CGYRO as well as several analytical estimates in literature have been used to calculate and compare the collisional linear physics of the ZFs and GAMs, both with adiabatic (i.e. passive) and real electrons. Generally, it was found that the analytical damping rates of GAMs and ZFs are of low quality as soon as collisions are switched on, even with adiabatic electrons. Moreover, the damping of GAMs by electrons is in practise always important close to the tokamak edge. Thereby the GAM and ZF physics depends very much on the quality of collision operator. Physically correct results require at least the gyrokinetic Landau collision operator and not just a model operator.

Matching of Fluid and Gyrokinetic Turbulence Simulations Targeting the Edge

Edge-relevant high-gradient collisionless ITG turbulence simulations robustly yield very similar results for two-fluid and gyrokinetic framework, as long as the turbulence is sufficiently strongly driven and the two-fluid equations are augmented with reduced transport coefficients that take into account the maximum kinetic fluxes due to the thermal particle velocity. However, even with the Sugama collision operator it turned out to be surprisingly difficult to obtain correct gyrokinetic turbulence simulations for very collisional resistive ballooning scenarios, which on physical grounds must agree with the fluid simulations because of the short mean free path. Here, the numerical dissipation at the high wavenumbers turned out to be critical, since the wave dispersion is much lower than for the collisionless cases. As an example, see snapshots of the quite dispersive high gradient ITG mode turbulence and of the hardly dispersive resistive ballooning turbulence for gyrokinetic simulations (figure 24): It is quite visible that the ITG case is much smoother and shows less fine scale structures than the ballooning case.

With density gradient driven turbulence (without temperature gradients), the resistive ballooning simulations agree perfectly (~10 % in the transport) between two-fluid and gyrokinetic simulations, as expected. But with ion or electron temperature gradients providing the drive to the turbulence, the turbulence intensity turns out to be quite different by a factor ~3.

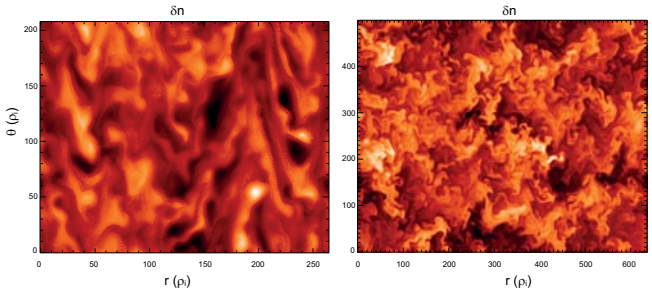

Figure 24: Snapshot of density fluctuations in poloidal cross section of gyrokinetic collisionless high-gradient ITG (left) and very collisional resistive ballooning simulation (right); left figure is very dispersive, while right figure is hardly dispersive and shows fluid like turbulence structures and details.

Guided by this specific mismatch we analysed the effective ion and electron transport coefficients within the gyrokinetic code (based on the Sugama model operator) and compared these with the Braginskii values (based on the Landau collision operator) used by the fluid code and found specifically for the ion heat conduction an error of 50 % within the gyrokinetic results. But also the Braginskii model is erroneous due to the assumption of infinite ion/electron mass ratio and several overlooked transport processes.

Gyrokinetic Landau Collisions

Motivated by the above, great progress has been made in the development of a machine precision linearized gyrokinetic Landau collision operator. This comprises with equal importance the matrix elements for the gyro-centre transformed collision operator for the gyrokinetic simulations, and a translation of the gyrokinetic collisions into Braginskii style fluid transport coefficients. The achieved accuracy is with 11-16 digits far greater than the currently known approximations (0-4 digits) and the computation is not limited to only two species or the infinite-mass-ratio approximation.

6D Kinetic Simulation of Tokamak Turbulence

Semi-Lagrangian 6D Vlasov codes are a possible way out of the dilemma posed by the extreme conditions at the tokamak edge (high gradient, fluctuation levels and collisions), albeit at large computational cost, which however may be subdominant in the beginning age of exascale-computing.
Using the semi-Lagrangian 6D Vlasov code BSL6D, unsheared slab ITG turbulence runs were carried out. This type of run can be carried out with periodic boundary conditions and for adiabatic electrons, which reduces the computational domain requirements and, due to the elimination of the plasma waves, the required time resolution is only of order of the ion gyrofrequency. Comparing the runs with gyrokinetic runs with the same parameters, very good agreement was found for the linear growth rate and frequency, and similar saturation level. A striking difference to the gyrokinetic results is the excitation of modes close to harmonics of the ion Larmor frequency (modified ion Bernstein waves) during the turbulence saturation (figure 25), whose investigation is currently under way.

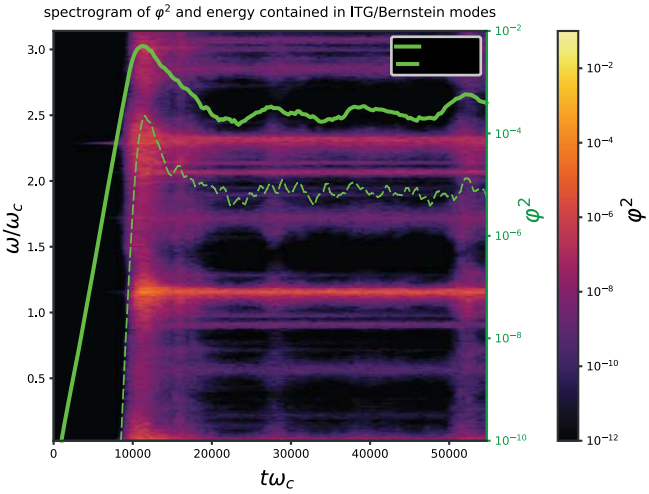

Figure 25: Energy content versus time for the turbulence modes and ion Bernstein waves as logarithmic plot and color coded as spectrogram; the linear growth phase is well recognisable before $t\omega_c = 10\,000$, the ion Bernstein waves are around the multiples of 1.15 ω_c.

Kinetic-fluid Hybrid Models

Plasma waves in magneto-hydrodynamic (MHD) fluids can be resonantly excited by energetic particles (EPs) with thermal speeds much faster than ambient particles, e.g. in the range of the Alfvén velocity in Fusion devices, or a fraction of the speed of light as in space. Such wave-particle interactions are observed for instance in deuterium-tritium fusion reactors, where hot α-particles can destabilize shear Alfvén modes and thus compromise confinement time. Another example is the interaction of energetic electrons in the solar wind with Whistler waves propagating in Earth's magnetosphere. This interaction can lead to new types of electromagnetic waves whose spectrograms show discrete elements with rising or falling frequencies with respect to time (also known as frequency chirping). The dynamics of such processes is inherently nonlinear and evolves on long time scales compared to the cyclotron period or the thermal transit time of plasma particles. Numerical studies are thus challenging, as they require an accurate and stable solution of nonlinear PDEs over long periods of time. Our approach towards this goal is two-fold:

a) work with appropriate reduced models that represent a suitable compromise between physics content and numerical cost (→ kinetic-fluid hybrid (KFH) models), and b) use modern numerical methods that guarantee long-time stability and accuracy (→ structure-preserving finite elements with particles-in-cell – GEMPIC.) The principle of KFH models is to describe the bulk of the plasma by fluid equations and the energetic particles by a kinetic equation. Hence, the costly kinetic equation (5D or 6D phase space) is to be solved only for the minor population of EPs, while the relatively "cheap" fluid equations (3D configuration space) describe the majority of the plasma. Moreover, in case the plasma bulk is described by the MHD equations, the simulation of Alfvén waves is straight-forward, and the effect of EPs on these waves can be readily identified. In our KFH group we focus on the Hamiltonian kinetic-MHD current coupling and pressure coupling models, as well as various Vlasov-Maxwell models with mass-less electrons, including drift-kinetic approximations. In the last years we have carried out several asymptotic derivations of these models, clarifying their validity in typical magnetic fusion scenarios. GEMPIC methods allow for a structure-preserving integration of the derived KFH models; this means that important conservation properties of the continuous model such as energy, magnetic topology, div(B)=0 and others can be transferred to the discrete level. This guarantees the long-time stability and accuracy needed for describing the target physics. For the purpose of writing codes for the various KFH models we developed a Python library for the GEMPIC framework called "Hylife" (Hybrid finite element library). The library provides a sequence of finite element spaces, along with suitable projection operators into these spaces that allow for a structure-preserving discretization of hyperbolic PDEs. The basis functions are high-order B-splines on 1D, 2D and 3D tensor-product grids. Mapped domains are allowed and the corresponding pullback- and pushforward operations are provided in Hylife. For costly operations the library uses Fortran kernels, which are included via the Python-to-Fortran converter "pyccel". This allows to combine the high-level Python features with Fortran computing speed. Up to now, two KFH codes have been developed based on Hylife:

STRUPHY (STRUcture-Preserving Hybrid Code)

This code implements the current coupling MHD-Vlasov hybrid model in 3D for arbitrary mapped domains (without singularity). The MHD part is linear for the moment, but the particle-field coupling is fully nonlinear. The EPs (Vlasov) are parallelized using MPI. In a first publication we could show that STRUPHY exactly preserves the initial energy for a shear Alfvén wave test case; it also conserves div(B)=0 and the mass up to machine precision, irrespective of mesh parameter and metric coefficients, and for arbitrary long time, i.e. deep into the nonlinear phase. The time stepping is implicit for the MHD part but explicit for the EPs. This leads to a time step constraint due to the cyclotron motion. In order to remedy this fact we plan to replace the full orbit Vlasov equation by a drift-kinetic equation in the near future and by a fully gyrokinetic equation afterwards. We also plan to investigate asymptotic-preserving particle pushers such as the Pauli-particle method, which could be directly implemented in the current version of STRUPHY.

HYCHO (HYbrid Code for CHOrus Waves in Space)

HYCHO was the first code developed within Hylife and was also used as a testing ground for the further development of the library. It is a code for the 1D cold plasma equations coupled to the full-orbit Vlasov equation for the EPs. HYCHO allows for non-homogeneous magnetic backgrounds, such as dipole fields, which enables the efficient simulation of chorus waves chirping in space plasmas. The code has very similar features to STRUPHY (structure-preservation, MPI parallel), but it is still limited to just one spatial dimension. The next development steps are the extension to 3D within the Hylife framework.

The Pyccel-Sympde-Psydac Software Framework

In order to facilitate the use of advanced numerical tools related to Finite Element Exterior Calculus that preserve the structure of the underlying model, we are developing a software framework based on Python. The user only needs to input the equations describing the model and some discretization parameters in a python script. The code is then generated automatically and is parallel. It can be accelerated if needed by converting parts in Fortran using the Pyccel tool. The individual software pieces are the following:

Pyccel

Pyccel is a static Python-to-Fortran compiler, which uses type inference to assign a Fortran datatype to every variable in a Python code. In order to initiate this automatic process, the user only needs to declare the types of the function arguments through simple annotations. The generated Fortran code can be called from Python and is consistently faster than popular alternatives (Cython, Numba, Pythran). Pyccel is written in Python 3, is targeted at high-performance computing applications, and supports OpenMP pragmas and direct calls to BLAS & LAPACK.

Recently implemented features encompass an improved handling of multi-dimensional Numpy arrays, the support for Python tuples, booleans and recursive functions, the ability to allocate arrays on stack memory, an improved type-inference algorithm able to traverse all modules in a large project, multi-platform support (Linux, macOS, Windows), and a simple installation procedure with pip (Python package manager). Moreover, a recent change in the parser and the refactoring of our abstract syntax tree has drastically reduced the time

required for parsing large Python files. We are currently implementing a C printer for Pyccel, which allows to generate C code instead of Fortran, and we are working toward removing f2py from our dependencies which would allow to support Python classes.

Sympde

Sympde is an extension of the Sympy Python library for symbolic calculus.
It provides a symbolic description of partial differential equations in weak form, thanks to differential operators, integrals, function spaces, coordinate transformations. It can handle mapped multi-patch domains, DeRham sequences, and push-forward and pull-back operators.

Psydac

Psydac is a high-level finite-element library in Python 3, that uses high-order splines, mapped domains and MPI parallelization. In order to use Psydac, the user provides a geometry analytically or through an input file, and then defines the model equations in symbolic form (weak formulation) using Sympde, which provides the mathematical expressions and checks the semantic validity of the model. Once a finite element discretization has been chosen, Psydac maps the abstract concepts to concrete objects, the basic building blocks being MPI-distributed vectors and matrices. For computationally intensive operations (matrix and vector assembly, matrix-vector products, etc.), Psydac generates ad-hoc Python code which is accelerated using either Numba or Pyccel. It can in particular handle inhomogeneous Dirichlet and Neumann boundary conditions, second-order differential operators, mixed finite-element formulation for system of equations, the Nitsche penalty method for Dirichlet boundary conditions, and multi-patch domains. Currently undergoing is the implementation of a finite element exterior calculus (FEEC) framework.

Scientific Staff

C. Albert, J. Ameres, T. Blickhan, C. Bressan, M. Campos Pinto, B. Dingfelder, A. Dodhy-Würsching, J. Dominguez, E. Franck, F. Fambri, M. Gaja, I. Garnelo Abellanas, L. Guidi, Y. Güclü, S. Hadjout, K. Hallatschek, R. Hatzky, F. Hindenlang, O. Hoenen, K. Kormann, M. Kraus, J. Lakhlili, N. Legouy, O. Luk, O. Maj, M. Mazza, L. Mendoza, D. Nille, H. Oberlin, F. Patritzi, B. Perse, R. Preuss, K. Rath, A. Ratnani, M. Räth, M. Restelli, B. Scott, G. Strohmayer, C. Tronci, N. Tronko, T. Tyranowski, U. von Toussaint, A. Yurova, E. Zoni.

Guests

K. S. Kang (TU München, D), S. Possanner (TU München, D), M. Khallaayoune (Sup Galilée, Villetaneuse, FR), B. Rubino-Moyner (CNRS Orléans, FR).

High Level Support Core Team

Head: Dr. Roman Hatzky

Tasks of the High Level Support Team

Already with the start of the EFDA HPC for Fusion (HPC-FF) project in 2009, it became clear that it is insufficient to only provide a dedicated HPC machine for the European fusion community. Therefore, the High Level Support Team (HLST) was established to make an optimal use of the hardware possible. Since then, the HLST has provided support to scientists from all EUROfusion Research Units (RUs) for the development and optimisation of their codes on the dedicated HPC machines of EUROfusion. The current machine is MARCONI-FUSION, which is hosted by CINECA in Bologna, Italy. It has a compute power of about 10 petaflop/s. Furthermore, the HLST has had a bridging function between the users on the one side and the system and vendor personnel on the other side, to guarantee an efficient handling of the users' support requests on EUROfusion HPC machine issues.
The HLST support currently covers the following tasks:

- Parallelise codes using e.g. OpenMP and/or MPI standards for massively parallel computers;
- Improve the performance of existing parallel codes, both at the single node and inter-node levels;
- Provide support for high performance parallel I/O;
- Support the transfer of codes to new multiprocessor architectures like MIC and GPU;
- Choose or, if necessary, adapt algorithms and/or mathematical library routines to improve applications on targeted computer architectures;
- Give feedback to the community based on experience gained from specific project work;
- Provide guidance to young scientists on available training activities in HPC, including upcoming new computer architectures;
- Provide consultancy to scientists within the RUs working on HPC;
- Assess the "MARCONI-FUSION" tickets submitted by the users to the user support of CINECA;
- Monitor and improve the performance of the "MARCONI-FUSION" supercomputer.

In the middle of 2020, the HLST consists of a core team of seven persons based at the Max-Planck-Institut für Plasmaphysik in Garching plus five persons situated at EUROfusion consortium associates, i.e. Barcelona Supercomputing Center (BSC), Dublin City University (DCU) and Swiss Plasma Center (SPC). The team members are HPC experts with a background in developing large scientific applications. They are specialists in numerical algorithms and parallel computing. The work force of HLST consists of 10 ppy/y and the average number of projects finished per year is approximately twelve.

Over its operational time of eleven years, the HLST provided support through more than 130 projects with principle investigators from 14 countries. This enabled RUs from all over Europe to get access to HPC support. Especially the smaller RUs benefited from this opportunity, as it is more difficult for them to obtain high quality HPC support using local resources. The success of the HLST proves that it is not sufficient to only provide access to HPC resources. Additionally, it is necessary to provide access to high quality HPC support to the scientists of EUROfusion.
The HLST uses its web site *https://www.efda-hlst.eu* to disseminate the annual reports of the HLST core team. These documents accumulated to approximately a thousand pages and give detailed insights into the outcome of the HLST projects of the core team. Their purpose is twofold: on the one hand, they are a specific knowledge base (how-to manuals) of HPC within EUROfusion and on the other hand, they provide full transparency on how the HLST resources are spent.
From 2017 to 2020, the HLST core team has been involved in 29 different projects submitted by scientists from all over Europe. As an example, we present an overview of the work being done for three of these projects.

CINCOMP Project

We performed different benchmarks and tests in order to determine the performance of the A2 (Intel Knights Landing) and A3 (Intel Skylake) partitions of MARCONI-FUSION. Issues were found that significantly limit their use. The MARCONI support team resolved many of them, a few, however, are still under investigation.
The so-called "three code benchmark", consisting of production codes in fusion, was executed regularly in order to check the stability of MARCONI-FUSION in terms of the execution time for real production codes. It was found that the wall clock time of codes could fluctuate significantly from one run to the next. Fluctuations in the execution time of more than 20 % for the A3 partition were detected. The fluctuation problem seems to be related to the MPI communication in combination with the Intel Omni-Path interconnect.
A modified version of the "three code benchmark" was developed in order to determine the performance of the GPU cluster MARCONI100. This cluster went into operation in April 2020 and is based on the IBM POWER9 architecture and NVIDIA Volta GPUs. In addition, low-level benchmarks like the STREAM benchmark, show a high memory bandwidth for MARCONI100's hosts (95 % of the theoretical value) and GPUs (94 % of the theoretical value). Around 90 % of the peak performance was reached with the DGEMM benchmark on the GPUs. The NVIDIA NVLink test provides high, very stable and symmetric bandwidth between all pairs of CPUs and GPUs for both Host to Device and Device to Host communication.

FLUXO Project

The high order 3D Discontinuous Galerkin code Fluxo was developed to solve the 3D full MHD equations, including nonlinear and resistive terms. It has an explicit time integration and uses unstructured hexahedral meshes. The code aims to improve the scalability of 3D non-linear MHD simulations of fusion plasmas. Fluxo is pure-MPI parallelised and production runs of O(10,000) MPI ranks are possible.
The OPT-DG projects pursued the strategy to improve the single-core performance of Fluxo via explicit vectorization techniques using the AVX-512 instruction set available on the Intel Skylake architecture. Profiling the code exposed the computationally intensive routines. These were kept in a reduced version of Fluxo, which was introduced to facilitate subsequent analysis and modifications. A series of code refactoring changes were made to improve the re-usage of data stored in memory and/or reduce the number of retired FLOPs. This yielded considerable gains for Fluxo's standard discretization method, with speedups of about a factor of two compared to the fastest variant of the original code. However, for the more demanding entropy-conserving discretization method, the figures were considerably more modest, reaching only improvements of 5-10 %.
Intel VTune showed that there was an underutilisation of the hardware vector resources. A suite of simple tests mimicking Fluxo's array memory layout allowed to develop an understanding for why this was so, even though no data-dependencies were present in the computationally heavy loops. They could then be vectorized by ensuring that the array dimension targeted for vectorization was contiguous in memory. This involved performing several local data transpositions to change the order of the array indexes accordingly. Even though these operations introduced some overhead, the gains coming from a more efficient usage of the available vector registers largely superseded it. While the vectorization gave an additional increase in performance for the standard discretization, which could reach a total speedup of about a factor of three compared to the original code, it was the gains yielded for the entropy-conserving discretization that really showed the importance of exploiting vectorization in modern computer architectures. Compared to the original code, or even to its refactored counterpart that is only marginally faster, the vectorized (simplified) Fluxo code could reach the same solution four times faster.

PICOPT/MULTIKIN Project

The PICOPT, PICOPT2 and MULTIKIN projects investigated future directions for efficient gyro-kinetic PIC simulations and performed meaningful optimisations. The initial efforts comprised researching the current status of community codes and future HPC paradigms (GPUs, vectorization and performance portability), as well as the familiarisation

with the underlying theory. Utilising this knowledge, the performance of EUTERPE's particle pushing algorithm was approximately doubled by code reordering and implementing explicit vectorization OpenMP directives. Investigations into EUTERPE's load balance uncovered and solved a problem related to the linking step with Intel compilers, which had reduced the performance of EUTERPE by up to 27 % (wall time). Finally, the possibility of re-implementing important EUTERPE kernels in Kokkos, in order to achieve performance portability, was analysed.

Scientific Staff

T. Fehér, K. S. Kang, S. Mochalskyy, N. Moschüring, P. Nair, T. Ribeiro, P. S. Verma.

Max Planck Princeton Cooperation

Max Planck Princeton Research Center for Plasma Physics

Head: Prof. Dr. Sibylle Günter, Prof. Dr. Per Helander

MPPC was established in 2012 as a framework for collaboration between the Max Planck Institutes for Plasma Physics, Astrophysics and Solar System Research on the one hand, and the Princeton Plasma Physics Laboratory and Department of Astrophysical Sciences on the other. It has resulted in common research projects and exchange of staff between Germany and Princeton. Recent workshops have been held in Greifswald (2017), Princeton (2018), Tokyo (2019) and Göttingen (2020).

Stellarators with Permanent Magnets

Stellarators, tokamaks and other devices for fusion plasma confinement use electromagnets to create the magnetic field. In the case of stellarators, the required magnetic-field coils can be very complicated and contribute significantly to the overall cost of the device. In a PPPL-Greifswald collaboration, it could be shown that permanent magnets can be used to shape the plasma and drastically simplify the coils [1]. Permanent magnets cannot create toroidal magnetic flux but they create poloidal flux and thus twist magnetic field lines. Toroidal-field coils are therefore unavoidable, but much (or all) of the plasma shaping could be accomplished by permanent magnets. In contrast to coils, they can easily be arranged in complicated patterns and do not require power supplies or cooling, but suffer from other disadvantages, such as limitations in field strength, non-tunability, and the possibility of demagnetization. The central mathematical question is how to arrange permanent magnets to produce a desired magnetic field inside the plasma.

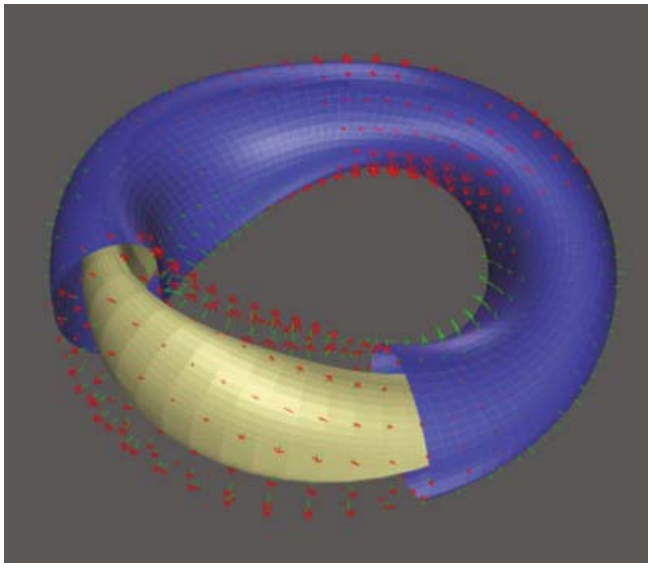

Figure 1: Magnetization vector field of permanent magnets shaping a quasi-axisymmetric stellarator plasma.

It could be shown that this problem is mathematically no more difficult than that of finding suitable coils in ordinary stellarator design. There is great freedom in the choice of how to place the permanent magnets, and this freedom can be used to minimise the volume required by the magnets and to optimise plasma access.

Electromagnetic Effects in Microinstabilities of Wendelstein 7-X Plasmas

The design of Wendelstein 7-X was based on a comprehensive optimisation effort, where the magnetic field was carefully tailored to maximise plasma performance insofar that this could be calculated at the time. Thanks to the separation of regions with "bad" magnetic curvature and trapped particles, it has been found that the magnetic geometry of W7-X exhibits favourable properties concerning microinstabilities. Accordingly, in the landscape parameterised by the density and temperature gradients, electrostatic ion-temperature-gradient-driven (ITG) modes and trapped-electron modes (TEM) are avoided in an instability-free "valley" that forms at intermediate values of the gradients [2,3]. However, if the plasma pressure is increased, electromagnetic effects can modify this picture significantly. To some extent, the increased pressure can stabilise both ITG and TEM modes, but kinetic ballooning modes (KBMs) can become unstable. Analytical and numerical studies of these modes show major changes in the stability landscape for high-pressure plasmas, which could be important for turbulent transport. In addition, they could also be connected to MHD-like events that are observed during high-density operation in Wendelstein 7-X.

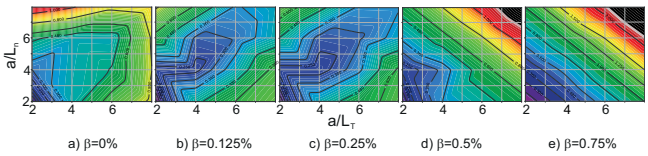

Figure 2: Growth rates (colorcoded) as a function of normalised density and temperature gradients, a/L_n and $a/LT_{i,e}$, normalised wavelength ky in the range from 0.05 to 3.0, Wendelstein 7-X standard configuration (FTM, "bean" tube).

Sawtooth Crashes in Wendelstein 7-X

In Wendelstein 7-X, the vacuum rotational transform, ι, has a rather small shear and does not cross any major rational surfaces. Nevertheless, during plasma operation it can be modified by electron cyclotron current drive (ECCD) in such a way that the resulting ι profile passes through low-order rational values, potentially triggering magneto-hydrodynamic (MHD) events. Indeed, Wendelstein 7-X plasmas are sometimes subject to repetitive collapses of core confinement during co- and counter ECCD in the plasma core [4]. The large crashes are usually accompanied by a noticeable (~0.6 kA) jump in the total plasma current.

Even though the exact origin of the plasma instability is not entirely clear, the fast crash is likely to involve the formation of magnetic islands and magnetic reconnection. One of the key questions is what happens to the plasma as a result of these events. Based on the assumption that, in such a crash, the plasma seeks to minimise its magnetic energy while keeping the magnetic helicity and toroidal flux constant, a mathematical model based on Taylor relaxation was adopted to predict the nonlinear evolution of the plasma current.
To calculate the pre-crash equilibrium VMEC equilibrium code is used, while post-crash equilibrium relaxed states are calculated using SPEC (Stepped Pressure Equilibrium Code) code. SPEC can find minimum plasma-energy states, subject to the different constraints, in nested sub-volumes, by extremising the energy functional. The results are in semi-quantitative agreement with the experimentally observed current jumps during large crashes in Wendelstein 7-X.

Seeding of Tearing Modes by Internal and External Perturbations in Tokamaks

Magnetic reconnection is common in both astrophysical and fusion plasmas. In tokamaks, it is important, for instance, in the "seeding" and development of tearing modes. In case of forced magnetic reconnection, the drive for the tearing mode is provided either by background MHD instabilities (sawteeth, fishbones, edge-localised modes (ELMs), etc) or by external magnetic perturbations. As a result, the mode can appear at much lower values of normalised pressure (β_N) than the onset value where the seed island from noise. This type of tearing mode formation is considered to be one of the most dangerous ones for future fusion devices like ITER. Experimental investigation of forced tearing-mode seeding in ASDEX Upgrade and DIII-D shows that internal crash events (sawteeth and fishbones) create a kink mode at the resonant surface where the island will be formed. This kink has the same helicity as the subsequent island, and simple magnetic measurements are not able to distinguish between kink and island structures. Local ECE measurements show that the kink is coupled to the internal post-crash activity and evolves into an island on a longer timescale than the crash time and, moreover, is delayed with respect to the crash. It is demonstrated that this observation is valid both for high and low β_N discharges. This seeding process is sensitive to the plasma rotation profile, in particular the difference in the rotation frequencies between a seed perturbation and the resonant surface. The process itself is similar to the seeding of NTMs with external perturbations, which was also investigated in ASDEX Upgrade both numerically and experimentally. Numerical studies with the nonlinear MHD code JOREK demonstrate all three phases of mode seeding observed in the experiment with external perturbations: (1) slow-down of the plasma rotation, where the kink mode is important; (2) optimal rotation for best flux penetration accompanied by fast island growth; and (3) non-linear evolution of the island. Hysteresis in the island size evolution between the current ramp-up and current ramp-down in external coils was also observed, as analytically predicted.

Scientific Staff

K. Aleynikova, F. Atour, A. Banon Navarro, K. Camacho, M. Drevlak, T. Görler, J. Graw, S. Günter, P. Helander, S. Henneberg, M. Hölzl, V. Igochine, F. Jenko, M. Kuczynski, P. Lauber, D. Michels, G. Plunk, R. Ramasamy, D. Told, X. Wang, M. Weidl, A. Zocco.

Guests

M. Cole (PPPL, USA), G. Hammett (PPPL, USA), R. Mukherjee (PPPL, USA).

Plasmas beyond Fusion

Plasma for Gas Conversion

Head: Prof. Dr.-Ing. Ursel Fantz

Low temperature plasmas (non-equilibrium or thermal) are very promising as an efficient method for storage of energy via conversion of CO_2 into value-added chemicals, i.e. "solar fuels" when produced from renewable energies. The expertise and knowledge existing in the ITED division on low temperature plasma physics and its diagnostics triggered establishment of P4G group in 2017.

The paradigm shift currently taking place in the energy sector redefines the value of energy forms and therefore makes the use of excess production from intermittent renewable energy sources attractive for synthesis of liquid fuels from raw materials such as CO_2, syngas or biomethane. Besides the classical conversion by electrochemical and thermochemical synthesis, the conversion through plasma processes becomes a promising option. Low temperature plasmas (non-equilibrium or thermal) offer unique opportunities for tuning processes in the gas phase, and in gas interaction with surfaces. Compared with the so far established processes, large amounts of reactive species can be produced on demand, without use of rare-earth materials. State-of-the-art is an energy efficiency of about 50 %, but pushing the value higher mostly comes at a price of largely reduced conversion efficiency. So far a limited number of systematic studies have been carried out worldwide [1,2,3].

Activities of the Plasma for Gas Conversion (P4G) group started in 2017 with focus on investigating CO_2 microwave plasmas. Compared to other plasma discharges being developed for CO_2 valorization, the chosen technology of microwave plasmas (MW) allows treating large gas flows with short transit times at highest energy efficiency and can be easy scaled up to the megawatts range. The research is aimed at fundamental understanding of the dynamic of the CO_2 plasma in order to determine dominant pathways of the CO_2 conversion in the pressure range from 0.3 to 1000 mbar (gas flows in vortex configuration up to 200 slm), and to find routes to optimize conversion and energy efficiency. In collaboration with other institutes (IGVP at University of Stuttgart, IHM and IMV at KIT) the incorporation in a complete cycle starting from CO_2 gas and renewable energy, until fuel is produced, is envisaged as part of the PoF IV program of the HGF. This cycle is composed of several steps where the plasma is involved in the first step of CO_2 dissociation into CO. Following steps are gas separation, hydrogen addition and synthesis step (such as Fischer-Tropsch synthesis) towards long hydrocarbon chains.

The first plasmas in air and in nitrogen were ignited in November 2017, in a provisional lab used to build the microwave plasma setup, to test the first plasma diagnostics (optical emission spectroscopy and mass spectrometry), and to gain knowledge of the available parameter space. In September 2018, first CO_2 plasma has been ignited in newly constructed lab designed and built according to the quite challenging safety regulations for CO_2 operation at large flows. Two microwave experiments operating at 2.45 GHz and power levels of up to 3 kW are established: the plasma torch operated in resonator configuration in the pressure range 10-1000 mbar (similar setup as IGVP) , and a surfaguide experiment operated in the pressure range 0.3-100 mbar. The plasma diagnostics comprise (i) nanosecond laser (gas temperature, rotational and vibrational temperatures), (ii) tunable dye laser (density of ground state species densities such as O and CO, and vibrational distribution of CO_2 molecules), (iii) calibrated mass spectrometer (gas analysis and determination of conversion and energy efficiency), (iv) fast optical emission spectroscopy (determination of rotational and vibrational temperatures, and excited species density), and (v) a fast ICCD camera for plasma imaging.

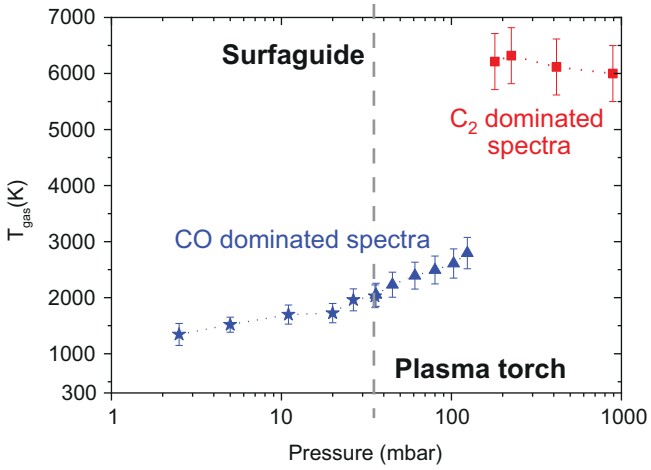

Figure 1: Gas temperature determined by optical emission spectroscopy from either molecular bands of CO or C_2 in the two microwave experiments covering the pressure range from 2 mbar to quasi-atmospheric pressure.

At non-equilibrium plasma conditions (the vibration temperature of a molecule is significantly higher than the rotational temperature of a molecule), two possible routes of CO_2 dissociation are possible; direct electron impact and vibration excitation, where the vibrational excitation route is energetically more efficient. In thermal equilibrium conditions, the CO_2 dissociation follows the thermal equilibrium at the given temperature [4]. Figure 1 shows the gas temperature determined by optical emission spectroscopy from the dominant species in the spectra, i.e. either the CO molecule or the C_2 molecule. Two plasma regimes can be clearly recognized separated by the sudden jump of the gas temperature at about 150 mbar. Below 150 mbar, the gas temperature increases with pressure from 1400 K to 3000 K, the plasma is diffusive and exhibits properties of a non-equilibrium plasma.

At pressure above 150 mbar the gas temperature is about 6000 K being comparable to the vibrational temperature, which means a thermal equilibrium is established. In addition, the plasma is in the contracting mode with the radius limited by the skin depth of the MW (2-4 mm) as measured with the ICCD images, while the inner radius of the quartz tube is 13 mm. Figure 2 shows the respective conversion and energy efficiency quantified by mass spectrometry for different gas flows and power levels of the discharges. In addition, the values expected by pure thermal dissociation are calculated using the measured gas temperature as input.

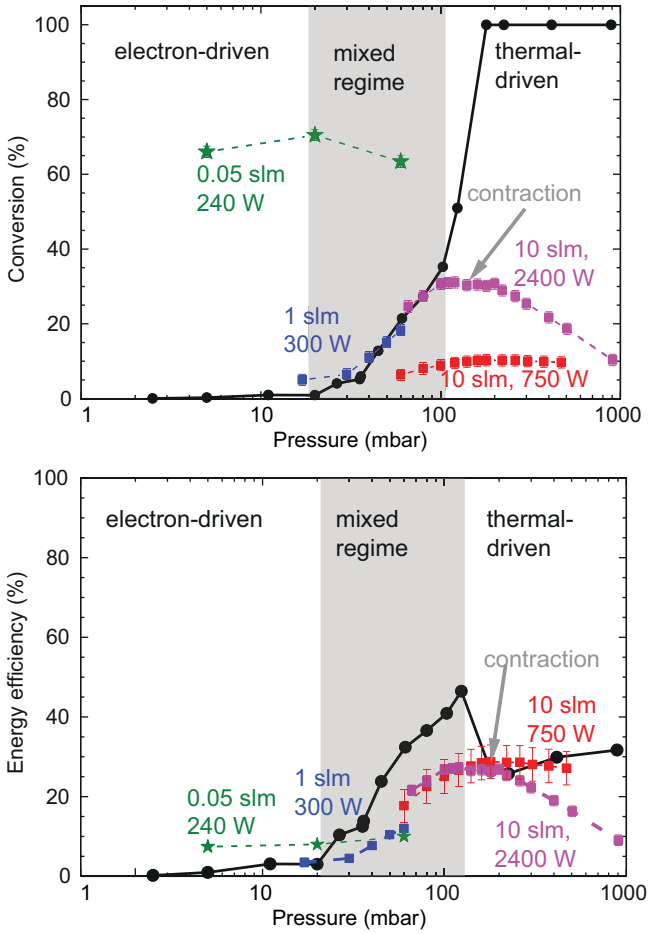

Figure 2: Conversion and energy efficiency measured in the microwave experiments as a function of pressure. For comparison the expected values of the thermal conversion process is given using the measured gas temperatures (figure 1).The pressure domain is divided according to the dominant dissociation mechanism (electron driven, thermal driven or mixed regime).

As expected, the electron-driven regime is distinguished by a high conversion (slightly above 60 %) but at cost of energy efficiency which is below 10 %. Contrary, conversion and energy efficiency of about 30 % can be reached simultaneously in the thermal-driven regime. In the pressure range between 20 mbar and 100 mbar (marked gray in figure 2) both electron driven and thermal driven dissociation contribute to the measured CO_2 dissociation. According to thermal dissociation the molecule should be fully dissociated, indicating that the conversion is restricted by the size of the plasma (limited by the skin depth), the backward reaction ($CO+O \rightarrow CO_2$), and efficiency of hot and cold gas mixing.

Experimentally, in the afterglow of the pulsed measurements the temperature decay of about 3×10^6 K/s has been measured, which according to chemistry model used to investigate the dominant reaction pathways is sufficiently high that the above mentioned recombination is negligible. To investigate gas mixing of hot plasma and surrounding cold gas, the swirl configuration has been modelled by turbulent fluid calculations. The estimated inward radial flux of CO_2 gas from the edge towards the center of the plasma is calculated to be comparable with the total CO outflow from the plasma. This indicates that in the contracted mode the CO production is limited by the inward CO_2 flow into the plasma, which is driven by a turbulent gas mixing. The fluid simulations and pulsed measurements demonstrate that gas flow dynamics limits the conversion rates and therefore the gas temperature gradients drive CO_2 dissociation rates. To enhance the effect of gas mixing, modifications of the plasma torch have been started. Adding a nozzle in the effluent an increase of conversion and energy efficiency of about 50 % is measured at quasi-atmospheric pressure (conversion increased from 14 % to 22 %, energy efficiency increased from 17 % to 26 %).

In general, the optimization of thermal or non-equilibrium plasmas depends on the route to follow: for energy storage one would prefer high energy efficiency even at lower conversion rates coupled with re-use of unconverted CO_2 gas and hence use thermal plasmas. For CO_2 valorization where available energy is abundant high conversion rates can be achieved with non-equilibrium.

From 2021 the group and the activities will expand within the PoF IV framework (MTET, topic of chemical energy carriers, subtopic power-based fuels and chemicals) in the created collaboration network of IGVP (U Stuttgart), EPP (U Augsburg), KIT, and FZJ. In addition to CO_2 conversion, it is planned to investigate plasma activation of low-energy molecules such as methane to contribute to the hydrogen technologies utilizing, e.g., the dry reforming process ($CH_4+CO_2 \rightarrow 2CO+2H_2$). Also N_2 conversion via N_2/H_2 plasmas (for ammonia formation or hydrogen storage) will be started together with plasma catalysis processes.

Scientific Staff

U. Fantz, E. Carbone, A. Hecimovic, F. D'Isa, L. Vialetto, C. Brochet.

Magnetic Confinement of Electron-Positron Plasma PAX, APEX and EPOS

Head: Prof. Dr. Thomas Sunn Pedersen

Efforts to create the first magnetically confined, low-temperature electron-positron plasma are advancing. We are building a levitated dipole trap and beginning plans for an optimized stellarator. Intense positron pulses will be delivered from an accumulation and storage system soon to be installed on the NEPOMUC positron source. Experiments in a prototype dipole trap demonstrated lossless injection and well-confined single particle orbits.

Overview of the Project

Successful creation of a magnetically confined quasi-neutral electron-positron plasma with a Debye length much smaller than the system size would open a new frontier for laboratory plasma physics. If, in addition to mass symmetry, the two species have the same density and temperature profiles, theory predicts linear, and in some situations, non-linear stability to typical sources of microturbulence in magnetized plasmas. There is some chance that this system could be the world's first laboratory plasma that is free of anomalous transport. It would also represent a clean test of gyrokinetic theory and simulation in the electrostatic limit due to the very small normalized plasma pressure (beta) and gyroradius. The experimental approach is shown in figure 1. We use the intense positron source NEPOMUC at the FRM II reactor and a sequence of positron traps (Positron Accumulation eXperiment – PAX) for cooling, compressing and storing large numbers of positrons (ultimately up to 10^{11}). The stored positrons will be delivered to one of two magnetic traps, a levitated dipole (A Positron-Electron eXperiment – APEX) or an optimized stellarator (Electrons and Positrons in an Optimized Stellarator – EPOS). This ERC grant funded project benefits from collaborations with the Technische Universität München (Christoph Hugenschmidt and Markus Singer), University of California San Diego (Cliff Surko and James Danielson), Tokyo University (Haruhiko Saitoh), the University of Greifswald (Lutz Schweikhard and Stephan König), and Lawrence University (Matt Stoneking), as well with the Stellarator Theory group at IPP (Per Helander, Alexey Mishchenko, and Daniel Kennedy).

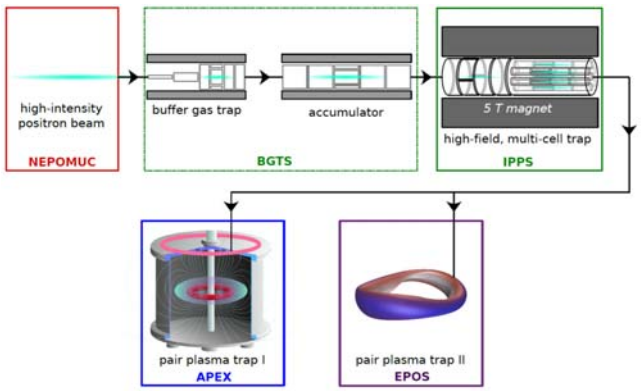

Figure 1: Overview of the strategy for creating a magnetically confined electron-positron plasma. Positrons from the NEPOMUC source at FRM II reactor are cooled, compressed, accumulated and, ultimately stored in the PAX (BGTS+IPPS) system. They are then delivered in pulses to either the APEX levitated dipole or the EPOS stellarator and combined with electrons.

Positron Accumulation – PAX

To achieve plasma densities (at temperatures in the range of 0.1-1 eV) in a 10 liter confinement volume will require 10^{10}-10^{11} positrons, and an equal number of electrons. We are modifying a buffer-gas-trap and accumulator system for installation on the NEPOMUC beamline. Such traps are standard apparatus in positron research and can collect, cool, compress, and store up to 10^9 positrons. This installation will augment the capabilities of the NEPOMUC positron source for experimenters doing materials research as well as for the plasma physics experiments described here. Further, we are developing a high-capacity positron storage system that uses a 5-T superconducting magnet. This requires perfecting techniques from the field of non-neutral plasma physics in order to shelve positron pulses coming from the accumulator into a set of up to 21 storage cells.

Levitated Dipole – APEX

The dipole magnetic field is common in astrophysical settings where it is observed to confine plasma. In an earthbound laboratory, the circular coil required to produce such a field must be magnetically levitated and there are a few examples of such experiments (e.g. LDX at MIT and RT-1 in Tokyo). We are building a compact levitated dipole to trap electron-positron plasma (see figure 2 for a schematic).

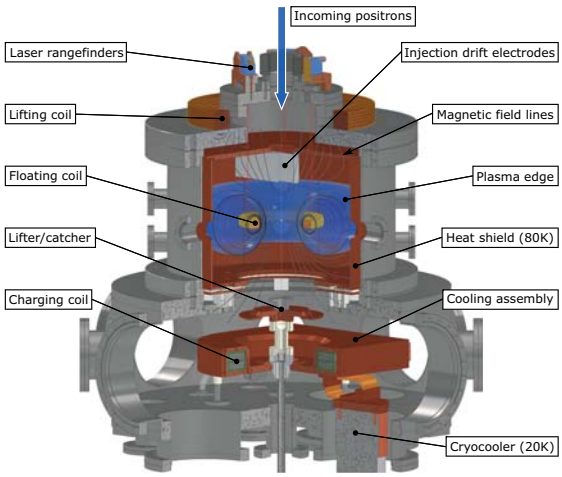

Figure 2: Design of the APEX levitated dipole. Positrons enter from above and are transferred to the closed field line region using E×B drift, magnetic mirroring and electrostatic reflection. The main magnetic field is produced by a levitated high temperature superconducting coil. Levitation is accomplished using a water-cooled lifting coil after mechanical lifting of the floating coil from the cooling and charging station located in the lower chamber.

This device uses a high T_c superconducting coil (with mass <2 kg, radius approximately 7.5 cm and current >30 kA-t) to produce fields around one tesla close to the coil. The coil is inductively charged using a second superconducting coil and magnetically levitated using a water-cooled copper coil that employs active feedback to stabilize the levitation. The SC coils have been ordered and will be delivered by 31.01.2021. We anticipate achieving levitation times longer than one hour by shielding the coil from room-temperature thermal radiation using a cooled (80 K) copper shield. Positrons from the PAX storage system will be delivered in pulses and moved onto closed field lines using an E×B drift technique. We will either pre-load electrons in the trap (since the dipole configuration can support either non-neutral or quasi-neutral plasma equilibria) or inject them in pulses alternating with the arrival of positron pulses.

Prototype Dipole – Positron Injection and Trapping

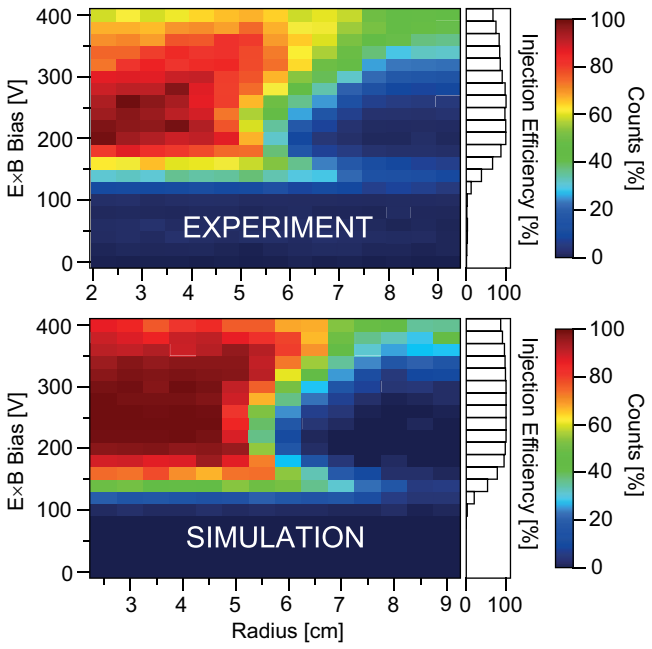

Figure 3: Heat maps of (a) experimental and (b) simulated gamma ray counts due to annihilation of positrons on an insertable target probe as a function of probe insertion and bias on the electrodes used to drift positrons onto field lines in the confinement region. Lossless injection is achieved in the region of darkest red. Simulations produce a close match to the experimental measurements when all significant trap asymmetries are included.

We developed the E×B drift injection technique using a prototype trap with a supported permanent magnet to produce the dipole field. Positrons from both the primary and re-moderated NEPOMUC beams have been successfully injected into the dipole field without losses using a combination of E×B drift, magnetic mirroring, and electrostatic reflection. Particle trajectory simulations that accurately model the magnetic and electrostatic fields in this experiment produce a good match to experimental measurements (figure 3) and offer guidance in designing the levitated dipole and stellarator traps. In addition to injection, the confinement of positrons in the single-particle regime has been measured in the prototype trap. Figure 4 shows the confinement under two conditions, A and B. In condition A an electrostatic bias was applied to the magnet to reduce positron losses on the magnet surface. In this case, the confinement is longer than one second, and is limited by diffusion associated with collisions with residual gas neutrals. In the levitated dipole experiment, lower residual pressure will extend the lifetime of single-particle orbits and fewer particles will be lost on the coil since particles that would do so will pass through the center of the coil instead. Recently, we successfully injected positrons into the prototype trap in the presence of a substantial electron space charge, an encouraging result for future efforts to achieve plasma densities.

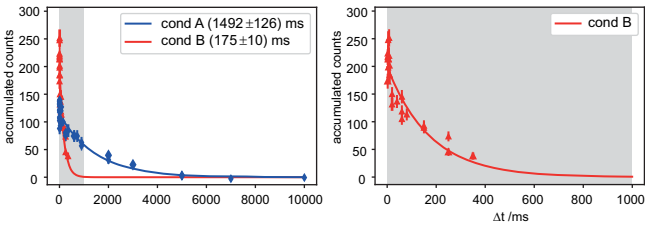

Figure 4: Gamma ray counts reflecting positron annihilation when the prototype trap is dumped by switching on certain electrodes at the desired dump time. In condition A, the magnet was biased positively to eliminate losses on its surface, leading to confinement in excess of one second. In condition B, significant losses occurred on the grounded magnet. In both cases, diffusion is consistent with elastic scattering by residual gas atoms.

Optimized Stellarator – EPOS

Eve Stenson is leading the development of an optimized stellarator for electron-positron plasma studies. This project is supported by a Helmholtz Young Investigator grant (started 01.12.2019) and is synergistic with as well as complementary to the levitated dipole. Stellarator optimization algorithms continue to advance at a rapid rate and this project is positioned to both benefit from and contribute to those advances. Since the target optimization parameters for positron-electron plasma confinement are quite different from those of a fusion-relevant device, this project permits a test of optimization in a new parameter regime. At this point, the device is imagined to have a roughly 10 liter confinement volume and make use of high temperature superconducting coils and perhaps 3D printed coil forms.

Scientific Staff

T. Sunn Pedersen, H. Saitoh (thru 2018), M. R. Stoneking (2019-present), E. V. Stenson, U. Hergenhahn, J. Horn-Stanja, A. Deller (2019-present), A. Card (2019-present), S. Nißl, M. Singer, P. Steinbrunner (2019-present), N. Paschkowski, A. Zettl (2020).

Publications, Figures and References

Publications
2017-2020

Bibliography

The bibliography – articles, books and inbooks, conference papers, theses, PhD-theses, habilitations, laboratory reports, lectures – can be found under the link
https://www.ipp.mpg.de/publications

Patents

Brendel, A. with colleagues from MTU Aero Engines GmbH: Verschleißschutzbeschichtung mit Rissstopp-Funktion durch Rissumleitung. Freigabe der Deutschen Patentanmeldung 10 2010 060 152.7 am 19.09.2017.

Brockmann, R.: Verfahren und Vorrichtung zur Leckprüfung. Erfindungsmeldung: 21.03.2005. Freigabe der Deutschen Patentanmeldung 502007004486 am 31.01.2017.

Erckmann, V., Dammertz, G. and Schmid, M.: Advanced collector sweeping with homogenous power deposition of electron beams in high-power rf vacuum tubes. Freigabe des Japanischen Patents am 12.09.2017.

Pedersen, T. S. and Paschkowski, N.: Anordnung elektrischer Leiter und Verfahren zur Herstellung einer Anordnung elektrischer Leiter. Erteilung des Deutschen Patents für die Deutsche Patentanmeldung 10 2014 017 857.9 am 03.01.2017. Benennung folgender Länder im Zuge der nationalen Phase aus der PCT Anmeldung: Japan, Südkorea, China, USA und Kanada.

Pedersen, T. S. and Paschkowski, N.: Anordnung elektrischer Leiter und Verfahren zur Herstellung einer Anordnung elektrischer Leiter. Erteilung der Chinesischen Patentanmeldung CN107210110B am 09.11.2018. Erteilung der europäischen Patentanmeldung Nr. 15798332.1 am 26.07.2018 (Europäisches Patent 3 227 894).

Krampitz, R. and MOL Katalysatortechnik GmbH: Verfahren zur Wasserbläschen-Beize von Edelstahl-Schweißnähten. Erfindungsmeldung vom 24.04.2019. Inanspruchnahme der Erfindung durch das IPP. Deutsche Patentanmeldung durch die Firma MOL, IPP als Mitanmelder.

Manhard, A., von Toussaint, U. and Stienecker, M.: Lateral hochaufgelöster Wasserstoffdiffusionsnachweis durch optische Indikatormethode. Erfindungsmeldung vom 06.06.2019. Inanspruchnahme der Erfindung durch das IPP. Derzeitige Ausarbeitung einer Deutschen Patentanmeldung durch die Patentanwälte.

Pedersen, T. S. and Paschkowski, N.: Anordnung elektrischer Leiter und Verfahren zur Herstellung einer Anordnung elektrischer Leiter. Aufgabe des Dt. Patents Nr. 10 2014 017 857 beim DPMA aufgrund des Doppelschutzverbotes am 13.11.2019. Weiterführung des Deutschen Patents innerhalb des Europäischen Patents 3 227 894.

Mlynek, A., Ford, O. and Plöckl, B.: Drehhalterung zur Drehung eines optischen Elements, insbesondere für ein Polarimeter. Erteilung des Deutschen Patents Nr. 10 2015 007 729 am 16.01.2020.

Heinemann, B., Hopf, C., Fröschle, M., Eckerskorn, M. and den Harder, N.: Ion beam extraction system with variable grid gap for extended operational space. Erfindungsmeldung vom 27.01.2020. Die Erfindung wurde durch das IPP in Anspruch genommen. Einreichung einer Patentanmeldung PCT/EP2020/067321 am 22.06.2020.

Sunn Pedersen, T. and Paschkowski, N.: Anordnung elektrischer Leiter und Verfahren zur Herstellung einer Anordnung elektrischer Leiter. Aufgabe der US-Patentanmeldung Nr. 15/531,570, der Japanischen Patentanmeldung Nr. 2017-529988, der Kanadischen Patentanmeldung Nr. 2,967,703 sowie der Koreanischen Patentanmeldung Nr. 10-2017-7016980.

Manhard, A., von Toussaint, U. and Stienecker, M.: Lateral hochaufgelöster Wasserstoffdiffusionsnachweis durch optische Indikatormethode. Erfindungsmeldung vom 06.06.2019. Inanspruchnahme der Erfindung durch das IPP. Einreichung einer Deutsche Patentanmeldung Nr. 10 2020 111 959.3 am 04.05.2020

Kaunert, K. and Kurzan, B.: Laserlichtschranke. Erfindungsmeldung vom 11.08.2020. Inanspruchnahme der Erfindung durch das IPP. Ausarbeitung einer Deutschen Patentanmeldung durch die Patentanwälte.

Electronic Report

For a complete electronic version of this report follow the link www.ipp.mpg.de/report_en.

Figures

ASDEX Upgrade

Fig. 4: U. Plank et al., Nuclear Fusion Letter 60, 74001 (2020).
Fig. 5: M. Griener et al., Nuclear Materials and Energy (submitted).
Fig. 6: M. Cavedon et al., Nuclear Materials and Energy 18, 275-280 (2019), doi: 10.1016/j.nme.2018.12.034.
Fig. 7: D. Silvagni et al., Nuclear Fusion 60, 126028 (2020).
Fig. 8: M Willensdorfer et al., Plasma Physics and Controlled Fusion 58, 114004 (2016).
Fig. 9: N Leuthold, Ph.D. Thesis, Ludwig-Maximilian University Munich, May 2020.
Fig. 10: L Sanchis et al., Plasma Physics and Controlled Fusion 61, 014038 (2019).
Fig. 11: M Faitsch et al., Nuclear Materials and Energy 12, 1020 (2017).
Fig. 12: D Brida et al., Nuclear Fusion 57, 116006 (2017).
Fig. 13: J. R. Pinzon et al., Nuclear Fusion 59, 074002 (2019).
Fig. 14: T. Luda et al., Nuclear Fusion 60, 036023 (2020); T. Luda et al., Ph.D. Thesis, Aix-Marseille University (2020); Nuclear Fusion (to be submitted).

Wendelstein 7-X

Figs. 7-10: H.-S. Bosch et al., IEEE Transactions on Plasma Science, 48(6), 1369-1375 (2020).
Fig. 21: A. Pavone et al., Review of Scientific Instruments 89, 10K102 (2018).
Fig. 26: Photo: G.Wurden, LANL.

ITER Cooperation Project

Fig. 5: F. Mackel et al., Fusion Engineering and Design 146, Part A, 622-625 (2019).

Plasma-facing Materials and Components

Fig.: Photo: H. Gietl, IPP.

Theoratical Plasma Physics

Fig. 2 (left): A. Di Siena et al., Nuclear Fusion 58, 054002 (2018).
Fig. 2 (right): A. Di Siena et al., Nuclear Fusion 59, 124001 (2019).
Fig. 4: O. Linder et al., Nuclear Fusion 60, 096031 (2020).
Fig. 14 (left): G. G. Plunk et al., Physical Review Letters 118, 105002, (2017).
Fig. 14 (right): G. G. Plunk and A. Bañón Navarro, New Journal of Physics 19(2), 025009, (2017); G. G. Plunk, Physics of Plasmas 24, 034506 (2017).
Fig. 15: G. G. Plunk et al., Physical Review Letters 122, 035002 (2019).
Fig. 16: J. A. Alcusón et al., Plasma Physics and Controlled Fusion, 62, 035005 (2020).

Max Planck Princeton Research Center for Plasma Physics

Fig. 1: P. Helander et al., Physical Review Letters 124, 095001 (2020).

Magnetic Confinement of Electron-Positron Plasma PAX, APEX and EPOS

Fig. 1: M. R. Stoneking et al., Journal of Plasma Physics (submitted).
Fig. 3: S. Nißl et al., Physics of Plasmas 27, 052197 (2020).
Fig. 4: J. Horn-Stanja et al., Physical Review Letters 121, 235003 (2018).

References

ASDEX Upgrade

[1] V. Rohde et al., Fusion Engineering and Design 157, 111630 (2020).
[2] M. Schubert et al., EPJ Web of Conferences 87, 02010 (2015).
[3] A. Herrmann et al., Fusion Engineering and Design 146, 920-923 (2019).
[4] J. Stober et al., Plasma Physics and Controlled Fusion 62, 024012 (2020).
[5] C.-P. Käsemann et al., Fusion Engineering and Design 146, 714-718 (2019), doi: 10.1016/j.fusengdes.2019.01.062.
[6] N. Arden et al., Fusion Engineering and Design 146, 2698-2702 (2019), doi: 10.1016/j.fusengdes.2019.04.089.
[7] C.-P. Käsemann et al., Fusion Engineering and Design 123, 289-294 (2017), doi: 10.1016/j.fusengdes.2017.05.035.
[8] K. C. Behler et al., Fusion Engineering and Design 159, 111873 (2020), doi: 10.1016/j.fusengdes.2020.111873
[9] V. Bobkov et al., EPJ Web of Conferences 157, 03005 (2017), doi: 10.1051/epjconf/201715703005
[10] V. Bobkov et al., AIP Conference Proceedings 2254, 040005 (2020).
[11] W. Tierens et al., Nuclear Fusion 59, 046001 (2019) doi: 10.1088/1741-4326/aaf455.
[12] W. Zhang et al., Plasma Physics and Controlled Fusion 59, 075004 (2017), doi: 10.1088/1361-6587/aa6fe5.
[13] G. Suárez López et al., Plasma Physics and Controlled Fusion 61, 125019 (2019).
[14] M. Usolceva et al., Plasma Physics and Controlled Fusion 61, 115011 (2019), doi: 10.1088/1361-6587/ab476d.
[15] W. Tierens et al., Physics of Plasmas 27, 010702 (2020), doi: 10.1063/1.5128070.
[16] W. Zhang et al., Nuclear Fusion 60, 09600 (2020).
[17] R. Lunsford et al., NuclearFusion 59, 126034 (2019).
[18] T. Härtl et al., Fusion Engineering and Design 124, 283 (2017).
[19] O. Kudlacek et al., Fusion Engineering and Design 146, Pt. A, 1145-1148 (2019), doi: 10.1016/j.fusengdes.2019.02.026.
[20] O. Kudlacek et al., 12th IAEA Technical Meeting on Control, Data Acquisition and Remote Participation for Fusion Research (CODAC 2019). Daejeon, 2019-05-13 to 2019-05-17.
[21] T. C. Blanken et al., Fusion Engineering and Design 147, 111211 (2019) doi: 10.1016/j.fusengdes.2019.05.030.
[22] F. Felici et al., 28th IAEA Fusion Energy Conference (IAEA 2020), Nice, 2021-05-10 to 2021-05-15. https://conferences.iaea.org/event/214/contributions/17341/
[23] T. O. S. J. Bosman et al., 31st Symposium on Fusion Technology, Virtual Edition, 2020-09-20 to 2020-09-25.
[24] M. Bernert et al., Nuclear Fusion (accepted), doi: 10.1088/1741-4326/abc936
[25] M. Bernert et al., 28th IAEA Fusion Energy Conference (IAEA 2020), Nice, 2021-05-10 to 2021-05-15. https://conferences.iaea.org/event/214/contributions/17115/
[26] F. Janky et al., Fusion Engineering and Design 146, Pt. B, 1926-1929 (2019)
[27] E. Fable et al., 47th European Physical Society Conference on Plasma Physics (EPS 2020), Sitges, 2021-06-21 to 2021-06-25.
[28] W. Treutterer et al., Fusion Engineering and Design 146, Pt. A, 1073-1076 (2019).
[29] F. Janky et al., 12th IAEA Technical Meeting on Control, Data Acquisition and Remote Participation for Fusion Research (CODAC 2019), Daejeon. 2019-05-13 to 2019-05-17.
[30] M. Bernert et.al, Plasma Physics and Controlled Fusion 57, 014038 (2015).
[31] M. Maraschek et.al, Plasma Physics and Controlled Fusion 60, 014047 (2018).
[32] B. Sieglin et.al, Fusion Engineering and Design 161, 111958 (2020).
[33] G. F. Harrer et al., Nuclear Fusion 58, 112001 (2018), doi: 10.1088/1741-4326/aad757.
[34] G. Harrer et al., Nuclear Fusion (to be submitted).
[35] B. Labit et al., Nuclear Fusion 59, 086020 (2019), doi: 10.1088/1741-4326/ab2211.
[36] M. Faitsch et al., Nuclear Materials and Energy (submitted).
[37] J. Hillesheim et al., 27th IAEA Fusion Energy Conference. IAEA, Vienna, EX/4-1 (2019).
[38] U. Plank et al., Nuclear Fusion Letter 60, 74001 (2020), doi: 10.1088/1741-4326/ab8e11.
[39] M. Cavedon et al., Nuclear Fusion 60, 66026 (2020), doi: 10.1088/1741-4326/ab8777.
[40] Y. R. Martin et al., Journal of Physics: Conference Series 123, 012033 (2008).
[41] P. David et al., 17th International Workshop on H-mode Physics and Transport Barriers (HMWS 2019), Shanghai, 2019-10-09 to 2019-10-11; (to be submitted).
[42] M. Willensdorfer et al., Plasma Physics and Controlled Fusion (to be submitted).
[43] M. Griener et al., Review of Scientific Instruments 88, 033509 (2017), doi: 10.1063/1.4978629.
[44] M. Griener et al., Review of Scientific Instruments 89, 10D102 (2018), doi: 10.1063/1.5034446.
[45] M. Griener et al., Plasma Physics and Controlled Fusion 60, 025008 (2018), doi: 10.1088/1361-6587/aa97e8.
[46] M. Griener et al., Nuclear Materials and Energy (submitted).
[47] M. Griener et al., Plasma Physics and Controlled Fusion (to be submitted).
[48] D. I. Refy et al., Nuclear Fusion 60, 056004 (2020), doi: 10.1088/1741-4326/ab7594.
[49] M. Dunne et al., Plasma Physics and Controlled Fusion 59 014017 (2017), doi: 10.1088/0741-3335/59/1/014017.

[50] E. Wolfrum et al., Nuclear Materials and Energy 12, 18-27 (2017), doi: 10.1016/j.nme.2017.01.002.
[51] L. Frassinetti et al., Nuclear Fusion 59, 076038 (2019), doi: 10.1088/1741-4326/ab1eb9.
[52] A. Kallenbach et al., Plasma Physics and Controlled Fusion 60, 045006 (2018), doi: 10.1088/1361-6587/aaab21.
[53] L. Guimarais et al., Nuclear Fusion 58, 026005 (2018), doi: 10.1088/1741-4326/aaa339.
[54] F. M. Laggner et al., Nuclear Fusion 58, 046008 (2018), doi: 10.1088/1741-4326/aaaa43.
[55] M. Cavedon et al., Nuclear Materials and Energy 18, 275-280 (2019), doi: 10.1016/j.nme.2018.12.034.
[56] F. M. Laggner et al., Plasma Physics and Controlled Fusion 58, 065005 (2016), doi: 10.1088/0741-3335/58/6/065005.
[57] F. M. Laggner et al., Nuclear Fusion 58, 046008 (2018), doi: 10.1088/1741-4326/aaaa43.
[58] F. Mink et al., Plasma Physics and Controlled Fusion 58, 125013 (2016), doi: 10.1088/0741-3335/58/12/125013.
[59] A. F. Mink et al., Nuclear Fusion 58, 026011 (2018), doi: 10.1088/1741-4326/aa98f7.
[60] M. Hoelzl et al., Contributions to Plasma Physics 58 (6-8), 518-528 (2018), doi: 10.1002/ctpp.201700142.
[61] A. F. Mink et al., Plasma Physics and Controlled Fusion 60, 125011 (2018), doi: 10.1088/1361-6587/aae33a.
[62] E. Trier et al., Plasma Physics and Controlled Fusion 61, 045003 (2019), doi: 10.1088/1361-6587/aaf9c3.
[63] J. Galdon-Quiroga et al., Physical Review Letters 121, 025002 (2018), doi: 10.1103/PhysRevLett.121.025002.
[64] A. Medvedeva et al., Plasma Physics and Controlled Fusion 61, 085011 (2019), doi: 10.1088/1361-6587/ab2575.
[65] B. Vanovac et al., Nuclear Fusion 58, 112011 (2018), doi: 10.1088/1741-4326/aada20.
[66] L. Guimarais et al., Nuclear Fusion 59, 126041 (2019), doi: 10.1088/1741-4326/ab431b.
[67] V. Nikolaeva et al., Plasma Physics and Controlled Fusion 60, 055009 (2018), doi: 10.1088/1361-6587/aab4c5.
[68] F. M. Laggner et al., Plasma Physics and Controlled Fusion 60, 025002 (2018), doi: 10.1088/1361-6587/aa90bf.
[69] E. Viezzer et al., Nuclear Fusion 57, 022020 (2017), doi: 10.1088/0029-5515/57/2/022020.
[70] E. Viezzer et al., Nuclear Fusion 58, 026031 (2018), doi: 10.1088/1741-4326/aaa22f.
[71] E Viezzer et al., Plasma Physics and Controlled Fusion 62, 024009 (2020), doi: 10.1088/1361-6587/ab5b1d.
[72] T. Happel et al., Nuclear Materials and Energy 18, 159-165 (2019), doi: 10.1016/j.nme.2018.12.022.
[73] D. Silvagni et al., Nuclear Fusion 60, 126028 (2020).
[74] N. Bonanomi et al., (to be submitted).
[75] T. Happel et al., Nuclear Fusion (submitted).
[76] P. Manz et al., Nuclear Fusion 60, 96011 (2020),. doi: 10.1088/1741-4326/ab9e17
[77] L. Gil et al., Nuclear Fusion Letter 60, 54003 (2020), doi: 10.1088/1741-4326/ab7d1b.
[78] A. Kallenbach et. al., Nuclear Fusion (accepted) 2020, doi: 10.1088/1741-4326/abbba0.
[79] M. Willensdorfer et al., Plasma Physics and Controlled Fusion 58, 114004 (2016).
[80] M. Willensdorfer et al., Nuclear Fusion 57, 116047 (2017).
[81] D. A. Ryan et al., Plasma Physics and Controlled Fusion 59, 024005 (2017).
[82] D. A. Ryan et al., Plasma Physics and Controlled Fusion 60, 065005 (2018).
[83] D. A. Ryan et al., Plasma Physics and Controlled Fusion 61, 095010 (2019).
[84] Y. Liu et al., Physics of Plasmas 24, 056111 (2017).
[85] F. Orain et al., Nuclear Fusion 57, 22013 (2017).
[86] N. Leuthold et al., Plasma Physics and Controlled Fusion 59, 055004 (2017).
[87] W. Suttrop et al., Nuclear Fusion 58, 096031 (2017).
[88] T. Eich et al., Nuclear Materials and Energy 12, 84-90 (2017).
[89] M. Willensdorfer et al., Physical Review Letters 119, 085002 (2017).
[90] M. Willensdorfer et al., Plasma Physics and Controlled Fusion 61, 14019 (2019).
[91] T. Cote et al., Nuclear Fusion 59, 16015 (2019).
[92] N. Leuthold, Ph.D. Thesis, Ludwig-Maximilian University Munich, May 2020.
[93] M. Valovic et al., Plasma Physics and Controlled Fusion 60, 085013 (2019).
[94] F. Orain et al., Physics of Plasmas 26, 042503 (2019).
[95] J. Galdon Quiroga et al., Physical Review Letters 121, 25002 (2018).
[96] L. Sanchis et al., Plasma Physics and Controlled Fusion 61, 014038 (2019).
[97] M. Faitsch et al., Nuclear Materials and Energy 12, 1020 (2017).
[98] M. Faitsch et al., Plasma Physics and Controlled Fusion 61, 14008 (2019).
[99] D. Brida et al., Nuclear Materials and Energy 19, 205 (2019).
[100] D. Brida et al., Nuclear Fusion 57, 116006 (2017).
[101] P. Manas et al., Nuclear Fusion 59, 014002 (2019).
[102] P. A. Schneider et al., Nuclear Fusion 57, 066003 (2017).
[103] P. A. Schneider et al., Nuclear Fusion (to be submitted).
[104] F. Ryter et al., Nuclear Fusion 59, 096052 (2019).
[105] N. Bonanomi et al., Nuclear Fusion 59, 126025 (2019).
[106] A. Kappatou et al., 27th IAEA Fusion Energy Conference, IAEA, Vienna, EX/P8-1 (2019).
[107] R. M. McDermott et al., Plasma Physics and Controlled Fusion 60, 095007 (2018).
[108] A. Kappatou et al., Plasma Physics and Controlled Fusion 60, 055006 (2018).

[109] R. M. McDermott, Nuclear Fusion (to be submitted), (2020).
[110] A. Kappatou et al., Nuclear Fusion 59, 056014 (2019).
[111] C. Bruhn et al., Plasma Physics and Controlled Fusion 60, 085011 (2018).
[112] P. Manas et al., Plasma Physics and Controlled Fusion 59, 035002 (2017).
[113] P. Manas et al., Nuclear Fusion 60, 056005 (2020).
[114] C. Angioni et al., Nuclear Fusion 57, 056015 (2017).
[115] C. Angioni et al., Nuclear Fusion 57, 022009 (2017).
[116] T. Odstrcil et al., Plasma Physics and Controlled Fusion 60, 014003 (2018).
[117] C. Angioni et al., Nuclear Fusion 57, 116053 (2017).
[118] C. Angioni et al., Physics of Plasmas 25, 082517 (2018).
[119] E. Fable et al., Nuclear Fusion 59, 076042 (2019).
[120] W. Hornsby et al., Nuclear Fusion 57, 046008 (2017).
[121] W. Hornsby et al., Nuclear Fusion 58, 056008 (2018).
[122] J. R. Pinzon et al., Nuclear Fusion 59, 074002 (2019).
[123] R. Bielajew et al., 46th EPS Conference on Plasma Physics, European Physical Society, Geneva, P5.1017 (2019).
[124] R. Ochoukov et al., Review of Scientific Instruments 89, 10 (2018).
[125] R. Ochoukov et al., Nuclear Fusion 59, 014001 (2019).
[126] R. Ochoukov et al., Nuclear Fusion 59, 086032 (2019).
[127] R. Ochoukov et al., in preparation (2020).
[128] A. Kappatou et al., 45th EPS Conference on Plasma Physics, European Phyical Society, Geneva, O2.105 (2018); in preparation (2020).
[129] G. Tardini et al., Nuclear Fusion 59, 046002 (2019).
[130] A. Jakobsen et al., 45th EPS Conference on Plasma Physics, European Phyical Society, Geneva, P5.1042 (2018).
[131] A. van Vuuren et al., Review of Scientific Instruments 90, 103501 (2019)
[132] A. van Vuuren, Ph.D. Thesis (2020); in preparation (2020).
[133] E. Fable et al., Nuclear Fusion 56, 026012 (2016).
[134] C. Angioni et al., Nuclear Fusion 59, 106007 (2019).
[135] I. Erofeev et al., Nuclear Fusion 57, 126067 (2017).
[136] T. Luda et al., Nuclear Fusion 60, 036023 (2020).
[137] T. Luda et al., Ph.D. Thesis, Aix-Marseille University (2020); Nuclear Fusion (to be submitted).
[138] F. Ryter et al., Nuclear Fusion (to be submitted), (2020).
[139] G. Verdoolaege et al., Nuclear Fusion (to be submitted), (2020).
[140] R. Dux et al., Nuclear Fusion 60, 126039 (2020), doi: 10.1088/1741-4326/abb748.
[141] H. J. Sun et al., Plasma Physics and Controlled Fusion 59, 105010 (2017), doi: 10.1088/1361-6587/aa7777.
[142] H. J. Sun et al., Plasma Physics and Controlled Fusion 61, 014005 (2019), doi: 10.1088/1361-6587/aae33c.
[143] H. J. Sun et al., Plasma Physics and Controlled Fusion 62, 025005 (2019), doi: 10.1088/1361-6587/ab5259.
[144] T. Eich et al., Nuclear Fusion 60, 056016 (2020), doi: 10.1088/1741-4326/ab7a66.
[145] B. D. Scott, Physics of Plasmas 12, 062314 (2005).
[146] P. Manz et al., Physics of Plasmas 27, 22506 (2020), doi: 10.1063/1.5133839.
[147] T. Eich et al., Nuclear Materials and Energy 12, 84-90 (2017), doi: 10.1016/j.nme.2017.04.014.
[148] D.Silvagni et al., Nuclear Fusion 60, 126028 (2020), doi: 10.1088/1741-4326/abb423.
[149] D. Brida et al., Plasma Physics and Controlled Fusion 62 105014 (2020).
[150] T. Nishizawa et al., Plasma Physics and Controlled Fusion 62, 085005 (2020).
[151] Lunt T. et al., Plasma Physics and Controlled Fusion 62, 105016 (2020). doi: 10.1088/1361-6587/aba9ff.
[152] M. Griener et al., Review of Scientific Instruments 89, 10D102 (2018), doi: 10.1063/1.5034446.
[153] M. Griener et al., Review of Scientific Instruments 88, 33509 (2017), doi: 10.1063/1.4978629.
[154] M. Griener et al., Plasma Physics and Controlled Fusion 60, 025008 (2018), doi: 10.1088/1361-6587/aa97e8.
[155] A. Drenik et al., Physica Scripta T170, 014021 (2017).
[156] A. Drenik et al., Nuclear Fusion 59, 04601 (2019).
[157] T. Reichbauer et al., Fusion Engineering and Design 149, 111325 (2019).
[158] K. Krieger et al., Physica Scripta T170, 14030 (2017).
[159] I. Zammuto et al., Fusion Engineering and Design 136, 1052-1057 (2018).
[160] R. Neu et al., Journal of Nuclear Materials 511, 567-573 (2018).
[161] A. Bock. et al., Nuclear Fusion 57, 126041 (2017).
[162] A. Bock et al., Physics of Plasmas 25, 056115 (2018).
[163] J. Stober et al., Plasma Physics and Controlled Fusion 62, 024012 (2020).
[164] M. Reisner et al., Nuclear Fusion 60, 082005 (2020).
[165] I. Krebs et al., Physics of Plasmas 24, 102511 (2017).
[166] O. Ford et al., Review of Scientific Instruments 86, 093504 (2016).
[167] R. Fischer et al., Fusion Science and Technology 69, 526-536 (2016).
[168] R. Fischer et al., Nuclear Fusion 59, 056010 (2019).
[169] V. Igochine et.al., Nuclear Fusion 57,116027 (2017).
[170] V. Igochine et.al., 47th European Physical Society Conference on Plasma Physics (EPS 2020), Sitges, 2021-06-21 to 2021-06-25.
[171] Ye. O. Kazakov et al., 27th IAEA Fusion Energy Conference, IAEA, Vienna, EX/8-1 (2018).
[172] Y. Kazakov et al., “Physics and applications of 3-ion ICRF scenarios for fusion research”, Physics of Plasmas (to be submitted).
[173] A. Kappatou et al., 45th EPS Conference on Plasma Physics, European Physical Society, Geneva, O2.105 (2018).

[174] A. Kappatou et al., Nuclear Fusion (accepted) (2020), doi: 10.1088/1741-4326/abca57.
[175] M. Mantsinen et al., 47th European Physical Society Conference on Plasma Physics (EPS 2020), Sitges, 2021-06-21 to 2021-06-25.
[176] V. Bobkov et al., AIP Conference Porceedings 2254, 040005 (2020).
[177] M. Mantsinen et al., 28th IAEA Fusion Energy Conference, Nice, 2021-05-10 to 2021-05-15 https://conferences.iaea.org/event/214/contributions/17312/.

JET Cooperation

[1] J. Hobirk et al., Nuclear Fusion 58, 076027 (2018).
[2] N. Bonanomi et al., Nuclear Fusion 59, 96030, (2019).
[3] S. Glöggler et al., Nuclear Fusion 59, 126031 (2019).
[4] M. Bernert et al., Nuclear Materials and Energy 12, 111-118 (2017).
[5] M. Faitsch et al., Plasma Physics and Controlled Fusion 62, 085004 (2020).
[6] A. V. Chankin et al., Plasma Physics and Controlled Fusion 61, 075010 (2019).
[7] T. Eich et al., Nuclear Fusion Letter 58, 034001 (2018).
[8] M. Sertoli et al., Review of Scientific Instruments 89, 113501 (2018).
[9] C. Angioni et al., Physics of Plasmas 25, 82517 (2018).
[10] N. Bonanomi et al., Nuclear Fusion 59, 126025, (2019).
[11] A. V. Chankin et al., Plasma Physics and Controlled Fusion 60, 115011 (2018).

Wendelstein 7-X

[1] S. A. Bozhenkov et al., Nuclear Fusion 60, 066011 (2020).
[2] R. C. Wolf et al., Physics of Plasmas 26, 082504 (2019).
[3] C. D. Beidler et al., Nature (submitted).
[4] M. Jakubowski et al., Physical Review Letters (submitted), (2020).
[5] A. Langenberg et al., Physics of Plasmas 27, 052510 (2020).
[6] R. C. Wolf et al., Plasma Physics and Controlled Fusion 61, 014037 (2019).
[7] M. Zanini et al., Nuclear Fusion 60, 106021 (2020).
[8] A. Spanier et al., Fusion Engineering and Design (submitted), (2020).
[9] S. Äkäslompolo et al., Nuclear Fusion 58, 082010 (2018).
[10] S. Äkäslompolo et al., Fusion Engineering and Design 146A, 862 (2019).
[11] S. A. Lazerson et al., Nuclear Fusion 60, 076020 (2020).
[12] H. W. Patten et al., Physical Review Letters 124, 155001 (2020).
[13] A. Pavone et al., Review of Scientific Instruments 89, 10K102 (2018).
[14] A. Pavone et al., Plasma Physics and Controlled Fusion 61, 075012 (2019).
[15] O. Ford et al., Review of Scientific Instruments 91, 023507 (2020).
[16] K. J. Brunner et al., Journal of Instrumentation 13, P09002 (2018).
[17] K. J. Brunner et al., Journal of Instrumentation 14, P11016 (2019).
[18] W. Biel et al., Fusion Eng. Design 146, 465 (2019).
[19] N. Chaudhary et al., Journal of Instrumentation 15, P09024 (2020), doi:10.1088/1748-0221/15/09/P09024.
[20] K. Ogawa et al., Journal of Instrumentation 14, C09021 (2019).
[21] S. Äkäslompolo et al., Journal of Instrumentation 14, C10012 (2019).
[22] S. A. Lazerson et al., Review of Scientific Instruments 90, 09350 (2019).
[23] D. Moseev et al., Review of Scientific Instruments 90, 013503 (2020).
[24] D. Moseev et al., Journal of Instrumentation 15, C05035 (2020).
[25] L. Krier et al., Physics of Plasmas (submitted), (2020).
[26] J. P. Koschinsky et al., Contributions to Plasma Physics 60, e201900186 (2020).
[27] G. Fuchert at al., Nuclear Fusion 60, 036020 (2020).
[28] A. Dinklage et al., Nuclear Fusion 59, 07601 (2019).

Joint Research Projects on ASDEX Upgrade and Wendelstein 7-X

[1] M. Zanini et al., Nuclear Fusion 60, 106021 (2020).
[2] E. Strumberger and S. Günter, Nuclear Fusion 60, 106013 (2020).
[3] Y. Qingquan et al., Nuclear Fusion 60, 076024 (2020).
[4] T. Lunt et al., Plasma Physics and Controlled Fusion 62, 105016 (2020), doi: 10.1088/1361-6587/aba9ff.
[5] K. Schmid and T. Lunt, Nuclear Materials and Energy 17, 200 (2018).
[6] K. Schmid and T. Lunt, Physica Scripta T171, 014006 (2020).
[7] T. Nishizawa et al., Plasma Physics and Controlled Fusion 62, 085005 (2020).
[8] V. Perseo et. al., Review of Scientific Instruments 91, 013501 (2020).
[9] V. Perseo et. al., Nuclear Fusion 59, 124003 (2019).
[10] B. Geiger et al., Nuclear Fusion 59, 046009 (2019).
[11] Th. Wegner et al., Nuclear Fusion (accepted).
[12] R. McDermott, Plasma Physics and Controlled Fusion 60, 095007 (2018).
[13] U. Stroth et al., Nuclear Fusion (accepted), doi: 10.1088/1741-4326/abbc4a.

ITER Cooperation Project

[1] B. Heinemann et al., Fusion Engineering and Design 136, 569 (2018).
[2] D. Wünderlich et al., Nuclear Fusion 59, 084001 (2019).
[3] D. Wünderlich et al., Review of Scientific Instruments 90, 113304 (2019).
[4] A. Mimo et al., Review of Scientific Instruments 91, 013510 (2020).
[5] W. Kraus et al., AIP Conference Proceedings 2052, 040004 (2018).
[6] C. Wimmer et al., Review of Scientific Instruments 91, 013509 (2020).
[7] E. Poli et al., Nuclear Fusion 55, 013023 (2015).
[8] H. Weber et al., EPJ Web of Conferences 8, 01002 (2015).
[9] A. Köhn et al., Plasma Physics and Controlled Fusion 60, 075006 (2018).
[10] A. Snicker et al., Plasma Physics and Controlled Fusion 60, 014020 (2018).
[11] A. Pataki et al., Fusion Engineering and Design 146, 2479-2482 (2019).
[12] F. Penzel et al., Review of Scientific Instruments 89, 10E109 (2018).
[13] H. Meister et al., Fusion Engineering and Design (accepted), (2020).
[14] F. Penzel et al., Fusion Engineering and Design 121, 100-104 (2017).
[15] H. Meister et al., Fusion Engineering and Design 146, 1015-1018 (2019).
[16] A. Arkhipov et al., Fusion Engineering and Design 146, Pt. A, 1262-1266 (2019).
[17] F. Mackel et al., Fusion Engineering and Design 146, Pt. A, 622-625 (2019).
[18] A. Arkhipov et al., IEEE Transactions on Plasma Science 48, 1661-1665 (2020).
[19] Bandaru V. et al., Physical Review E 99, 063317 (2019).
[20] Krebs I. et al., Physics of Plasmas 27, 022505 (2020).
[21] P. Aleynikov and B. N. Breizman, Nuclear Fusion 57, 046009 (2017).
[22] C. Paz-Soldan et al., Physical Review Letters 118, 255002 (2017).
[23] C. Paz-Soldan et al., Nuclear Fusion 59, 066025 (2019).
[24] B. N. Breizman et al., Nuclear Fusion 59, 083001 (2019).

Theoratical Plasma Physics

[1] C. D. Stephens et al., Physics of Plasmas 24, 102517 (2017).
[2] P. Crandall et al., Computer Physics Communications 255, 107360 (2020)
[3] R. W. Brzozowski et al., Physics of Plasmas 26, 042511 (2019).
[4] C. D. Stephens et al., Physics of Plasmas 27, 052504 (2020)
[5] A. Di Siena, Ph.D. Thesis, University of Ulm (2019)
[6] C. D. Stephens, https://gitlab.com/qualikiz-group/QuaLiKiz-documents/-/blob/master/reports/Stephens_QuaLiKiz_Derivation.pdf
[7] M. Maurer et al., Journal of Computational Physics 420, 109694 (2020).
[8] A. Bañón Navarro et al., Plasma Physics and Controlled Fusion 62, 105005 (2020).
[9] D. Michels et al., Computer Physics Communications (submitted).
[10] J. Citrin et al., Physical Review Letters 111, 155001 (2013).
[11] A. Di Siena et al., Nuclear Fusion 58, 054002 (2018).
[12] A. Di Siena et al., Physics of Plasmas 26, 052504 (2019).
[13] A. Di Siena et al., Physical Review Letters 125, 105002 (2020)
[14] A. Di Siena et al., Nuclear Fusion 59, 124001 (2019).
[15] A. Mishchenko et al., Computer Physics Communications 238, 194 (2019).
[16] A. Biancalani et al., Plasma Physics and Controlled Fusion 59, 054004 (2017).
[17] A. Biancalani et al., Journal of Plasma Physics 84, 725840602 (2018).
[18] F. Vannini et al., Physics of Plasmas 27, 042501 (2020).
[19] I. Novikau, et al., Physics of Plasmas 27, 042512 (2020).
[20] O. Linder et al., Nuclear Fusion 60, 096031 (2020)
[21] M. Weiland et al., Nuclear Fusion 58, 082032 (2018).
[22] M. Weiland et al., Nuclear Fusion 59, 086002 (2019).
[23] R. Fischer et al., Nuclear Fusion 59, 056010 (2019).
[24] A. Stegmeir et al., Physics of Plasmas 26, 052517 (2019).
[25] W. Zholobenko et al., Contributions to Plasma Physics 60(5-6), e201900131 (2020).
[26] T. Body et al., Contributions to Plasma Physics 60(5-6), e201900139 (2020).
[27] M. Boesl et al., Contributions to Plasma Physics 60(5-6), e201900117 (2020).
[28] D. Grošelj et al., Astrophysical Journal 847, 28 (2017).
[29] D. Grošelj et al., Physical Review Letters 120, 105101 (2018).
[30] D. Grošelj et al., Physical Review X 9, 031037 (2019).
[31] E. Strumberger and S. Günter, Nuclear Fusion 57, 016032 (2017).
[32] E. Strumberger and S. Günter, Nuclear Fusion 59, 106008 (2019).
[33] Yu Q. et al., Nuclear Fusion 58, 054003 (2018).
[34] M. Hoelzl et al., "The JOREK non-linear extended MHD code and applications to large-scale instabilities and their control in magnetically confined fusion plasmas. Nuclear Fusion" (in preparation).
[35] I. Holod et al., "New developments regarding the JOREK solver and physics based preconditioner", Journal of Computational Physics (in preparation).

[36] V. Bandaru et al., Physical Review E 99, 063317 (2019).
[37] N. Nikulsin et al., Physics of Plasmas 26, 102109 (2019).
[38] I. Krebs et al., Physics of Plasmas 27, 022505 (2020).
[39] F. J. Artola et al., "3D simulations of vertical displacement events in tokamaks: A benchmark of M3D-C1, NIMROD and JOREK". Physics of Plasmas (submitted).
[40] D. Meshcheriakov et al., Physics of Plasmas 26, 042504 (2019).
[41] M. Hoelzl et al., Physics of Plasmas 27, 022510 (2020).
[42] V. Bandaru et al., "Magnetohydrodynamic simulations of runaway electron beam termination in JET". Plasma Physics and Controlled Fusion (in preparation).
[43] M. Hoelzl et al., Contributions to Plasma Physics 58, 518 (2018).
[44] F. Mink et al., Nuclear Fusion 58, 026011 (2018).
[45] A. Cathey Cevallos et al., "Non-linear magnetohydrodynamic simulations of type I edge localized mode cycles intokamak plasmas and their underlying triggering mechanism". Nuclear Fusion (accepted).
[46] F. Orain et al., Physics of Plasmas 26, 042503 (2019).
[47] S. Futatani et al., "Transition from no-ELM response to pellet ELM triggering during pedestal build-up -- insights from extended MHD simulations". Nuclear Fusion (submitted)
[48] A. Cathey et al., "Comparing natural and pellet triggered ELMs via non-linear extended MHD simulations". Plasma Physics and Controlled Fusion (in preparation)
[49] P. Helander and A. Zocco, Plasma Physics and Controlled Fusion, 60, 084006 (2018).
[50] G. G. Plunk et al., Physical Review Letters 118, 105002 (2017).
[51] G. G. Plunk and A. Bañón Navarro, New Journal of Physics 19, 025009 (2017);
G. G. Plunk, Physics of Plasmas 24, 034506 (2017).
[52] G. G. Plunk et al., Physical Review Letters 118, 105002 (2017).
[53] A. Zocco et al., Physics of Plasmas 27, 022507 (2020).
[54] G. G. Plunk et al., Physical Review Letters 122, 035002 (2019).
[55] G. G. Plunk. Journal of Plasma Physics, 86(4), 175860402 (2020), doi:10.1017/S0022377820000872.
[56] G. G. Plunk et al., Journal of Plasma Physics 83(4), 715830404 (2017).
[57] J. A. Alcusón et al., Plasma Physics and Controlled Fusion 62, 035005 (2020).
[58] G. G. Plunk et al., Journal of Plasma Physics 83(4), 715830404 (2017).
[59] J. A. Alcusón et al., Plasma Physics and Controlled Fusion 62, 035005 (2020).
[60] P. Helander, Journal of Plasma Physics 83(4), 715830401 (2017).
[61] P. Helander, Journal of Plasma Physics 86(2), 905860201 (2020).
[62] K. Aleynikova and A. Zocco, Physics of Plasmas 24, 092106 (2017).
[63] K. Aleynikova et al., Journal of Plasma Physics 84(6), 745840602 (2018).
[64] A. Zocco et al., Journal of Plasma Physics 84(3), 745840303 (2018).
[65] A. Sharma et al., Plasma Physics and Controlled Fusion 59, 105002 (2017).
[66] T Windisch et al., Plasma Physics and Controlled Fusion 59, 105002 (2017).
[67] A Zocco et al., Journal of Plasma Physics 85(6), 905850607 (2019).
[68] 15th IAEA Technical Meeting on Energetic Particles in Magnetic Confinement Systems, Princeton, NJ, 2017-09-05 to 2017-09-08 (Poster);
C. Slaby et al.: Nuclear Fusion 58, 082018 (2018), doi: 10.1088/1741-4326/aaaed3.
[69] 45th Conference on Plasma Physics (EPS 2018), Prague, 2018-07-02 to 2018-07-06 and Joint Varenna-Lausanne International Workshop on the Theory of Fusion Plasmas, Varenna, 2018-08-27 to 2018-08-31 (Poster);
C. Slaby et al., Journal of Physics: Conference Series 1125, 012019 (2018),
doi: 10.1088/1742-6596/1125/1/012019.
[70] C. Slaby et al., Nuclear Fusion 59, 046006 (2019), doi: 10.1088/1741-4326/aafe31.
[71] 12th IAEA Technical Meeting on Control, Data Acquisition and Remote Participation for Fusion Research (CODAC 2019). Daejeon, 2019-05-13 to 2019-05-17;
C. Slaby et al., Nuclear Fusion 60, 112004 (2020), doi: 10.1088/1741-4326/ab7c28.
[72] P. Aleynikov et al., Journal of Plasma Physics 85, 905850105 (2019).
[73] N. B. Marushchenko et al., Computer Physics Communications 185, 165-176 (2014).
[74] M. Hirsch et al., 46th EPS Conference on Plasma Physics, European Physical Society, Geneva, P2.1054 (2019).
[75] N. B. Marushchenko et al., EPJ Web of Conferences 203, 01006 (2019).
[76] A. Mishchenko et al., Journal of Plasma Physics 84(2), 905840201 (2018).
[77] M Drevlak et al., Nuclear Fusion 59, 016010 (2019).
[78] S. A. Henneberg et al., Nuclear Fusion 59, 026014 (2019).
[79] Lobsien et al., Journal of Plasma Physics 86(2), 815860202 (2020).
[80] Lobsien et al., Nuclear Fusion 60, 046012 (2020).
[81] A. Mishchenko et al., Journal of Plasma Physics, 84(2), 905840201 (2018).
[82] D. Kennedy et al., Journal of Plasma Physics 84(6), 905840606 (2018).

[83] D. Kennedy and A. Mishchenko, Journal of Plasma Physics 85(5), 905850502 (2019).
[84] D. Kennedy et al., Journal of Plasma Physics 86(2), 905860208 (2020).235003 (2018).

Max Planck Princeton Research Center for Plasma Physics

[1] P. Helander et al., Physical Review Letters 124, 095001 (2020).
[2] P. Helander et al., Nuclear Fusion 55, 053030 (2015).
[3] J. Alcuson et al., Plasma Physics and Controlled Fusion 62, 035005 (2020).
[4] R. Wolf et al., Physics of Plasmas 26, 082504 (2019).

Plasma for Gas Conversion

[1] R. Snoeckx and A. Bogaerts, Chemical Society Reviews 46 (19), 5805-5863 (2017), doi: 10.1039/c6cs00066e.
[2] A. J. Wolf et al., Plasma Sources Science and Technology 29, 025005 (2020), doi: 10.1088/1361-6595/ab5eca.
[3] F. D'Isa et al., Plasma Sources Science and Technology 29, 105009 (2020), doi: 10.1088/1361-6595/abaa84.
[4] A. Fridman, Plasma Chemistry, Cambridge University Press (2008).

Appendix

How to reach IPP in Garching

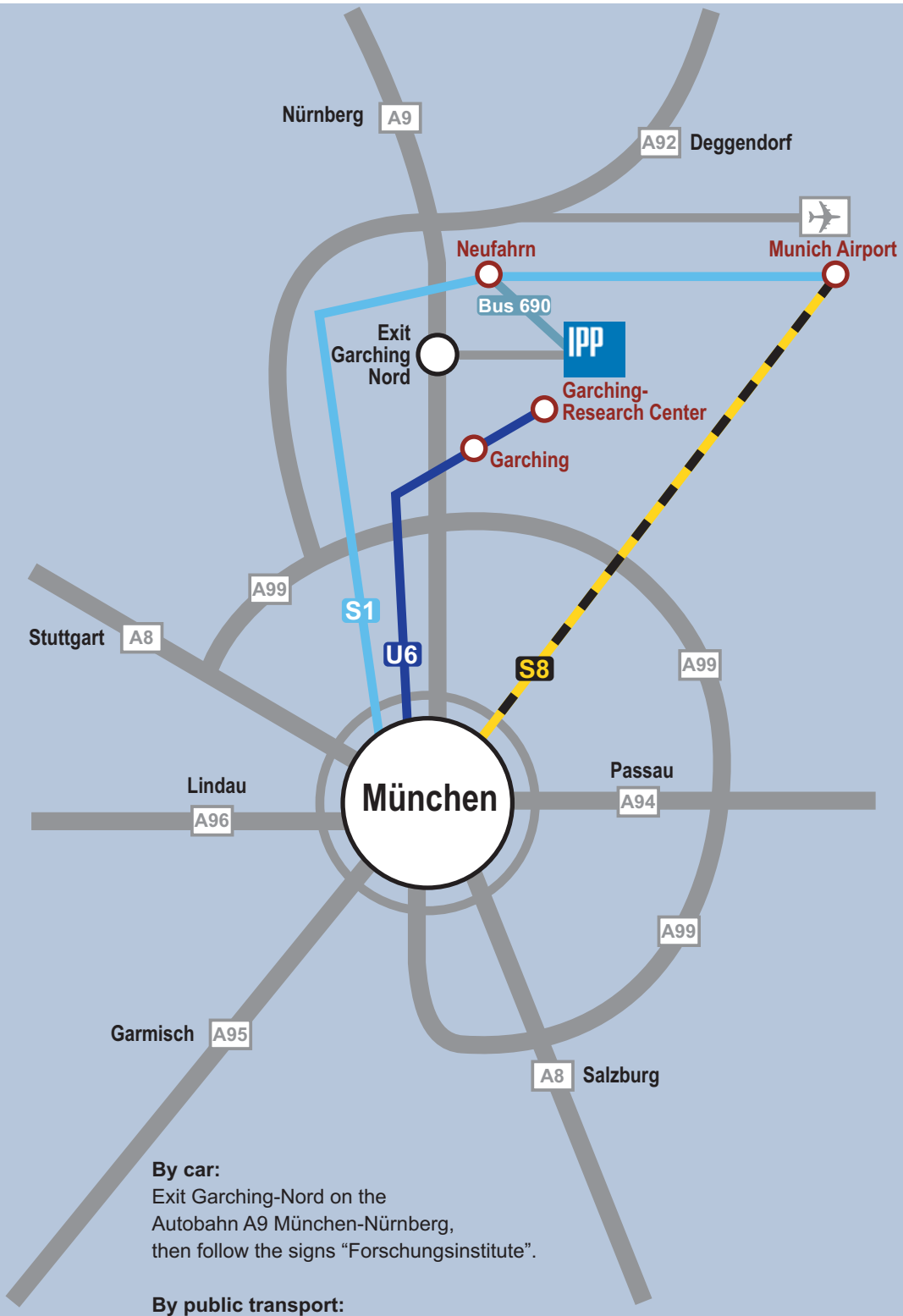

By car:
Exit Garching-Nord on the
Autobahn A9 München-Nürnberg,
then follow the signs “Forschungsinstitute”.

By public transport:
Any S metro from Munich Main Station to Marienplatz,
metro U6 to Garching-Forschungszentrum;
or from Airport Munich: S1 to Neufahrn, then bus 690
to "Garching Forschungszentrum" (only on weekdays).

How to reach Greifswald Branch Institute of IPP

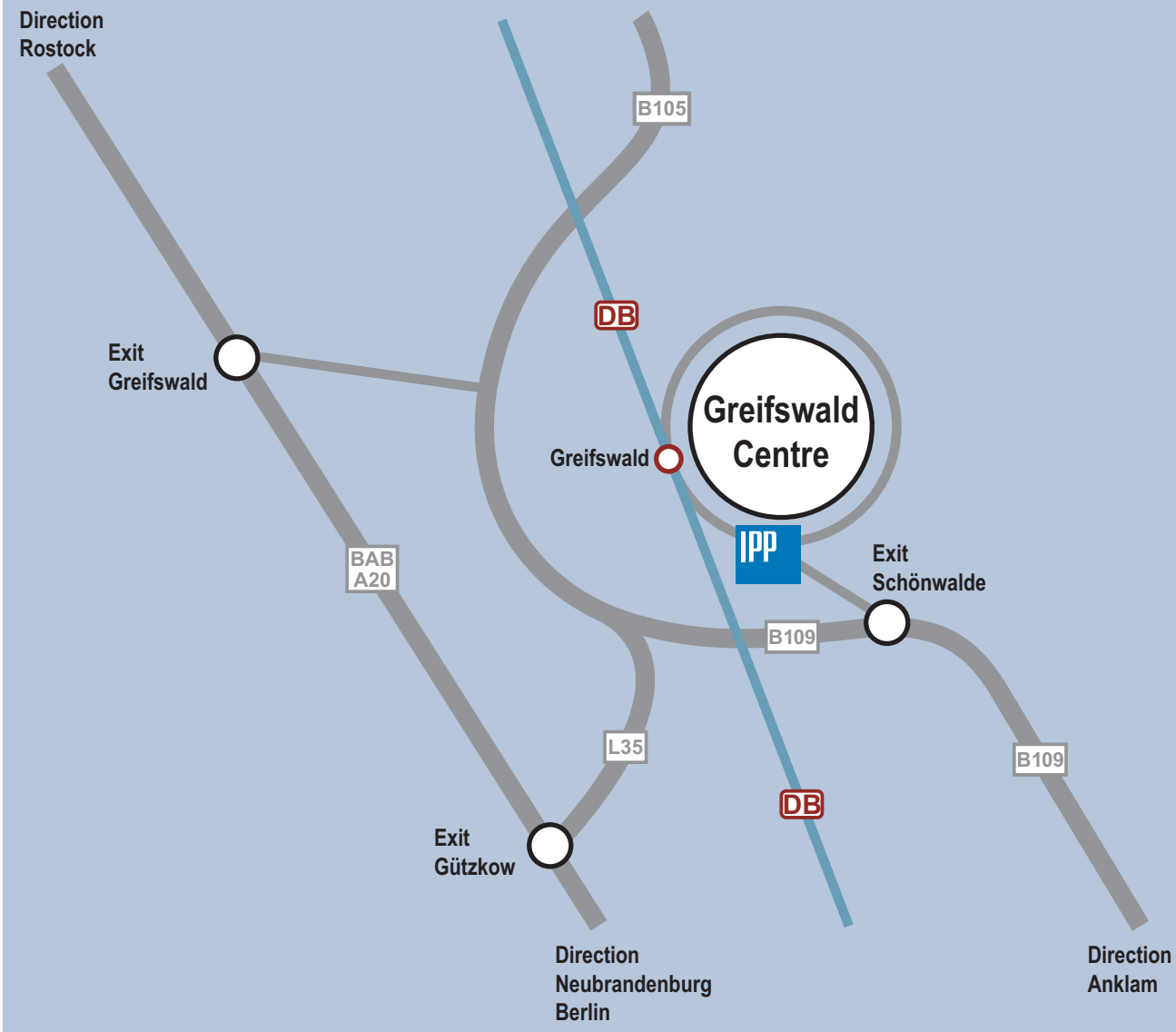

By air and train:
Via Berlin: from Berlin Brandenburg Airport (BER) by train to Berlin Hauptbahnhof (central station) or Berlin Gesundbrunnen, then by train to Greifswald main station
Via Hamburg: from the airport to main Railway Station, by train to Greifswald main station.

By bus:
From Greifswald-Railway Station (ZOB) by bus No. 3 to the "Elisenpark" stop.

By car:
Via Berlin, Neubrandenburg to Greifswald **or** via Hamburg, Lübeck, Stralsund to Greifswald, in Greifswald follow the signs “Max-Planck-Institut”.

IPP in Figures

Funding

In 2019 IPP received approx. 16 % of its total funding from the European Union. Of the basic national funding 90 % is met by the Federal Government and 10 % by the states of Bavaria and Mecklenburg-West Pomerania. European and national funding amounted to approx. 130 million euros.

Scientific Staff

At the end of September 2019 IPP had a total of 1.171 members of staff, 453 of them worked at IPP's Greifswald site. The workforce comprised 277 researchers and scientists, 83 postgraduates and 68 postdocs

Organisational Structure

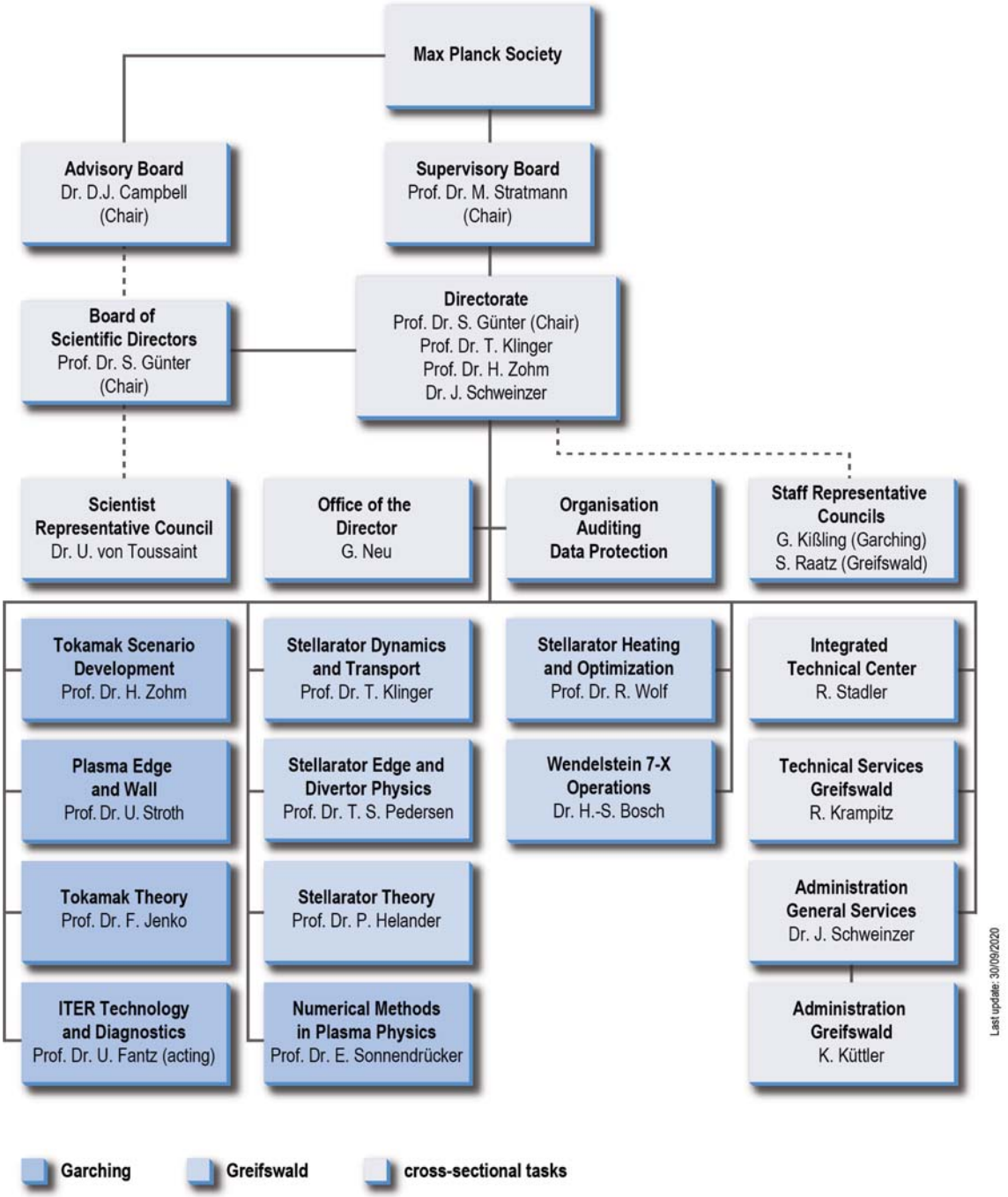

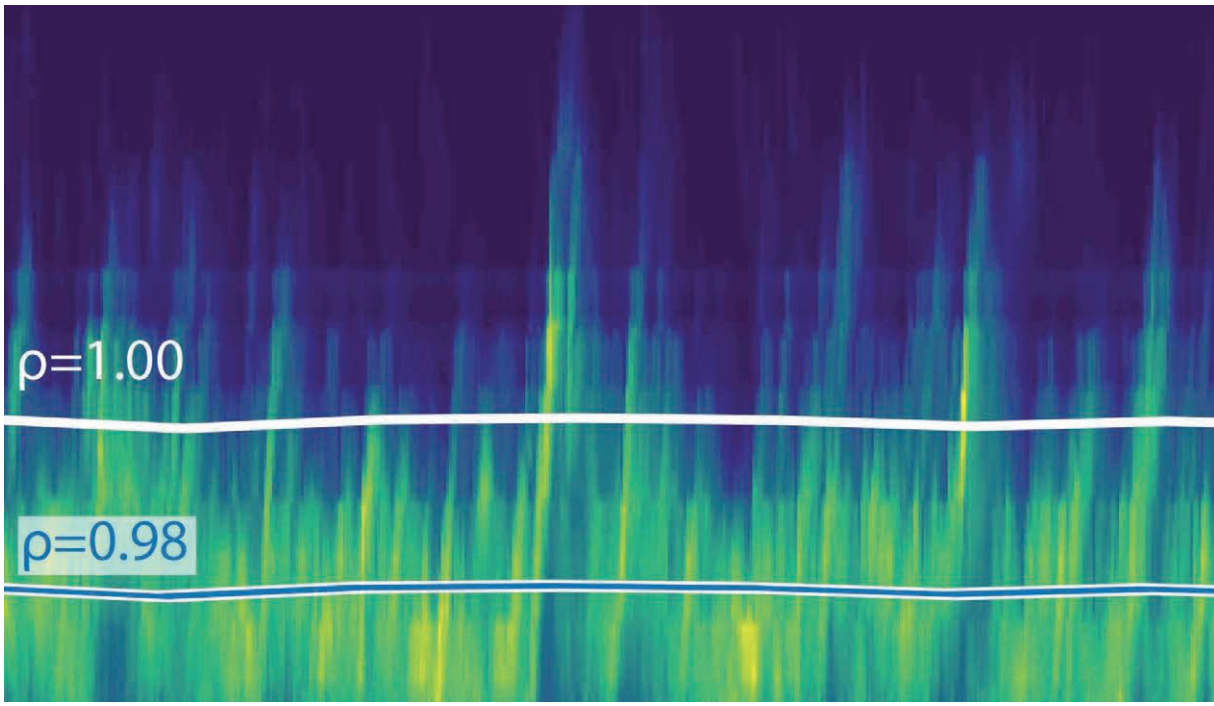

Imprint

Scientific Report 2017 - 2020
Max-Planck-Institut für Plasmaphysik (IPP)
Boltzmannstraße 2, D-85748 Garching bei München
phone +49 89 3299-01, info@ipp.mpg.de,
www.ipp.mpg.de

Technical Editor
Andrea Henze

Further Information
Part of this work has been carried out within the framework of the EUROfusion Consortium and has received funding from the European Union's Horizon 2020 research and innovation programme under grant agreement number 633053. The views and opinions expressed herein do not necessarily reflect those of the European Commission.

All rights reserved
Reproduction – in whole or in part – subject to prior written consent of IPP and inclusion of the names of IPP and the author.

Printing
Lerchl Druck, Freising
2020 Copyright by IPP, Printed in Germany, ISSN 0179-9347

Max-Planck-Institut
für Plasmaphysik